

NORTHWESTERN UNIVERSITY

Tribology and Corrosion in CoCrMo Alloys and Similar Systems

A DISSERTATION

SUBMITTED TO THE GRADUATE SCHOOL
IN PARTIAL FULFILLMENT OF THE REQUIREMENTS

for the degree

DOCTOR OF PHILOSOPHY

Field of Materials Science and Engineering

By

Emily E. Hoffman

Evanston, IL

March 2017

© Copyright by Emily E. Hoffman, 2017

All Rights Reserved

Tribology and Corrosion in CoCrMo Alloys and Similar Systems

Emily E. Hoffman

The artificial hip is a rich environment for the tribologist. This research investigated tribology and corrosion in CoCrMo alloy hip implants and extended the characterization methods and analyses to similar systems. The first project examined differences in corrosion behavior in the biomedical CoCrMo alloy using TEM and EDS. At the corroding grain boundaries, we found nanoscale chromium-rich carbides. These carbides caused chromium depleted zones which leads to corrosion, a process commonly referred to as sensitization. The chromium depletion and grain boundary crystallography data were used to develop a model showing nanoscale sensitization initiated grain boundary crevice corrosion. The next area of research looked at nanotribology of solid lubricants and formation of tribolayers. In situ TEM was used to directly observe the sliding interface of nanoflakes of molybdenum disulfide. Investigating low friction mechanisms of the lamellar solid lubricant revealed that the deck-of-cards sliding assumption present in the literature was not true. Instead, we showed sliding and transfer layer formation occurred at one interface only. The in situ sliding tests also revealed that the nanoflakes are unstable during sliding due to rolling, reorientation, flake pull apart, and adhesion changes. The final project analyzed a variety of carbon tribofilms, including the tribolayer found in metal-on-metal hips and the varnish tribofilm that forms in industrial machines. We characterized the carbon varnish film and showed similarities to published work on other graphitic carbon films. By comparing the nanoscale bonding and formation mechanisms, striking similarities were found that could inspire future cross-discipline advancements. Together, this work examined the relationships between wear, corrosion, and tribology to connect nanoscale structure and composition to applied performance.

Acknowledgments

First I would like to acknowledge my advisor Laurie. Thank you for being patient and encouraging. Thank you for allowing me to make my graduate experience my own with the programs and the internship that I wanted to pursue. Additionally, I would like to thank my committee, Dr. Ken Shull, Dr. Peter Voorhees, Dr. Markus Wimmer, and Dr. Ali Erdemir.

There are many people who helped me scientifically. Ben Myers, thank you for managing the FIB and for always being willing to help troubleshoot. To the TEM managers, Jinsong Wu at EPIC, Alan Nicholls at UIC, and Jie Wang and Nestor Zaluzec at Argonne, thank you for your training and help. Thank you for giving me the skills I needed to complete this thesis.

Thank you to the excellent Marks Group, both past and current. It has been a pleasuring sharing the journey of graduate school with you. Yifeng, I am glad that I had you as a mentor when I entered the Marks Group. Your calm, patience, sense of humor, and intelligence were traits to learn from. Pooja, thank you for starting your interesting work on the CoCrMo samples. It was great to learn from you and carry on the work. Thank you Alex, we have accomplished so much together. Thanks to Tiffany for putting together a great webpage for my tribology videos.

I've met many wonderful and interesting people during graduate school who have encouraged me. Thank you to the wonderful mat scis. It's been a pleasure to be in this department with such fun, smart, and caring people. I have been proud to be part of MSSA and every mat sci IM sports team. Ricardo, Bernie, Elizabeth, Dana, and Sauza, thank you for the food adventures, cook outs, yoga, and plain old goofing off. To my wonderful roommate David, I could not have asked for a better roommate in my last year of grad school. To Stephanie, thank you for diving into the world of SWE with me, it's been fun. Thank you to Erin, for listening to me when I needed to talk the most. Thanks to Ellen, who got me to volunteer at the Moth in Chicago, befriended me, and

introduced me to her welcoming group of friends. Asa, Emily, Sam, Margaret, and Emily, thank you for all the camping, picnics, and perspective.

To my family, thank you for always believing that I would be successful. Thank you to my mom and dad for listening to me as I worried and providing a relaxing and loving home to escape to for the holidays. Thank you to my siblings Amanda, Ethan, Maddie, and Becca. And always thank you to my best friend, Laurel, who is basically family too.

To my partner Sam, thank you. I am so glad I found you. Thank you for encouraging me to bike around the city and drink Belgian beer. Thank you for asking me about my research and my career aspirations. Thank you for reading over my cover letters and doing case practices with me. Thank you for proofing my work, including this thesis. I look forward the fun to be had with you.

I also want to formally acknowledging my funding sources. The majority of this work was funded by the National Science Foundation, Grant Number CMMI-1030703. The experiments in Chapters 4 and 5 were performed at the Electron Microscopy Center of the Center for Nanoscale Materials at Argonne National Laboratory, a U.S. Department of Energy, Office of Science, Office of Basic Energy Sciences User Facility under Contract No. DE-AC02-06CH11357. I would also like to thank ATI Allvac for the original donation of the CoCrMo alloy materials used in Chapters 2 and 3, and C.C. Jensen and Dyna Power Parts of the varnish materials used in Chapter 6.

I have been personally funded through the Department of Defense National Defense Science and Engineering Graduate Fellowship (NDSEG). In 2012, I was funded by the Biotechnology Training Center Cluster Program, a National Science Foundation training program. In 2013, I received a fellowship from my sorority through the Delta Gamma Foundation Graduate Fellowship. I am thankful to have been well-supported throughout my graduate career.

List of Abbreviations

| | |
|--------|--|
| ADF | annular dark field |
| AFM | atomic force microscopy |
| APT | atom probe tomography |
| BCS | bovine calf serum |
| BF | bright field |
| CDZ | chromium depleted zone |
| CoCrMo | cobalt chromium molybdenum |
| CSL | coincidence site lattice |
| CVD | chemical vapor deposition |
| DLC | diamond like carbon |
| DF | dark field |
| DOS | degree of sensitization |
| EBSD | electron back scatter diffraction |
| EDS | energy dispersive X-ray spectroscopy |
| EELS | electron energy loss spectroscopy |
| EIS | electrochemical impedance spectroscopy |
| EPR | electrochemical potentiokinetic reactivation |
| ETEM | environmental transmission electron microscopy |
| FIB | focused ion beam |
| FTIR | Fourier transform infrared spectroscopy |
| GACC | grain boundary assisted crevice corrosion |

| | |
|---------------------|---|
| HAADF | high angle annular dark field |
| HC | high carbon |
| HOPG | highly ordered pyrolytic graphite |
| IF-MoS ₂ | fullerene like molybdenum disulfide |
| IGC | intergranular corrosion |
| IGSCC | intergranular stress corrosion cracking |
| LEAP | laser emission atom probe |
| MEMS | microelectromechanical system |
| MoM | metal-on-metal |
| MoP | metal-on-polyethylene |
| MoS ₂ | molybdenum disulfide |
| NEMS | nanoelectromechanical system |
| OIM | orientational image mapping |
| PBS | phosphate buffered saline |
| PVD | pulse vapor deposition |
| SIFT | soft interface fracture transfer |
| SIMS | secondary ion mass spectroscopy |
| STEM | scanning transmission electron microscopy |
| TEM | transmission electron microscopy |
| THA | total hip arthroplasty |
| UHMWPE | ultra-high molecular weight polyethylene |
| VTR | video tape recorder |
| XPS | X-ray photoelectron spectroscopy |

Contents

| | | |
|-------|---|----|
| 1 | Background..... | 25 |
| 1.1 | Tribology..... | 25 |
| 1.2 | Hip Implants..... | 27 |
| 1.3 | Solid Lubricants | 30 |
| 1.4 | Microscopy: TEM and In-situ TEM | 33 |
| 1.5 | Outline of Research..... | 36 |
| 2 | Grain Boundary Assisted Crevice Corrosion in CoCrMo Alloys | 38 |
| 2.1 | Introduction..... | 39 |
| 2.2 | Grain Boundary Sensitization | 42 |
| 2.3 | Methods..... | 48 |
| 2.3.1 | CoCrMo Alloy..... | 48 |
| 2.3.2 | Electrochemical Corrosion Testing | 49 |
| 2.3.3 | Electron Backscatter Diffraction | 50 |
| 2.3.4 | White Light Interferometry | 51 |
| 2.3.5 | Focused Ion Beam | 52 |
| 2.3.6 | Transmission Electron Microscopy and Energy Dispersive X-ray Spectroscopy | 53 |
| 2.3.7 | Atom Probe Tomography | 54 |
| 2.4 | Results..... | 54 |

| | |
|---|-----|
| | 9 |
| 2.5 Grain Boundary Assisted Crevice Corrosion (GACC) Model..... | 65 |
| 2.5.1 Local Grain Boundary Attack..... | 66 |
| 2.5.2 Including the Role of Crevice Corrosion..... | 70 |
| 2.6 Discussion | 72 |
| 2.7 Conclusions | 76 |
| 3 Effect of Coincident Site Lattice and Chromium Segregation on Grain Boundary Assisted Crevice Corrosion in CoCrMo Alloys | 77 |
| 3.1 Introduction | 78 |
| 3.2 Methods..... | 81 |
| 3.2.1 Sample Preparation..... | 81 |
| 3.2.2 Scanning Electron Microscopy..... | 82 |
| 3.2.3 White Light Interferometry | 83 |
| 3.2.4 Focused Ion Beam | 84 |
| 3.2.5 Transmission Electron Microscopy | 84 |
| 3.3 Results | 85 |
| 3.3.1 Grain Boundary Misorientation..... | 85 |
| 3.3.2 Effect of Misorientation on Carbide Precipitates | 90 |
| 3.3.3 HAADF and EDS Quantification of Chromium Depletion..... | 93 |
| 3.4 Corrosion (GACC) Model Expansion to Type II Grain Boundaries | 99 |
| 3.5 Discussion | 103 |
| 3.6 Conclusions | 105 |

| | |
|--|-----|
| | 10 |
| 4 Soft Interface Fracture Transfer in Nanoscale MoS ₂ | 106 |
| 4.1 Introduction | 107 |
| 4.2 Experimental Methods | 112 |
| 4.3 Results | 114 |
| 4.4 Discussion | 120 |
| 4.5 Conclusions | 125 |
| 4.6 Video Captions..... | 126 |
| 5 Molybdenum Disulfide Sliding Modes | 127 |
| 5.1 Introduction | 127 |
| 5.2 Materials and Methods..... | 132 |
| 5.3 Results | 134 |
| 5.4 Discussion | 144 |
| 5.5 Conclusions | 147 |
| 5.6 Video Captions..... | 148 |
| 6 Graphitic Carbon Films Across Systems..... | 149 |
| 6.1 Introduction | 150 |
| 6.2 Systems | 154 |
| 6.2.1 Friction Polymers | 155 |
| 6.2.2 DLC Coatings | 160 |

| | | |
|-------|--|-----|
| | | 11 |
| 6.2.3 | Varnish in industrial machines | 161 |
| 6.2.4 | MoM Hips..... | 167 |
| 6.2.5 | MEMS | 169 |
| 6.2.6 | Non-tribology: Catalysis Coke | 171 |
| 6.2.7 | Other Examples: Cast Iron, Video Tape, Nanocomposite Coating | 173 |
| 6.3 | Mechanisms of Formation..... | 176 |
| 6.3.1 | Pressure, Temperature, and Friction..... | 176 |
| 6.3.2 | Depositions and Adsorption | 178 |
| 6.3.3 | Polymerization and Organometallics..... | 180 |
| 6.3.4 | Catalytic Activity and Fresh Surfaces | 182 |
| 6.3.5 | Graphitization | 184 |
| 6.3.6 | Nanoparticles and Metal Particles | 185 |
| 6.4 | Discussion | 186 |
| 6.4.1 | Similarities..... | 186 |
| 6.4.2 | Thermodynamics | 188 |
| 6.4.3 | Future Opportunities..... | 191 |
| 6.5 | Conclusions | 192 |
| 7 | Future Work..... | 194 |
| 7.1 | CoCrMo Alloy | 194 |
| 7.1.1 | Experiments with the Current CoCrMo Alloy Samples..... | 194 |
| 7.1.2 | Future Directions of CoCrMo Alloy Research..... | 195 |
| 7.2 | Varnish..... | 198 |

| | |
|--|-----|
| | 12 |
| 7.3 In situ..... | 200 |
| 7.3.1 Improving our Experimental Setup | 200 |
| 7.3.2 Further Analysis of Current Experiments..... | 204 |
| 7.3.3 Similar Materials | 207 |
| 7.3.4 New Collaborations for In Situ Sliding..... | 207 |
| 8 References..... | 210 |
| 9 Curriculum Vitae | 240 |

List of Tables

| | |
|---|----|
| Table 2.1 Composition of the high-carbon CoCrMo alloy. | 48 |
| Table 2.2 EDS quantification, Figure 2.14 carbide. | 62 |
| Table 2.3 EDS quantification, Figure 2.15 | 63 |
| Table 2.4 Summary of Averaged EDS quantifications. | 63 |
| Table 2.5 EDS quantification, Figure 2.16 carbide. | 64 |
| Table 3.1 High-carbon CoCrMo alloy composition. | 81 |
| Table 3.2 EDS quantification of key regions in Figure 3.10 | 95 |
| Table 3.3 EDS quantification of key regions in Figure 3.11 | 95 |
| Table 3.4 EDS quantification of key regions in Figure 3.12 | 96 |
| Table 3.5 EDS quantification of key regions in Figure 3.13 | 96 |

List of Figures

| | |
|---|----|
| Figure 1.1 An ancient tribologist in the tomb of Tehuti-Hetep, circa 1880 B.C. The man at the foot of the statue is pouring a lubricant (from Ref [1]). | 26 |
| Figure 1.2 Asperities on asperities as the magnitude of magnification increases. | 27 |
| Figure 1.3 (a) Complete total hip replacement system with modular parts and (b) X-ray showing implanted metal-on-metal hip replacement [10]. | 29 |
| Figure 1.4 The layered structure of MoS ₂ allows for low friction sliding between monolayer sheets. | 31 |
| Figure 1.5 Schematic of the holder. A tip is brought into contact with the sample during observation in the microscope. Both the normal force (AFM holder) and I-V characteristics can be measured during the experiments, in addition to normal TEM imaging and spectroscopies. | 35 |
| Figure 2.1 Carbide presence at a grain boundary may take the form of (a) a complete network along the grain boundary, (b) micron scale precipitates along some parts of the boundary, or (c) nanoscale precipitates unable to be seen at the micron scale. | 44 |
| Figure 2.2 From Panigrahi et al. [65]. Relative frequencies of grain boundary geometries for corroded and immune boundaries. The fcc grain boundary geometries are listed in order of decreasing lattice coincidence. | 46 |
| Figure 2.3 From Panigrahi et al. [65]. (a) As received wrought structure with 3-5 μm grains. (b) After 24 hour anneal at 1230 °C the grains grew to 100-300 μm with few second phases. (c) Corroded surface of as received wrought. (d) Corroded surface after 24 hour anneal at 1230 °C. Note the differing scale bars. | 49 |

- Figure 2.4 (a) SEM image showing a single grain boundary being cut from the bulk sample, (b) the lamellar viewed in SEM comprising of the two grains with the grain boundary, indicated by the dotted line down the middle, (c) a sample viewed in TEM again with the dotted line on the grain boundary, and (d) layout of a typical corroded sample..... 52
- Figure 2.5 The EBSD generated (a) SEM images, (b) OIM images, and (c) labeled CSL boundaries of the scanned region, later identified in the FIB/SEM for TEM sample preparation..... 55
- Figure 2.6 Depth and width measurements collected from 3D profilometry showed that the corrosion width was approximately 2-5 times larger than its corresponding depth. With square as CSL and diamond as non-CSL, each point represents a single boundary, where the arrows represent the range of the multiple measurements along that boundary..... 55
- Figure 2.7 The initial examination in bright field TEM showed (a) the corroded boundaries have a wavy structure, where each bend was a carbide feature at the boundary, whereas (b) immune boundaries were straight and featureless..... 57
- Figure 2.8 (a) Bright field TEM image with an EDS map, Co = green, Cr = red, and Mo = blue from a JEOL 2100. The dotted line indicates the grain boundary, with a chromium enhancement. Line scans (b) and (c) indicate the change in concentration at the carbide..... 57
- Figure 2.9 (a) Bright field image of a grain boundary with a chromium-rich carbide. (b) Diffraction pattern of grain 1, (c) diffraction pattern of the feature showing a $M_{23}C_6$ carbide grain structure, and (d) diffraction pattern of grain 2. 58
- Figure 2.10 The chart summarizes the samples measured in each category and if carbides were present. The boundary can be either CSL or non-CSL, and either be corroded

or immune. The proportion of samples in each category represents the approximate frequency seen in the bulk sample..... 58

Figure 2.11 (a) The lens shape of the chromium-rich carbide with (b) the HREM showing the shared epitaxial alignment with the concave grain..... 59

Figure 2.12 Dark field selecting for (a) grain 1 and (b) grain 2, show the epitaxial nature of the chromium-rich carbide to the grain on the concave side of the lens. 59

Figure 2.13 The distinct shape of the chromium-rich carbides has been previously modeled by a copper indium alloy, with α as the trailing grain, α' as the forward grain, and β as the carbide [129]. 60

Figure 2.14 The chromium depleted region around a chromium-rich carbide, with (a) the ADF image, (b) an extracted line scan to show the CDZ, (c) cobalt, (d) chromium, and (e) molybdenum. The arrow indicates where the line scan was taken, and the circles indicate where the EDS spectra were quantized, reported in Table 2.2..... 62

Figure 2.15 The chromium depleted region between two chromium-rich carbides, with (a) the ADF image, (b) cobalt, (c) chromium, and (d) molybdenum. The chromium depletion is measured along a 150 nm section of grain boundary between two carbides and found to be sensitized by 2%. The circles indicate where the EDS spectra were quantized in Table 2.3. 63

Figure 2.16 Carbides less than ~50 nm did not show measurable chromium depletion, with (a) the ADF image, (b) cobalt, (c) chromium, and (d) molybdenum. The circles indicate where the EDS spectra were quantized in Table 2.5. 64

Figure 2.17 (a) A 10 nm thick slice of LEAP acquisition that intersected with a grain boundary and a carbide. (b) Composition profile through the edge of the carbide showing the chromium segregation. (c) The gallium present from FIB thinning segregated to the boundaries in the sample (black), which leaves a track of where the grain boundary is located. (d) The chromium concentration evaporating mainly

at the grain boundaries of the carbide with a patch of uneven evaporation on the edge..... 65

Figure 2.18 The macro view of sensitization has large regions of chromium depletion, leading to incomplete oxide formation around the sensitized boundary. In nanoscale sensitization, the oxide is not significantly diminished. The chromium depletion is on a nanometer scale along the boundary..... 67

Figure 2.19 The model for grain boundary assisted crevice corrosion includes the CDZ width (L), the distance between atoms along the grain boundary (a), the distance between atoms perpendicular to the grain boundary (b), and the depth of one monolayer of atoms removed from the surface (d). The weighted average diameter of Co and Cr can be used for a, b, and d, while L is measured from the EDS maps. 67

Figure 2.20 The chromium oxide layer with the light gray representing the bulk, the dark gray representing the oxide, the black arrows representing the Cr^{3+} movement and the blue lines representing the CrOH^{2+} concentration. As the chromium dissolution products accumulate in the crevice, the reaction down is quenched and the corrosion occurs out towards the walls of the crevice. The ions and albumin proteins are not to scale, but to serve as a representation. In the human body, many more ions and proteins would be present. 71

Figure 3.1 (a) A SEM image and (b) its corresponding EBSD map showing preferentially corroded CoCrMo grain boundaries and the different grain orientations. (c) CSL boundaries are labelled with red lines, twin boundaries are labelled with black lines, and randomly oriented grain boundaries are labelled with grey lines..... 86

Figure 3.2 Representative examples of a (a) Type I, (b) Type II, and (c) Type III grain boundary as indicated by the arrows. 87

Figure 3.3 Profilometry measurements of the same region of interest can be shown as (a) a 2D projection and (b) a 3D reconstruction. Depth profiles of representative (c) Type

I, (d) Type II, and (e) Type III boundaries are shown. Type III boundary profiles, taken from 3 different sites along the boundary, show a large variance in the depth measurements. 87

Figure 3.4 Corrosion crevice depth was plotted with respect to the CSL Σ number. The three classes of boundaries and their respective corrosion depths are shown. 89

Figure 3.5 Crevice measurements collected from 3D profilometry show that widths of the corroded grain boundaries are approximately 2-5 times larger than its corresponding depth. The arrows represent the range of measurements along the boundary 89

Figure 3.6 BF TEM showed that a partially corroded $\Sigma 27$ boundary was faceted by carbides. 91

Figure 3.7 (a) The immune $\Sigma 17$ grain boundary was straight without deviations and did not show carbides. (b-c) Electron diffraction patterns collected at the adjacent grains confirmed the presence of a grain boundary. 91

Figure 3.8 BF TEM image of lens shaped carbides (indicated by arrows) at a partially corroded $\Sigma 25$ grain boundary. 92

Figure 3.9 (a) Two carbides of approximately 100 nm are found along the $\Sigma 13$ boundary. Line scans from the HAADF image show (b) two peaks representing the two carbides and (c) a single peak showing the Cr content across the center of a carbide. 93

Figure 3.10 HAADF image from a corroded $\Sigma 13$ grain boundary with the corresponding EDS maps. Chemical quantification from the indicated sites are summarized in Table 3.2. 95

Figure 3.11 HAADF image of a corroded $\Sigma 25$ grain boundary accompanied with the corresponding EDS maps. Cr depletion zones are present in between carbides along

- the boundary. Chemical quantification from the indicated sites are summarized in Table 3.3. 95
- Figure 3.12 Platelet shaped precipitates were found along a $\Sigma 25$ boundary with low corrosion. Chemical quantification from the indicated sites are summarized in Table 3.4. 96
- Figure 3.13 Platelet shaped precipitates were also observed in a corroded $\Sigma 7$ boundary. Chemical quantification from the indicated sites are summarized in Table 3.5. 96
- Figure 3.14 The Cr depletion at one Type I ($\Sigma 7$) and four Type II ($\Sigma 25$, $\Sigma 13$) boundaries are related to the corrosion susceptibility. Note that the energy value for these ranks from lowest to highest as $\Sigma 7$, $\Sigma 25$, $\Sigma 13$ 98
- Figure 3.15 Interfacial energies associated with different lattice configurations at CSL grain boundaries have been shown to be a good predictor for the severity of corrosion. The arrows in grey represent the range of the measurements observed. 100
- Figure 4.1 (a) Diagram of the usual nomenclature used in the literature and in this chapter. (b) Diagram of the commonly proposed “deck-of-cards” sliding, where each layer undergoes a fraction of the entire sliding. Here the sliding is distributed throughout the entire flake. (c) Our results show the soft interface fracture sliding, where the sliding takes place in-between flakes or the in-between the most disordered sheets within a flake. The other parts of the stack remain stationary. 110
- Figure 4.2 Experimental setup of the in situ sliding test. (a) Photograph of the holder with mounted sample. (b) Drawing to show the orientation of the fractured Si edge and AFM tip orientation. (c) TEM image of the boxed region showing the sample, AFM tip, and an arrow to a MoS_2 flake on the edge. 113
- Figure 4.3 Three examples of soft interface fracture transfer layers forming, with initial states of (a-1), (b-1), and (c-1) and final states after fracture of the transfer layer of (a-2),

(b-2), and (c-2). (a-3), (b-3), and (c-3) show extracted video frames with the dotted line showing the soft interface. Scale bars are 20 nm. 115

Figure 4.4 (a) The ball of MoS₂ rolled between the AFM tip and the Si surface. (b) The feature rolled without slipping, indicated by the circle markers. (c) The ball hit the oriented MoS₂ flakes and changed from rolling to sliding. (d,e) The sliding of the transfer flake. (f) The top flake as a transfer flake on the ball. c-f include an orientation marker to show the ball stopped rolling and the black arrow points to the transfer flake. Scale bar is 20 nm. 116

Figure 4.5 (a) The area before any contact with the future transfer flake noted with the bracket and (b) the same sheets adhered to the sliding ball. Scale bar is 20 nm. 117

Figure 4.6 (a)-(c) Stages of the SIFT layer sliding from the bottom flake, and (d) adhesion to the Si surface after SIFT. Scale bar is 20 nm. 118

Figure 4.7 (a)-(c) The Si substrate slid right and (d)-(f) slid left to highlight the bending of the transfer flake, showing the evolving soft interface. Scale bar is 10 nm. 119

Figure 4.8 The soft interface fracture process of the stack of flakes from Figure 4.2 example b. The initial stack (a) fractures at the weakest interface indicated with the dotted line. (b) The SIFT layer is created on the tip and the next soft interface fracture point is indicated with the dotted line. (c) The transfer layer has adhered to the shape of the tip, and further removal of the weakest layers are seen. (d) The last misaligned flake is indicated with the dotted line. (e) All misaligned flakes are removed from both the initial stack and from the transfer layer as well. Both the flake on the substrate's and the transfer flake's surfaces are made of a primarily continuous sheet of MoS₂. 121

Figure 5.1 (a) Nomenclature used for the nanoflakes, showing the stack, flake, and sheets. Unsubstantiated proposed mechanisms for (b) the formation of a nanoscale tribofilms and (c) individual nanotube exfoliation. 129

- Figure 5.2 (a) The sample mounted in the in situ holder was a 1 mm sample attached to a ~4 mm W wire. Here is a sample next to a metric ruler, ruler lines are 1 mm. (b) The Si substrate can be broken from the W-tip and mounted on a Cu washer for later EDS analysis. Scale bar is 1 mm. 133
- Figure 5.3 The fractured, electron-transparent edge of a Si substrate sample. 134
- Figure 5.4 (a) Example of a MoS₂ flake and (b) intensity scan showing 12 clear layers of 0.64 nm thickness. 135
- Figure 5.5 (a) Original MoS₂ flakes, and then after (b) 3 passes, (c) 8 passes, and (d) 13 passes. Scale bar is 100 nm. 136
- Figure 5.6 (a) Original MoS₂ flakes, (b) after 10 passes, and (c) after 1 coarse pass. Scale bar 50 nm. 137
- Figure 5.7 (a)-(c) Extracted frames of rolling of MoS₂ as the Si substrate moves to the right (Video 8). White circle showing the rolling contact. (d) The same crumpled ball after rolling with scale bar. (e) An alternative formation of a ball, a round flake (Video 4). 138
- Figure 5.8 Extracted videos (Video 9) of (a) a ball of MoS₂. (b) When it comes in contact with the AFM tip, (c) the ball pulled apart, indicated with the black arrow. (d) When brought back in contact with the Si, the pulled apart flake reoriented parallel to the Si surface and then (e) as the Si substrate moved to the left, motion indicated by the white arrow, the flake became a transfer layer and slid with the AFM tip. Scale bar is 20 nm. 139
- Figure 5.9 (a) MoS₂-MoS₂ flake that showed minimal adhesion and (b) MoS₂ flakes were offset and then in MoS₂-Si contact, which showed significant adhesion (Video 10). 140

- Figure 5.10 (a) Neutral position of the AFM tip, indicated by the dotted line. (b) MoS₂ – MoS₂ contact displacement from adhesion the frame before the adhesion breaks, with the adhesion force per unit area ~22MPa. (c) MoS₂ on Si contact displacement from adhesion the frame before the adhesion breaks, with the adhesion force per unit area ~270 MPa..... 141
- Figure 5.11 When the Si substrate was pulled down there was high adhesion. When the substrate was pulled left, then the MoS₂ ball rolled and there was minimal adhesion as it broke contact (Video 11). Scale bar is 20 nm. 141
- Figure 5.12 (a) MoS₂ flake before adhesion and (b) after the edges jumped to adhesion with the AFM tip, with the arrow being ~3.4 nm. The number indicates the frame number, with each frame being 0.05 s (Video 12). 143
- Figure 5.13 (a) The edges of the MoS₂ sheets in contact with the Si AFM tip. The sheets bent about 25° in contact, and (b) as the tip moved up the edges stayed in contact due to adhesion, bending up to 65° (Video 13). (c) Image after the sliding, showing five layers at the end of the flake..... 143
- Figure 6.1 Wear tests using PAG oil formulations, forming (a) minimal wear and (b) varnish film formation [189]. At a different size scale, MEMS gears (c) before testing and (d) after failure caused by adhesion [190]..... 151
- Figure 6.2 Metal-on-metal hip implants, MEMS gears, and industrial machines are all lubricated with hydrocarbons. Through friction and wear at the metal interface, the organic material reacts to form similar carbon films..... 153
- Figure 6.3 Similar micron-scale appearance of the carbon films after sliding contact. (a) Friction polymer [193], (b) DLC [206], (c) varnish tribolayer, (d) hip explant tribolayer [16], (e) MEMS wear film [190], and (f) cast iron glaze [207]. 157
- Figure 6.4 Raman spectra of (a) friction polymer [200], (b) DLC [208], (c) varnish, (d) hip explant tribolayer [16], and (e) catalyst [209]. All examples show a broad G band

at $\sim 1550\text{ cm}^{-1}$ and a D band at 1350 cm^{-1} indicating the presence of nanographitic carbon. 158

Figure 6.5 Electron energy loss spectroscopy of (a) DLC (sample 29-88 in figure) [210], (b) varnish, (c) hip explant tribolayer [16], and (d) catalyst substrate [211]. The ratio of the π^* peak to the σ^* peak indicate percent graphitic bonding [212,213]. All spectra include graphite for reference. 159

Figure 6.6 Two forms of varnish deposition: (a) show moving sludge varnish removed by a filter (part courtesy CC Jenson) and (b) deposited and cured shiny varnish film (part courtesy Dyna Power Parts). 163

Figure 6.7 Inside the dual-beam SEM-FIB, the Omniprobe (a) came into contact with a varnish flake and (b) transferred the flake to a TEM grid. (c) In the TEM, a thin edge of the flake was found for EELS analysis. 165

Figure 6.8 FTIR spectrum of the varnish coated metal surface after background subtraction and removal of CO_2 peak. Peaks indicate the presence of water ($3850, 3750\text{ cm}^{-1}$), sp^3 bonding (2925 cm^{-1}), and sp^2 bonding ($2850, 1700, 1650, 1550, 1450, 800, 700\text{ cm}^{-1}$). 166

Figure 6.9 A MEMS switch lubricated in air and pentanol, showing the buildup of wear when unlubricated [272]. 170

Figure 6.10 (a) The lubricant derived carbon film that forms during sliding on the nanocomposite surface, (b) design of the nanocomposite surface composition, and (c) Raman spectra of the film (indicated as 4 in the figure) presented with Raman spectra references of diamond (indicated with 1) and graphite (indicated with 2). United States Patent and Trademark Office [297]. 175

Figure 6.11 Similarities in reaction diagrams showing organic precursors turning into pre-graphitic condensation products in friction polymers and coke. (a) For a friction polymer, general pyrolysis scheme of phosphates through thermal degradation

[321]. (b) For coking, carbonium ion mechanism for formation of higher aromatics from benzene and naphthalene [322]. 187

Figure 6.12 Ternary phase map based upon for various carbon films [247], including proposed approximate placement for proteins and oil lubricants, which shows their respective sp^2 , sp^3 , and hydrogen contents. This provides a map of the dynamic change of these materials into graphitic films. 188

Figure 6.13 Examples of input energy causing graphitization in DLC and NFC carbon films. (a) At increasing heat treatment temperatures, DLC film became increasingly graphitic, measured by Raman spectroscopy [225]. (b) During in situ sliding, NFC film became more graphitic measured by EELS [59]. 189

Figure 7.1 The geometry of the AFM tip, Si substrate sample that is movable in three directions, and the MoS_2 flakes that sit at the edge. 201

Figure 7.2 (a) The standard AFM tip from Nanofactory, (b) the homemade tip by Yifeng Liao, and (c) a close up of the AFM cantilever in the Nanofactory tip. The white arrows indicate the AFM cantilever, the cantilever next to it is for comparison in the electronic circuit. The black arrow points to where the cantilever was on the homemade AFM tip, and the dotted line indicates where it was before it broke off. The gold wires and patterning on the chip allow for connection to the computer software. The in situ coordinates system is indicated. 202

Figure 7.3 A homemade AFM tip would need to be calibrated. The in situ coordinates system is crucial to note because the Y-direction is important for adhesion force and the X-direction is important to the friction force. 203

Figure 7.4 The theoretical method to measure the friction force during sliding. As the sample moves to the left, indicated by the blue arrow, the displacement of the AFM tip can be measured in the X-direction, indicated by the black arrows. This measurement would be done in post facto video frame-by-frame analysis. 204

1 Background

Great advancements in science and engineering can come from thinking outside the box – bridging previously unrelated disciplines and finding connections. This connecting of disciplines can be difficult in modern university departments, yet materials science relishes in variety of thought and breadth of backgrounds. It is here in the field of materials science that my research brought together medicine, metallurgy, microscopy, and lubrication. We can find more similarities than differences in these fields and reach interesting conclusions.

Four components of background will be presented in this chapter: tribology, hip implants, solid lubrication, and in situ transmission electron microscopy (TEM). In the later chapters, further project-specific background will be presented.

1.1 Tribology

Tribology is the study of surfaces in contact; it can be defined simply as the study of friction. Two surfaces in contact and with relative motion form the basis for tribology research, yet the field also includes investigates friction and wear through structure, materials selection, and lubrication. These factors have been realized since the time of the construction of the pyramids shown in Figure 1.1 [1]. Even though friction is an old field of study, only a fragmented understanding exists of the fundamental mechanisms. Tribology is a multiscale problem, where we need to understand the fundamental materials science relationship between structure and properties at all size scales. It is only when we understand atomic through macro scale, that will we be able to make revolutionary rather than incremental improvements.

Tribology is not only an interesting materials science phenomena, it is a major component of the economy. Studies over the past forty years estimate that 4-5% of industrialized countries' gross domestic product is consumed by tribological losses, which can happen at any stage of device lifetime, from manufacturing to operation [2,3]. Tribology research can design new materials with favorable friction and wear properties. The most ambitious goal would be to create models that quickly and accurately predict friction properties from starting contact conditions and basic principles of materials deformation.

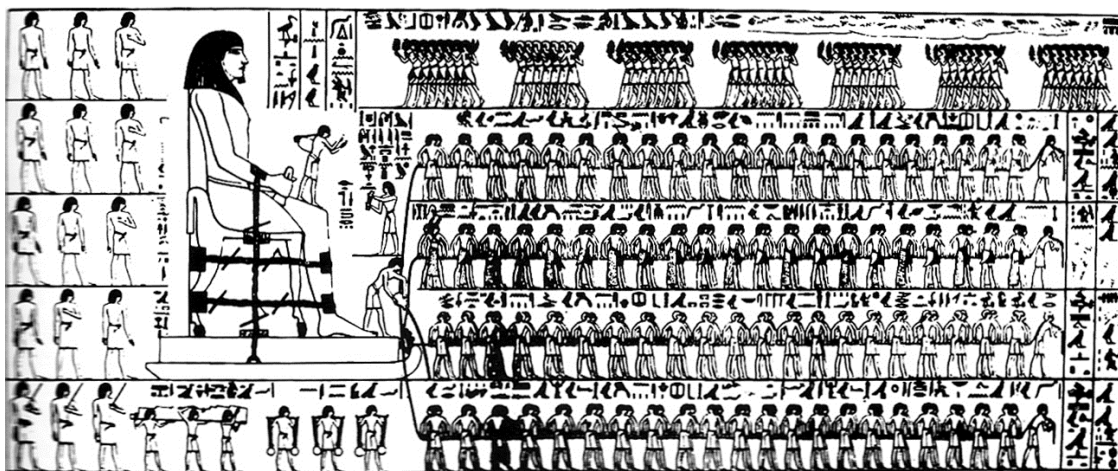


Figure 1.1 An ancient tribologist in the tomb of Tehuti-Hetep, circa 1880 B.C. The man at the foot of the statue is pouring a lubricant (from Ref [1]).

Furthermore, solid lubricants are an innovative aspect of tribology that can provide less toxic option than traditional oils, and can also be pushed to more extreme environments. Solid lubricants can provide favorable mechanical and tribological properties, especially in protective coatings, which makes this topic an active field of research. Solid lubricants investigated in this work will be further introduced in section 1.3. Tribology is complex with relevant factors including load, atmospheric environment, chemical composition, crystalline structure, temperature, sliding speed, third bodies, and roughness. Often these parameters are initially studied through macroscale

coefficient of friction and wear volume measurements. Tribology becomes even more complex as the analysis extends to the nanoscale; complications of sliding and friction mechanisms are further exposed at smaller scales. At the nanoscale, contact is made not by the entire surface, but by asperity-asperity contacts. In solid-solid interfaces, asperity contacts are the more fundamental unit of tribological analysis. With the asperity contacts, a seemingly smooth surface at the macroscale will show a nanoscopically rough surface, as shown in Figure 1.2 [4]. Early work on the surface interactions between two metal surfaces, brought to atomic contact, was done by Bowden and Tabor [5,6]. Understanding nanoscale asperity contact leads to a richer understanding of friction; we are able to more thoroughly understand lubrication and wear mechanisms.

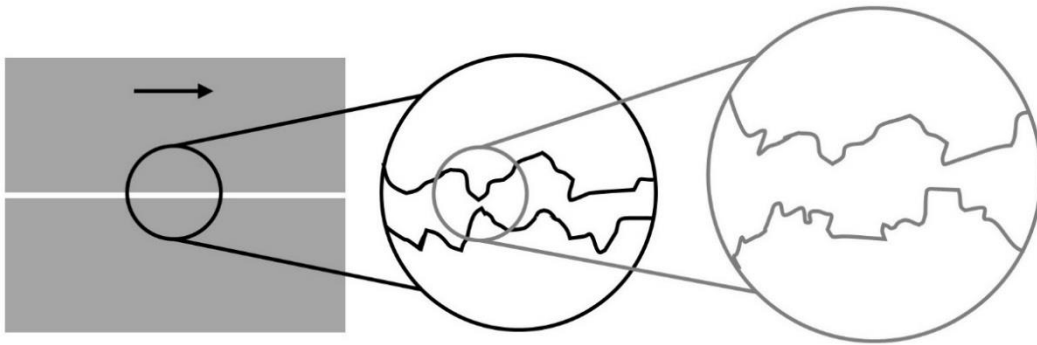


Figure 1.2 Asperities on asperities as the magnitude of magnification increases.

1.2 Hip Implants

The total hip replacement in the human body is a system rich in tribology phenomena with many unknown variables. The metal-metal interfaces in these hip replacements present a complex and interwoven system that incorporates wear, lubrication, and corrosion. The metal-on-metal (MoM) hip system allows for study of these areas separately as well as the study of how they

influence each other. By understanding wear, lubrication, and corrosion, implant material degradation can be mitigated to improve performance of biomedical alloys.

Since the 1970s, cobalt-chromium-molybdenum (CoCrMo) alloys have been used as biomedical materials, especially for MoM hip replacement implants. Even with improving designs, ion and particle release from articulating surfaces and modular interfaces of these orthopedic implants continue to pose significant clinical problems. The degradation occurs in the harsh physiological environment due to a synergism of mechanical and electrochemical forces, called tribocorrosion. Immune response to toxic ions, osteolysis, mechanical loosening, and eventual failure of the implant are current clinical problems [7]. Total hip arthroplasty (THA), however, is still the most clinically successful treatment for end stage osteoarthritis of the hip, with the number of THA performed annually in the United States expected to grow by 174% from 2005 to 2030 [8]. The demand for CoCrMo alloy biomaterial implants, over a half million annually, will continue to grow as the “Baby Boomer” population ages. The increasing demand provides motivation for relevant research on improvements to CoCrMo alloys.

Osteoarthritis may result in a patient’s need for prosthetic joint implants of the hips and knees, and THA is one of the most clinically successful treatments of hip osteoarthritis. The most common implant, the metal-on-polyethylene (MoP), consists of a CoCrMo alloy femoral ball and an ultra-high molecular weight polyethylene (UHMWPE) cup. The MoP implants have shown low wear and long term survivorship, but the polyethylene wear particles can cause the hip replacement to fail [9]. As patients live longer, metal-on-metal (MoM) implants could hold promise for implants that last a patient’s lifetime.

CoCrMo alloys have been in use as biomedical materials since the 1970s because of the advantageous bulk mechanical properties [9]. CoCrMo alloys can be predictably modified by casting, annealing, hot forging, and cold working to assume precise specifications [11-15]. MoM joints are known to have the lowest wear rates as compared to MoP, yet the usage of the CoCrMo alloy MoM joints has recently diminished due to widespread clinical concerns regarding metal ion release to the surrounding tissue and an overall systemic response [9,7]. Hip replacements have multiple interfaces: the articulating interface between ball and cup and the modular interfaces between the neck and stem components, shown in Figure 1.3 [10]. Metal-metal interfaces are still prevalent in hip replacement reconstructions, however, because polymer and ceramic implants still use multipart, modular metal components. At both the articulating interface and the modular interfaces, friction arises as nanoscale asperities come into contact and wear to produce nanoparticles. Due to the complex nature of materials degradation processes involving simultaneous mechanical and chemical reactions, how the materials are released from the articulating surface and from the modular interfaces to the human body is still unclear. Using nanoscale analysis, new insights into the wear process that takes place in the material within hundreds of nanometers of the surface can be achieved.

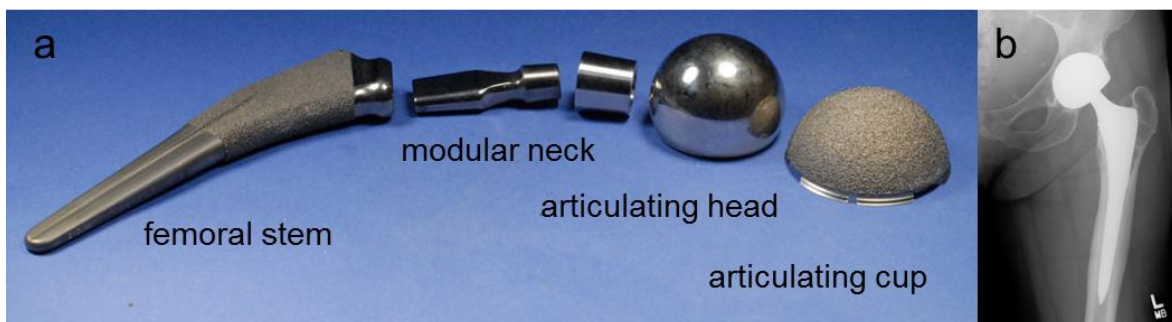


Figure 1.3 (a) Complete total hip replacement system with modular parts and (b) X-ray showing implanted metal-on-metal hip replacement [10].

Furthermore, there is evidence of formation of tribofilms on the articulating surfaces of MoM hip retrievals [16]. These tribofilms are carbon-rich deposits that are presumed to be formed from synovial fluids and form as irregular deposits tens to hundreds of nanometers thick [17-19]. The composition has been investigated using X-ray photoelectron spectroscopy (XPS) and energy dispersive X-ray spectroscopy (EDS), showing the layer is principally organic with oxidized Co, Cr, and Mo, and traces of Ca, P, S, and Na [17-19]. Later through electron energy loss spectroscopy (EELS) analysis, it was found that the organic carbon was graphitic in nature and was proposed to act as a solid lubricant [16]. In vitro studies suggest that the tribological processes contribute significantly to the formation of the tribofilms on MoM hip replacements.

1.3 Solid Lubricants

In this work, we use the MoM tribolayer as inspiration to study other metal-metal interfaces that form tribolayers and other solid lubricant tribolayers. For example, industrial machines have metal-metal articulating surfaces that use organic lubricants to reduce friction. The industrial system of metals cycling against each other in a hydrocarbon-rich environment can serve as a parallel system to the MoM hips. Both systems form tribolayers that evolve during use, and the nanoscale composition and structure will be compared in this research. Further background on the industrial tribolayers and other parallel systems will be presented in Chapter 6.

The MoM hip tribolayer is classified as a solid lubricant, and to fully understand the MoM hip system, we must understand solid lubricant mechanisms. In addition to the graphitic solid lubricant of the hip, it is beneficial to study standard solid lubricants to understand common lubrication and wear mechanisms. It is worthwhile to further discuss the background of the general field of solid

lubricants. These films, nanoparticles, and tribolayers are a rich subject in tribology research as these materials have the potential to drastically improve performance in unique environments. Solid lubricants are surface coatings or a component in self-lubricating composites. There are four distinct types of solid lubricant materials: carbon-based (graphite, diamond like carbon), transition metal dichalcogenides (MoS_2 , WS_2), polymers (PTFE), and soft metals (silver, gold, tin) [20]. These materials can be applied as thin films and coatings on triboactive components, such as bearings, gears, and hard drives, in order to reduce friction, wear, and debris formation [21]. In addition to the lubricant material, the surface material can also effect performance. The wear surfaces can exhibit influential chemistry, microstructure, and crystallographic texture, which can then effect properties during sliding. Tribological contact with a solid lubricant usually results in the formation of a transfer layer, a layer of material from the surface that becomes adhered the counterface during sliding. Understanding the contact and the transfer layer is important because the primary mechanism of low friction is interfacial sliding between the initial coating and the transfer film.

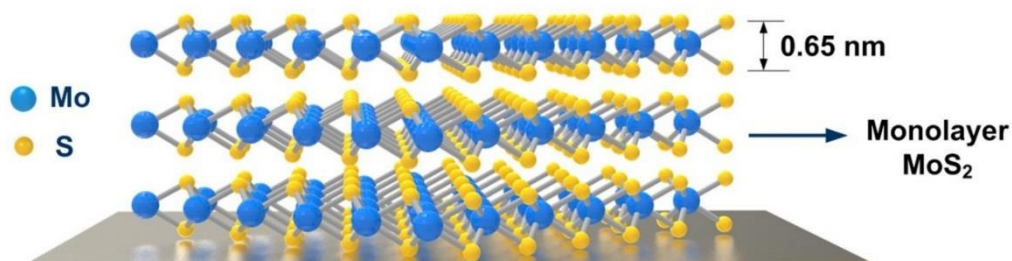


Figure 1.4 The layered structure of MoS_2 allows for low friction sliding between monolayer sheets.

In addition to the sliding between the contact and substrate, lamellar solid lubricants have further triboactivity mechanisms based on their structure. On the atomic level, graphitic carbon

and molybdenum disulfide (MoS_2) have a lamellar structure of stacked covalently-bonded sheets separated by weak Van de Waals forces holding the stack together [22]. The layered structure and interlamellar spacing of MoS_2 can be seen in Figure 1.4. In graphite the sheets are hexagonally bonded carbon, and in MoS_2 the sheets are Mo layered with S on top and bottom. The lubricating behavior stems from the intermechanical weakness of the crystal structure, which allows for sliding to occur between the sheets [22]. With shear force, the basal planes slide over one another by intracrystalline slip, leading to the formation of a transfer film on rubbing contact.

Multiscale MoS_2 investigation has shown macroscale friction reduction and nanoscale tribological mechanisms. The lamellar material has practical uses, with lubrication applications in machinery used in space [23-25]. The triboactivity and the friction-mitigation of MoS_2 surface film depends on the integrity of the film, contact pressure, humidity, film thickness, temperature, and presence of contaminants [26-28]. Pin-on-disk sliding tests are often used to study the wear, wear scar, and wear particles generated during sliding [20,29-33]. MoS_2 has been shown to form transfer layers [34,35], including both microscale thick films [36] and crystalline monolayer transfer films [37]. A large area of MoS_2 work that should be considered comes from fullerene like MoS_2 (IF- MoS_2) nanoparticles, with many studies by Lahouij et al. [38-42]. However, there are still many unknowns in solid lubricant tribology, including key processes of lubrication and wear evolution during use. Often unknowns in tribology come from the buried interface where sliding occurs. In situ transmission electron microscopy allows for high resolution imaging at this triboactive interface. Capturing the nanoscale asperity contacts can show the fundamental mechanisms of lamellar solid lubricants.

1.4 Microscopy: TEM and In-situ TEM

Transmission electron microscopy will serve as the primary analysis technique in this work, as it enables the characterization of structural and chemical properties at the nanoscale. For this work, TEM is particularly useful because it can be used to understand a variety of metal and solid lubricant systems. Additionally, a particular focus of this work will be the analysis of tribological properties, which can be achieved by using our group's in-situ holder within a TEM. Both the TEM characterization tools and the in situ holder setup allow for unique analysis of tribological systems.

Single asperity wear, corrosion in CoCrMo alloys, and tribolayer formation all can be investigated at the nanoscale using TEM as it provides techniques for both structural and chemical characterization. Chemical analysis techniques such as electron energy loss spectroscopy (EELS) and energy dispersive spectroscopy (EDS) can probe elemental composition and provide bonding information. Advanced TEM techniques allows for characterization down to the atomic scale.

For wear of single asperity contact and solid lubricant behavior, in-situ TEM can be used to gather information as the tribological surfaces are in contact. The classic buried interface problem has historically burdened experiments in tribology as there is the inability to directly observe the sliding contact. The in-situ setup allows for the observation of tribologically relevant experiments, while monitoring nanoscale changes in real time. Sliding interfaces and composition changes have been studied in a detailed manner by scanning probe microscopy [43-45], quartz crystal microbalance [46-48] and surface force apparatus techniques [49]. A number of in situ techniques have been developed which can obtain information such as optical spectroscopies [50-53] or x-ray photoelectron spectroscopy [54]. Some work has shown dynamic processes at monolayer

interfaces [55-57], such as motion of misfit dislocations [58], but interpretation issues remain resulting from volume averaged measurements. Although the methods show friction phenomena at the nanoscale, direct insight into single asperity-asperity contact is not shown. This is often the case in CoCrMo alloy implant wear studies, as the tribology studies come from ex-plants and observation of tissue samples, instead of direct observation of asperity interaction.

An ideal experiment to understand single asperity interactions would be to slide a single asperity against a surface, while imaging at the atomic scale in real time. The structural and chemical signals would be recorded to correlate with the motion and the applied force of the system. This experimental setup is not currently possible, but some aspects can be approached. Many challenges inherent to TEM, such as the high vacuum environment, the high energy electron beam, and very strong magnetic field, have limited the options for designing in-situ systems. In situ TEM holders must be made of materials that can withstand the environmental limits, be mechanically compatible, and allow for unconventional sample loading or alignment.

Within recent years, however, commercial systems have exploited the type of instrumentation developed for scanning probe microscopy within a transmission electron microscope, such as systems from Humming Bird, Hysitron, and Nanofactory. Experiments can now be performed at a higher resolution and imaged in real time. A small tip, either an atomic force microscopy (AFM) tip or one designed for nanoindentation experiments, can be slid against or indented into the tribological material of interest. The basic in-situ concept is illustrated in Figure 1.5.

Coupling this system with the many electron microscopy techniques available, a variety of structural and chemical changes can be recorded. Imaging at different resolutions as well as using chemically sensitive probes such as EELS and EDS are possible within this system design. The

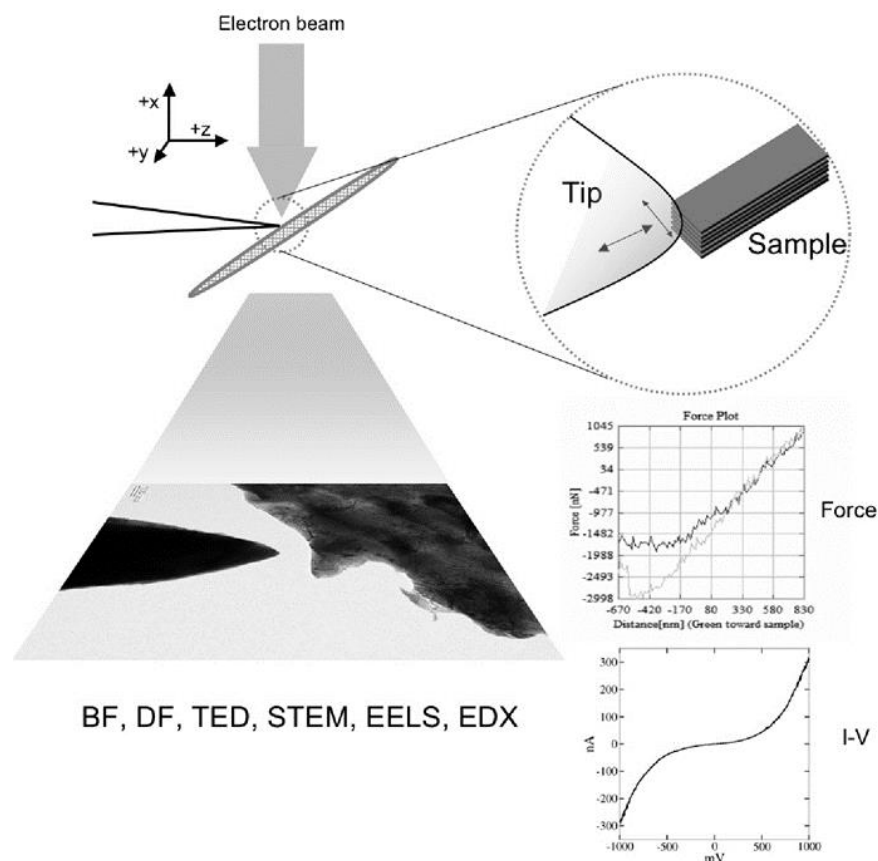


Figure 1.5 Schematic of the holder. A tip is brought into contact with the sample during observation in the microscope. Both the normal force (AFM holder) and I-V characteristics can be measured during the experiments, in addition to normal TEM imaging and spectroscopies.

electron beam combined with the piezoelectric drivers can cause vibration and reduce the resolution to approximately 0.2 nm. In-situ TEM provides experimenters the ability to design lubrication systems that mimic MoM hip systems or solid lubrication interfaces. Previous work in the Marks group has used the Nanofactory AFM and STM holders, which have had differing sample and sliding geometries. Merkle and M'ndange-Pfupfu investigated carbon films and tribochemical reactions during sliding [59-61]. Liao investigated wear in CoCrMo alloys, including looking at wear and recrystallization [62-64]. With this system, tribological properties, such as wear particle generation and tribofilms formation, can be observed and recorded in real time.

1.5 Outline of Research

The initial aim of this research was to study tribology and corrosion in CoCrMo alloy hip implants and similar systems. This research is roughly presented in three projects. Environments where tribology, corrosion, and chemical activity come together provide seemingly endless questions to ask and problems to investigate. The overall aim of this thesis is to address these problems using nontraditional approaches, in order to find valuable connections to advance the fields. This work can inform future hip implant design, improve general understanding of metal corrosion, and explain mechanisms of solid lubricants. Materials science is the interdisciplinary tool for tying fundamental materials processes to macroscale behavior.

This thesis addresses three project areas. Chapter 2 and 3 cover corrosion of the CoCrMo alloy, specifically focusing on grain boundary corrosion. The goal was to further characterize why some grain boundaries corroded and why some were left completely immune. Chapter 2 presents the grain boundary assisted crevice corrosion work. We found that the grain boundaries that did corrode had nanoscale chromium-rich carbides present. The carbides caused chromium depleted zones, commonly referred to as sensitization. This chapter includes a thorough review of sensitization literature in the introduction. Using TEM and EDS, the chromium depletion data was used to develop a model showing the sensitization level initiates the grain boundary crevice corrosion. Chapter 3, performed in conjunction my BS/MS mentee Alex Lin, furthers the CoCrMo alloys grain boundary corrosion work to refine our characterization of the crystallography of the grain boundaries. His work performed additional analysis for coincidence site lattice grain boundaries, a special case of grain boundary that was sometimes immune and sometimes corroded.

The second area of research is in situ tribology sliding tests on solid lamellar lubricants in a transmission electron microscope. In Chapter 4, molybdenum disulfide sliding was investigated with in situ TEM, and we developed the soft interface fracture transfer (SIFT) mechanism. The background on MoS₂ as a solid lubricant is included in the introduction of this chapter. Investigating the low friction mechanisms of the lamellar solid lubricant revealed the previous deck-of-cards sliding assumptions are not true. Instead we showed sliding and transfer layer formation occurred at one interface only. Chapter 5 builds on the MoS₂ SIFT mechanism of Chapter 4 by showing other MoS₂ stability mechanisms. We observed rolling, reorientation, flake pull apart, and adhesion mitigation. This work demonstrated that lamellar lubricants can continuously evolve during sliding with a multitude of sliding and wear mechanisms.

The third area of research reviews the current state of the field of graphitic carbon films. The MoM hip tribolayer and the industrial carbon film varnish initially sparked our interest. In Chapter 6, a review of graphitic carbon films is presented, along with original research on varnish. Varnish is a carbon tribofilm that forms in industrial machines, and we show the similarities to carbon films. We characterized the nanoscale composition of the varnish and compared it to published work on other graphitic carbon films. The fields included are friction polymers, diamond like carbon (DLC) coatings, varnish from industrial lubricants, the tribolayer from MoM hip replacements, microelectromechanical systems (MEMS), and catalysis coke. Through this comparison, we found striking similarities that could inspire future cross-discipline advancements.

Finally, Chapter 7 summarizes the research and discusses future work that can stem from the results presented in this thesis.

2 Grain Boundary Assisted Crevice Corrosion in CoCrMo Alloys

Investigations of metal-on-metal hip implants are challenging because of the complex physiological environment in which the implant operates. Research on the performance of hip implants can focus on many factors or a single factor at a time. While some studies focus on hip retrieval analysis to understand the effects of the body's complete environment, other studies isolate the effects of these forces by studying simulated wear, electrochemical reactions, or biochemical pathways. By including factors in a study, the experiment is closer to the human body biological environment; by removing factors, more controlled analysis can be done for individual contributors. Here, we focus on the materials science of the metal used in many implants, a CoCrMo alloy. We looked at a sample of material that had undergone only corrosion, which allowed our analysis to focus specifically on nanoscale crystallography and composition. Through diving deep, we understand how corrosion initiates at grain boundaries. This work can inform the larger community studying the tribological and biological influences.

Cobalt chromium molybdenum alloys have been extensively used for biomedical implants, but are susceptible to grain boundary corrosion due to local chromium depletion, what is called sensitization. Grain boundary sensitization can directly cause an implant to fail. In this work, we extended the understanding of chromium depleted zones in CoCrMo alloys and their role in corrosion to the nanoscale. Selected boundaries were analyzed from the millimeter to the nanometer scale in order to link the chemical composition and crystallographic structure to the observed local corrosion behavior. The shape and severity of grain boundary corrosion crevices were measured and related with the coincidence site lattice geometry. Additionally, direct high resolution energy dispersive X-ray spectroscopy maps of chromium depleted zones at the grain

boundaries were measured to completely characterize the grain boundary properties. Chromium depleted zones were found in 100% of corroded grain boundaries, yet were too small to follow classical models of sensitization. We found that nanoscale regions of chromium depletion have significant effects on corrosion initiation. This depletion leads to a grain boundary crevice corrosion model connecting the material's chemical composition with electrochemical driving forces that control crevice corrosion propagation. The conclusions and model presented can be used to improve processing techniques for CoCrMo and other alloys.

This work was inspired by the masters work of Pooja Panigrahi, and it continues the results from her publication “Intergranular pitting corrosion of CoCrMo biomedical implant alloy” [65]. Material in this chapter is reproduced from the article “Grain Boundary Assisted Crevice Corrosion in CoCrMo Alloys” by Emily E. Hoffman, Alex Lin, Yifeng Liao, and Laurence D. Marks; *Corrosion*, 2016 [66].

2.1 Introduction

As the “baby boom” generation ages and as patients continue to live longer and have more active lives, the demand for hip replacements has risen. Injury and osteoarthritis often require patients to need a hip or knee replacement. The number of total hip arthroplasties in the United States is expected to grow from 2005 by at least 174% to 572,000 implants by 2030 [8,67].

Since the 1970s, cobalt chromium molybdenum (CoCrMo) alloys have been approved as implantable biomedical materials for hip replacements [9]. Advantages of this metal alloy include the good bulk mechanical properties, which can be predictably modified by various processing techniques such as casting, annealing, hot forging, and cold working [11-15]. Of the different

articulating joint interfaces available for hip implants, metal-on-metal (MoM) is known to have one of the lowest wear rates compared to systems with the polymer polyethylene [9,68]. The MoM implants, however, have generated serious clinical concerns due to metal wear products released into the surrounding tissues [7]. One of the major degradation processes that affects all metallic implants in vivo is corrosion [69-71]. While CoCrMo alloys have good tribological properties and are especially corrosion resistant because of a passive oxide surface film, cobalt and chromium cations and nanoparticles have been detected in patients with implants [14,72-75]. Clinically observed complications from corroding CoCrMo alloys include metal hypersensitivity, metallosis (metallic staining of the surrounding tissue), excessive periprosthetic fibrosis, and adverse local tissue responses (which can include extensive necrosis of periprosthetic tissues); all of which have contributed to CoCrMo alloys falling out of favor at present. While there are developments with new alloys and increasing use of materials other than CoCrMo alloys such as titanium for the primary mechanical supports in implants, many CoCrMo alloys still continue to be used and currently exist in millions of patients worldwide. It is medically unreasonable (and detrimental to a patient's health) to remove an implant that is not displaying any signs of unfavorable physiological reactions. Considering the millions of MoM hip replacements in use worldwide, we need a better understanding of the fundamental processes of grain boundary corrosion in these alloys. Beyond the medical applications, understanding corrosion of CoCrMo alloys is important for naval and industrial applications.

In all forms of CoCrMo alloys, with variations in carbon concentrations, precipitates, and microstructures, the dominant corrosion protection comes from the formation of a chromium oxide thin film at the surface. In many cases of extended corrosion, there is not a constant mass loss per

unit area, rather preferential mass loss at grain boundaries, carbide phases, or defects. A particularly significant contribution to in vivo corrosion is the rapid mass loss near the intersection of grain boundaries of the metallic alloy and the protective oxide. This is often called “grain boundary sensitization,” and the alloys that easily corrode after certain heat treatments are described as sensitized [76-78]. In alloys with chromium, the most common explanation of local sensitization is a local reduction in the chromium concentration [14,76,79,80].

When failed implants were removed from patients and investigated, intergranular corrosion was found on all modulating parts of the implant. Degradation resulted from both mechanical wear and electrochemical dissolution [69,77,81]. Scanning electron micrographs proved specific attacks at grain boundaries and carbide phases, often penetrating deep into the microstructure and causing grain fallout [81]. In CoCrMo alloys, these particles and ions generated from the grain boundary attack pathogenically contribute to osteolysis and aseptic loosening, which can lead to the need for a revision surgery [81,82]. As will be discussed in more detail below, the majority of the evidence for boundary attack is based upon rather large-scale segregation at the 0.1-10 micron scale. There are few investigations illuminating segregation at the nanoscale, which leaves open the question of what takes place with much finer-scale segregation at the nanoscale.

In this work, we investigate the nanoscale structure and segregation in CoCrMo alloys that has often been overlooked in microscale carbide precipitate analysis. Through analysis of carbide phases and chemical compositions at grain boundaries, grain boundary properties are connected to the occurrence of local grain boundary corrosion attack. High-resolution characterization techniques, including transmission electron microscopy (TEM) and energy dispersive X-ray spectroscopy (EDS), show the chemical segregation that occurs at the nanoscale. By modeling the

grain boundary energies, we were able to predict the grain boundary corrosion and obtain insights into developing the next generation of CoCrMo alloys.

The structure of this chapter is as follows. In this chapter, we first present a background on sensitization to clarify terms used in literature and establish the field as relevant to CoCrMo alloys. Next, we describe the various techniques used to characterize the CoCrMo corroded alloy and present the TEM images, composition data, and quantitative EDS statistics. Based upon the EDS quantitative composition data, we present a model, grain boundary assisted crevice corrosion (GACC), that combines the energy of coincidence site lattices and sensitized grains to explain the shape of crevice corrosion observed at the grain boundaries. Finally, we conclude by connecting these results to future designs of CoCrMo alloys for biomedical or other uses.

2.2 Grain Boundary Sensitization

We provide here a brief overview of grain boundary sensitization as currently understood in the literature as a prelude to the nanoscale results described later. The term sensitization, as currently used in the literature, is the change in an alloy's corrosion properties as result of heat treatments [69,70,83-85,78,86]. For a variety of chromium-containing alloys and others such as magnesium-containing alloys, sensitization is widely used to describe the basic cause of intergranular corrosion (IGC) and intergranular stress corrosion cracking (IGSCC) [87-94]. The most general use of sensitization refers to a local reduction of the concentration of a protective alloying element. While this may not be the only possible reason for preferential corrosion at grain boundaries, it is the most commonly invoked source. For the specific case of CoCrMo alloys herein, we will use sensitization as it is applied to other chromium containing alloys, with "grain

boundary sensitization” referring to the formation of chromium depleted zones (CDZ) adjacent to grain boundaries due to the formation of chromium-rich carbides [76,95]. When steel, nickel and cobalt alloys are processed, annealed, and heat treated, chromium-rich carbides precipitate primarily at the grain boundaries, causing chromium depletion in the immediate surrounding regions [76,96,97]. The understanding of corrosion due to sensitization has motivated over 90,000 published studies, as grain boundary sensitization can directly lead to failure in high performance alloys.

Chemical segregation along grain boundaries has been most commonly studied in stainless steels, with fewer studies focusing on nickel or cobalt alloys. For stainless steels, the goal often is to develop processing time-temperature heat treatment maps of carbon content, chromium content, alloying time, and alloying temperature; the maps thereby direct engineers to safe, corrosion resistant alloys [87,98-100]. Various heat treatments have been studied to reduce the volume fraction of chromium carbides, attempting to ensure that chromium is even throughout the matrix, and promote the formation of protective oxide in order to control the corrosion resistance of a metal [83,84,90]. In general, the samples were analyzed for corrosion resistance by a range of methods at the mesoscale, with the target of comparing several different alloys and microstructures and their relative corrosion rates.

The effects of sensitization were often demonstrated through accelerated corrosion testing, and then measured through electrochemical tests, including potentiodynamic tests, potentiostatic tests, and electrochemical potentiokinetic reactivation tests [76,96,101-104]. The term “degree of sensitization” (DOS) is widely used and loosely defined, and it usually refers to the intensity and size of the CDZ at the grain boundaries [80,88,97,105,106]. The DOS was usually inferred from

electrochemical tests or fit by a model, but rarely directly measured. The chromium depleted zones explain the corrosion because the depletion left the alloy unable to form the necessary Cr_2O_3 protective oxide in that region [14,78,83,84,107-109].

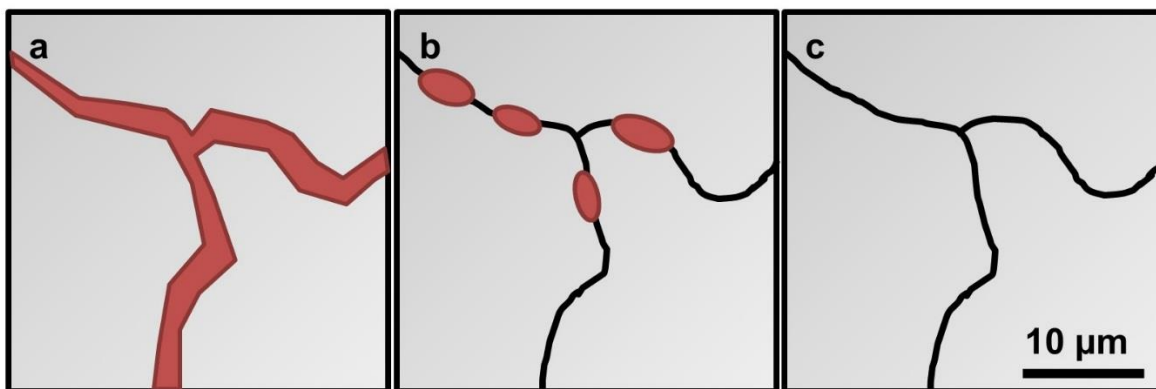


Figure 2.1 Carbide presence at a grain boundary may take the form of (a) a complete network along the grain boundary, (b) micron scale precipitates along some parts of the boundary, or (c) nanoscale precipitates unable to be seen at the micron scale.

It is widely considered in the literature that carbides play a major role in grain boundary sensitization, as the formation of chromium carbides at the grain boundary leaves nearby zones of chromium depletion [86,101,105,110,111,106]. This concept was based upon observations at the microscale that often showed materials with carbide phases along an entire grain boundary [86,96,101]. As shown in Figure 2.1, the carbide coverage can be a complete phase along a grain boundary as in 1 a, micron scale precipitates as in 1 b, or unnoticed nanoscale precipitates as in 1 c. In CoCrMo alloys, only carbides such as those in 1 a and 1 b have been observed to date with light or scanning electron microscopy. Often the presence of carbides was enough to conclude that a CDZ was present, and it was assumed that grain boundary sensitization was the cause of the corrosion [78,84,102]. Some chemical profiles have indicated that the composition of the carbides

were chromium carbide (Cr_{23}C_6) and that in CoCrMo alloys some carbides were molybdenum carbides (Mo_6C) [80,83,110,112]. Even including stainless steel, sensitization has only been studied down to hundreds of nanometers. It is unknown if carbides and CDZs of smaller length scales effect corrosion properties.

In addition to chemical composition of carbides and the chromium depleted zone, the geometric organization of a grain boundary lattice can also affect carbide formation and therefore sensitization [89,100,101,113]. Grain boundary crystallographic orientation is typically quantified using the coincidence site lattice (CSL) approach, where the crystal structures of the adjoining grains are classified as having a repeating match in their crystal structure pattern along the boundary (described by a Σ value). Boundaries with low CSL have been found to inhibit the depletion of soluble chromium in the vicinity of the grain boundary and therefore resist the formation of carbides and CDZs, leading to improved corrosion resistance [65,101,114]. For example, in nickel, grain boundaries with $\Sigma < 29$ were considered to have “special” properties [79,114]. In heat treated CoCrMo alloys from Panigrahi et al.’s work [65], grain boundaries below $\Sigma 9$ were immune to corrosion, as shown in Figure 2.2. While boundaries below $\Sigma 9$ were 100% immune and 70% of general boundaries did corrode, the CSLs from $\Sigma 11$ - $\Sigma 35b$ had a varied trend in corrosion. This implies that CSL is not the only factor controlling corrosion susceptibility. Additionally, boundaries with intrinsic dislocations along the boundaries have been demonstrated to act as sinks for solutes, i.e. forming chromium carbides. Intergranular boundary defects can act as preferential sites for breakdown of the protective oxide film, and with increasing chromium depletion, the barrier to initiate corrosion at these sites is reduced [79]. The goal of understanding the role of CSL in corrosion is to enable engineering of the grain boundary orientations to favor

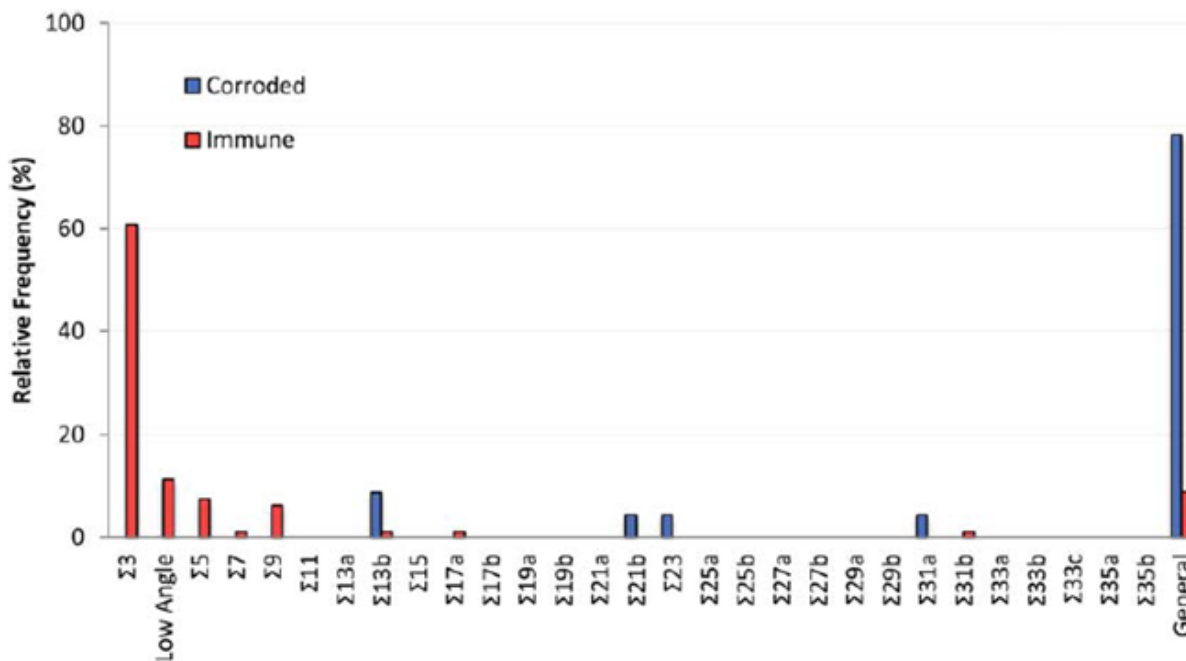


Figure 2.2 From Panigrahi et al. [65]. Relative frequencies of grain boundary geometries for corroded and immune boundaries. The fcc grain boundary geometries are listed in order of decreasing lattice coincidence.

boundaries that resist corrosion, in order to improve the bulk corrosion resistance [113,115-118].

Models have been developed to predict the extent of sensitization, focusing primarily on stainless steels and on the length and temperature of the heat treatment [80,88,105,106]. Proposed models used three parameters to characterize CDZ: coverage, width, and depth [96]. Coverage is the proportion of the grain boundary length covered by CDZs. Width is the extent of the depleted zone perpendicular to the grain boundary. Depth is the minimum level of chromium in the depleted zone. Additionally, previous work has attempted to link the width of sensitization to the width of the crevice corrosion observed, but it was always shown that the crevice is much larger than the sensitized region in the model [88,96]. Width was always found to be narrower than the electrochemically corroded area and not a predictor of corrosion intensity.

The stainless steel models have used thermodynamic calculations to analyze the equilibrium concentration of chromium in the matrix at the carbide-matrix interface [86,88,119]. The quantitative composition of sensitization reported for stainless steel often cites Stawstrom and Hillert, where sensitization was said to occur at less than 13 at% Cr for a width greater than 20 nm at the grain boundary [88]. It was reported in stainless steels that when the level of chromium in the depletion falls below 12-13 at%, the passive film over the depleted region becomes easily breached to initiate corrosion and degradation [86,88], leading most stainless steel models to use an approximate alloy composition of ~19 at% Cr and to assume sensitization around ~13 at% Cr [106,120-122]. These models for sensitization have not been expanded to cobalt alloys, and involved precipitates on a scale of 100s of nanometers to microns, without consideration of nanoscale precipitates.

Much less is known about CoCrMo alloys compared to stainless steels. Some steels studies have done EDS line scans on the range of 100s of nanometers to directly measure CDZ, and then linked the composition data to predictive models. These models, however, were often for micron sized carbides with large CDZs. In CoCrMo alloys, the scale of investigation has also focused on micron sized carbides and extensive carbide phases along an entire boundary [78,109]. The majority of the sensitization conclusions were made after electrochemical measurements were taken. Previous studies have at most taken point compositions or coarse micron scale line scans across carbides and CDZs, often presenting only one composition profile scan [83,84,110]. Some studies have characterized the nanoscale compositions of various carbides [123], but not in relation to heat treatment or corrosion, and there are studies which looked at CSL, heat treatment, and corrosion, but did not consider composition [65,79,124].

To summarize this section, grain boundary sensitization due to mesoscale segregation is fairly well understood in many steels and less so in CoCrMo alloys. The extent that grain boundary sensitization concepts at this large scale can or should be used for segregation at the nanoscale is a rather open question.

2.3 Methods

2.3.1 CoCrMo Alloy

The CoCrMo alloy used was a high-carbon (HC) wrought alloy from ATI Allvax, US, with a composition corresponding to ASTM F 1537-08 [125]. The composition is given in Table 1. The samples' heat treatments, microstructure, and electrochemical treatment have been described in previous work by Panigrahi, et al. [65] For this study, a HC wrought pin annealed at 1230°C for 24 hours was used, as this anneal was most successful in reducing overall corrosion rate and localizing corrosion to grain boundaries, with examples of corrosion shown in Figure 2.3 [65]. After the anneal, the sample was quenched in water.

Table 2.1 Composition of the high-carbon CoCrMo alloy.

| at% | Co | Cr | Mo | C | Mn | Si | Ni | Fe |
|-----|---------|------|-----|------|-----|------|-----|-----|
| | Balance | 30.3 | 3.6 | 1.14 | .73 | 1.34 | .17 | .14 |

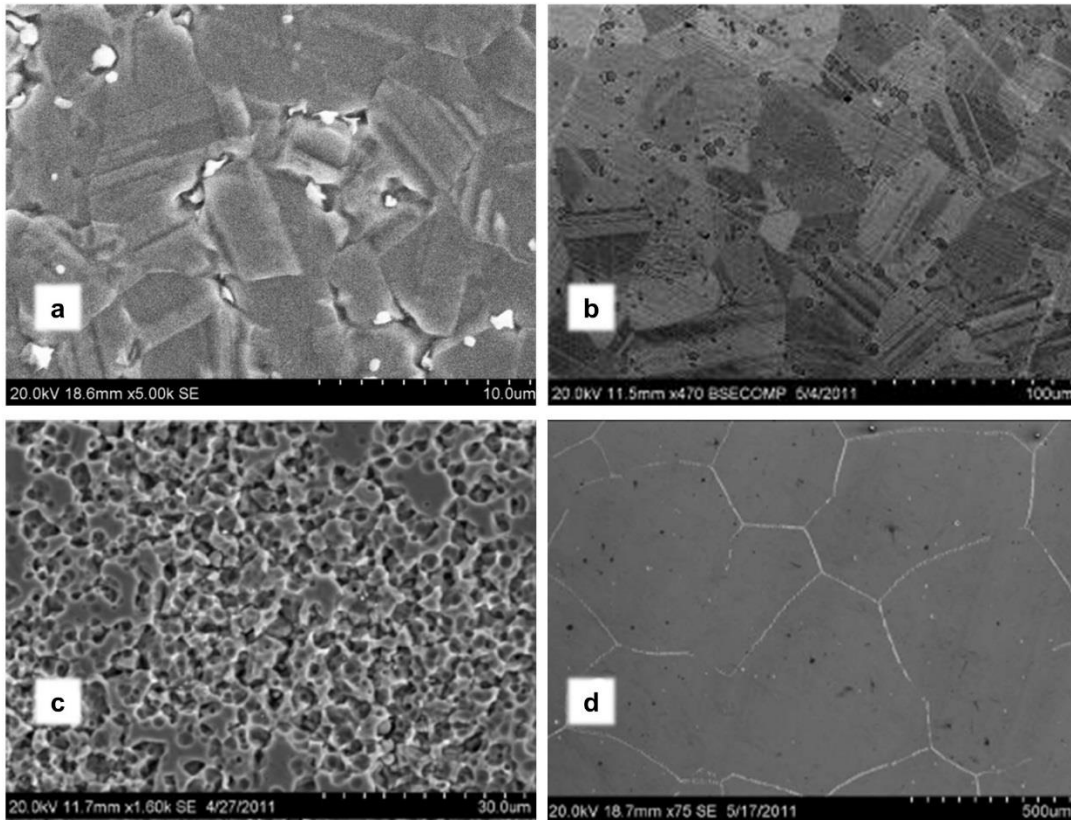


Figure 2.3 From Panigrahi et al. [65]. (a) As received wrought structure with 3-5 μm grains. (b) After 24 hour anneal at 1230 $^{\circ}\text{C}$ the grains grew to 100-300 μm with few second phases. (c) Corroded surface of as received wrought. (d) Corroded surface after 24 hour anneal at 1230 $^{\circ}\text{C}$. Note the differing scale bars.

2.3.2 Electrochemical Corrosion Testing

For the sample of CoCrMo alloy previously studied by Panigrahi, et al. [65], the electrochemical corrosion testing and properties are described in detail in the previous publication. To summarize, the samples were mechanically polished immediately prior to electrochemical corrosion testing. The sample was then corroded in a custom four-chamber electrochemical cell that served as a working electrode, along with a graphite counter electrode and a saturated calomel electrode reference electrode. The corrosion cell was filled with 10 mL of bovine calf serum (BCS) with a protein content of 30 g/L, buffered to a basic pH of 7.4, and placed in a hot water bath

maintained at 37 °C to mimic physiological conditions. Buffering a biological solution typically involves adding phosphate-buffered saline (PBS), NaCl, or NaOH.

A standard protocol was used for the electrochemical tests. The tests began with a potentiostatic test to standardize the surface, followed by an electrochemical impedance spectroscopy test. A potentiodynamic (cyclical polarization) test was performed to corrode the sample and measure the current at each applied potential. The samples were anodically polarized from -0.8 V to 1.8 V at a scan rate of 2 mV/s and then reversed back down to -0.8 V at the same rate. Using the corrosion current from Panigrahi et al.'s results and Faraday's equation, the dissolution rate was calculated to be 2.98×10^{-3} mm/yr. Based on the previous study, congruent dissolution is assumed in our later analysis.

2.3.3 Electron Backscatter Diffraction

Electron backscatter diffraction (EBSD) methods were used to create orientational image maps (OIM) of selected regions of the annealed CoCrMo alloy sample. A FEI Quanta ESEM with an EBSD detector was used to acquire and index diffraction patterns for multiple 2D arrays on the sample surface. An accelerating voltage of 20 kV and a step size of 0.5 μm were used, as these conditions supplied enough resolution and signal to map the CSLs of relevant grain boundaries. Orientational indexing from the Kikuchi patterns was performed using the commercially available Oxford AZtec EBSD processing software, assuming a single fcc-Co matrix phase. Using the Oxford Tango software, noise reduction was performed to minimize the role of the roughness of the corroded surface, and misorientation matrices for each grain boundary were calculated from the Euler angles. Each grain boundary was mapped as a high-angle or a low-angle grain boundary.

For the high-angle boundaries ($>15^\circ$ misorientation angle), the Brandon Criterion [126] was used to determine the reciprocal CSL density Σ based on the geometric three-dimensional misorientation with lattice coincidence for fcc crystals.

2.3.4 White Light Interferometry

A Bruker Contour GT-K 3D optical microscope equipped with a Mirau interferometer objective lens was used to quantitatively measure the topography of the corroded grain boundaries. The white light interferometer had a lateral resolution limited by the wavelength of light and a finer z-axis resolution limited by the sensitivity of the light intensity detector [127]. This technique was used to measure the width of corroded grain boundaries and depth of corroded regions with respect to the surrounding surface.

A magnification of 40x was used to capture the profile of the corroded surface in a 2D projection of approximately 250 μm in length and 300 μm in width. In total, 25 grain boundaries, 13 CSL boundaries and 12 non-CSL boundaries, were characterized for their depth and width. For each individual grain boundary, 15-20 depth and width measurements were collected along the boundary. On average, a single depth measurement was acquired per 0.5-1.0 μm along the boundary. The width of the corroded boundary was acquired by measuring the distance between the two edges of the corroded crevice at the boundary. The mean of the depth and width measurements were computed, along with the range, to a 95% confidence level.

2.3.5 Focused Ion Beam

A FEI NanoLab dual-beam focused ion beam (FIB) system was used to prepare lamellar TEM samples from the annealed CoCrMo alloy. The FIB used a scanning electron imaging beam operated at 5 kV and 1.4 nA and a focused ion milling beam orientated at 52° to the electron beam operating at 30 kV from 9.2 nA to 48 nA. Specific grain boundaries were identified from the OIM

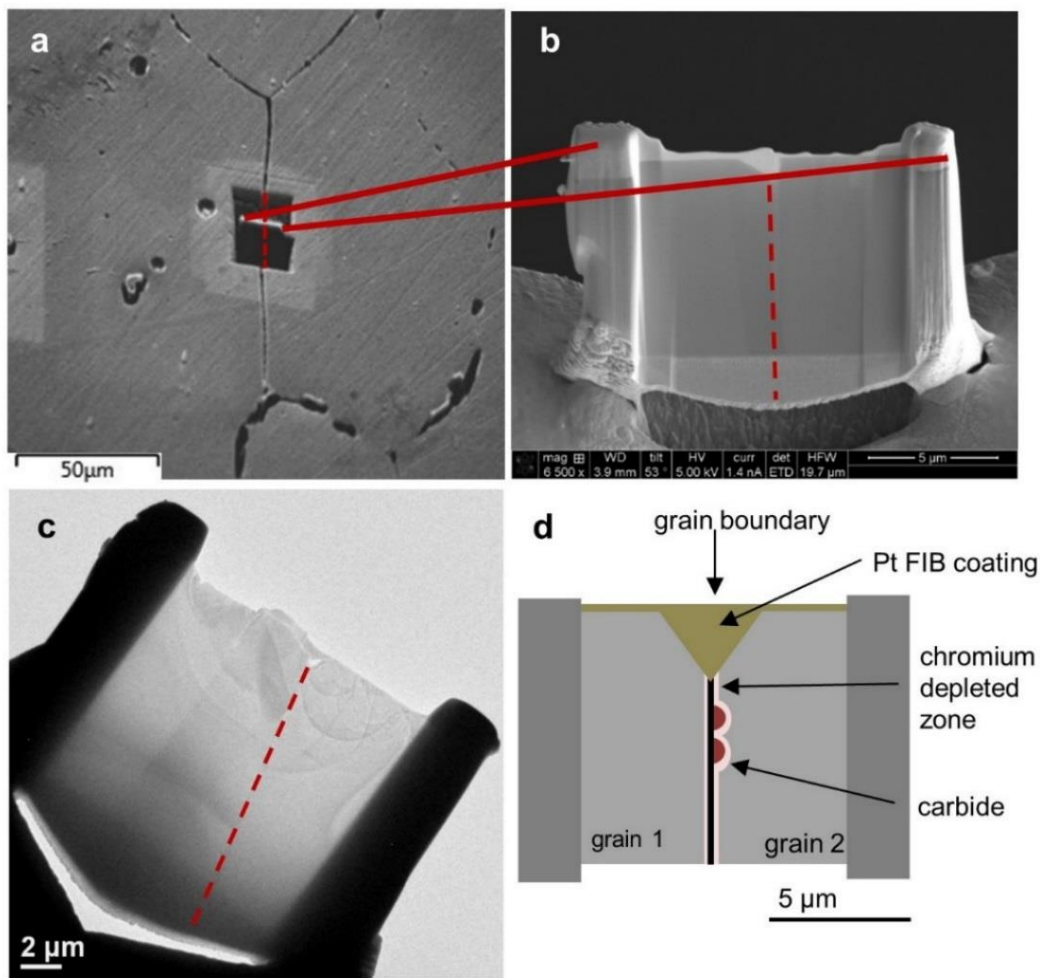


Figure 2.4 (a) SEM image showing a single grain boundary being cut from the bulk sample, (b) the lamellar viewed in SEM comprising of the two grains with the grain boundary, indicated by the dotted line down the middle, (c) a sample viewed in TEM again with the dotted line on the grain boundary, and (d) layout of a typical corroded sample.

data and a cross section of the boundary was made into a ~100 nm thick, electron-transparent TEM sample for further analysis. The lamellar sample created was a cross section of the grain boundary, approximately 5 μm on either side of the boundary and 5 μm deep below the bulk surface, as shown in Figure 2.4. Twenty-two grain boundary FIB samples were prepared. Twelve corroded boundaries and 10 immune boundaries were prepared and imaged, including 10 non-CSL corroded grain boundaries, 2 CSL corroded boundaries, 5 non-CSL immune boundaries, and 5 CSL immune boundaries.

FIB was also used to prepare grain boundary samples for use in local-electrode atom-probe (LEAP) tomography. The samples were prepared by the lift out process and sharpened by milling, with special attention paid to orienting a grain boundary through the area of the sharpened tip [128]. A platinum protective layer and a final milling at 5 kV was used to prevent ion implantation in the region of interest.

2.3.6 Transmission Electron Microscopy and Energy Dispersive X-ray Spectroscopy

TEM was performed to analyze the structure and composition of the grain boundary FIB samples to compare between corroded and immune boundaries. A JEOL 2100 TEM was used for bright field, dark field, diffraction, and high resolution imaging, and EDS chemical analysis. The EDS on the JEOL 2100 had a 1 nm probe size, with most analysis confined to line scans for minimum noise, and processed through Inca software.

TEM was also performed on a JEOL ARM200CF with a windowless EDS detector for high resolution EDS mapping of 4 selected grain boundary FIB samples. The aberration corrected ARM provided an EDS analysis probe size of approximately 0.13 nm. For carbide composition

quantification, measurements were taken from 2-4 carbides per boundary for each sample. The EDS quantification spectra were taken from three regions of each carbide – the carbide, the CDZ, and the matrix, and these are indicated in the maps. The maps were collected and analyzed using the Oxford AZtec TEM software.

2.3.7 Atom Probe Tomography

Atom probe tomography (APT) analysis was performed using a LEAP tomograph manufactured by Imago Scientific Instruments. The analysis was formed at a specimen temperature of 25 K, a pulse repetition frequency of 500 kHz, a laser energy of 40 pJ, and a detection rate of 0.01%. Reconstruction was done by means of IVAS 3.6.8 using SEM profiles of the tips for the shape reference. Line scans were generated using 2D regions of interest and normalized to remove gallium atoms from the composition.

2.4 Results

The annealed and corroded alloy was first examined with EBSD to determine relevant grain boundaries for representative TEM samples. The EBSD OIM produced three maps for each scanned region: the SEM image, OIM image, and the labeled CSL boundaries image, as shown in Figure 2.5. The same regions mapped in EBSD were later found in the FIB SEM, and known CSL and non-CSL samples were prepared for TEM analysis. White light interferometry was used to characterize the morphology of corroded boundaries that were both CSL and non-CSL. From the depth and width characterization of corroded crevices, it was determined that CSL boundaries

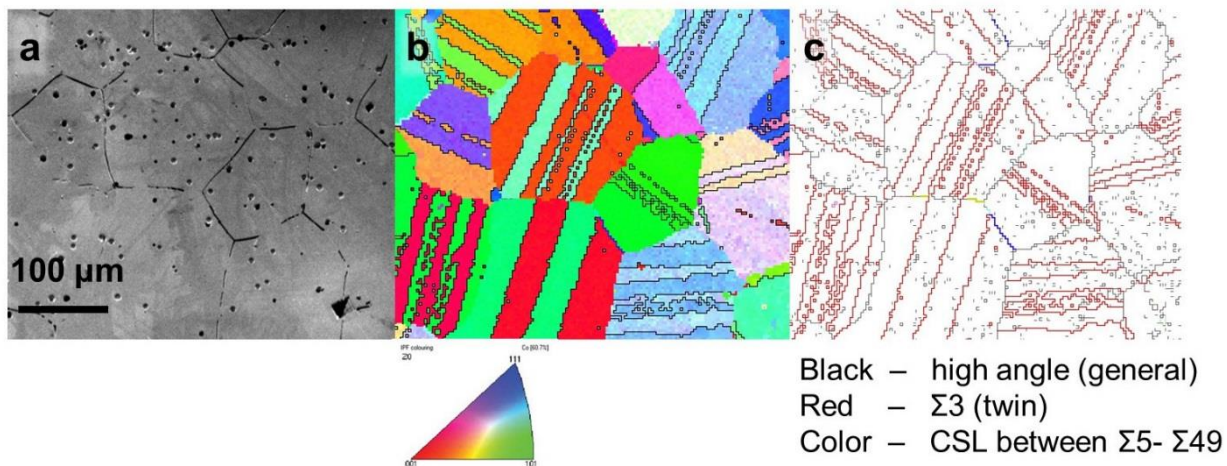


Figure 2.5 The EBSD generated (a) SEM images, (b) OIM images, and (c) labeled CSL boundaries of the scanned region, later identified in the FIB/SEM for TEM sample preparation.

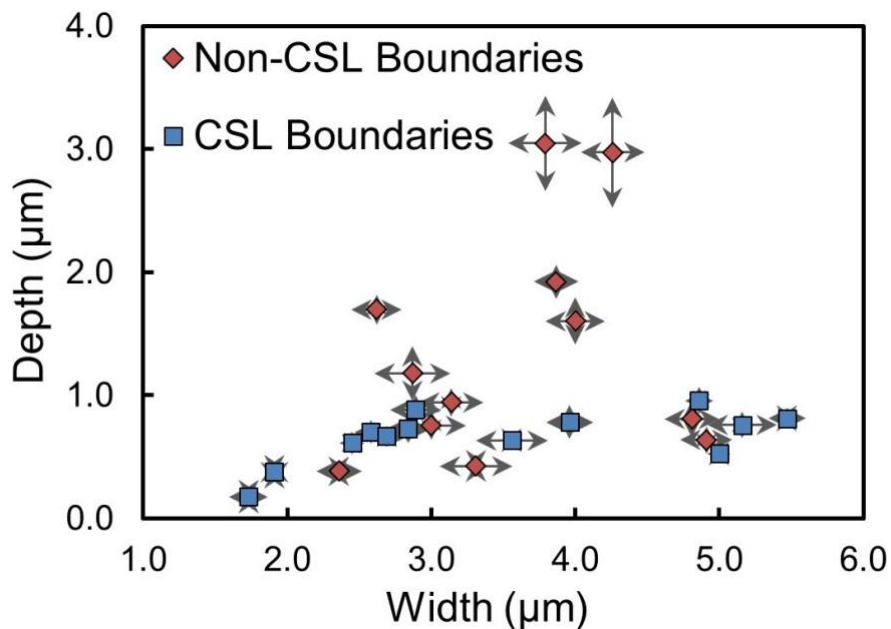


Figure 2.6 Depth and width measurements collected from 3D profilometry showed that the corrosion width was approximately 2-5 times larger than its corresponding depth. With square as CSL and diamond as non-CSL, each point represents a single boundary, where the arrows represent the range of the multiple measurements along that boundary.

corroded between 0.18–0.96 μm in depth and 1.73–5.47 μm in width. For non-CSL boundaries, the corrosion depth ranged from 0.38–3.05 μm and the width ranged from 2.36–4.91 μm , as summarized in Figure 2.6. The corrosion depth upper-threshold was observed to be about 1.0 μm in CSL boundaries, whereas non-CSL depth observations showed a much larger and deeper range of crevice depth. The 3D profilometry results indicated that the widths of the corroded grain boundaries were 2–5 times larger than the corresponding depths.

The initial examination of corroded and immune samples in bright field TEM showed that the corroded boundaries had a wavy structure, later determined to be due to chromium-rich carbides, whereas immune boundaries were straight without deviations. Representative examples are both shown in Figure 2.7. Using EDS maps and line scans in the JEOL 2100, the features along the corroded grain boundary were determined to be chromium enhancements, as seen in an example boundary in Figure 2.8. As shown in Figure 2.9, the carbide structure was confirmed through diffraction of the two grains and the carbide in-between, showing that the intergranular carbides have the expected M_{23}C_6 composition. To summarize the standard TEM analysis, all 10 of the corroded boundaries contained chromium-rich carbides dotted along the grain boundaries, while all five of the CSL immune boundaries did not show carbides, and four of the five immune boundaries did not show carbides. The results of the 22 grain boundary samples are summarized in the chart of Figure 2.10. The one immune boundary with carbides showed that the carbides were on a size scale <50 nm, less than half of the size of the other corroded boundaries' carbides.

The chromium-rich carbides were lens shaped, and shared epitaxial alignment with the grain on the concave side of the carbides, as demonstrated in an example boundary in Figure 2.11 and Figure 2.12. Figure 2.11 a shows a bright field TEM image and Figure 2.11 b shows a high

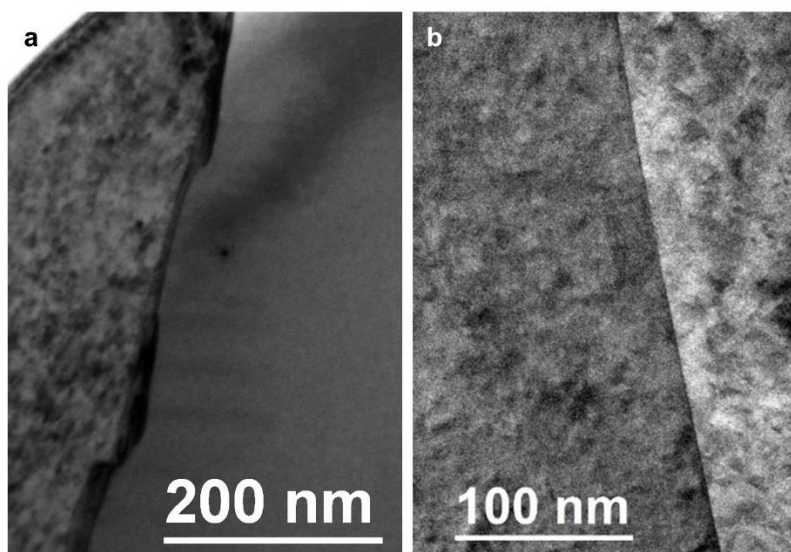


Figure 2.7 The initial examination in bright field TEM showed (a) the corroded boundaries have a wavy structure, where each bend was a carbide feature at the boundary, whereas (b) immune boundaries were straight and featureless.

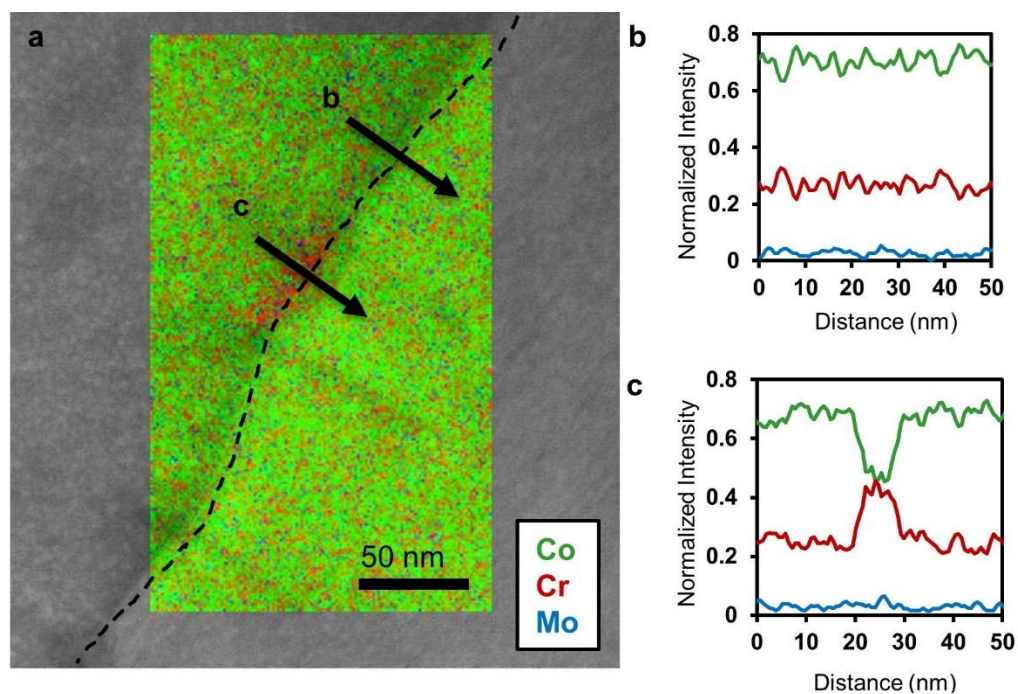


Figure 2.8 (a) Bright field TEM image with an EDS map, Co = green, Cr = red, and Mo = blue from a JEOL 2100. The dotted line indicates the grain boundary, with a chromium enhancement. Line scans (b) and (c) indicate the change in concentration at the carbide.

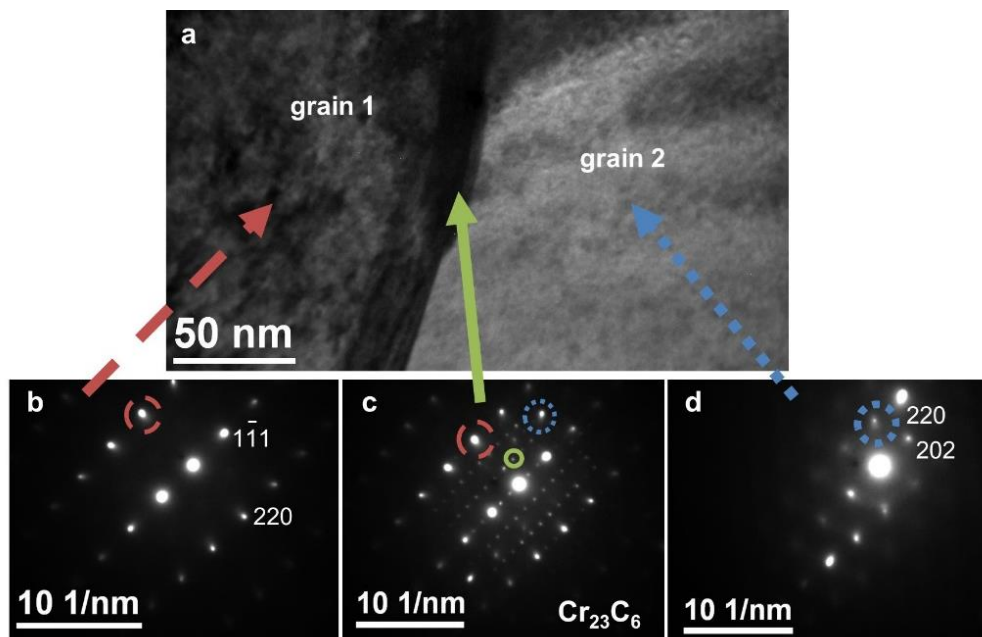


Figure 2.9 (a) Bright field image of a grain boundary with a chromium-rich carbide. (b) Diffraction pattern of grain 1, (c) diffraction pattern of the feature showing a $M_{23}C_6$ carbide grain structure, and (d) diffraction pattern of grain 2.

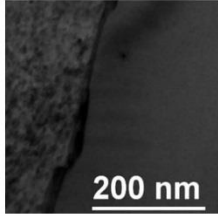
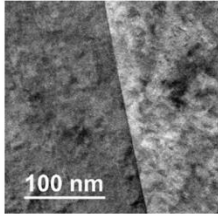
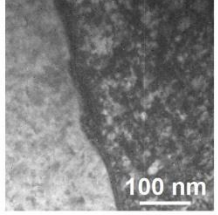
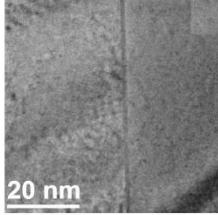
| | Corroded | Immune |
|------------------|---|---|
| Non-CSL boundary | Carbides (N=10) No Carbides (N=0)  | Carbides (N=1) No carbides (N=4)  |
| CSL boundary | Carbides (N=2) No Carbides (N=0)  | Carbides (N=0) No Carbides (N=5)  |

Figure 2.10 The chart summarizes the samples measured in each category and if carbides were present. The boundary can be either CSL or non-CSL, and either be corroded or immune. The proportion of samples in each category represents the approximate frequency seen in the bulk sample.

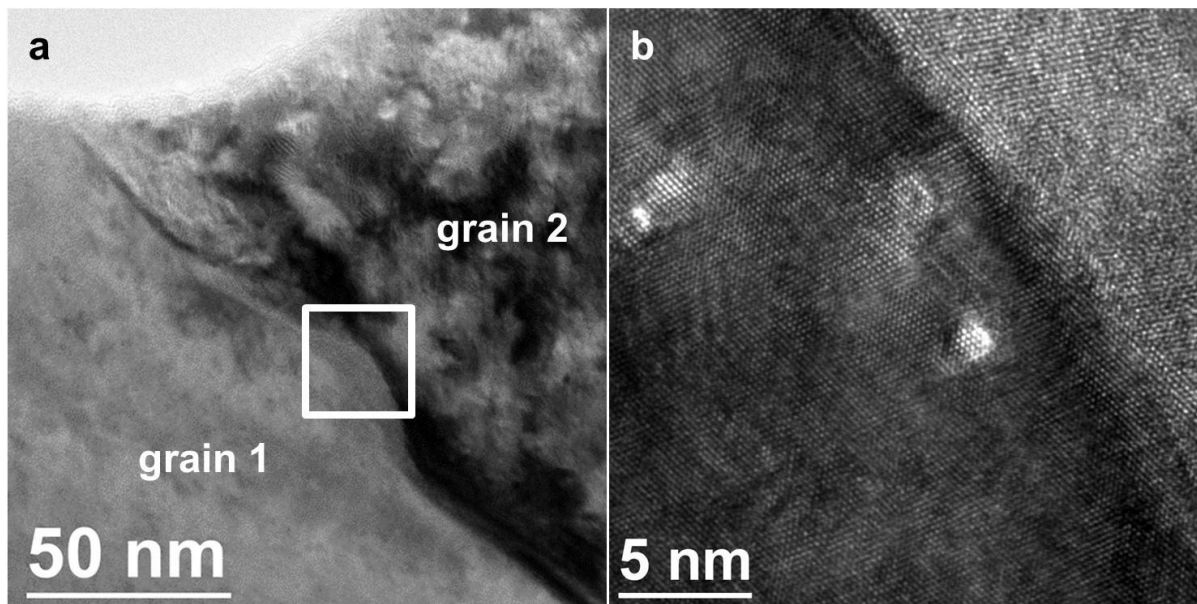


Figure 2.11 (a) The lens shape of the chromium-rich carbide with (b) the HREM showing the shared epitaxial alignment with the concave grain.

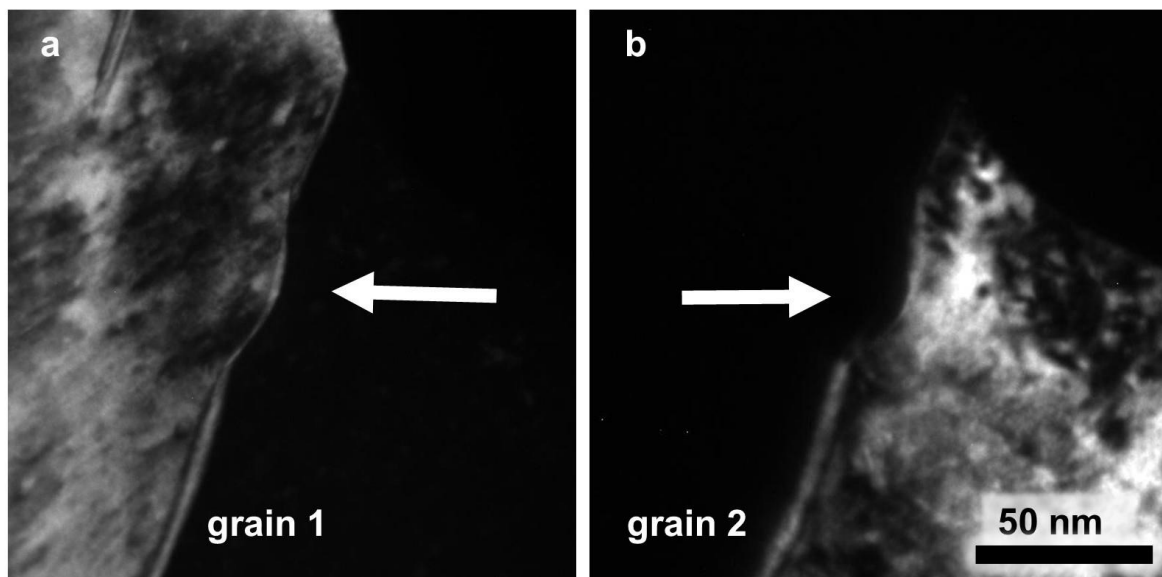


Figure 2.12 Dark field selecting for (a) grain 1 and (b) grain 2, show the epitaxial nature of the chromium-rich carbide to the grain on the concave side of the lens.

resolution image with the carbide epitaxy to grain 1. Figure 2.12 shows the same sample, confirming the carbide epitaxy through dark field TEM. In dark field, a particular diffraction spot can be selected and only the grains of that orientation will appear bright. The bump out feature of the carbide was shown when the crystallographic orientation of grain 1 was selected in dark field in Figure 2.12 a. When the crystallographic orientation of grain 2 was selected in Figure 2.12 b, the carbide feature was dark like the rest of grain 1. This implies that the carbide had the same orientation as grain 1. Comparable carbide shape and evolution has been previously modeled for

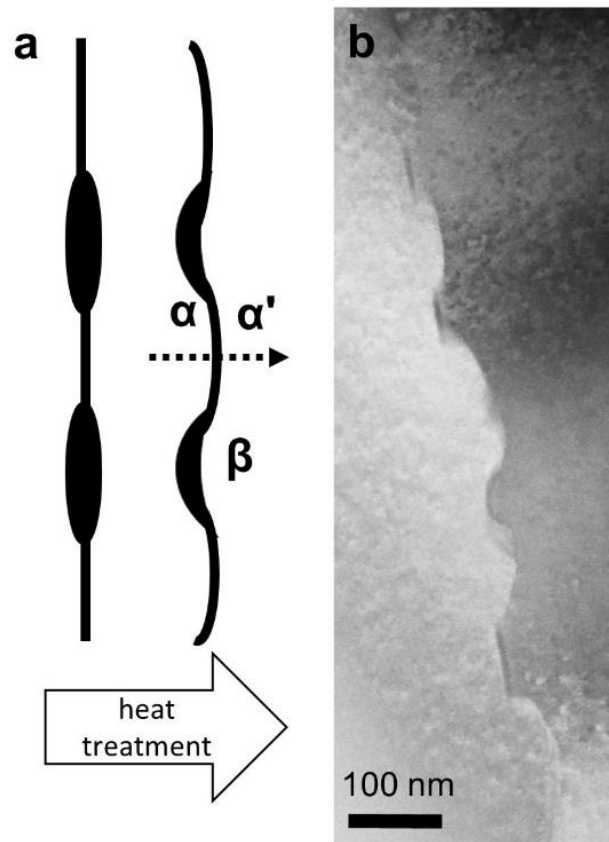


Figure 2.13 The distinct shape of the chromium-rich carbides has been previously modeled by a copper indium alloy, with α as the trailing grain, α' as the forward grain, and β as the carbide [129].

a copper indium alloy, as diagramed in Figure 2.13 [129]. The driving force for carbides to segregate during the initial casting was the reduction of the surface energy between the bulk grains and the grain boundary, replacing a high-energy boundary, α/α' with a low-energy boundary, α/β and α'/β . These carbides formed on the disordered, high-energy boundary, agreeing with other sensitization and CSL models [79,124,129].

A representative annular dark field (ADF) image and high-resolution EDS map, in Figure 2.14, shows the lens-shaped chromium-rich carbide at the grain boundary of the CoCrMo alloy. The clearest EDS signal showed the primary elements of the composition, Co, Cr, and Mo as maps and with a quantized chart from key regions in Table 2.2. The area around the carbide was a CDZ, i.e. the chromium composition was reduced around the carbide and along the grain boundary. The depleted zone normal to the grain boundary plane was at the same length scale as the width of the carbides, about ~10 nm, seen in the line scan in Figure 2.14 b. For another carbide map in Figure 2.15, the CDZ extended along the grain boundary with a comparable length scale to the length of the carbide, with compositions at these regions quantized in Table 2.3. This is seen in the maps, but was confirmed through the quantified EDS regions. High-resolution EDS scans were taken along 2-5 carbides of each of the four samples. The average carbide composition, matrix composition, and depleted zone compositions are shown in Table 2.4. For the singular immune sample with carbides, the <50 nm carbides were included in the EDS scans. The chromium depletion in these carbides, i.e. the difference in the matrix chromium composition and the chromium composition along the grain boundary, was less than 2 at% Cr, as shown in Figure 2.16. The composition is shown in Table 2.5. This size of carbide became small enough to no longer cause a chromium depleted zone, which left that grain boundary immune.

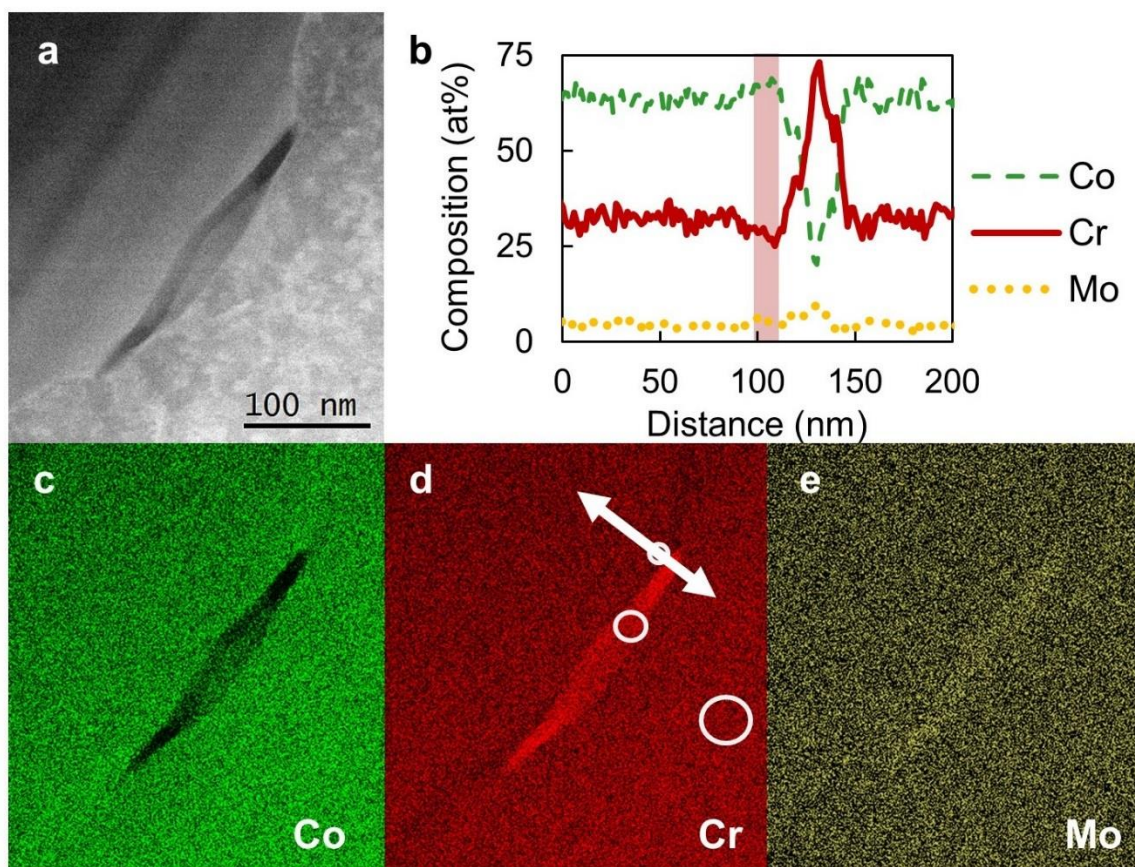


Figure 2.14 The chromium depleted region around a chromium-rich carbide, with (a) the ADF image, (b) an extracted line scan to show the CDZ, (c) cobalt, (d) chromium, and (e) molybdenum. The arrow indicates where the line scan was taken, and the circles indicate where the EDS spectra were quantized, reported in **Table 2.2**.

Table 2.2 EDS quantification, **Figure 2.14** carbide.

| | Co (at%) | Cr (at%) | Mo (at%) |
|---------|----------|----------|----------|
| Matrix | 62.5 | 33.6 | 2.9 |
| Carbide | 18.7 | 73.8 | 8.0 |
| CDZ | 68.3 | 23.0 | 5.1 |

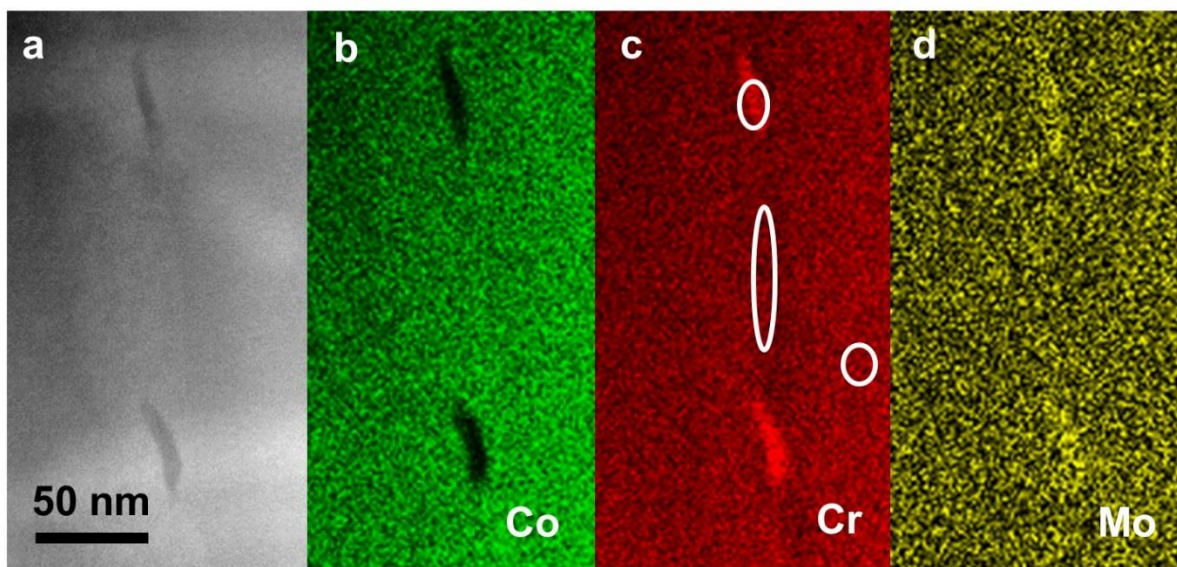


Figure 2.15 The chromium depleted region between two chromium-rich carbides, with (a) the ADF image, (b) cobalt, (c) chromium, and (d) molybdenum. The chromium depletion is measured along a 150 nm section of grain boundary between two carbides and found to be sensitized by 2%. The circles indicate where the EDS spectra were quantized in **Table 2.3**.

Table 2.3 EDS quantification, **Figure 2.15**.

| | Co (at%) | Cr (at%) | Mo (at%) |
|---------|----------|----------|----------|
| Matrix | 62.5 | 31.1 | 4.2 |
| Carbide | 37.5 | 53.7 | 6.7 |
| CDZ | 64.3 | 29.1 | 4.2 |

Table 2.4 Summary of Averaged EDS quantifications.

| | Co (at%) | Cr (at%) | Mo (at%) |
|---------|----------------|-----------------|---------------|
| Matrix | 62.9 ± 1.5 | 30.6 ± 1.4 | 4.4 ± 0.7 |
| Carbide | 29.6 ± 7.8 | 62.4 ± 8.9 | 7.8 ± 1.2 |
| CDZ | 69.2 ± 2.7 | 23.8 ± 2.19 | 4.2 ± 0.9 |

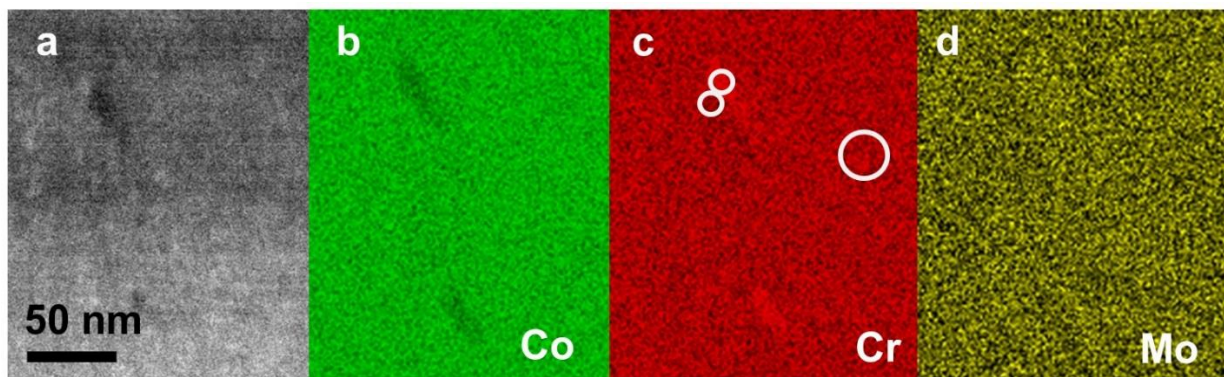


Figure 2.16 Carbides less than ~50 nm did not show measurable chromium depletion, with (a) the ADF image, (b) cobalt, (c) chromium, and (d) molybdenum. The circles indicate where the EDS spectra were quantized in **Table 2.5**.

Table 2.5 EDS quantification, **Figure 2.16** carbide.

| | Co (at%) | Cr (at%) | Mo (at%) |
|---------|----------|----------|----------|
| Matrix | 64.5 | 31.5 | 3.9 |
| Carbide | 56.5 | 39.0 | 4.5 |
| CDZ | 67.0 | 30.0 | 3.3 |

We note that the size or volume fraction of the carbides scales approximately with the intensity of chromium depletion near them; larger carbides cause larger chromium depletion. This indicates that there is a local “chromium conservation” in regions 20-40 nm on either side of the grain boundaries, and no long-range diffusion of chromium, at least for the conditions used to make these samples.

Atom probe tomography complemented the EDS results, a region containing a grain boundary and a carbide is shown in Figure 2.17. The shape of the carbide was ~60 nm along the boundary by ~10 nm wide, with a similar lens shape to those observed via electron microscopy. A line scan taken through the slice, as shown in Figure 2.17 b, shows that the composition of the matrix was

30 at% Cr and the composition in the carbide was 90 at% Cr; the exact composition could not be determined with a high accuracy because of uneven evaporation from the sample.

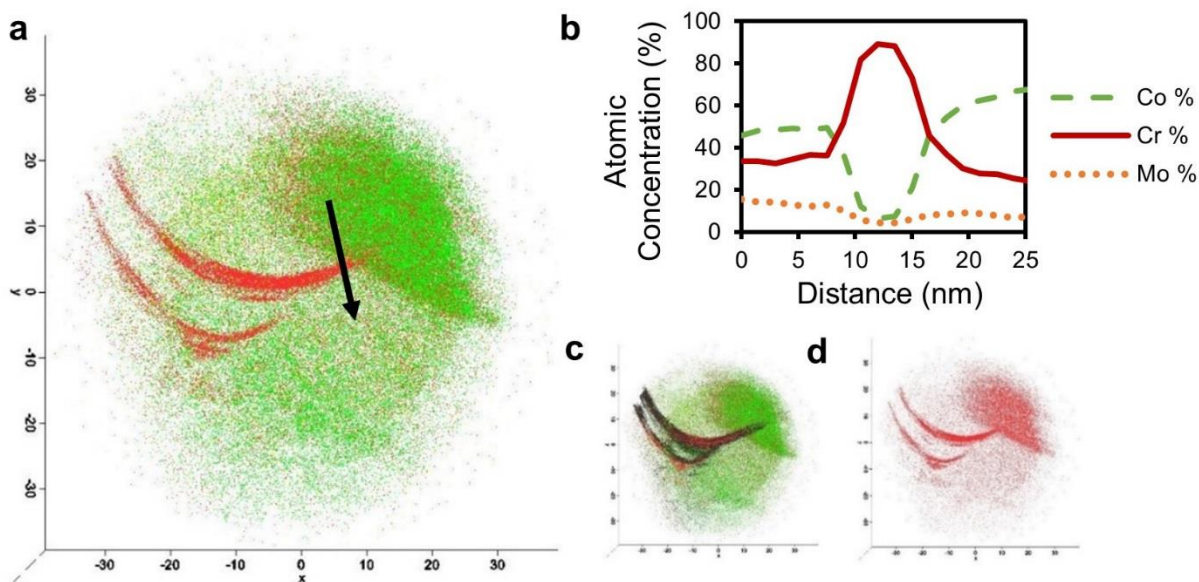


Figure 2.17 (a) A 10 nm thick slice of LEAP acquisition that intersected with a grain boundary and a carbide. (b) Composition profile through the edge of the carbide showing the chromium segregation. (c) The gallium present from FIB thinning segregated to the boundaries in the sample (black), which leaves a track of where the grain boundary is located. (d) The chromium concentration evaporating mainly at the grain boundaries of the carbide with a patch of uneven evaporation on the edge.

2.5 Grain Boundary Assisted Crevice Corrosion (GACC) Model

Having now presented the experimental results, we turn to developing a general model for corrosion associated with nanoscale precipitates to connect nanoscale segregation with corrosion. As described earlier, the primary focus of the current literature has been on large precipitates at grain boundaries, two to three orders of magnitude larger than what we observed. These micron carbides lead to extensive regions of chromium depletion, and the detailed mechanism of sensitization is not necessarily the same for the samples herein; we found less segregation that was

also spatially inhomogeneous. We need to extend prior models to finer-scale segregation. We will first consider first the grain boundary component, showing that both the grain boundary energy and local chromium concentration play a role in corrosion properties. We then extend the model to include local crevice corrosion for a more complete description of grain boundary accelerated crevice corrosion.

2.5.1 Local Grain Boundary Attack

The difference in composition between the chromium depleted and matrix compositions leads to a difference in the corrosion potentials that effected the dissolution of the CoCrMo alloy. The main composition change was a chromium depleted zone next to a chromium rich $M_{23}C_6$ carbide. There is an enhancement of Mo in the $M_{23}C_6$ carbide, a common result of alloys with both Mo and Cr in the $M_{23}C_6$ carbides, but no difference in the CDZ. The Mo concentration does not change in the CDZ, therefore the average composition of the matrix and CDZ can be renormalized to include only Co and Cr.

The first step is to model the manner in which the nanoscale segregation and grain boundary energy impact corrosion initiation; we need to understand whether the energy change for corrosion due to local chromium depletion dominates the energy due to removal of the grain boundary. Figure 2.18 shows the differences between macro and nano scale corrosion. For macro sensitization, the alloy composition becomes so chromium depleted that the protective oxide cannot form. We argue that this model does not scale to the nanoscale because the depletion was too small to significantly change the oxide coverage. Chromium oxide growth over nanoscale depleted regions have been shown for regions <20 nm in CrZr alloys [130] and for other alloys

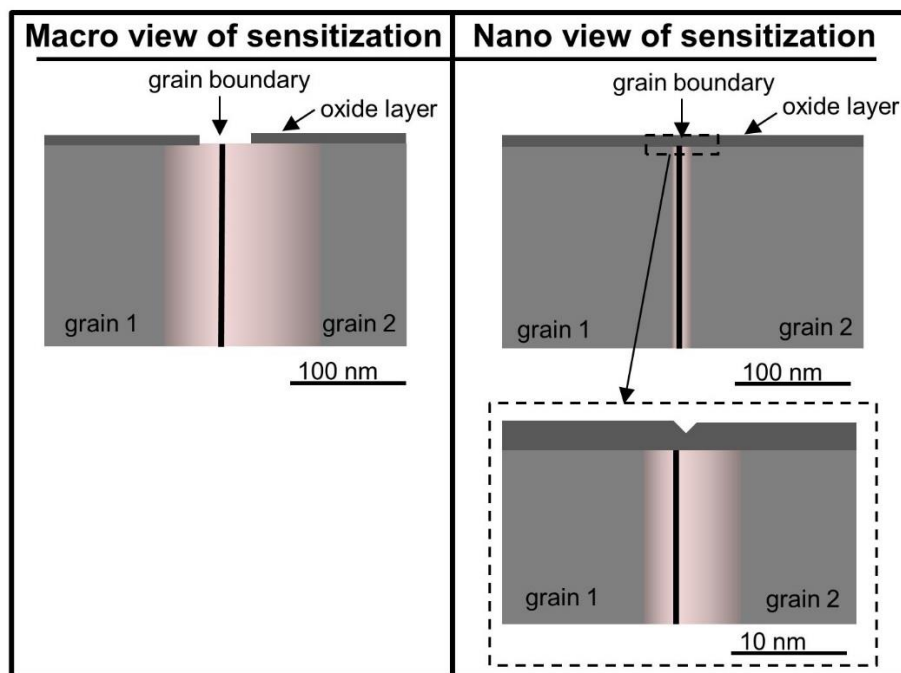


Figure 2.18 The macro view of sensitization has large regions of chromium depletion, leading to incomplete oxide formation around the sensitized boundary. In nanoscale sensitization, the oxide is not significantly diminished. The chromium depletion is on a nanometer scale along the boundary.

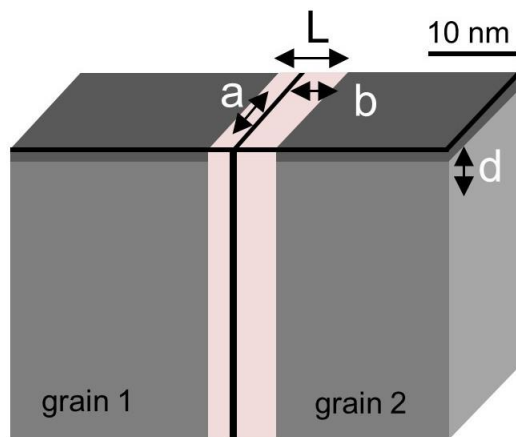


Figure 2.19 The model for grain boundary assisted crevice corrosion includes the CDZ width (L), the distance between atoms along the grain boundary (a), the distance between atoms perpendicular to the grain boundary (b), and the depth of one monolayer of atoms removed from the surface (d). The weighted average diameter of Co and Cr can be used for a , b , and d , while L is measured from the EDS maps.

[131], so this is a reasonable assumption of oxide overgrowth in our CDZ of ~10 nm. Instead of a broken CrO₂ oxide layer, we focus on the grain boundary energy and chromium depletion magnitude at the boundary by comparing the grain boundary energy for CSL and non-CSL with the grain boundary energy effect of a CDZ.

It has been previously shown that as the chromium content of an alloy decreases the corrosion potential increases [132,133], and here we can approximate that the CoCrMo alloy would follow a similar trend. In Kelly et al. [132], a Fe-Cr alloy with 20 at% Cr corrodes at -370 mV SCE and the alloy with 14 at% Cr corrodes at -310 mV SCE. At this level of chromium depletion, the corrosion potential increases 10 mV per 1 at% Cr decrease. Using the EDS data of the quantified chromium depletion zone in our experiments, the chromium reduction was, on average, 7.1 at% Cr. The change in corrosion potential from the matrix to the CDZ would be 71 mV, designated as $\Delta\mu$.

$$\Delta\mu = \mu_{matrix} - \mu_{CDZ} \quad \text{Equation 2.1}$$

$$\Delta\mu = -71 \text{ mV} \quad \text{Equation 2.2}$$

The electrochemical difference was converted to joules using a weighted average for composition for the charge unit of Co and Cr, as:

$$\Delta\mu = -71 \text{ mV} * 2.3e = -0.1633 \text{ eV} \quad \text{Equation 2.3}$$

$$\Delta\mu = 2.61 \times 10^{-20} \text{ J} \quad \text{Equation 2.4}$$

With the electrochemical potential difference of the matrix and the chromium depleted zone, we calculated the difference in grain boundary energy between these two compositions. The

parameters considered for the model are shown in Figure 2.19, with L the width of the CDZ, a the distance between atoms along the grain boundary, b the distance between atoms perpendicular to the grain boundary, and d the depth of corrosion set to one monolayer. We defined the energy of the grain boundary ΔE_{GB} and energy lost due to the chromium depleted zone ΔE_{CDZ} per unit length of both as

$$\Delta E_{GB} = -\gamma_{GB}d \quad \text{Equation 2.5}$$

$$\Delta E_{CDZ} = \Delta\mu \frac{L}{ab} \quad \text{Equation 2.6}$$

The interfacial grain boundary energy was approximated using the molecular dynamics results of an Fe-Cr system with 30 at% Cr, as Fe and Co have the same surface energy values as pure materials [134,135]. The weighted average of the atomic diameters of Co and Cr is 0.382 nm, and this value was used for a , b , and d . The γ_{GB} of the CoCrMo alloy grain boundaries varies from 0.4 J/m² to 1.4 J/m². We found the average chromium depletion change is 7.1 at%, and we also found that there were less extreme areas with Cr reduction as low as 3 at% ($\Delta\mu = -30$ mV), so we can use this range as a conservative estimation. The width of the CDZ ranged from 5-10 nm. Therefore, the grain boundary energy and the depletion energy reduction ranges were calculated as

$$\Delta E_{GB} = -1.53 \times 10^{-7} \frac{mJ}{m} \text{ to } -5.35 \times 10^{-7} \frac{mJ}{m} \quad \text{Equation 2.7}$$

$$\Delta E_{CDZ} = -3.78 \times 10^{-7} \frac{mJ}{m} \text{ to } -17.9 \times 10^{-7} \frac{mJ}{m} \quad \text{Equation 2.8}$$

As these ranges overlap, the model indicates that both the intrinsic grain boundary energy as well as the local chromium depletion are relevant; unlike the case for very large precipitates as

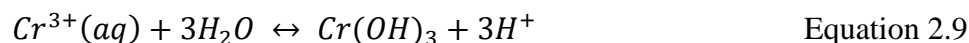
mentioned earlier. High-energy boundaries without chromium depletion would show preferential attack, as would low-angle boundaries with some level of depletion. However, as indicated in the experimental results section the precipitates occur more at the high-energy boundaries. We conclude that for the nanoscale precipitates herein both factors influenced corrosion sensitivity.

2.5.2 Including the Role of Crevice Corrosion

The compositional depletion and the energy gain from removing the boundary provides the driving force for the initial attack at the grain boundary, but this does not fully explain the experimental data. The dissolution rates for crevices and pits have long been linked to kinetic Wulff models that show the shape of a crevice is dependent on individual dissolution rates along various directions [136]. In our alloy, we have the dissolution rate down the boundary which affects the depth, and the dissolution rate normal to the boundary which will influence the width. If the local energy terms were the only driving force, the attack would be straight down the boundary and approximately as wide as the width of the CDZ. This, however, was not the case; the width of the attack was orders of magnitude larger than the depletion zone. Hence once attack has initiated at the boundary, a second mechanism has to be dominant.

We need to expand the model to include the crevice corrosion that develops around the grain boundaries. In crevice corrosion, the degrading environment is a confined volume. As the corrosion begins, the pH drops and hydrogen ions are created, which accelerate corrosion. This reaction is Equation 2.9. In addition to the chromium ions, albumin protein, sodium, potassium, and chlorine were also present during electrochemical testing. Diffusion in the crevice can limit the corrosion reactions, as illustrated in Figure 2.20. To proceed in crevice corrosion, chromium

ions must come from the surface, yet if this reaction is quenched, a back reaction producing chromium oxide and oxygen vacancies will cause the corrosion to stop, as in Equation 2.10.



We can see evidence for this crevice corrosion in our results of the crevice width-depth data shown in Figure 2.6. Overall, the widths of the corroded boundaries were 2-5 times larger than the depths. This is reasonable because our boundaries were undergoing only mild chemical segregation, compared to typically studied levels of sensitization for much larger precipitates in the literature. We can further understand other crevice trends observed. As seen in the TEM images, the carbides were inhomogenously spaced along the boundaries. With local grain

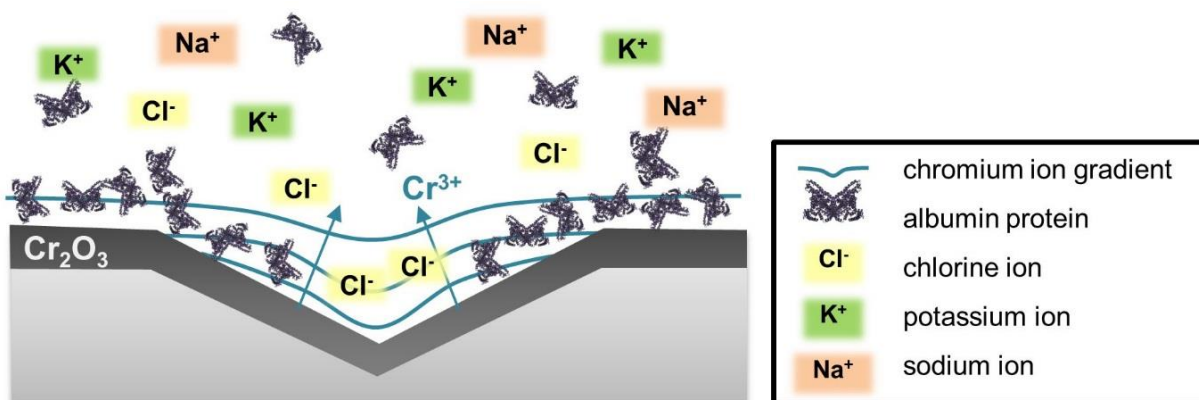


Figure 2.20 The chromium oxide layer with the light gray representing the bulk, the dark gray representing the oxide, the black arrows representing the Cr^{3+} movement and the blue lines representing the CrOH^{2+} concentration. As the chromium dissolution products accumulate in the crevice, the reaction down is quenched and the corrosion occurs out towards the walls of the crevice. The ions and albumin proteins are not to scale, but to serve as a representation. In the human body, many more ions and proteins would be present.

boundary nucleation followed by crevice corrosion the model predicts that there would be fluctuations in both the depth and width corrosion driving forces, depending on the local carbide concentration. As confirmed in our data, there were large local fluctuations in the width and depth in all boundaries, represented by the arrows ranges of each data point in Figure 2.6. Differences in carbide concentrations were also observed for corroded CSLs and non-CSLs, with corroded CSLs containing smaller and fewer carbides. The model predicts that non-CSLs would have lower width to depth ratios, and indeed that is seen in the width-depth data. This was also seen in the depth data, as most CSLs only corrode to about 1 μm , with widths from 2-5 μm . Non-CSLs, on the other hand, corroded down to 3 μm , with widths from 3-5 μm . The carbides provided a larger driving force down the boundary in these non-CSL cases, consistent with the model.

By combining grain boundary sensitization and the crevice corrosion into the GACC model, we are able to link the depth and width driving forces for corrosion to understand the behavior observed in the CoCrMo alloy grain boundaries with the nanoscale precipitates.

2.6 Discussion

We have demonstrated herein that chromium depletion in these CoCrMo alloys occurs at the nanoscale. The nanoscale chromium-rich carbides combine with the grain boundary properties to affect the localized corrosion susceptibility. The precipitates by themselves are not the full story unlike in the case with conventional and more macroscopic precipitation studies present in the literature. With the GACC model, we interpreted that the CDZ led to the start of a crevice at the grain boundary, which then led to runaway corrosion at that location. Our GACC model accounts for why we saw some higher level CSLs corrode. If a carbide sensitized one region of the exposed

boundary in the higher level CSLs, then it was enough to initiate corrosion. In this chapter, we have only reported on high-angle semi-random grain boundaries; in Chapter 3 additional details on lower energy grain boundaries will be described.

Other models have recognized the difference between the chromium depleted zone and the actual corroded crevice [88,120]. For our CoCrMo alloys, the depletion of chromium was ~1-10 nm in width, while the crevice on top of the trench was as wide as 5 μm . While previous models did not link these two results, we linked our width-depth ratio data to the width dissolution rate and the basic diffusion in the crevice. Using our width-depth measurements across many crevices, we concluded that the width corrosion was due to the quenched depth corrosion, causing both driving forces to occur, but with stronger width corrosion. This width-depth ratio data provided cross-verification of the GACC model.

To compare with the existing literature, we look for established minimum chromium composition levels. For CoCr bimetals, the minimum Cr to prevent corrosion is not well established; it was reported at 20% or 30% Cr [137,138]. Here we turn to stainless steel for a more thoroughly studied material for comparison. In stainless steel models, it was known that stainless steel has a composition around 19 at% Cr and a sensitization with CDZs around 13 at% Cr [88,106,120-122]. This drop is a 6 at% composition drop or a 32% reduction in chromium. We can compare this to the EDS data of the matrix and CDZ of our samples. The matrix compositions across the CoCrMo alloy samples matched our expected values for the composition, with a standard deviation of 1.3 at%, approximately equal to the 1% expected error with EDS. The largest standard deviation came from the carbide cobalt and chromium values, which was not surprising because the thickness of the carbides and the thickness of the sample above and below the carbide

varied. Therefore, the EDS spectra measured an uncontrolled ratio of the carbide and the matrix, causing a large variance of the carbide compositions. Our CDZ mapping showed an average composition of 23.8 at% Cr, a 6.8 at% composition drop of a 22% decrease in chromium from the matrix composition of 30.6 at% Cr. Our results for chromium depletion measurements suggested that a smaller change than the 32% reduction proposed for stainless steels has an effect on the corrosion performance in CoCrMo alloys.

While these comparisons are useful, it needs to be noted that to approximate physiological conditions our corrosion tests were performed in a bovine calf serum (BCS) with a protein content of 30 g/L, buffered to a basic pH of 7.4 solution with phosphate-buffered saline. This is an accepted approximation for the conditions in-vivo, and it is well established that one cannot simply use, for instance, salt solutions to obtain physiologically relevant results. The BCS solution contains albumin proteins, sodium, potassium, and chlorine ions as well as lipids, vitamins, amino acids, attachment factors, growth factors, hormones and other components essential for cell growth. It is certainly far from a simple electrolytic solution, so there may well be substantial differences in the detailed electrochemical processes taking place. The solution may also be evolving in time, as previous studies have demonstrated the roles of proteins and molybdates in the electrochemical properties of CoCrMo alloys and its metal oxide behavior [139], with those experiments indicating that molybdates released from the metal were leading to cross-linking of the proteins into gels.

The idea of comparing orientational grain boundary energy and electrochemical energy differences based on the differences in corrosion potential of the compositions is an initial model that needs expansion. Much more is occurring at the surface and at the grain boundaries as CoCrMo alloys corrode in the human body. To list only a few, there may be contributions from

surface energy changes due to protein adsorption, catalytic decomposition (denaturing) of proteins, and the formation of protective graphitic layers. For hip implants, both the mechanical wear and the corrosion need to be considered for performance. In our work, the electrochemical corrosion test is a static test without tribological wear occurring; Mathew et al. has shown the synergistic corrosion effects of the physiological solution and triboactivity [140]. There may also be important issues related to fretting assisted corrosion particularly at the junctions of modular devices. These we will leave to future work.

It is useful to make a few comments about what compositions should be used for implant materials. The results of this work indicate that more precise specifications are needed for the CoCrMo alloys used for implants. In the 1970s, sensitized stainless steels were used as poorly-performing implant material before more routine structural sampling was employed to ensure that intergranular corrosion would not be immediately detrimental to implant integrity [77]. Great advancements, especially in stainless steels, have allowed for ways to control carbides and CDZs through temperature and length of processing times, yet this understanding needs to be extended to nanoscale carbides and to CoCrMo alloys. The ASTM standard that dictates the CoCrMo alloy for surgical implants specifies that the material must “have a homogeneous microstructure with an average grain size of ASTM No. 5 or finer” [125]. This standard neglects the presence of precipitated carbides, and the acceptable size and acceptable regions of a CDZ. The nanostructure must be analyzed as well. Nanoscale analysis must be used for characterization as the CDZs measured in this work were shown to have significant effects on the corrosion properties. The CoCrMo alloy nanostructure would therefore affect the in vivo performance properties.

For future hip implants, perhaps precisely engineered CoCrMo alloys with suitable heat treatments could be designed as the metallurgical structure could be controlled at the microscale down to the nanoscale, including the potential to control corrosion through grain boundary engineering [113,115-117]. Controlling the CSLs could lead to a metal designed with controlled surface grains. The material on the surface could be protective by controlling the carbide presence and the chromium depleted zones, which would lead to a well-performing alloy, even if the material has internally sensitized regions.

2.7 Conclusions

- ❖ Chromium depletion occurs in this CoCrMo alloy, and it can occur on the nanoscale. The nanoscale chromium-rich carbides and the grain boundary geometry both determine the localized corrosion susceptibility.
- ❖ The grain boundary assisted crevice corrosion (GACC) model explains how the chromium depleted zones initiate corrosion at particular grain boundaries, which is then further propagated by crevice corrosion.

3 Effects of Coincident Site Lattice and Chromium Segregation on Grain Boundary Assisted Crevice Corrosion in CoCrMo Alloys

This chapter expands the work in Chapter 3 on grain boundary assisted crevice corrosion (GACC). In that work, we examined grain boundaries that were either completely corroded or immune, with primary characterization by coincidence site lattice (CSL) mapping and nanoscale composition at boundaries. We found that the corroded grain boundaries were all non-CSL and had carbides, whereas the immune boundaries were all CSL and did not have carbides. However, there was a middle case left to consider. Some mid-value CSL grain boundaries partially corroded. There were open questions of the composition and structure at these middle case grain boundaries.

The influence of grain boundary interfacial energy on the structure of carbides and the local segregation of chromium were investigated at the nanoscale for coincident site lattice boundaries in a CoCrMo alloy. Grain boundaries of varying degrees of misorientation were examined by optical profilometry and transmission electron microscopy, and samples of the grain boundary precipitates were analyzed with energy dispersive X-ray spectroscopy. Low- Σ coincident site lattice boundaries were found to have both fewer carbide precipitates and smaller degrees of sensitization and are more resistant to intergranular attack. Similar to general high-angle boundaries, the combination of chromium depletion and the grain boundary energy acts as the initiator of corrosion. After initiation, crevice corrosion enlarges the initial site of the attack.

This work is also inspired by the masters work of Pooja Panigrahi, and continues her publication “Intergranular pitting corrosion of CoCrMo biomedical implant alloy” [65] and my publication reproduced in Chapter 3 “Grain Boundary Assisted Crevice Corrosion in CoCrMo Alloys” [66]. Material in this chapter is reproduced from the article “Effects of Grain Boundary

Misorientation and Chromium Segregation on Corrosion of CoCrMo Alloys” by Alex Lin, Emily E. Hoffman, and Laurence D. Marks; *Corrosion*, 2016 [141]. The work in this chapter was done in conjunction with Alex Lin.

3.1 Introduction

Orthopedic replacements for hips and knees are some of the most successful procedures for patients with severe osteoarthritis and rheumatoid arthritis. Currently, more than 300,000 total hip replacement operations are performed annually in the United States [142], and this number is predicted to reach 1,800,000 by 2050[67]. Metal-on-metal (MoM) replacements made of cobalt chromium molybdenum alloys (CoCrMo) have attracted interest as an alternative to metal-on-polyethylene (MoP) implants because of their excellent mechanical properties, superior wear and corrosion resistance, longer service duration, and reduced inflammation response [143,9]. CoCrMo alloys, however, corrode at several micrometers per year, which can lead to damaging nanoparticle debris and ion release [19,144-146]. Thus, even though the overall corrosion rate is low, adverse side effects remain a challenge. Considering the millions of MoM hip replacements currently in use worldwide, we need a better understanding of the processes of corrosion in CoCrMo biomedical alloys.

The dominant corrosion protection in all CoCrMo alloys is a thin film of chromium oxide. As this alloy corrodes, the mass loss of material is not constant; there is often preferential corrosion at grain boundaries, carbide phases, and defects. This focused corrosion is often classified as “grain boundary sensitization,” and for alloys that include chromium, local sensitization is explained as a localized reduction of chromium [76-78]. Sensitization has been extensively studied in stainless

steel, with studies dating back to the 1930s [76]. Most notably, Stawstrom et al. reported that a 13 at% minimum Cr concentration is the threshold value to prevent sensitization [88]. More recent studies by Bruemmer et al. [80] and Pande et al. [147] clarified how Cr depletion occurs at the grain boundaries via the growth of nanoscale carbide precipitates. Bruemmer et al. [111] extensively studied Cr depletion zones of stainless steels using analytical TEM, and showed that no carbides were found and cracking was limited when the Cr concentration exceeded 16.5 at% at the grain boundary. For a full discussion of sensitization, see “2.2 Grain Boundary Sensitization” literature review section in Chapter 2 [66].

Microscale grain boundary sensitization was shown to affect corrosion in biomedical CoCrMo alloys. For high-carbon CoCrMo alloys, Montero-Ocampo and Martinez [148] showed that a large number of carbide precipitates depleted the matrix in Cr and Mo at grain boundaries to form $M_{23}C_6$ carbides ($M = Cr, Mo, Co$). Liao et al. [149] demonstrated with precession electron diffraction and high-resolution energy dispersive X-ray spectroscopy (EDS) that $M_{23}C_6$ and M_6C carbides were present in annealed CoCrMo alloys. Bettini et al. [110] characterized microscale carbides in CoCrMo and observed increased corrosion at the Cr depletion areas. These CoCrMo carbide and sensitization studies were mainly confined to the microscale and did not consider the full combination of heat treatment, grain boundary type, corrosion, and nanoscale chemical analysis.

The local Cr depletion varies with type of grain boundary; it is well established that many properties such as corrosion susceptibility, mechanical strength, and precipitate formation are connected to the grain boundary structure and interfacial energy [79,114,117,150,151]. In general, grain boundary structure is quantified using the coincidence site lattice (CSL) model, where grain boundaries can be classified as having repeating coincident lattice points along the boundary. The

degree of coincidence can be described by a Σ -value, which is the ratio of coincident lattice site area to the two-dimensional crystal unit cell area. Low- Σ grain boundaries have in general low interfacial energies although the Σ -value and the interfacial energy are not linearly related, i.e. $\Sigma 25$ has a smaller interfacial energy than $\Sigma 13$ in CoCrMo alloys.

For fcc metals such as stainless steels and Ni alloys, CSL boundaries with $\Sigma \leq 29$ are considered “geometrically special” and are less susceptible to intergranular corrosion [152]. The influence of grain boundary structure on sensitization and subsequent intergranular corrosion was studied by Palumbo et al. for Ni alloys [79]. Geometrically-special CSL boundaries have been found to inhibit the depletion of soluble Cr in the vicinity of the grain boundary and have enhanced corrosion resistance [114]. The size and spacing of the intergranular $M_{23}C_6$ carbides in Ni alloys were dependent upon the characteristics of the grain boundary. Smaller carbides were found at $\Sigma 3$ CSL grain boundaries, and larger carbides were found at higher Σ grain boundaries [153]. Carbide precipitation was influenced by CSL Σ and grain boundary interfacial energy; however, this relationship is still not clear in most alloys.

The relationship between CSL and intergranular corrosion was characterized by Panigrahi et al. [65] who examined the corrosion susceptibility of CoCrMo alloys for various annealing temperatures and times. Based on the grain boundaries observed in the study, 90% of the grain boundaries with reciprocal lattice coincidence $\Sigma 11$ or lower were completely immune to the in vitro electrochemical corrosion process. Hoffman et al. [66] established a model that compared corrosion susceptibility to grain boundary carbides and the Co and Cr contents at the boundaries by examination of high-energy, high- Σ boundaries. It was demonstrated that CoCrMo alloys had nanoscale carbide precipitates accompanied by Cr depletion zones along grain boundaries, similar

to observations of stainless steel. Additionally, the levels of Cr depletion at completely immune CSL boundaries were compared with the Cr depletion at completely corroded non-CSL boundaries. Larger precipitates and larger Cr depletion were found at high-energy boundaries, showing that Cr depletion at the interface can indicate corrosion susceptibility.

This study looks beyond the high-energy boundaries previously analyzed to the intermediate regime of lower energy boundaries that do corrode. By analyzing the morphology near the boundaries, we connected grain boundary properties to local corrosion susceptibility. High-resolution transmission electron microscopy (TEM) and energy dispersive X-ray spectroscopy (EDS) revealed the chemical compositions at the boundaries. Crevice depth measurements, collected from white light interferometry, quantified corrosion susceptibility across grain boundaries and indicated that deeper corrosion crevices are linked to larger Cr depletion, suggesting that higher energy boundaries have higher likelihood of corroding more severely.

3.2 Methods

3.2.1 Sample Preparation

Table 3.1 High-carbon CoCrMo alloy composition.

| at% | Co | Cr | Mo | C | Si | Mn | Ni | Fe |
|---------------|---------|------|-----|------|------|------|------|------|
| ASTM F1537-08 | Balance | 30.3 | 3.6 | 1.14 | 1.34 | 0.73 | 0.17 | 0.14 |

A high-carbon wrought CoCrMo alloy, in accordance to ASTM F1537-08, was annealed in an air furnace for 24 hours at 1230 °C and quenched in water. The alloy composition is given in Table 3.1. This heat treatment was chosen as it was most successful in reducing the bulk corrosion rate, localizing corrosion to grain boundaries, and optimizing the in vivo performance of the alloy. The

solution-annealed CoCrMo sample was then ground, polished to a mirror finish ($R_a \leq 10$ nm), and then electrochemically corroded according to the procedures used by Panigrahi et al. [65]. To summarize the corrosion conditions, the CoCrMo alloy sample was electrochemically corroded in a four-chamber corrosion cell. The sample was incorporated into the cell as the working electrode with a graphite counter electrode and a saturated calomel electrode reference electrode, all connected to a potentiostat. The cell was filled with 10 mL of bovine calf serum, containing a protein content of 30 g/L. The solution was buffered to a pH of 7.4 and the cell was placed in a hot water bath at 37 °C in order to simulate human physiological conditions.

Standard electrochemical corrosion procedures were followed. The tests began with a potentiostatic test, where a constant potential of -0.9 V was applied to remove the passive film and proteins that may have adsorbed on the metallic surface, followed by an electrochemical impedance spectroscopy (EIS) test. The EIS measurements were performed at frequencies from 100 kHz down to 10 mHz with an AC sine wave amplitude of 10 mV applied at the open circuit potential. A cyclic polarization test was then performed to corrode the sample and measure the current at each applied potential. The samples were polarized from -0.8 V to 1.8 V at a scan rate of 2 mV/s and then reversed back to -0.8 V at the same rate. Using the corrosion current from Panigrahi et al.'s results [65] and Faraday's equation, the dissolution rate was calculated to be 2.98 $\mu\text{m}/\text{yr}$ and assumed to be uniform

3.2.2 Scanning Electron Microscopy

Scanning electron microscopy (SEM) characterization was performed on the FEI Quanta ESEM operating at an accelerating voltage of 30 kV. Various regions of the electrochemically

corroded CoCrMo surface were imaged at magnification levels between 300x and 600x. An Oxford electron backscatter diffraction (EBSD) detector was then used to perform orientation image mapping (OIM) by collecting EBSD patterns of individual grains. A step size of 0.6 μm was used as it provided sufficient precision for obtaining crystallographic misorientation data with OIM. The acquired EBSD patterns were indexed using the commercially available Oxford AZtec EBSD processing software. Using the Oxford Tango post-processing software, noise reduction was performed in order to minimize artifacts caused by surface roughness. Additionally, the misorientation of relevant grain boundaries was determined. The Brandon Criterion [126] was used to classify the Σ -value, which is the ratio of coincident lattice sites to the two-dimensional crystal unit cell area, of each identified CSL grain boundary.

3.2.3 White Light Interferometry

3D profilometry on a Bruker Contour GT-K 3D optical microscope equipped with a Mirau interferometer objective lens was used to quantitatively determine the corrosion susceptibility by measuring the topography of various boundaries. In principle, the white light interferometer had a lateral resolution limited by the wavelength of light. The z-axis resolution was limited by the sensitivity of the light intensity detector, and as a result, resolutions on the order of 10 nm were readily achieved. As previously reported in Hoffman et al. [66], this technique was used to characterize the widths and depths of the crevices associated with the corroded grain boundaries. A total of 25 boundaries, 13 CSL boundaries and 12 non-CSL boundaries, of varying corrosion susceptibility were measured. Two-dimensional projections of approximately 250 μm by 300 μm were acquired in order to record the profile of the corroded surface, and 15-20 depth and width

scans were collected along each individual grain boundary. While measuring the depth of a crevice, the width was simultaneously acquired by measuring the distance between the two edges of the crevice. Reconstruction, specimen visualization, and measurements were performed using the Bruker Vision64 Analysis Software. The means of the depth and width measurements as well as the range to the 95% confidence level were then computed.

3.2.4 Focused Ion Beam

For further nanoscale analysis, TEM lamellae of CSL grain boundaries within the annealed CoCrMo alloy were produced in a dual-beam FEI Helios Nanolab focused ion beam (FIB) system. The CSL boundary of interest, identified from the EBSD OIM data, was milled out with focused ion beam operating at 30 kV from 9.2 nA to 48 nA. The boundary cross section was then transferred to a TEM grid and thinned to an electron-transparent TEM sample. The final CoCrMo lamellae spanned 3-4 μm on either side of the boundary and reached 4 μm deep below the bulk surface. Eight asymmetrically corroded CSL boundaries and two completely immune CSL boundaries were prepared into TEM lamellae samples.

3.2.5 Transmission Electron Microscopy

TEM imaging and elemental analysis of grain boundaries were performed using a combination of TEMs including the Hitachi H-8100, JEOL 2100F, and JEOL ARM200-CF, all operating at 200 kV. Bright field (BF) images, dark field (DF) images, and electron diffraction patterns were acquired on the Hitachi H-8100 from eight corroded CSL boundaries and two immune CSL boundaries. Annular dark field (ADF) imaging and high-angle annular dark field (HAADF)

imaging were performed on the JEOL 2100F and JEOL ARM200-CF, respectively. Analytical data including energy dispersive X-ray spectroscopy (EDS) mapping and line profiles were collected in scanning transmission electron microscopy (STEM) mode using an Oxford windowless detector. The EDS data was then processed by the Oxford AZtec TEM EDS Software. In order to characterize nanoscale grain boundary carbide precipitates and Cr depletion zones at CSL boundaries, five selected CSL boundaries of varying corrosion susceptibility were analyzed with HAADF imaging. EDS mapping was performed on sections of individual boundaries and chemical quantification data was probed from key sites within the maps. On average, six EDS maps were collected from each CSL boundary and five to eight sites were probed from each EDS map.

3.3 Results

3.3.1 Grain Boundary Misorientation

SEM imaging in combination with OIM analysis indicated that preferential intergranular corrosion had occurred, shown in Figure 3.1 (a-c). The OIM mapping in Figure 3.1 (c) labeled which boundaries were twin, CSL, or regular high angle boundaries. Highly-ordered twin boundaries were completely immune to corrosion attack; while, high-energy grain boundaries with fewer coincident lattice points were more susceptible to corrosion.

SEM image analysis further showed that there were three distinct types of boundaries that corroded: Types I, II, and III. Type I corresponds to those which showed minimal to no corrosion, less than 0.4 μm deep if at all. Type II and Type III showed definite corrosion. From analysis of the OIM data, Type I boundaries are twins or have a CSL value of $\Sigma 11$ or smaller whereas Type

II were larger. This was determined to be a threshold for corrosion resistance in a previous CoCrMo alloy study [65], and confirmed in our data. Type II and Type III boundaries both corroded, yet with different profile shapes and to different degrees. Type II boundaries were asymmetric, indicating that these intermediate misorientations, such as $\Sigma 17$ and $\Sigma 25$, were more resistant to corrosion attack in comparison to general high-angle grain boundaries. Out of 96 non-twin CSL boundaries, 57 of them corroded less than $1.0\ \mu\text{m}$. These boundaries were classified as Type II boundaries. Beyond $\Sigma 35$, corrosion depths of greater than $1.0\ \mu\text{m}$ were observed, similar to the corroded general boundaries. Based upon this data, the threshold between Type II and III was the CSL value $\Sigma 35$. It should be noted that the CSL threshold level which correspond to general high-angle boundaries is not completely fixed, and can vary with material. Representative example boundary morphologies of each type are shown in Figure 3.2.

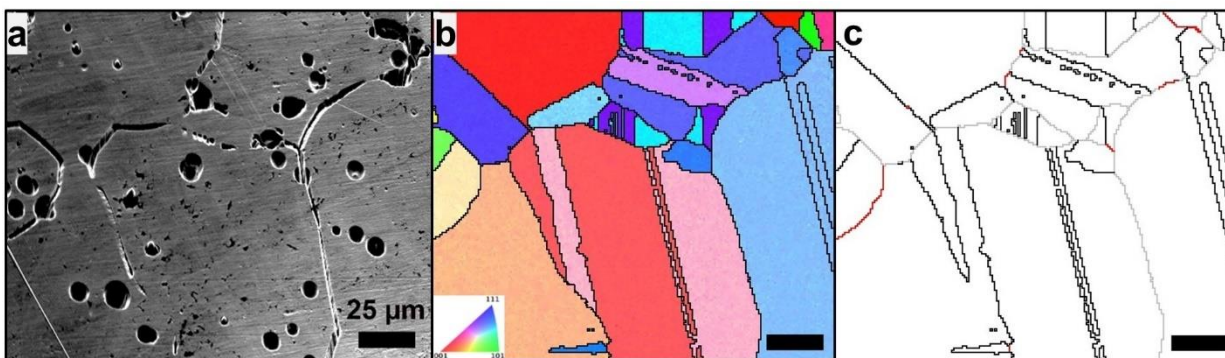


Figure 3.1 (a) A SEM image and (b) its corresponding EBSD map showing preferentially corroded CoCrMo grain boundaries and the different grain orientations. (c) CSL boundaries are labelled with red lines, twin boundaries are labelled with black lines, and randomly oriented grain boundaries are labelled with grey lines.

With the CSL data from the OIM mapping, the same grain boundaries were measured with 3D profilometry. Figure 3.3 (a) and (b) show a representative profilometry scan and (c-e) show the extracted 2D boundary profile scans for each boundary type. The depth profiles of the different classes of the boundaries illustrate the distinction between them. In Figure 3.3 (c), a slight divot

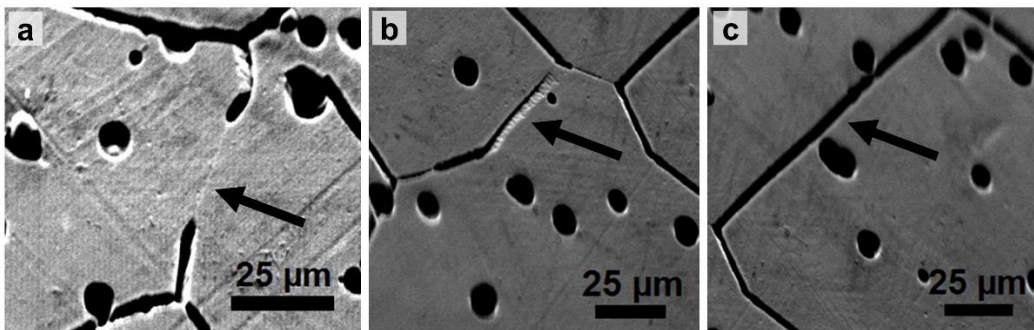


Figure 3.2 Representative examples of a (a) Type I, (b) Type II, and (c) Type III grain boundary as indicated by the arrows.

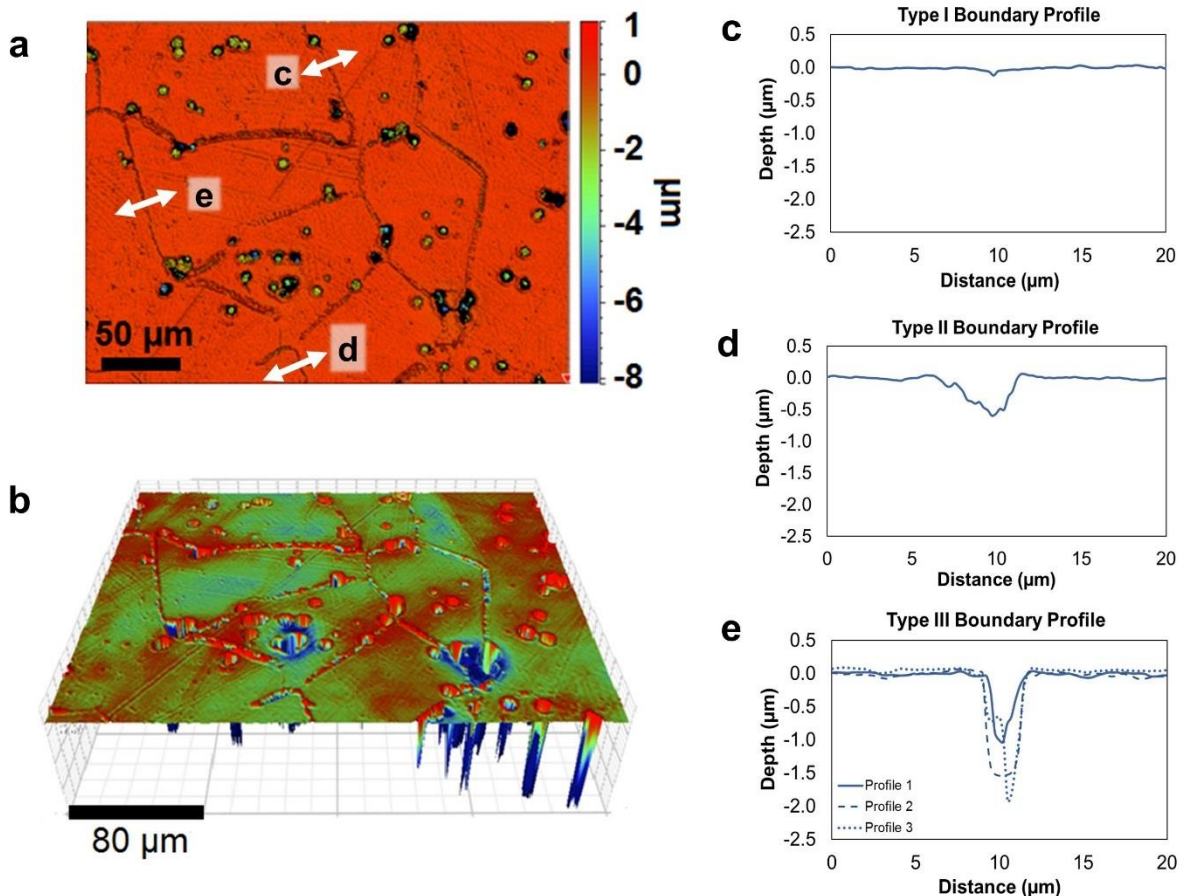


Figure 3.3 Profilometry measurements of the same region of interest can be shown as (a) a 2D projection and (b) a 3D reconstruction. Depth profiles of representative (c) Type I, (d) Type II, and (e) Type III boundaries are shown. Type III boundary profiles, taken from 3 different sites along the boundary, show a large variance in the depth measurements.

formed the Type I boundary, at most corroding to about 0.2 μm . In Figure 3.3 (d), the Type II boundary corroded asymmetrically to a depth of $\sim 0.6 \mu\text{m}$. In Figure 3.3 (e), the Type III boundary corroded the deepest, up to $\sim 2.0 \mu\text{m}$. This Type III representative example also shows the variety of depths and shapes that were observed along a single corroded Type III boundary.

The grain boundary depth versus Σ -value data is summarized in Figure 3.4 with the three boundary types indicated on the graph. Corrosion depth served as the measure of corrosion severity. Here, we observed a clear trend between the degree of lattice coincidence and corrosion depth. Type III boundaries had large crevice depth variations, which are designated by the vertical arrows in Figure 3.3. The arrows shown are not error bars, as they indicate the variation in corrosion depth for single boundaries as a function of position along the boundary.

The width and depth measurements showed an interesting trend. The measurements showed that widths are approximately 2-5 times larger than their corresponding depth, as summarized in Figure 3.5. Type III boundaries generally had lower width to depth ratios, as they corroded down to 3 μm , with widths from 3-5 μm . Type II boundaries, on the contrary, only corroded to about 1 μm , with widths ranging from 2-5 μm . The width-depth relation showed another indicative difference between the corrosion behaviors in Type II and Type III boundaries.

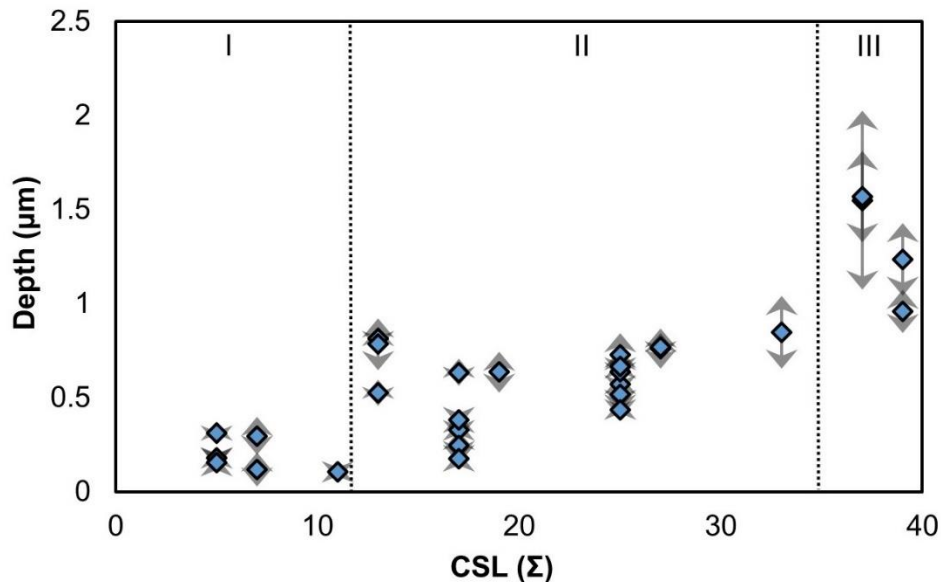


Figure 3.4 Corrosion crevice depth was plotted with respect to the CSL Σ number. The three classes of boundaries and their respective corrosion depths are shown.

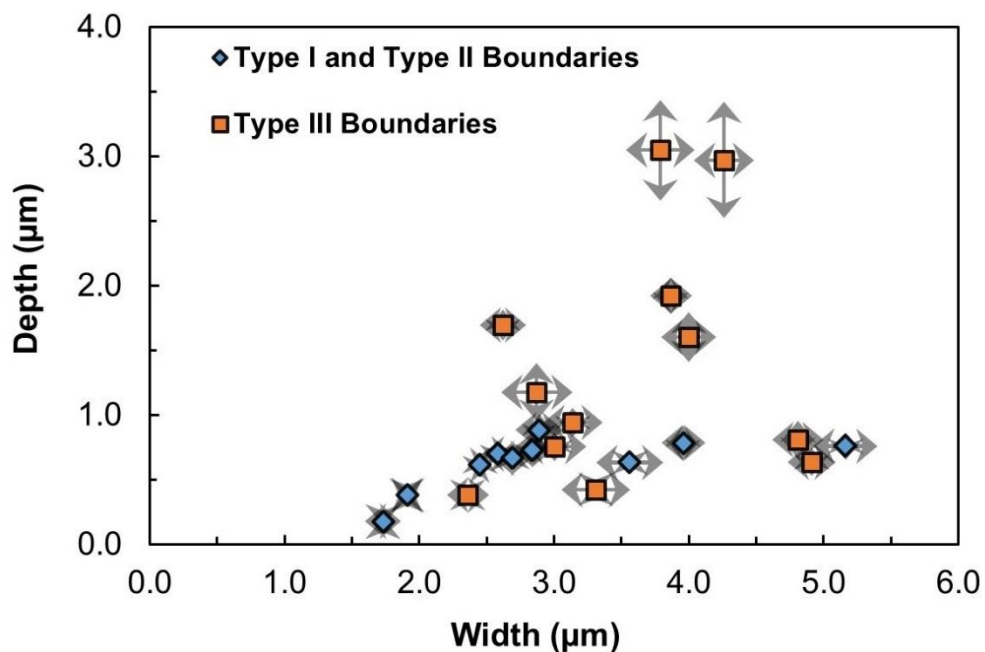


Figure 3.5 Crevice measurements collected from 3D profilometry show that widths of the corroded grain boundaries are approximately 2-5 times larger than its corresponding depth. The arrows represent the range of measurements along the boundary

To summarize, the grain boundary corrosion behaviors are:

- Type I CSL boundaries with $\Sigma \leq 11$. The majority of the boundaries in this class were immune to corrosion, showing no depth of corrosion. Of the boundaries that did corrode, the depth was less than 0.40 μm . These corroded boundaries looked like slight divots.
- Type II CSL boundaries between $\Sigma 13$ and $\Sigma 35$. Many of the CSLs fell within this regime. The crevices were typically asymmetrical and shallower than the general high-angle corrosion boundaries. 31 out of the 57 non-twin CSL boundaries belonged to this class. These corroded boundaries looked like angled wedges.
- Type III Non-CSL boundaries, also known as high-angle grain boundaries. These boundaries were typically severely corroded with corrosion crevice depths exceeding 1.0 μm . Work focusing on this class of boundaries has been previously described [66]. Boundaries belonging to this class often have large variations in the depth.

3.3.2 Effect of Misorientation on Carbide Precipitates

Previous work on Type III boundaries discussed the carbide morphology and corrosion behavior in detail [66]. Here, we focus primarily on Type II boundaries, with a brief analysis of two Type I boundaries to follow. Most of the boundaries presented here contained carbide precipitates, and there were two general features of interest observed in the experimental data, namely the precipitate structure and the local segregation around the precipitates.

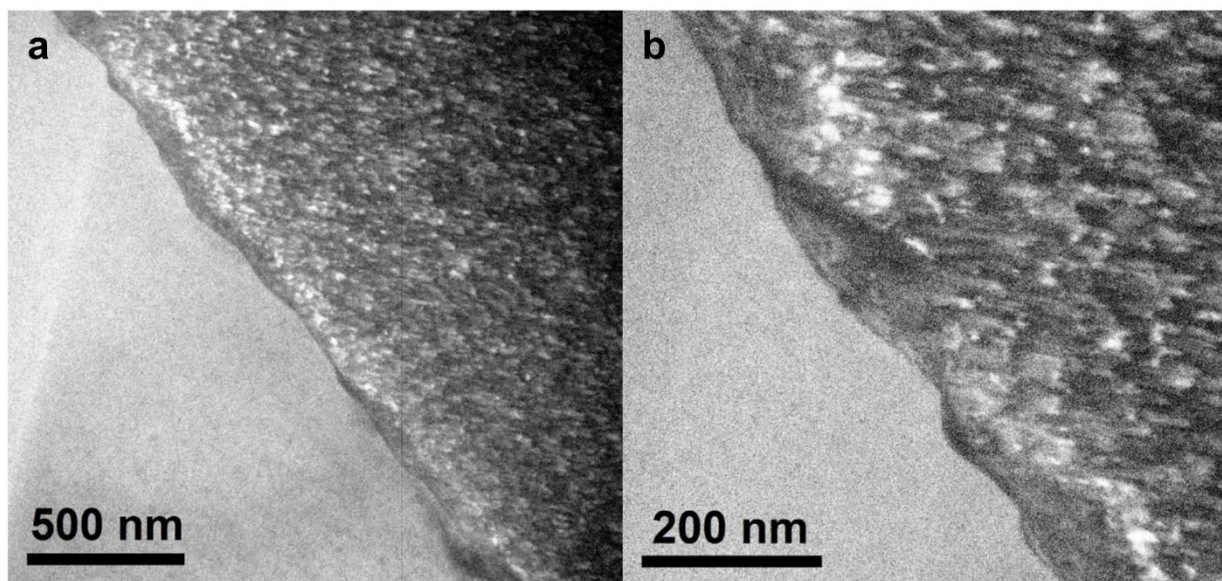


Figure 3.6 BF TEM (a) and (b) showed that a partially corroded $\Sigma 27$ boundary was faceted by carbides.

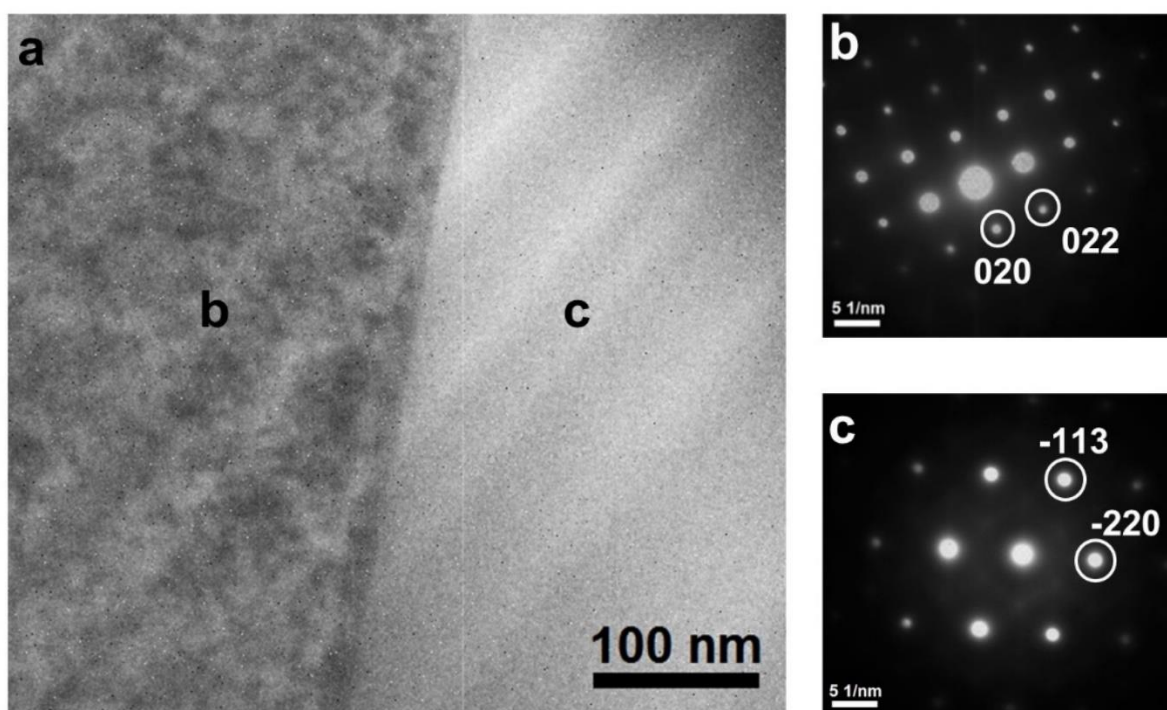


Figure 3.7 (a) The immune $\Sigma 17$ grain boundary was straight without deviations and did not show carbides. (b-c) Electron diffraction patterns collected at the adjacent grains confirmed the presence of a grain boundary.

We first describe the precipitate structure, and then we connect this information to the grain boundary energy. Initial TEM imaging of the eight Type II grain boundaries revealed faceting caused by the second phase carbides, with these sensitized boundaries appearing wavy and irregular, as shown in Figure 3.6. In contrast, one Type II immune boundary was also characterized as being “clean” with no carbides. This immune interface, shown in Figure 3.7 (a), was also almost completely straight. Figure 3.7 (b) and (c) show the diffraction patterns for each grain, with no evidence for carbides along the boundary. For all eight of partially corroded Type II boundaries, chromium-rich carbides were dotted along the grain boundaries. From BF TEM images as shown in Figure 3.8, nanoscale carbide precipitates of approximately 50-100 nm in length and 10-25 nm in width were observed. Most of the chromium-rich carbides observed were lens shaped, showing partial wetting of the grain boundary interface, similar to previous work on Type III boundaries [66].

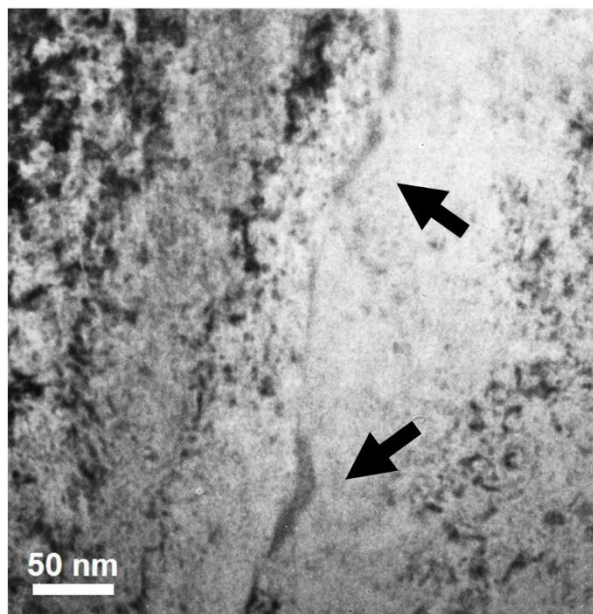


Figure 3.8 BF TEM image of lens shaped carbides (indicated by arrows) at a partially corroded $\Sigma 25$ grain boundary.

3.3.3 HAADF and EDS Quantification of Chromium Depletion

We now turn to the Cr segregation around the grain boundary precipitates and how this correlated with corrosion susceptibility and the size of the precipitates. The chemical compositions of the Cr depletion zones, specifically the Cr content, were measured using EDS. Figure 3.9 shows line scans that confirmed the presence of carbides and showed that the carbides were in multiple morphologies. Single and double particles were seen, but Cr depletion was not observed in the immediate vicinity of the carbides.

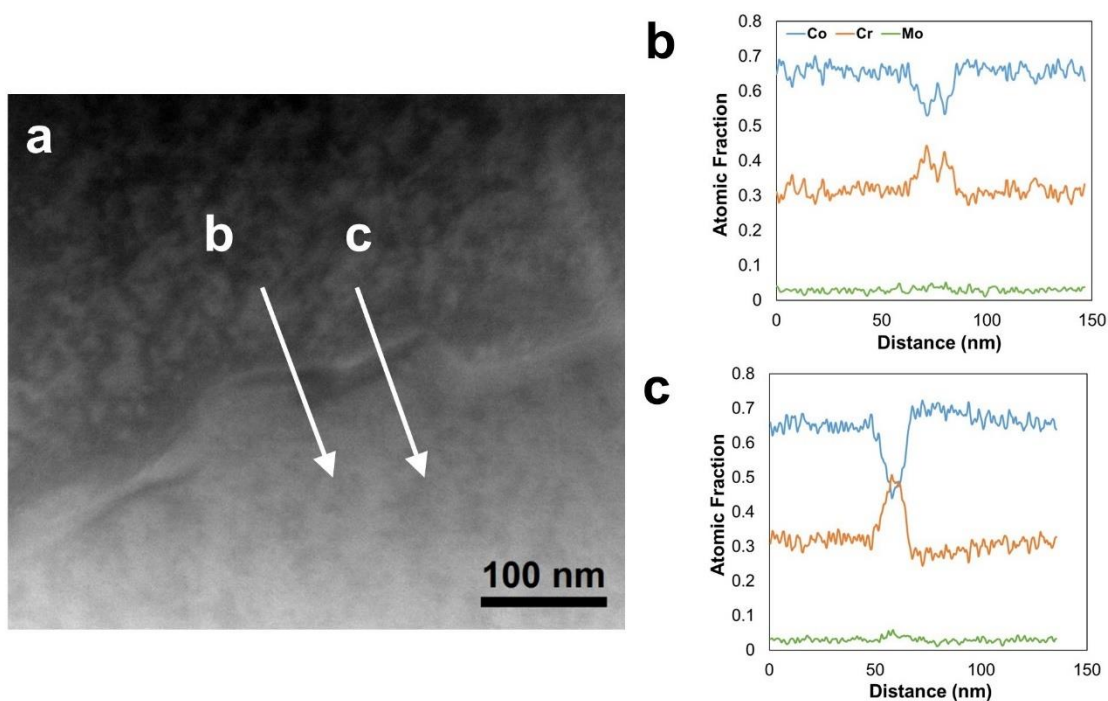


Figure 3.9 (a) Two carbides of approximately 100 nm are found along the $\Sigma 13$ boundary. Line scans from the HAADF image show (b) two peaks representing the two carbides and (c) a single peak showing the Cr content across the center of a carbide.

Further HAADF imaging coupled with EDS maps, which show the spatial variations of the composition, provided additional details of carbides and Cr depletion along Type II grain boundaries. Five HAADF images with corresponding EDS maps were measured; four representative EDS maps are shown in Figure 3.10 through Figure 3.13. Most carbides had the same lens shape as observed in BF TEM images, shown in Figure 3.6 and Figure 3.8. This shape was expected because it was observed in the previous work on Type III boundaries [66]. Figure 3.10, taken from the same region as Figure 3.9, is a $\Sigma 13$ boundary, and Figure 3.11 is a $\Sigma 25$ boundary. Both of these Type II boundaries showed lens carbides of 50-100 nm in length and 10-25 nm in width. Figure 3.12 shows another $\Sigma 25$ boundary, this with a different carbide morphology: “platelet” shaped carbides. In the Type II boundaries, the platelet carbides reached 100 nm in length; however, the maximum widths were only 10 nm. Two of the three $\Sigma 25$ CSL boundaries analyzed formed platelet shaped carbides. This links lower corrosion to more coherence between the boundary and the precipitates. Carbides were closer to the “platelet” shape than the lens shape in the low corrosion cases; the platelet shaped carbides can also be related to the energy of the CSL, which we will address later in the discussion.

Of the two Type I boundaries, one was completely immune and the other was a $\Sigma 7$ boundary that corroded to about 0.3 μm . The immune boundary appeared completely straight and was free of carbides; while, the partially corroded boundary, shown in Figure 3.13, contained small platelet shaped carbides of about 50 nm in length and 5 nm wide and had no significant effect on grain boundary faceting.

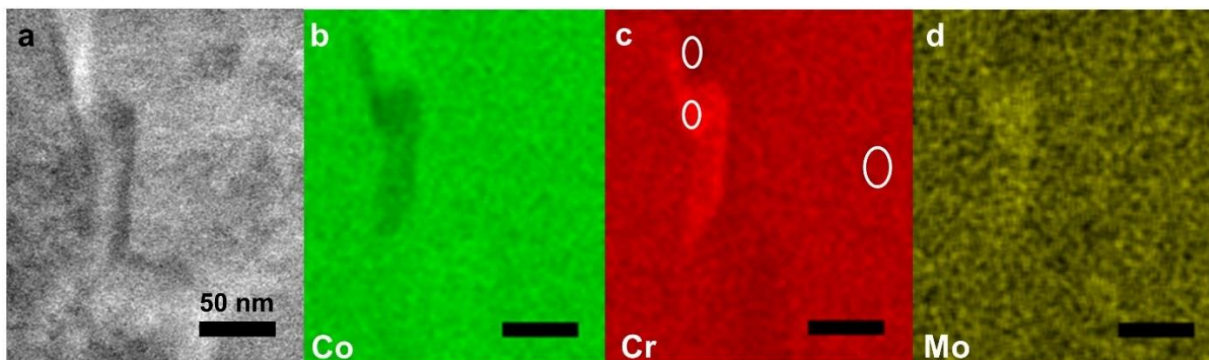


Figure 3.10 HAADF image from a corroded $\Sigma 13$ grain boundary with the corresponding EDS maps. Chemical quantification from the indicated sites are summarized in **Table 3.2**.

Table 3.2 EDS quantification of key regions in **Figure 3.10**.

| | Co (at%) | Cr (at%) | Mo (at%) |
|-------------------|----------|----------|----------|
| Matrix | 63.5 | 32.0 | 4.5 |
| Carbide | 48.1 | 46.0 | 5.9 |
| Cr Depletion Zone | 69.9 | 27.3 | 2.8 |

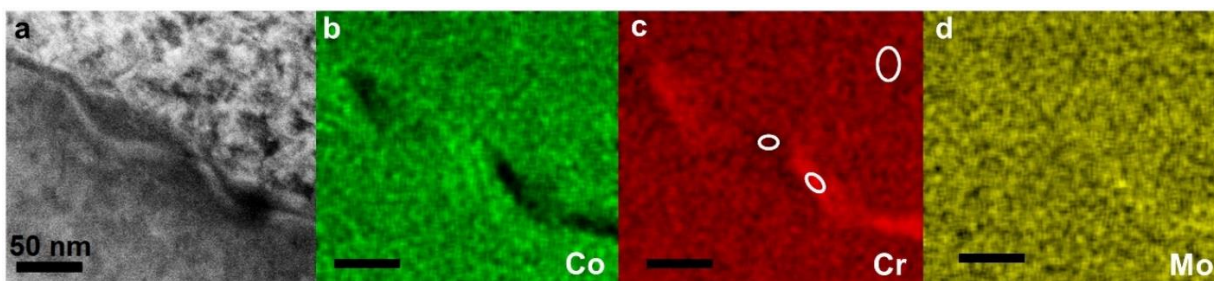


Figure 3.11 HAADF image of a corroded $\Sigma 25$ grain boundary accompanied with the corresponding EDS maps. Cr depletion zones are present in between carbides along the boundary. Chemical quantification from the indicated sites are summarized in **Table 3.3**.

Table 3.3 EDS quantification of key regions in **Figure 3.11**.

| | Co (at%) | Cr (at%) | Mo (at%) |
|-------------------|----------|----------|----------|
| Matrix | 63.3 | 32.9 | 3.8 |
| Carbide | 47.1 | 47.3 | 5.5 |
| Cr Depletion Zone | 69.0 | 28.3 | 2.7 |

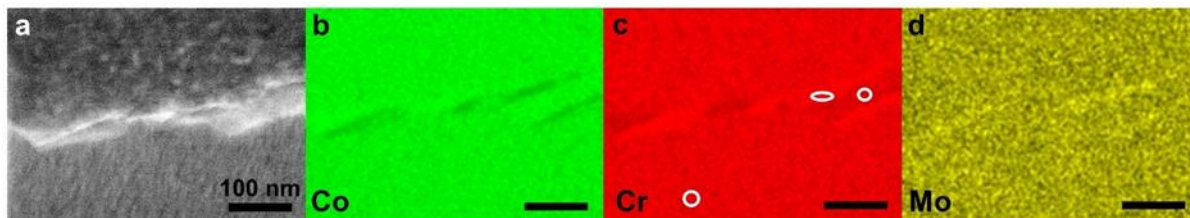


Figure 3.12 Platelet shaped precipitates were found along a $\Sigma 25$ boundary with low corrosion. Chemical quantification from the indicated sites are summarized in **Table 3.4**.

Table 3.4 EDS quantification of key regions in **Figure 3.12**.

| | Co (at%) | Cr (at%) | Mo (at%) |
|-------------------|----------|----------|----------|
| Matrix | 64.4 | 31.6 | 4.0 |
| Carbide | 57.4 | 38.6 | 4.0 |
| Cr Depletion Zone | 68.5 | 29.4 | 2.1 |

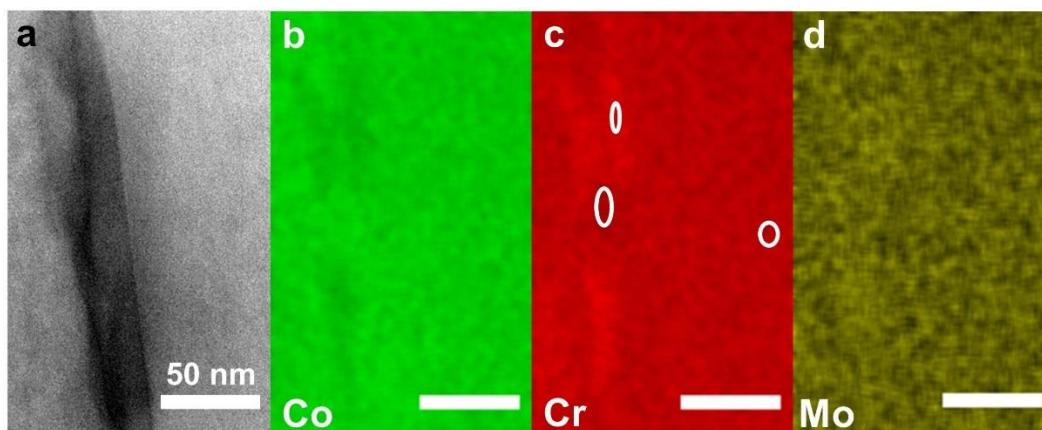


Figure 3.13 Platelet shaped precipitates were also observed in a corroded $\Sigma 7$ boundary. Chemical quantification from the indicated sites are summarized in **Table 3.5**.

Table 3.5 EDS quantification of key regions in **Figure 3.13**.

| | Co (at%) | Cr (at%) | Mo (at%) |
|-------------------|----------|----------|----------|
| Matrix | 65.3 | 31.3 | 3.4 |
| Carbide | 58.6 | 37.4 | 4.0 |
| Cr Depletion Zone | 66.4 | 29.9 | 3.7 |

When there were carbides present, Cr depletion zones (CDZ) were observed in the EDS maps. The presence of both $M_{23}C_6$ carbides and Cr depletion zones along the grain boundaries was confirmed by comparing the Co-K EDS maps, Cr-K EDS maps, and Mo-L EDS maps. Chemical quantification data from the $\Sigma 13$ Type II boundary is shown in Figure 3.10 and is summarized in Table 3.2. In this Type II boundary, which corroded to 0.8 μm , the area around the carbide contained a Cr depletion zone of about 5 at% Cr in between two carbides along the grain boundary. In contrast to the EDS data shown in Figure 3.9, the improved quality of EDS mapping in Figure 3.10 revealed the nanoscale Cr depletion zone. The area of the Cr depletion zone extended about 25 nm, approximately the width of the carbide precipitate, consistent with the previous observations made in Type III boundaries [66]. Additionally, the Cr depletion zones formed in all directions from the surface of the precipitates. This observation supports that there was a local “conservation” of Cr in the regions adjacent to the grain boundaries, and that Cr diffusion was also localized.

Less corrosion depth was found to correspond to smaller Cr depletion for a grain boundary. There was a smaller degree of Cr depletion and a smaller area of the Cr depletion zone. For $\Sigma 25$ Type II boundary in Figure 3.11, which had corroded approximately 0.7 μm , there was a depletion of 4.8 at% in Cr on average, shown by the quantitative EDS measurements in Table 3.3. In the lesser corroded $\Sigma 25$ Type II boundary from Figure 3.12, which corroded about 0.5 μm , the Cr depletion was approximately 2 at% Cr, with EDS values shown in Table 3.4. The $\Sigma 7$ corroded Type I boundary in Figure 3.13, which corroded to about 0.3 μm , showed levels of Cr depletion of slightly less than 2 at% Cr as summarized in Table 3.5. The completely immune Type I boundary contained no appreciable Cr depletion and no carbides were found along the boundary.

In addition, the Cr depletion zones in Figure 3.11 through Figure 3.13 were located in between the carbides and did not form in areas surrounding the precipitates as shown in Figure 3.10. The Cr depletion concentration corresponded well with the depth of corrosion observed at each boundary. The relationship between the level of Cr depletion and the amount of corrosion is summarized in Figure 3.14, noting the morphology shape as well. The Figure 3.12 $\Sigma 25$ boundary with lower Cr depletion and lower corrosion depth had platelet morphology (similar to the low energy $\Sigma 7$ boundary). In contrast, the Figure 3.11 $\Sigma 25$ boundary with higher Cr depletion and more corrosion had lens morphology (similar to the higher energy $\Sigma 13$ boundary).

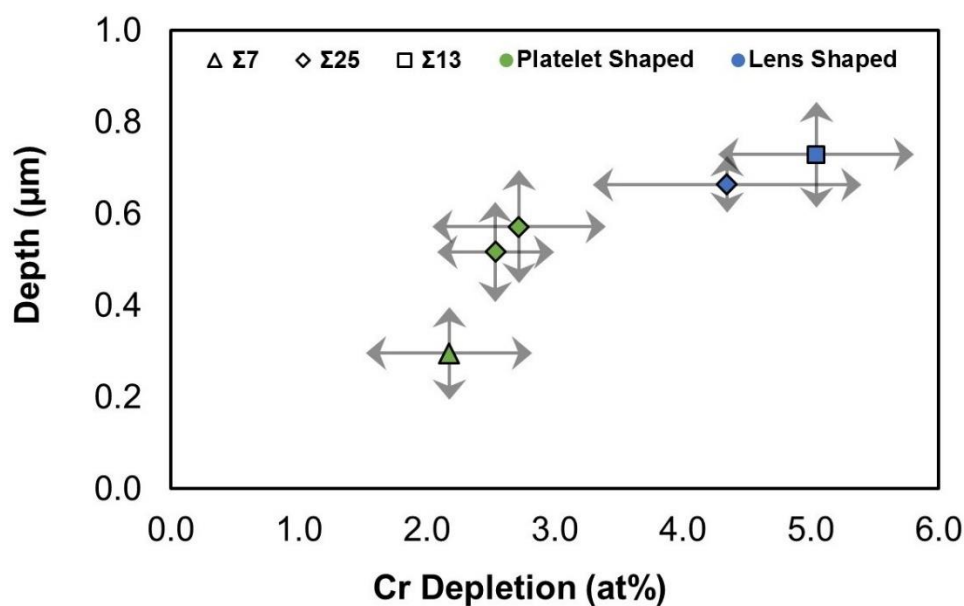


Figure 3.14 The Cr depletion at one Type I ($\Sigma 7$) and four Type II ($\Sigma 25$, $\Sigma 13$) boundaries are related to the corrosion susceptibility. Note that the energy value for these ranks from lowest to highest as $\Sigma 7$, $\Sigma 25$, $\Sigma 13$.

There was also an enhancement of Mo in the carbide, as shown in the EDS quantification in Table 3.3, Table 3.4, and Table 3.5. However, unlike Cr, there was no consistent reduction of Mo in the Cr depletion zone as the Mo content remained similar to the matrix. Additionally, some of

the changes in the Mo concentration, such as in Table 3.5, were so small that they could not be distinguished from the error associated with the EDS data, which is estimated to be around 1 at%.

In addition to verifying whether the grain boundaries were sensitized, it was also possible to compare the degree of sensitization by comparing the amount of Cr depletion to the matrix and the size of the Cr depletion zones at different CSL boundaries. The degree of the sensitization was linked to the size and shapes of the carbides, suggesting that there was a localized “conservation” of Cr near the precipitates. We previously noted the structural change of the precipitates from lens shape to platelet shape with different Σ -values, which we convert to grain boundary interfacial energy for further analysis in the discussion.

3.4 Corrosion (GACC) Model Expansion to Type II Grain Boundaries

We now turn to an explanation of the results, extending the model previously derived in Chapter 2 [66], where the sensitization of the grain boundaries is the initiating mechanism of grain boundary assisted crevice corrosion. First, interfacial energies of the experimental CSL values were estimated using previously published molecular dynamic calculations for fcc CSL grain boundaries of pure aluminum, nickel, and copper [154]. While this conversion is not rigorously accurate, it should reflect the general trends. Since CoCrMo alloys have a metastable fcc matrix, a scaling factor, determined from the calculated solid state surface energies [135] of the main alloying elements, was applied. The trend of corrosion depth versus interfacial grain boundary energy is shown in Figure 3.15. The 3D profilometry grain boundary depth measurements indicated that the degree of lattice coincidence is related to the corrosion depth of grain boundaries.

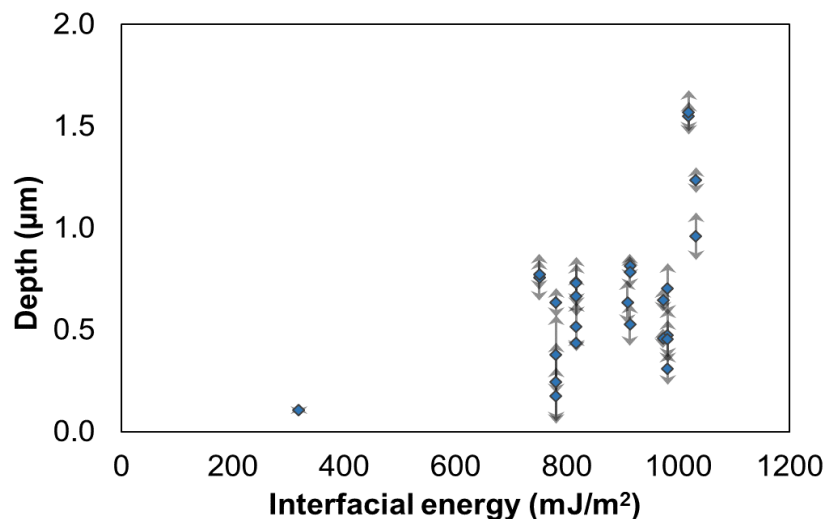


Figure 3.15 Interfacial energies associated with different lattice configurations at CSL grain boundaries have been shown to be a good predictor for the severity of corrosion. The arrows in grey represent the range of the measurements observed.

We now show that the GACC model for Type III boundaries developed presented in Chapter 2 [66] can be extended to Type II grain boundaries. This model compares the energy change of corrosion due to local Cr depletion to the energy change due to removal of the grain boundary, i.e. the grain boundary energy. The difference in composition between the matrix and the Cr depletion region leads to a difference in the corrosion potential that effects the dissolution. Using the EDS data of Cr depletion zones from Type II boundaries of varying degrees of corrosion, the average amount of Cr depletion observed in Type II boundaries ranged from 2.2 at% to 5.0 at% Cr, which was below the average 7.1 at% Cr depletion value observed in Type III boundaries [66]. As Cr content decreases, the corrosion potential increases, and the CoCrMo would follow the same trend; the corrosion potential increases 10 mV per 1 at% Cr decreases [132,133]. Following the model, the change in corrosion potential would range from -22 mV to -50 mV. The electrochemical

difference associated with Cr depletion, $\Delta\mu$, was then converted to joules using calculations outlined in the original GACC model [66].

$$\Delta\mu = \mu_{matrix} - \mu_{CDZ} \quad \text{Equation 3.1}$$

$$\Delta\mu = -22 \text{ mV to } -50 \text{ mV} \quad \text{Equation 3.2}$$

$$\Delta\mu = -8.10 \times 10^{-21} \text{ J to } -1.84 \times 10^{-20} \text{ J} \quad \text{Equation 3.3}$$

This can be compared to -2.61×10^{-20} J for Type III boundaries, and it is a factor of 1.5-3 smaller. Using the same atomic distances for a the distance between atoms along the grain boundary and b the distance between atoms perpendicular to the grain boundary, and the Cr depletion zone widths L as described in the original GACC model, we calculated ΔE_{CDZ} , which is the range for energy lost due to the Cr depletion zone per unit length. The experimental results of Type II boundaries expanded the range of ΔE_{CDZ} .

$$\Delta E_{CDZ} = \Delta\mu \frac{L}{ab} \quad \text{Equation 3.4}$$

$$\Delta E_{CDZ} = -2.77 \times 10^{-7} \frac{\text{mJ}}{\text{m}} \text{ to } -12.6 \times 10^{-7} \frac{\text{mJ}}{\text{m}} \quad \text{Equation 3.5}$$

This This compares to -3.78×10^{-7} to -17.9×10^{-7} mJ/m for Type III boundaries.[66] As calculated in Figure 3.15, the Type II boundaries examined had γ_{GB} values ranging between 780 mJ/m² and 973 mJ/m². By multiplying γ_{GB} with the weighted average of atomic diameters of Co and Cr (0.382 nm), indicated by d , we obtained the energy of the boundary per unit length.

$$\Delta E_{GB} = -\gamma_{GB}d \quad \text{Equation 3.6}$$

$$\Delta E_{GB} = -2.98 \times 10^{-7} \frac{\text{mJ}}{\text{m}} \text{ to } -3.72 \times 10^{-7} \frac{\text{mJ}}{\text{m}} \quad \text{Equation 3.7}$$

This compares to the ΔE_{GB} of -5.35×10^{-7} mJ/m for Type III boundaries [66]; a smaller value of -1.53×10^{-7} mJ/m was cited in the earlier work which is for Type I boundaries such as twins, which are immune.

The comparison of ΔE_{CDZ} and ΔE_{GB} values clearly shows that Type II boundaries fit within the GACC model as both the grain boundary interfacial energy and Cr depletion influenced corrosion sensitivity; neither dominates. The driving force is a factor of 1.5-2 smaller than for the Type III boundaries; we will leave to the discussion section more comparisons of the different boundaries.

To continue expanding the GACC model, crevice corrosion is considered to further explain the grain boundary crevice shapes that were observed in Type II boundaries. During crevice corrosion, oxygen diffusion is restricted by the small crevice opening and should be largely independent of the type of boundary. The crevice corrosion part of the model is to explain the width-depth relationship. The driving force down the crevice is due to the Cr depletion zone and the width is due to the chemistry in the crevice. The model predicts that higher energy Type III non-CSL boundaries would have lower width to depth ratios, and that is indeed what is shown in Figure 3.5.

3.5 Discussion

Similar to stainless steels, Cr is the main alloying element that provides the corrosion resistance in CoCrMo alloys. The relationship between the level of Cr depletion and the amount of observed corrosion is summarized in Figure 3.14. All of the observed Cr depletion values fall below the average Cr depletion in Type III boundaries, 7.1 at% Cr [66]. Of the Type II boundaries that we examined, the Cr depletion ranged between 2-5 at% Cr. Cr at the $\Sigma 13$ boundary depleted about 5 at% Cr. The average depletion values were between 2 at% Cr to 4.8 at% Cr across the three $\Sigma 25$ boundaries measured by EDS. In the corroded Type I boundary, a $\Sigma 7$, we also observed a 1.5 at% Cr depletion at the boundary. With decreasing grain boundary interfacial energies, there was less Cr depletion at the boundaries because the chromium-rich carbides were smaller and also less enriched in Cr. The Cr depletion is linked to the grain boundary orientation and both play a role in the corrosion susceptibility.

The combination of the Cr depletion and removal of the grain boundary is the initiator of the corrosion, but the real damage to the material (and to a patient with a CoCrMo implant) is from the subsequent crevice corrosion since this leads to a more extensive release of ions. Interestingly, this implies that there may be ways to mitigate corrosion in vivo by controlling the content of the pseudo-synovial fluid. The fluid concentrations may play a role in variations in the sensitivities of patients which are known to exist, albeit poorly understood; the physiological conditions may vary with age, gender, ethnicity and other factors [155-157].

As mentioned earlier, the energies of boundaries are not linear with the Σ value. As verification of this, we note that EDS data was collected at four Type II boundaries: for a $\Sigma 13$ and three $\Sigma 25$ boundaries. According the previously discussed method of calculating grain boundary interfacial

energies, the $\Sigma 25$ boundaries have lower energy than $\Sigma 13$. By cross referencing back to the profilometry measurements in Figure 3.5 and graphing with EDS Cr depletion in Figure 3.14, the three $\Sigma 25$ boundaries showed lower corrosion depths than the $\Sigma 13$. We also observed less Cr depletion at the more stable $\Sigma 25$ boundaries. The Type I $\Sigma 7$ boundary in Figure 3.14, which has significantly lower energy than $\Sigma 13$ or $\Sigma 25$, has the lowest corrosion depth and Cr depletion.

We previously note that a change in carbide morphology was observed along with a decrease in Cr depletion at Type II boundaries with low corrosion as well as Type I boundaries. Within the $\Sigma 25$ grain boundaries, we observed both lens shaped and platelet shaped carbides. This suggests that there are different energies associated with the $\Sigma 25$ boundaries. It is necessary to consider grain boundary plane orientation before accounting for deviations from CSL orientations. For example, certain sections of a $\Sigma 25$ CSL boundary may have a higher density of coincident lattice sites than other sections of much lower Σ -value [158]. It is also possible that boundaries of the same Σ -value have different distributions of coincident lattice points, resulting in different interfacial energies.

Given the experimental results herein, the performance of the alloy can be further optimized with grain boundary engineering. Introducing a larger proportion of geometrically-special CSL grain boundaries with thermo-mechanical processes, strain annealing, or strain recrystallization can potentially reduce localized corrosion at the nanoscale and improve the bulk performance of the alloy. Cahoon et al. [159] proposed that applied strain can influence the twin boundary density in pure fcc metals and Cu alloys. Shimada et al. [118] demonstrated with stainless steel that a small pre-strain prior to annealing minimized sensitization in electrochemical potentiokinetic reactivation (EPR) tests and enhanced the frequency of CSL boundaries. We believe these

processing methods can be extended to CoCrMo alloys. The optimization of thermomechanical treatment parameters to achieve favorable grain boundary character distributions and strong corrosion resistance will be critical for the realization of higher performance CoCrMo alloys.

Finally, we note that under the conditions of the electrochemical testing, Cr ions, sodium, potassium, chlorine, and proteins were present in the crevice. Since a bovine calf serum solution buffered with phosphate-buffered saline was used to simulate physiological conditions in vivo, other components such as vitamins, growth factors, amino acids, and hormones were present, causing the system to be complex in comparison to standard corrosion testing etchants. This environment causes complex corrosion that can be difficult to completely capture in a model and leaves open many further studies – particularly if one considers the different in vivo physiological conditions.

3.6 Conclusions

- ❖ 3D profilometry showed that crevice widths are 2-5 times larger than the crevice depths, with Type II boundaries falling closer the upper threshold of this range.
- ❖ Nanoscale chromium-rich carbides and Cr depletion zones were observed in Type II boundaries. With decreasing Cr depletion and grain boundary interfacial energy, the carbides were platelet shaped instead of lens shaped.
- ❖ Type II boundaries, defined to be CSL boundaries between $\Sigma 13$ and $\Sigma 35$, corroded less than 1.0 μm in depth. The average depletion ranged between 2-5 at% Cr, which influenced corrosion susceptibility.

4 Soft Interface Fracture Transfer in Nanoscale MoS₂

The focus of my research now shifts from metallurgical characterization of corrosion to in situ investigation of solid lubricants. In Chapter 4 and 5, I use our group's Nanofactory in situ nanotribology system to investigate the lamellar lubricants molybdenum disulfide (MoS₂). Crystalline MoS₂ is comprised of sheets that can slide past one another, similar to the structure and sliding in graphite. The in situ TEM holder allows for capture of high resolution images and high frame rate video. We imaged the sheets sliding between two contacting surfaces. This unique setup allows for observation of the "buried interface," the interface between two contacting solids, which is a challenge that often plagues tribology research. Our results and conclusions nicely follow work on MoS₂ that was begun in the 1980s and shows what the previous researchers proposed in models.

Molybdenum disulfide (MoS₂) nanoflakes, nanotubes, and nanoparticles are used as solid lubricants and oil additives. We investigate the formation of transfer layers due to fracture during sliding on commercially available MoS₂ nanoflakes. The sliding and fracture properties were observed in high frame rate videos and high resolution images captured using in situ transmission electron microscopy. The orientation of the flakes and the adhesion to the surface and to the contact asperity determined the weakest interface, which subsequently determined the fracture transfer layer. The fracture continued until both surface and counter surface lubricant layers were a single sheet. The fractured material created a transfer layer or wear particles. We did not observe the proposed "deck-of-cards" sliding, where the sliding is distributed between all the layers of a MoS₂ flake. Instead we captured video of an entire flake fracturing at a weak point in the MoS₂ sheets, a "weakest link" soft interface fracture model. The soft interface fracture transfer (SIFT) model is

not specific to MoS₂ layered nanoflakes, and we argue is a general mechanism in the formation of tribolayers.

Material in this chapter is reproduced from the article “Soft interface fracture transfer in MoS₂” by Emily E. Hoffman and Laurence D. Marks; *Tribology Letters*, under review.

4.1 Introduction

Mitigating friction is a major challenge, especially with exposure to extreme thermal and environmental conditions. Many engineering systems rely on solid interfacial films to reduce friction and wear. Particularly, space-born systems depend on solid phase lubrication, which include various movable devices such as gears, pumps, actuators, latches, antenna drives, and solar arrays [23,25]. Transition metal dichalcogenide (MoS₂, WS₂, NbSe₂, etc.) are the most common solid lubricants for space and have growing applications as oil additives in regular machinery [160]. With these advanced applications, however, there are still many unknowns in the field of tribology, including the processes of lubrication and wear [161].

Surface asperity interactions of metal surfaces in contact were analyzed by Bowden and Tabor in the 1960s [5]; this work made it clear that many of the fundamental processes of tribology are taking place on the micron to nanoscale. For solid lubricants, analysis at the nanoscale and atomic scale allows for understanding of the fundamental properties of sliding. During asperity contact, sliding can cause material transfer from one surface to another. In the triboactive region, the region where sliding takes place, a number of phenomena can occur: solid lubricant transfer to contacting surface (transfer layers), third body wear particles, rolling of particles, fracture, and

recrystallization [20]. Wear products can keep evolving; such as wear particles attaching to one of the contacting surfaces to form a transfer layer.

At the macroscale, the friction of MoS₂ surface film depends on the integrity of the film, contact pressure, humidity, film thickness, temperature, and presence of contaminants [26,27]. There are known wear modes of MoS₂, including deformation, fracture and reorientation, fatigue-induced blistering, adhesive wear plowing, and abrasion by foreign particles [22,21]. On the atomic scale, computation has shown that MoS₂ flakes can have friction anisotropy due to interlayer rotational misfit, showing that the orientation of the MoS₂ sheets determines the interactions of the sulfur atoms on the opposing sheets. This causes two orders of magnitude difference in friction [162]. It is crucial to bridge the atomic simulations to the micron-scale wear mechanism in MoS₂ in order to understand the formation of transfer layers [163].

On a microscopic scale, tribological wear processes studies have shown that tribolayers of softer materials can form through chip wear, where shearing off of the softer materials occurs at the asperity contact spot [163]. At the nanoscale, however, the formation and wear of transfer layers remains a topic of debate due to the buried interface problem: the triboactive layers and surfaces of interest are hidden and only accessible by post facto analysis, which leads to uncertainty.

At the nanoscale, MoS₂, along with the other dichalcogenide and the carbon solid lubricant graphite, have lubricating behavior stemming from an easy slip mode intrinsic to their crystal structure. MoS₂ is crystallized in a hexagonal structure, where a sheet of molybdenum atoms is sandwiched between two hexagonally packed sulfur layers. The bonding within the S-Mo-S sandwich is covalent and weak Van der Waals forces hold the sandwich together resulting in easy

interlamellar slip [20]. The shear of the sheets leads to transfer film formation on the rubbing counterface. Transfer layers of MoS₂ were recognized by Godet [34] and Singer [35], with studies by Wahl et al. [37] showing the formation of monolayers of crystalline MoS₂ following sliding and Hu et al. [36] investigating sheet alignment within ~500 nm thick transfer layers. The complexity of lamellar lubricants is that lubrication depends on the fact that the reactivity of the basal planes are essentially zero so that they can slide with low friction; however, the basal planes also need to bond to the surfaces that are being lubricated [164,165].

Understanding the mechanisms of tribolayer formation is critical to understanding wear and lubrication. In situ transmission electron microscopy imaging allows for recording of real time behavior of triboactive layers and directly addresses the problem of viewing the buried interface. Over the last few years there has been additional information available on nanoscale tribological processes made possible by in-situ microscopy. For reviews of in situ developments see work on general in situ [166], in situ TEM [167], and in situ single asperity [168]. In situ microscopy has shown that a single layer of MoS₂ can form a transfer layer and that the sheets slide against the counter MoS₂ surface [169]. Another study has shown interlayer shear stress of a single MoS₂ sheet attached to a charged probe [170]. Mechanical properties of MoS₂ sheets, focusing on elastic bending and strain energy during cleaving, have highlighted the unique properties of MoS₂ [171-173]. For instance, Lahouij has shown crystalline nanoparticles of MoS₂ “exfoliating” single sheets or layers of sheets during in situ sliding tests [38,42,39]. The development of the tribolayer and creation of transfer layers, however, has not been clearly shown in situ for flakes of MoS₂.

Many have proposed the “deck-of-cards” model for sliding of lamellar lubricants, especially for MoS₂ [20,169,174,175]. In this model, each S-Mo-S sheet is a “card,” which stacked up make

the molecular layers of the crystal “deck.” When encountering lateral force on the top of the deck, each of the cards in the deck would slide, like pushing over a deck of cards. The nomenclature to describe the MoS₂ morphology and deck-of-cards is illustrated in Figure 4.1. Each sheet takes on

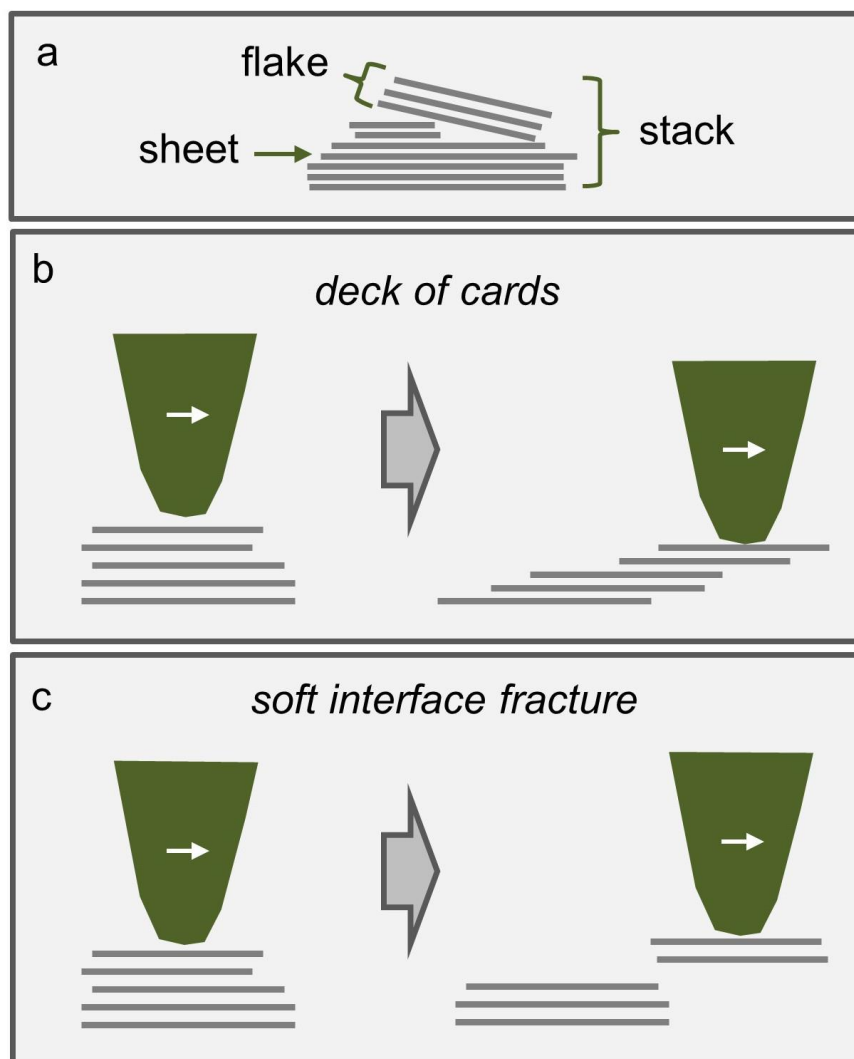


Figure 4.1 (a) Diagram of the usual nomenclature used in the literature and in this chapter. (b) Diagram of the commonly proposed “deck-of-cards” sliding, where each layer undergoes a fraction of the entire sliding. Here the sliding is distributed throughout the entire flake. (c) Our results show the soft interface fracture sliding, where the sliding takes place in-between flakes or the in-between the most disordered sheets within a flake. The other parts of the stack remain stationary.

a fraction of the force; the sliding is distributed between each sheet of the MoS₂ flake. The deck-of-cards argument was also studied by Fleischauer et al. [164,176-178]; it was framed in the context of intercrystalline slip versus intracrystalline slip. Deck-of-cards would be analogous to intercrystalline slip, with the lubrication coming from sliding between the basal planes distributed between all of the sheets. The counter idea is intracrystalline slip, with the sliding between crystals, where the sliding is between lamella of adjoining crystallites. It was predicted that intracrystalline slip was likely because coatings of aligned, dense nanocrystalline MoS₂ had good friction and wear properties. Neither deck-of-cards nor intracrystalline slip phenomena, however, have been observed on the nanoscale. It is not yet clear how many (or how few) layers are needed to accommodate interfacial shear with low friction. Are one or more layers needed on both counter bodies? As Wahl et al stated [175], “real-time TEM experiments hold the genuine possibility of answering the fundamental questions of how lamellar solid lubricants actually accommodate motion during sliding.”

In this study, in situ microscopy allows for nanoscale examination at the buried interface to see the fracture of stacks of nanoscale MoS₂ flakes. The fractured flake then forms a transfer layer. By imaging the interface and solid lubricant in real time through recording videos and high resolution images, the behavior of nanoscale flakes was investigated in a variety of contact situations. The structures of MoS₂ flakes on the surface were observed before, during, and after contact with a single asperity. Through this setup, we observed that the contact force caused the MoS₂ flakes to fracture at the soft interfaces between partially aligned sheets. This fracture at the soft interfaces between MoS₂ flakes during sliding created transfer layers, which we describe here in terms of a soft interface fracture transfer (SIFT) model. The fracture here is not intercrystalline

slip, but occurs between the nanoflakes as intracrystalline slip. We propose that the SIFT layers and mechanism is general in the creation and behavior of transfer layers in lamellar solid lubricant systems.

4.2 Experimental Methods

The sample was made from a fragment of a Si aperture TEM grid, fractured into about four pieces. The Si fractured along crystallographic planes to create a thin, electron-transparent edge. The MoS₂ nanoflakes are commercially available from Graphene Supermarket as Molybdenum Disulfide Pristine Flakes. The nanoflakes came in a dispersed solution, and the company indicated size of the nanoflakes was accurate. For sample preparation, approximately 10-15 drops were deposited on the Si fragment. The fragment sat on a hotplate set to 55 °C to speed solution evaporation. The sample was glued on a tungsten needle with M-bond to fit in the TEM sample holder mount.

An FEI Tecnai F20ST TEM at Argonne National Laboratory operated at 200 kV was employed for the in situ sliding tests. The sliding occurred in the vacuum environment of the TEM at less than 1×10^{-7} Torr. The experimental setup of the Nanofactory TEM/AFM holder is shown in Figure 4.2. A silicon atomic force microscopy (AFM) tip fabricated on a cantilever was used as the sliding counterpart with a spring constant of 5.6 N/m as provided by the vendor [179]. The sample can move three dimensionally in the holder in the TEM. The sample movement is driven by a piezomotor with resolutions of 0.2 Å in XY and 0.025 Å in Z. The sliding experiments took place at no load (within measurement error) with no detectable cantilever deflection.

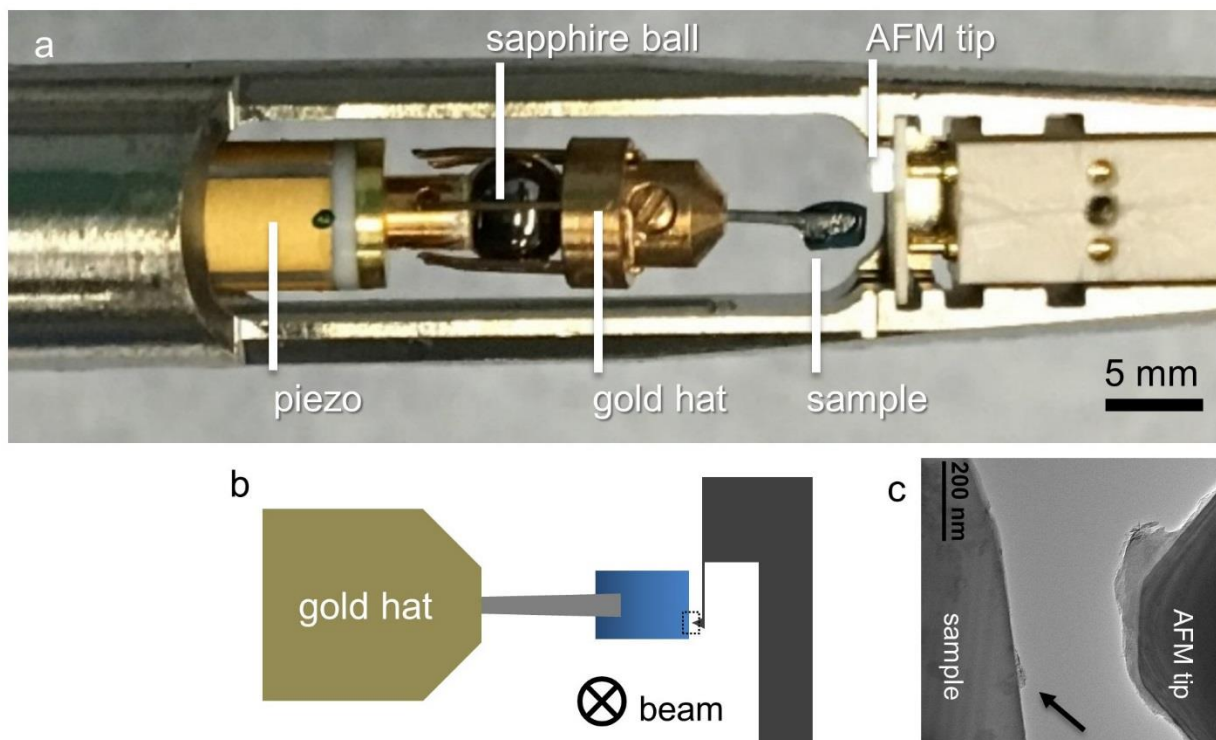


Figure 4.2 Experimental setup of the in situ sliding test. (a) Photograph of the holder with mounted sample. (b) Drawing to show the orientation of the fractured Si edge and AFM tip orientation. (c) TEM image of the boxed region showing the sample, AFM tip, and an arrow to a MoS₂ flake on the edge.

The processes were recorded using a TV-rate video camera. The extracted frames were processed by deinterlacing and adjusting the levels for clarity using the program GIMP.

Videos of the in situ sliding results are noted with the corresponding figures. The videos are available at <http://www.numis.northwestern.edu/Research/Staff/Emily/index.shtml> under “Thesis Videos.” Video caption are on the website and included at the end of this chapter.

4.3 Results

Three areas of ideal MoS₂ flakes were found in the TEM, with the MoS₂ sheets oriented parallel to the beam direction. Most flakes were between 30-150 nm long and 5-20 sheets thick. Sheet depth was assumed to be on the order of the flake length. The well-oriented stacks of flakes consisted of 2-3 clearly defined flakes. Figure 4.3 shows the three examples of stacks of MoS₂ flakes that occurred on the edge of the Si substrate. The initial state is shown in Figure 4.3 a-1, b-1, and c-1; here the stacks were in their original arrangement, untouched by the AFM tip. Example a-1 and c-1 had two flakes in the stack, and example b-1 had 3 flakes in the stack.

Within a stack of flakes, the distinction between flakes was identifiable by the disorder between the sheets of MoS₂. Within a single flake, the sheets are of approximately the same length and have few to no defects along the interface of the sheets. In the TEM, the order is observable by the straight and clear sheets that appear as black lines. In contrast, between flakes there is a misorientation with layers of half sheets (dislocations) inserted between the flakes. These disordered interface layers disrupt structure and Van der Waals bonding of the sheets.

To begin the sliding experiments, the AFM tip, representing a single asperity, was brought into contact with the stack of flakes, making contact at the top of the top flake, as seen in the three examples in Figure 4.3. When the AFM came within ~4 nm of the top flake, the AFM tip would jump to adhesion. The sample was moved into the AFM tip to a compressive force, then brought back down to slide at neutral force; there was no AFM cantilever deflection during sliding. This adhesion and the sliding motion thereafter caused fracture within the stack of flakes. The fracture occurred at the weakest interface, which was the interface between the flakes that had the most disorder. The videos of Figure 4.3 a-c are in Videos 1-3 respectively.

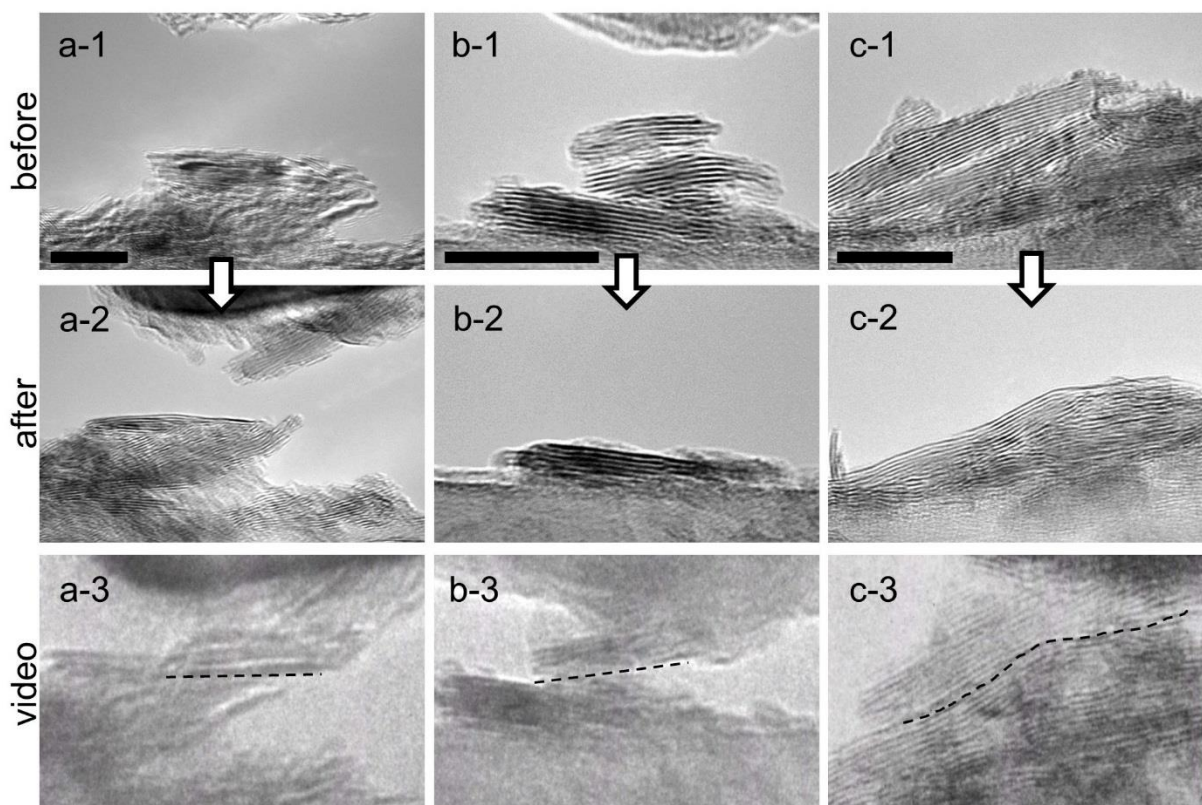


Figure 4.3 Three examples of soft interface fracture transfer layers forming, with initial states of (a-1), (b-1), and (c-1) and final states after fracture of the transfer layer of (a-2), (b-2), and (c-2). (a-3), (b-3), and (c-3) show extracted video frames with the dotted line showing the soft interface. Scale bars are 20 nm.

For examples a and c in Figure 4.3, the weakest interface was the boundary between the top flake and bottom flake, with stronger adhesion of the top flake to the AFM tip and the bottom flake to the Si substrate. For example b with three flakes, the weakest interface was between the middle and bottom flake. This is due to the orientation of the flakes. As seen in Figure 4.3 b-1, the top and middle flakes are parallel, whereas there is a misorientation of 18° between the middle and bottom flakes. The transfer layers can be seen mid-slide in Figure 4.3 a-3, 2 b-3, and 2 c-3, which were extracted from Video 1, 2, and 3 respectively. The flake that fractured and transferred to the tip created the transfer layer.

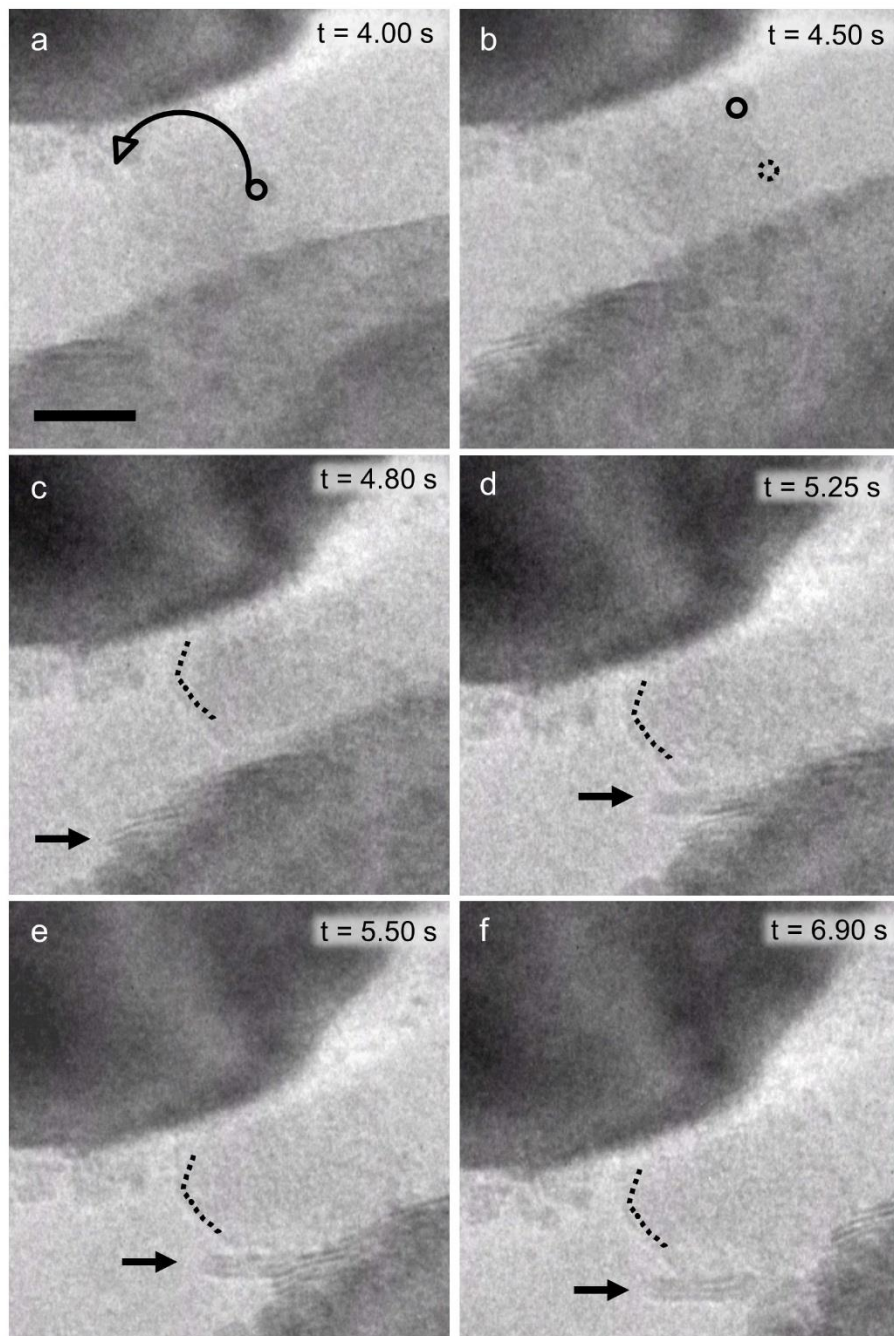


Figure 4.4 (a) The ball of MoS₂ rolled between the AFM tip and the Si surface. (b) The feature rolled without slipping, indicated by the circle markers. (c) The ball hit the oriented MoS₂ flakes and changed from rolling to sliding. (d,e) The sliding of the transfer flake. (f) The top flake as a transfer flake on the ball. c-f include an orientation marker to show the ball stopped rolling and the black arrow points to the transfer flake. Scale bar is 20 nm.

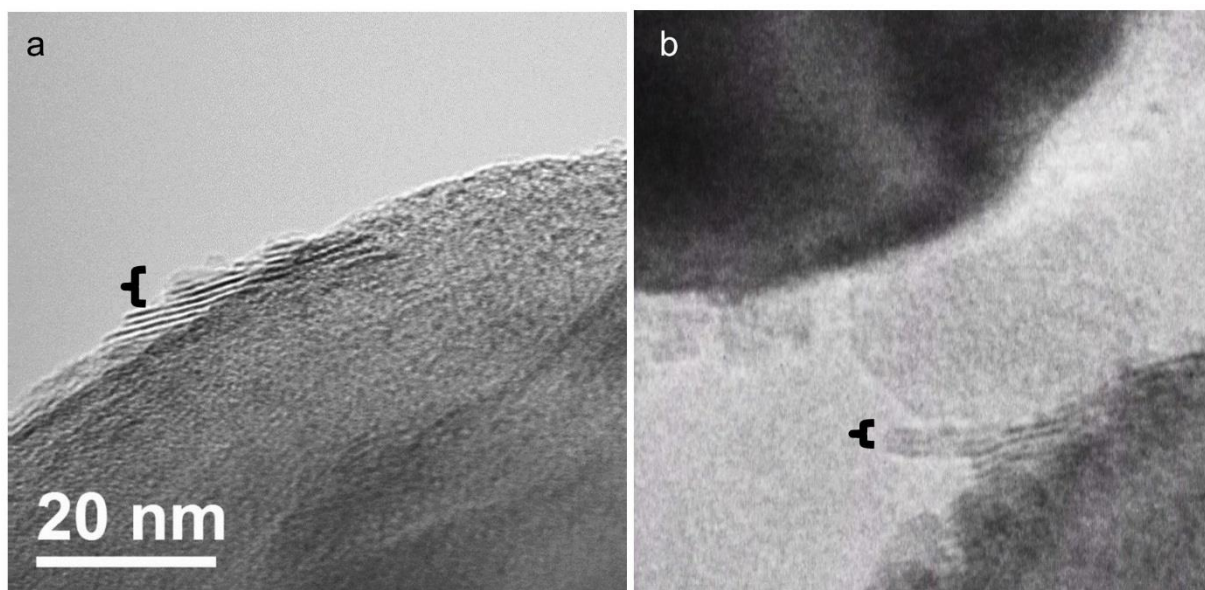


Figure 4.5 (a) The area before any contact with the future transfer flake noted with the bracket and (b) the same sheets adhered to the sliding ball. Scale bar is 20 nm.

As MoS₂ can wear in various modes, we also observed SIFT layers occurring with rolling MoS₂ flakes. During experimental sliding, a flake of MoS₂ 25 nm in diameter was rolled between the AFM tip and the Si surface, as shown in Figure 4.4 a and b from extracted frames from Video 4. For this SIFT example in particular, the rolling was better captured in Video 4 than in the extracted frames of Figure 4.4. When rolling, the ball encountered oriented stacks of MoS₂ flakes and changed from rolling to sliding; sliding became the mode of least friction. The sliding is seen in Figure 4.4 c-f, again extracted from Video 4. The top transfer flake of ~3 layers, in Figure 4.4 f, fractured from the bottom flakes on the Si surface and transferred to the ball. The fracture interface was the weakest interface in the flake. Figure 4.5 a shows an image of the area before sliding. Then the extracted video frame in Figure 4.5 b shows the transfer sheets moving to the ball and the bottom sheets adhering to the Si surface.

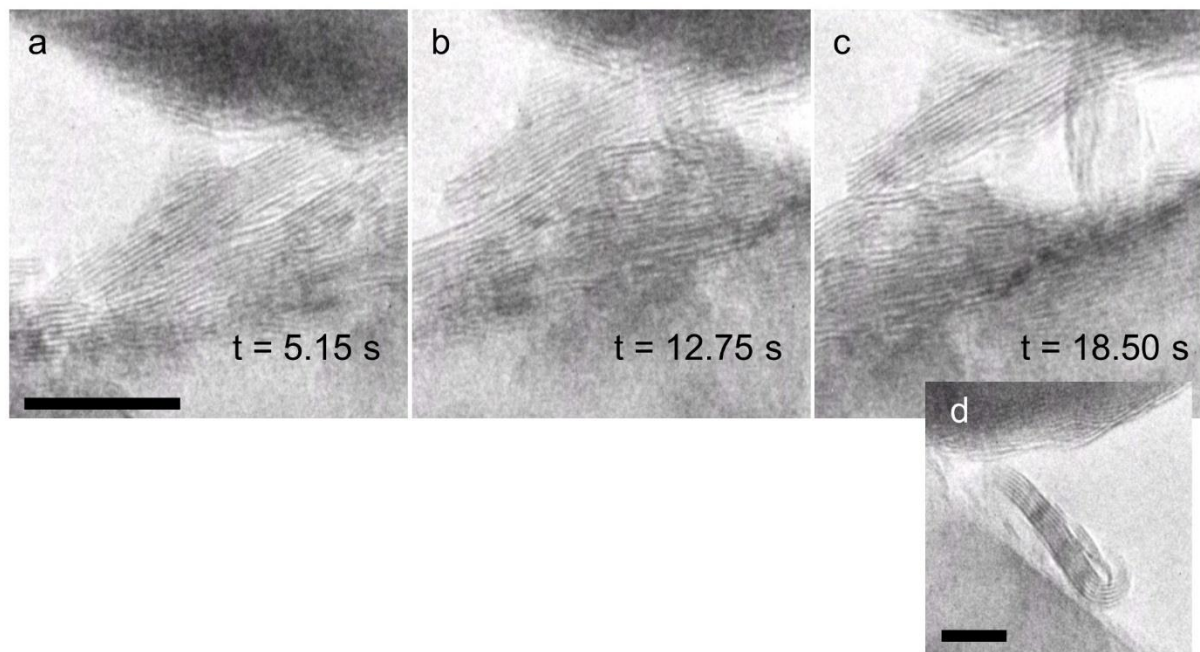


Figure 4.6 (a)-(c) Stages of the SIFT layer sliding from the bottom flake, and (d) adhesion to the Si surface after SIFT. Scale bar is 20 nm.

The sliding system is a dynamic process. The adhesion to the contacting interface, the tip in this case, was not permanent. Other attractive forces caused the transfer flake to jump back to the Si surface, usually at a random location and orientation. The transfer flake from Figure 4.3 example c is again highlighted in Figure 4.6. The stages of sliding are depicted in Figure 4.6 a-c (extracted from Video 3) and the jump of the transfer layer back to the substrate is seen in Figure 4.6 d (extracted from Video 5). After fracturing from the bottom flake, transferring to the AFM tip, and jumping back to the substrate surface, it is notable that the sheets left intact on the flake were highly aligned. These were the most strongly bonded to the substrate, where the other partial sheets of the flake fractured off to other more attractive surfaces during the transition jumps.

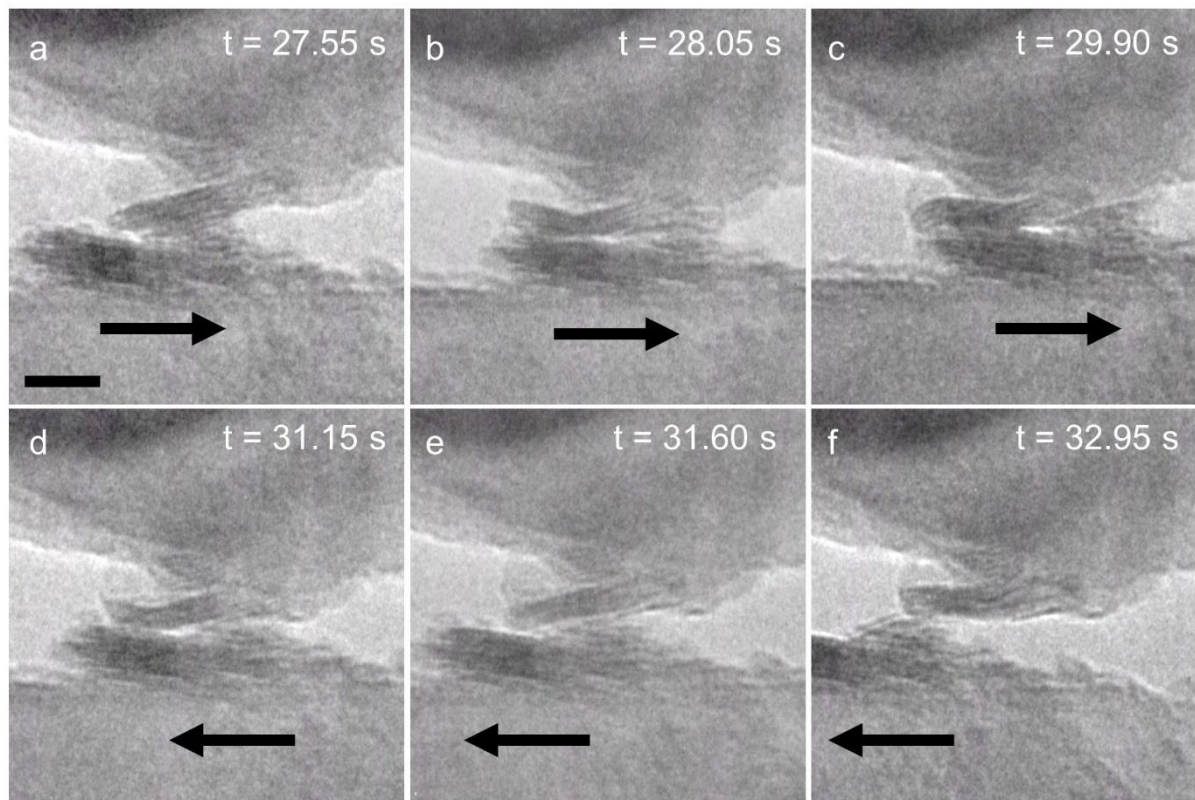


Figure 4.7 (a)-(c) The Si substrate slid right and (d)-(f) slid left to highlight the bending of the transfer flake, showing the evolving soft interface. Scale bar is 10 nm.

The fracture transfer layers occurred because there was a soft interface between the sheets, the weakest point in the stack of flakes. The soft interface is clearly seen in Figure 4.7 when the top transfer flake from Figure 4.3 example b was brought back in contact with the bottom flake and then slid back and forth. Figure 4.7 a-c shows the Si substrate sliding right and the transfer flake conforming in shape to have maximum alignment with both the AFM tip above and the sheet of MoS₂ on the bottom flake beneath. Then as the substrate is slid to the left, the flake continues to attract to both surfaces and forms evolving soft interfaces. Video of the process depicted in Figure 4.6 is found in the second half of Video 2. The SIFT layer curled and bent to keep the most contact with the soft interface, as this contact is the lowest energy orientation.

To show the evolution of soft interface fracture, sliding was continued until no more fracture occurred within a stack of flakes. The stack of flakes in Figure 4.3 example b was used to continue sliding, with the extracted frames from the video in Figure 4.8. First the initial fracture event occurred, shown in Figure 4.3, where the top two flakes became a transfer layer, Figure 4.8 a-b. Next, the transfer layer was slid gently back and forth on the bottom stack, shown in Figure 4.8 b-c. (The detail of the sliding step is in Figure 4.6.) In Figure 4.8 c, the transfer flake became adhered to the tip shape and some sheets were worn away. These minor instances of soft interface fracture from Figure 4.8 c-d are seen in Video 6. The initial stack was made of three clear flakes, but in Figure 4.8 c-e, a smaller partial flake stayed adhered to the bottom flake. The partial flake's misalignment to the bottom flake was only 10° . A coarse slide occurred between Figure 4.8 d-e, which caused the partial flake to fracture at the soft interface. This fracture is seen in Video 7. From this series of fractures, the four weakest soft interfaces are apparent. The final state of the stack, Figure 4.8 e, resulted in a flake parallel to the substrate. The tip tribolayer became conformal to the tip shape. Both the tribolayer's and the flake surface's ended with primarily continuous sheets at the sliding interface. At this state, dozens of sliding passes occurred with no change in morphology. Here no soft interfaces were present and sliding had become stable. The end state soft interface fracture was explained in depth for Figure 4.3 example 2, and it is relevant to note that it was also observed for example 1 and 3.

4.4 Discussion

Here we observed the buried interface of MoS₂ nanoflakes between a Si surface and a Si AFM tip using in situ electron microscopy. Through contact with the AFM tip asperity, the stacks of

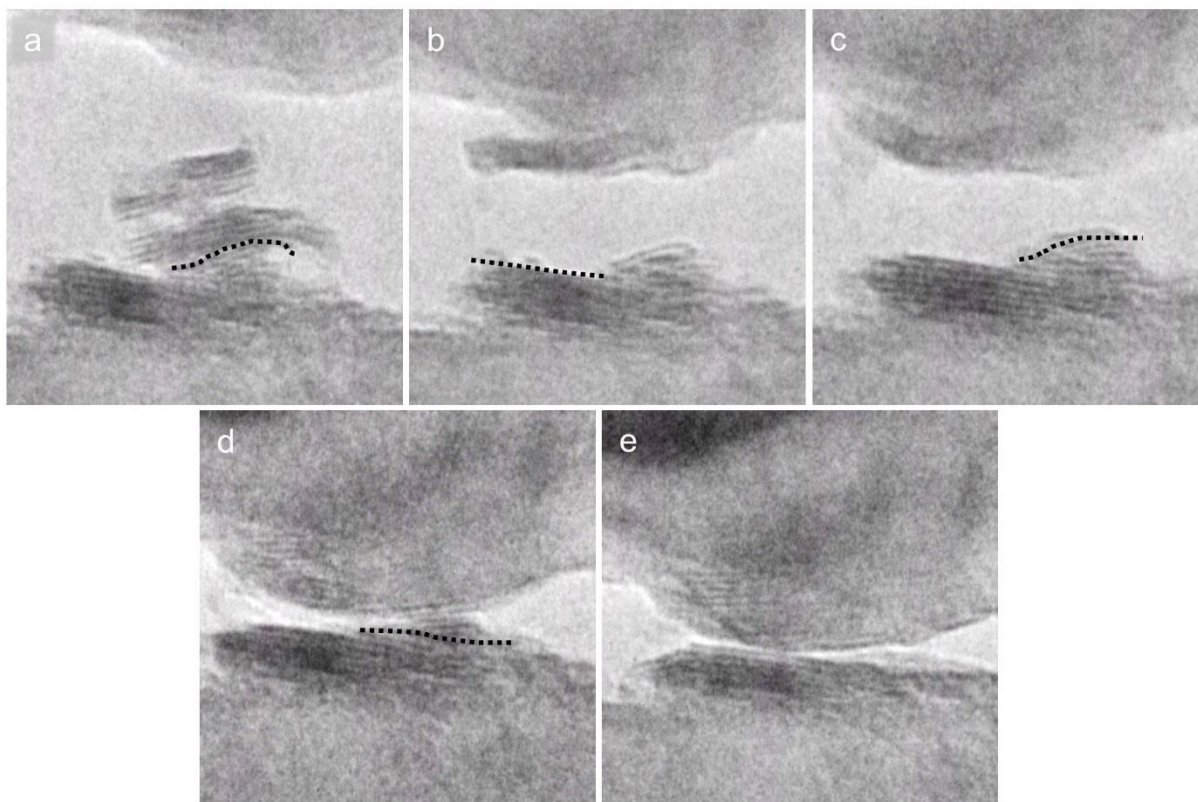


Figure 4.8 The soft interface fracture process of the stack of flakes from **Figure 4.2** example b. The initial stack (a) fractures at the weakest interface indicated with the dotted line. (b) The SIFT layer is created on the tip and the next soft interface fracture point is indicated with the dotted line. (c) The transfer layer has adhered to the shape of the tip, and further removal of the weakest layers are seen. (d) The last misaligned flake is indicated with the dotted line. (e) All misaligned flakes are removed from both the initial stack and from the transfer layer as well. Both the flake on the substrate's and the transfer flake's surfaces are made of a primarily continuous sheet of MoS₂.

MoS₂ flakes fractured at soft interfaces between disordered sheets. The soft fracture of an entire flake created a soft interface fracture transfer layer. The “deck-of-cards” model, where sliding is distributed between every sheet of a MoS₂ flake was not observed. The SIFT layer explains how transfer layers form during lamellar solid lubrication.

The SIFT layer formation is, most simply, a weakest link mechanism. The slip we saw was not intercrystalline, not collective between the lamella, but it was intracrystalline slip, between

individual nanoflakes. Instead of the deck-of-cards model, a more appropriate description would be links in a chain. When stressed, the weakest link breaks. If one of the pieces of the broken chain is again stressed, there is a new weakest link where fracture will occur. The weakest link as the source of failure is inherent throughout materials and size scales. It is rare that a macroscale intuition can apply down to the nanoscale, but here the “weakest link” model aptly describes the behavior.

An alternative, more mathematical way of making the same statement is to consider the activation energy barrier to deformation. Slip has to involve dislocations, either localized or delocalized depending upon the local bonding. In a pristine material for slip to start dislocation loops (or half loops) have to nucleate, a substantial energy barrier. When defects already exist the activation energy to nucleate defects is no longer required. Hence slip occurs at where dislocations already exist, for instance at interfaces (assuming that the relevant slip systems are available). For the deck-of-cards mechanism, it would have to be energetically favorable to simultaneously create a number of dislocations and have them move in a concerted fashion. While this is not impossible and could occur at existing low angle boundaries, it is unlikely at the small sizes herein.

In MoS₂ and in other lamellar lubricants, the weakest link is the layer with the most disorder. The forces presented in these stacks are covalent bonds and Van der Waals bonds. The sheets of MoS₂ are covalently bonded and these are not changing. The Van der Waals bonding occurs between the sheets of the MoS₂ flakes, and they also occur between the flakes and the Si substrate and Si tip (referred to as adhesion). Within stacks of flakes, disorder is most obviously seen in misorientation between flakes. In the three-flake stack example presented, in Figure 4.8, the initial fracture is between the flakes with the largest misalignment (the middle and bottom flake, 18°,

Figure 4.8 a-b). Next, there are sheets and small flakes removed from the top of the substrate flake and from the bottom of the transfer layer flake (Figure 4.8 b-d). Lastly, it takes a coarse, larger force to fracture the less aligned flakes (the partial flake and bottom flake, 10° , Figure 4.8 d-e). Through this evolution of flake morphology, we can see the hierarchy of weakest links. We see the major SIFT layers that create the initial transfer layer, but then we can also see minor soft interface fracture of partial layers. The surface refinement process is seen in Figure 4.8 as the partials imperfect flakes are removed.

The SIFT mechanism is a generic process. It can be subdivided by the type of fracture process that occurs: Mode I (fracture in tension caused by adhesion), versus Mode II or III (caused by shear) [180]. In our system in vacuum with freshly cleaved Si surfaces, the adhesion is strong between the MoS₂ nanoflakes and the Si. This allows our study to primarily focus on Mode II and III, shearing creation of the transfer layers. If we were to pull straight back to focus on Mode I, the soft interface fracture would not occur the same way – but would still occur.

We observe an endgame of the weakest link model once the most significant soft interfaces have been fractured. After the major SIFT layer fracture occurs, it can be inferred that the partial flake on the bottom flake, pictured in Figure 4.8 d, had stronger Van de Waals bonding than the transfer layer flake. The stronger bonding was due to the higher order between the sheets. There are not enough defects in the bonding between any of the partial flake layers for fracture to occur with the same level of force. This was a metastable state. Therefore, a larger force than the standard piezo motor was needed to fracture the partial flake, Figure 4.8 d-e. At this point in sliding, Figure 4.8 e, no soft interfaces were apparent, and sliding had reached a stable state. Both the Van de Waals bonding within the crystalline nanoflake and the adhesion between the flake and the Si were

higher than the Mode I fracture force. The Mode I fracture stress came from bringing the counterface flake in contact and pulling apart. We are further evaluating the various fracture modes and when the nanoflakes stop wearing from adhesion and sliding forces in Chapter 5.

The intra-crystalline slip observation supports the idea that best performing MoS₂ films should be made with small crystallites, such as the nanoflakes used here, because dense crystallites enable stable sliding lamellae surfaces to be generated on each face with only a small amount of the film wearing away in the process. At least one soft interface within the material is needed to create a transfer layer, but if you have all soft interfaces, the crystallites (nanoflakes in our experiments) will continuously break down until the film is gone. The *in situ* observations here have helped to establish the connection of how crystallites are free to move and be transferred, previously discussed by Fleischauer [164,165].

Further methods to understand the weakest link SIFT model would require measuring the force, approach angle, flake orientations, and adhesion. These factors contribute to soft interface fracture and the creation of a stable sliding interface. Metastable states were observed at some constant force sliding or for a limited number of passes. The final stable point was two complete sheets of MoS₂, one on the substrate and one on the asperity, as the sliding interface. In that case, soft interfaces were no longer present, except for the sliding interface.

These MoS₂ sliding experiments highlight that tribology is the study of weak interfaces. The creation, wear, and fracture at these soft interfaces needs to be well understood to be able to control the lubrication process. The soft interfaces allow for transfer layers to occur in lamellar solid lubricants and also explain how the triboactive surfaces wear into a stable state.

4.5 Conclusions

- ❖ The formation of transfer layers due to fracture during sliding on commercially available MoS₂ nanoflakes was investigated. The sliding and fracture properties were observed in high frame rate videos and high resolution images captured using in situ TEM.
- ❖ We did not observe the proposed “deck-of-cards” sliding, where the sliding is distributed between all the layers of a MoS₂ flake. Instead we saw an entire flake fracturing at a MoS₂ stack’s weak point, a “weakest link” soft interface fracture model. The SIFT model is not specific to MoS₂ layered nanoflakes, and we propose it is a general mechanism in the formation of tribolayers.

4.6 Video Captions

Video 1: Spot2_tribolayersliding

Video of Figure 4.3 a showing SIFT fracture.

Video 2: 3-10_spot3-1_sift

Video of Figure 4.3 b showing SIFT fracture (first half) and Figure 4.7 showing evolving soft interface contact (second half). Also video of Figure 4.8 a-b.

Video 3: 3-24_spot1_sift

Video of Figure 4.3 c and Figure 4.6 a-c showing SIFT and transfer layer shown in Video 5.

Video 4: 3-10_spot2_sift

Video of Figure 4.4 and Figure 4.5 of a rolling flake. Also shown in Figure 5.7.

Video 5: 3-24_spot1_transflake

Video of Figure 4.6 d showing the transfer flake after Video 3.

Video 6: 3-10_spot3-3_singlelayer

Video of Figure 4.8 c showing the soft interface fracture of partial flakes and sheets during piezo sliding.

Video 7: 3-10_spot3-5_flatten

Video of Figure 4.8 d-e showing the soft interface fracture of the partial flake from the bottom flake from coarse sliding.

5 Molybdenum Disulfide Sliding Modes

Work on molybdenum disulfide (MoS_2) flake fracture, which led to transfer layer formation, was presented in Chapter 4. An introduction to solid lubricants, as well as a discussion of soft interface fracture transfer, was presented. It was shown that MoS_2 does not slide through a distributed deck-of-cards mechanism, but instead the flakes fracture at the weakest interface of the MoS_2 sheets. This soft interface fracture helps to explain the formation of the transfer layer during sliding. Here, the previous background of MoS_2 solid lubricants will be summarized, and then the background will be expanded to include other relevant lamellar lubrication mechanisms.

Molybdenum disulfide nanoflakes show a variety of tribology and wear phenomena at the nanoscale. In situ TEM was used to capture the sliding and degradation process of MoS_2 nanoflakes on a silicon substrate. Here we present further discussion of MoS_2 sliding properties. During in situ sliding, we observed layer reorientation, flakes rolling into ball bearings, and reduction of adhesion. Using in situ TEM observations, we can better understand the lubrication mechanisms of lamellar solid lubricants.

5.1 Introduction

Mitigating friction is a significant challenge, and solid lubricants play an important role. MoS_2 is a well-known solid lubricant, with lubrication applications in the extreme environment of space [23-25]. MoS_2 has been shown to form transfer layers [34,35], including crystalline monolayer transfer films [37] and thicker films [36]. There are still many unknowns in solid lubricant tribology, however, including the processes of lubrication and wear evolution during sliding.

Layered lubricants break apart and reorient during sliding, which is important to both tribolayer formation and wear. Understanding the evolution of the nanoscale particle form can indicate where sliding occurs, or conversely, where it is hindered. The weak interlayer Van der Waals bonding is what allows the sheets in layered solid lubricants to slide past one another with little friction, while the in-plane covalent bonding remains intact [181]. The basal planes also need to bond to the surfaces that are being lubricated [165,178]. There is more left to understand about the wear of particles and the effects on adhesion.

Macroscale tribometer tests on MoS₂ can point to interesting areas for nanoscale investigation. Much of the initial work on MoS₂ was macroscale, pin-on-disk friction measurements [20,29-33]. The friction of MoS₂, can depend on film integrity, contact pressure, humidity, film thickness, temperature, and presence of contaminants [26-28]. Previous work on using TEM has shown reorientation and various sliding modes [21,37,169,175]. For example, nanoscale analysis has shown that amorphous MoS₂ can crystallize during sliding and that misoriented MoS₂ can reorient into parallel planes during sliding [37,181]. Other MoS₂ research areas also focus on nanoscale analysis, including work on characterization of synthesized particles [40,182] and in-situ tribology TEM work [38,167,169,170].

In the previous chapter on soft interface fracture transfer (SIFT) layers, the importance of analysis at nanoscale asperities was presented. Using in situ electron microscopy to observe asperity contacts allowed for understanding of fundamental properties of sliding. It was shown that the deck-of-cards mechanism for MoS₂ flakes, though often presented in the literature, was not proven during nanoscale sliding [20,169,174,175]. In the triboactive region, many other processes occur in addition to the soft interface fracture transfer, such as third body wear particles, rolling of

particles, and recrystallization. Similar to deck-of-cards, these mechanisms are often drawn as pictures without significant experimental proof, see examples of picture mechanisms in Figure 5.1. In many experimental setups, the triboactive layer is buried and cannot be monitored during testing [183-185]. The studies that are confined to micron-scale or post facto analysis can lead to poor assumptions of the nanoscale mechanisms.

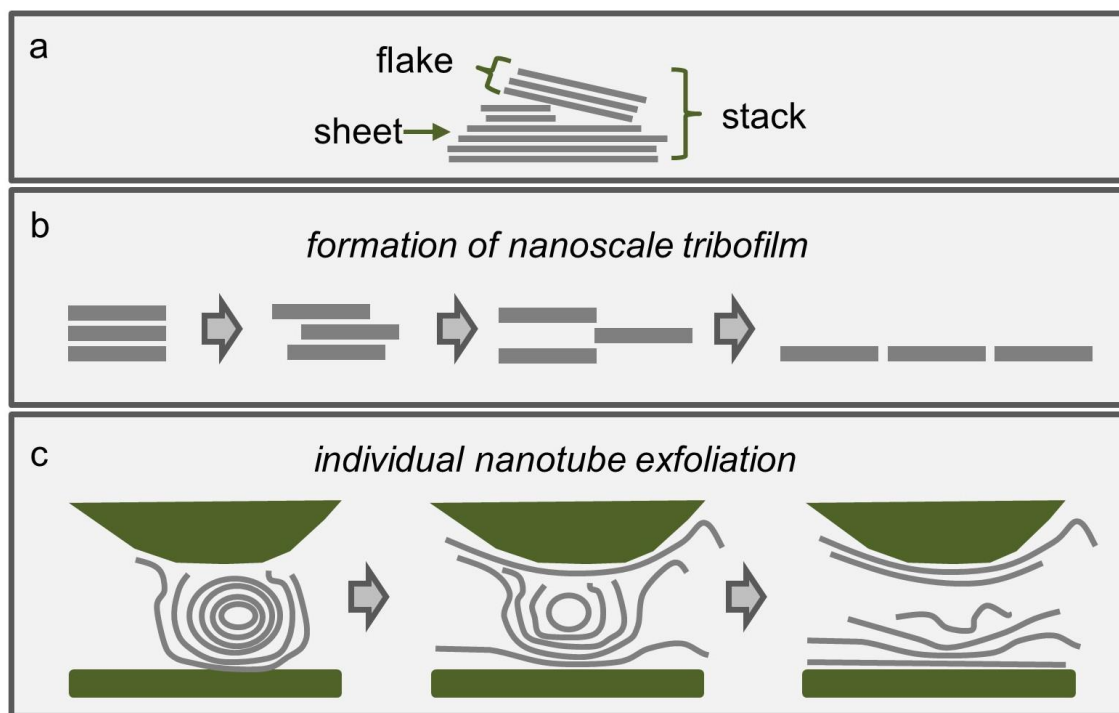


Figure 5.1 (a) Nomenclature used for the nanoflakes, showing the stack, flake, and sheets. Unsubstantiated proposed mechanisms for (b) the formation of a nanoscale tribofilms and (c) individual nanotube exfoliation.

A large area of nanoscale MoS₂ work comes from fullerene like MoS₂ (IF-MoS₂) nanoparticles, with many studies by Lahouij et al. [38-42]. The work on IF-MoS₂ and nanotube MoS₂ is relevant to consider because the particles often break up into sheets similar to MoS₂ nanoflakes, examined in this work. A difference is that IF-MoS₂ nanoparticles are synthesized, where the size, shape, and crystallinity are still topics of research [38,182]. When the particles are

highly crystalline and without defects, they roll and slide as a whole particle. When the particles are less crystalline, they exfoliate immediately and deliver MoS₂ layers to the surfaces [42]. When the rubbing surfaces are both steel, the particles will form adhered sheets on the surface; when the surfaces are alumina or diamond like carbon (DLC), sheets are not formed. The MoS₂ sheets are thought to be bonded to the steel surface as Fe-S bonding was observed [39]. For highly crystalline particles, the lubricating properties were not determined by the surface material because the lubrication method was due to rolling. When an IF-MoS₂ particle underwent compression and shear, the sheets began to reorient and the outer sheets exfoliated at a pressure of ~1 GPa [182]. The nanoparticles are considered good lubricants because of the rolling, sliding, and exfoliation-material transfer (ability to become a third body) [183].

Various forms of MoS₂ can also affect the adhesion of a surface. MoS₂ nanotube oil additives were found to significantly decrease friction and wear compared to the base lubrication [184-186]. Tribofilms were formed by the adhesion of MoS₂ nanosheets to the surface after, it was assumed, the nanotubes exfoliated and deformed. The exfoliation process and how the flakes become stably adhered to the surface, however, was not explicitly shown at the nanoscale. If IF-MoS₂ was added to a fully formulated oil (with dispersants), then there was no difference in performance because the MoS₂ was dispersed and could not deposit on the surface as a tribolayer [160]. In oil additive research, there are also proposed mechanisms of tribolayer formation from flakes that have not been shown in situ [185-187].

Beneficial film structure and corresponding mechanisms of sliding were proposed by Fleischauer et al. for MoS₂ sputter deposited films [164,165,176-178]. The films were primarily characterized by X-ray photoelectron spectroscopy and X-ray diffraction. The key conclusion was

that the MoS₂ films lubricate by means of intercrystalline slip, where intact crystallites within the film slide over each other [178]. The sliding crystallites did not fracture in the transverse direction of their basal planes because they observed no new reactive surfaces during wear. They found that if the crystallites, what we call nanoflakes in our samples, were too large for ideal conditions (for their case $300 \pm 100 \text{ nm} \times 400 \pm 100 \text{ nm}$), then they would cleave until they obtained the optimum particle dimensions for a given set of operating conditions (for their case ~ 100 to 150 nm per side). They observed that crystallites in an aligned, dense film would allow for stable sliding without excessive wear. Our work on MoS₂ SIFT layer formation in Chapter 4 began to show how nanoflakes break apart to create MoS₂-MoS₂ sliding interfaces, yet this is just one mechanism in the process. Fleischauer et al. [178] explained that future work would need to determine the right film conditions, optimum sizes of particles, and optimum friction of the particles.

In this work, in situ microscopy allows for nanoscale investigation at the buried interface of a lamellar solid lubricant, MoS₂ nanoflakes. During sliding, the flakes fractured, became transfer layers, and reduced adhesion between the Si interfaces. The flakes also rolled up into balls and then rolled as ball bearings between the surfaces. With further sliding and with particular adhesion, balls broke apart and became flakes again. The nanoflakes were observed before, during, and after contact with a single asperity tip. The structures of the MoS₂ sheets evolved based on orientation to the contacting asperity tip, presence of an adhered transfer layer, force of contact, and number of passes. This sliding and lubrication process was dynamic and could depend on many contributing factors. The nanoflakes were evaluated on the stability of the flakes during sliding and noting where and what changes took place for the various situations.

In this Chapter, I will show that there are many processes that occur which can be considered through a stable-energy-state framework. During sliding, the sheets continue to change until a stable morphology state is reached. From Newton's third law, the force that drives changes is the sum of the external load and the friction. If we are just sliding, this leads to the hypothesis that the sheets will continue to change until they achieve a low-friction configuration. The experimental evidence supports this general hypothesis specifically for MoS₂, but the hypothesis should be general.

5.2 Materials and Methods

The same MoS₂ SIFT experiment methods were used, as presented in Chapter 4, and we repeat the methods here. The sample was made from a fragment of a Si aperture TEM grid, fractured into about four pieces. The Si fractured along crystallographic planes to create a thin, electron-transparent edge. The MoS₂ nanoflakes are commercially available from Graphene Supermarket as Molybdenum Disulfide Pristine Flakes. The nanoflakes came in a dispersed solution, and the company indicated size of the nanoflakes was accurate. For sample preparation, approximately 10-15 drops were deposited on the Si fragment. The fragment sat on a hotplate set to 55 °C to speed solution evaporation. The sample was glued on a tungsten needle with M-bond to fit in the TEM sample holder mount.

An FEI Tecnai F20ST TEM at Argonne National Laboratory operated at 200 kV was employed for the in situ sliding tests. The sliding occurred in the vacuum environment of the TEM at less than 1×10^{-7} Torr. The experimental setup of the Nanofactory TEM/AFM holder is shown in Figure 5.2. A silicon atomic force microscopy (AFM) tip fabricated on a cantilever was used as the sliding counterpart with a spring constant of 5.6 N/m as provided by the vendor [179]. The

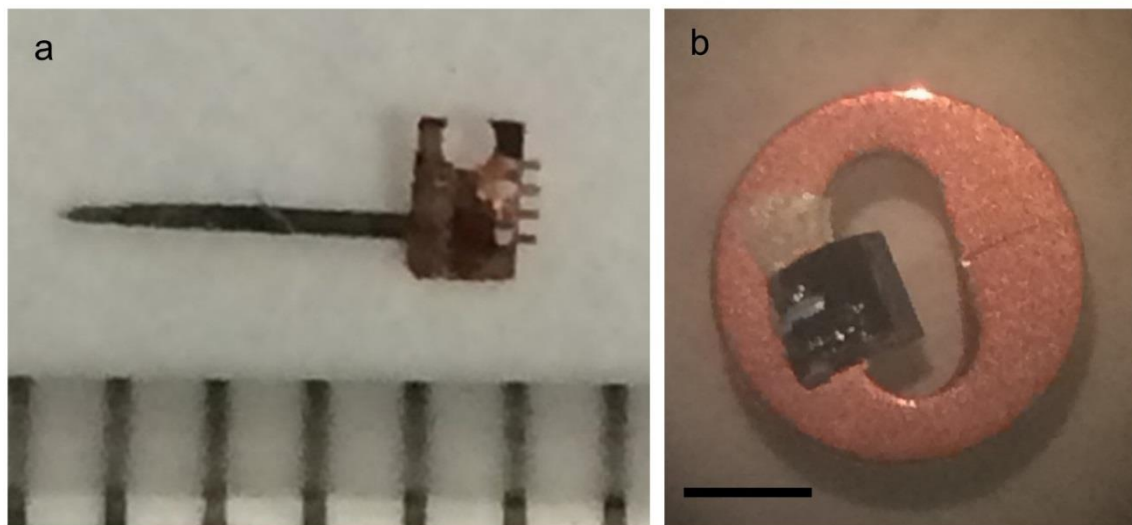


Figure 5.2 (a) The sample mounted in the in situ holder was a 1 mm sample attached to a ~4 mm W wire. Here is a sample next to a metric ruler, ruler lines are 1 mm. (b) The Si substrate can be broken from the W-tip and mounted on a Cu washer for later EDS analysis. Scale bar is 1 mm.

sample can move three dimensionally in the holder in the TEM. The sample movement is driven by a piezomotor with resolutions of 0.2 \AA in XY and 0.025 \AA in Z. The sliding experiments took place at no load with no cantilever deflection. The processes were recorded using a TV-rate video camera. The extracted frames were processed by deinterlacing and adjusting the levels for clarity using the program GIMP.

To expand on the sample preparation presented in the previous chapter, two alternative steps in sample analysis are shown in Figure 5.2. Figure 5.2 a shows one commonly used substrate, a copper FIB grid glued with M-bond to a tungsten wire, and the sample is next to a metric ruler. This length of substrate and tungsten wire was used because it allowed the sample to be close enough to the AFM tip in the sample holder mount without being too close to break the AFM tip during loading. In Figure 5.2 b, a Si fragment of interest was carefully removed from a tungsten wire and glued with silver paint to a copper TEM washer. This allowed for EDS analysis in a new

sample holder, as the Nanofactory AFM holder blocks the sample from the EDS detector. This setup provided a sufficient alternative for EDS exploration, although no relevant EDS data was gathered in this particular study.

Videos of the in situ sliding results are noted with the corresponding figures. The videos are available at <http://www.numis.northwestern.edu/Research/Staff/Emily/index.shtml> under “Thesis Videos.” The video captions are on the website and at the end of this chapter.

5.3 Results

With in situ experiments, a key step was developing a repeatable sample geometry that reliably worked in the AFM in situ holder. By fracturing the Si sample grids, we were able to make millimeter-long, electron-transparent edges of the Si substrate, such as in Figure 5.3. This simple

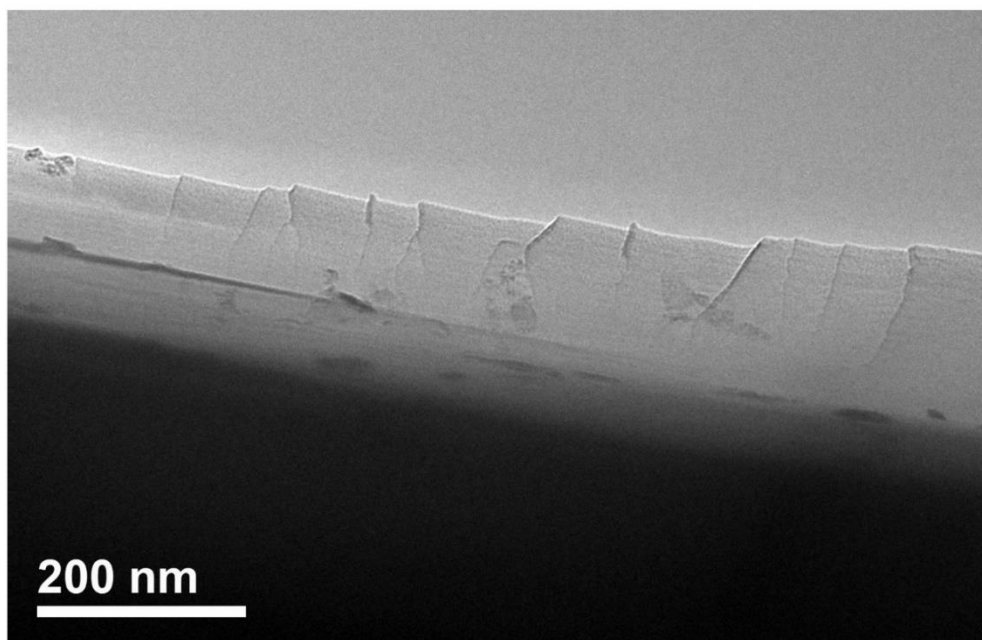


Figure 5.3 The fractured, electron-transparent edge of a Si substrate sample.

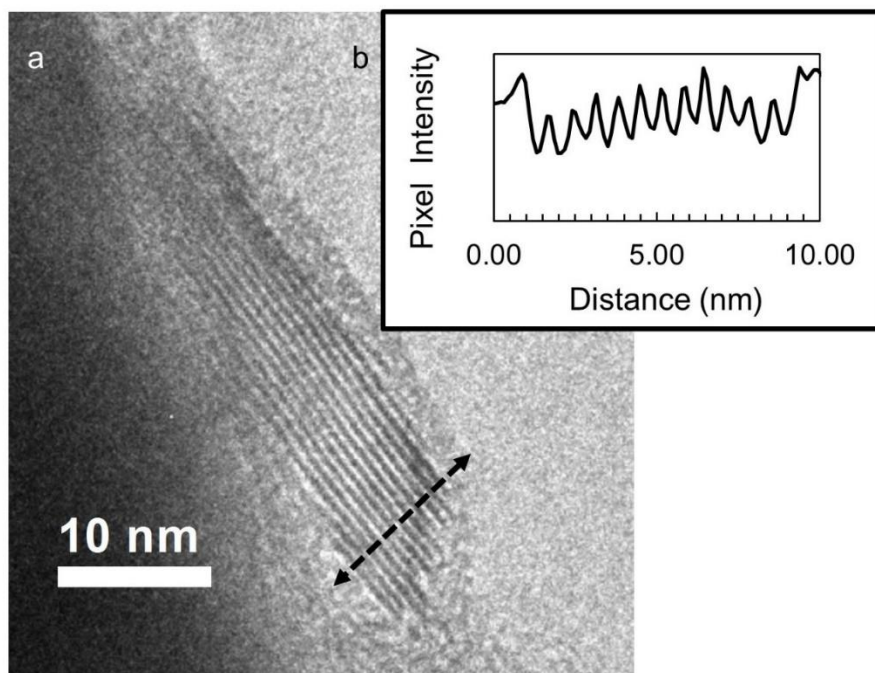


Figure 5.4 (a) Example of a MoS₂ flake and (b) intensity scan showing 12 clear layers of 0.64 nm thickness.

and reliable fabrication method meant that many samples could be made. Drop casting MoS₂ flakes on such a long edge lead to numerous spots where a MoS₂ flake or a stack of flakes were oriented parallel to the beam direction on the edge, such as the flake in Figure 5.4 a. The sheet spacing in Figure 5.4 b shows the clear layers of MoS₂, with the image intensity profile showing the signature 0.64 nm sheet spacing. Most flakes were between 30-150 nm in length and 5-20 sheets thick, with the depth of the sheets assumed to be on the order of the length.

Even though the flake orientation was not controlled and varied on the substrate, flakes on the edge of the Si or flakes with sheets oriented along the beam could be found. An example set of two flakes was analyzed for a side-by-side comparison of two geometries. Figure 5.5 a shows the original orientation of the two flake stacks. The left stack's sheets were primarily oriented parallel

to the substrate, while the right stack's sheets were oriented in multiple directions. The AFM tip was brought in contact with the surface and slid back and forth over both stacks. Images were recorded after three passes in Figure 5.5 b, eight passes in Figure 5.5 c, and 13 passes in Figure 5.5 d. After sliding, the side-by-side flakes showed that sliding effected the more parallel flakes differently than the misaligned flakes. The parallel stack had minimal change; some volume was lost, most likely due to some transfer layers removed during sliding. However, the mixed orientation stack developed into a small base of parallel sheets and some wear particles. The wear particles were primarily balls and became more spherical as sliding progressed. Parallel flakes were more stable during sliding and less of the flake volume wore away.

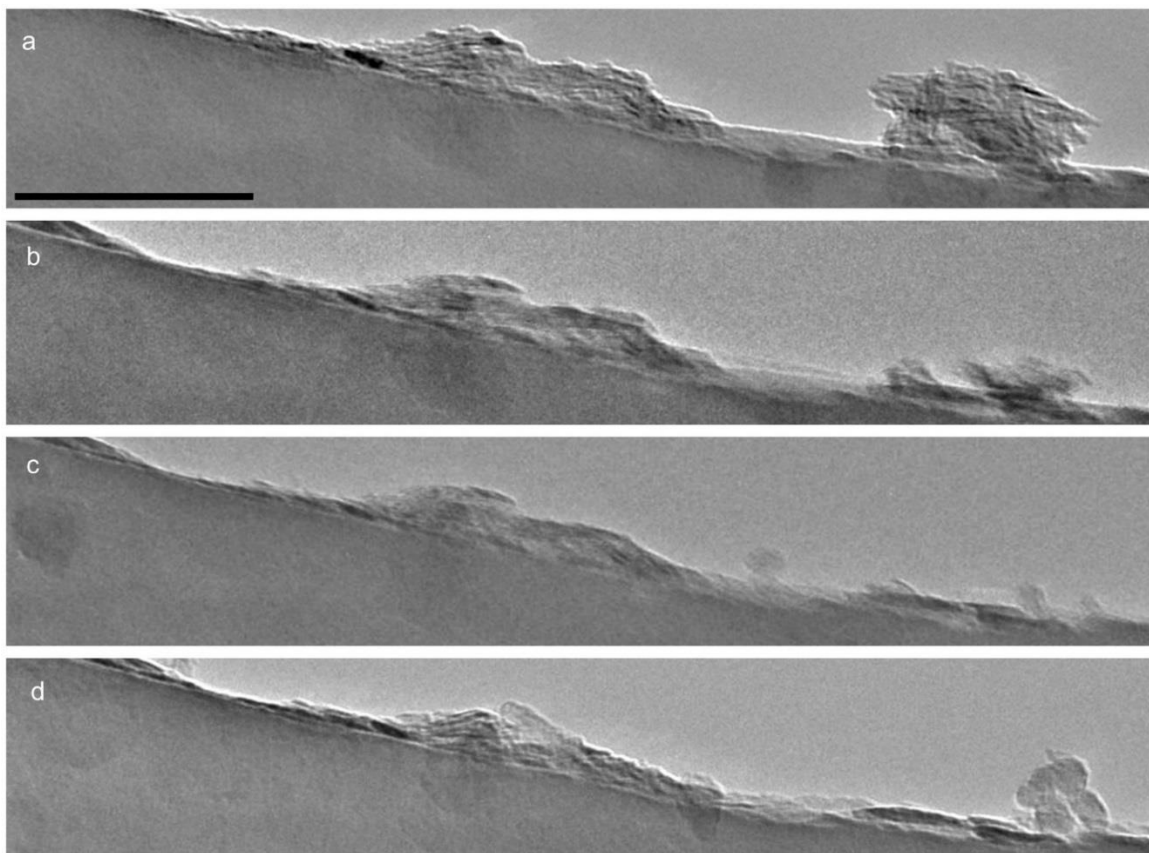


Figure 5.5 (a) Original MoS₂ flakes, and then after (b) 3 passes, (c) 8 passes, and (d) 13 passes. Scale bar is 100 nm.

Another example of MoS₂ flake behavior was demonstrated through gentle and coarse sliding. The piezo control produced gentle sliding (~1 nm/s), while the pulse motion produced coarse sliding (<100 nm/s). In this sliding example, the flake of interest was imaged before sliding, shown in Figure 5.6 a, and imaged after 10 passes of gentle sliding, shown in Figure 5.6 b. Then one coarse pass removed most of the flake, shown in Figure 5.6 c. During the gentle sliding, little volume of the flake was lost, and most of the change was due to removal of surface sheets, making the remaining flake more parallel to the sliding surface. After one coarse slide, the flake was mostly removed, except for the bottom few sheets of the MoS₂ flake. The bottom sheets were energetically stable enough to remain adhered to the substrate.

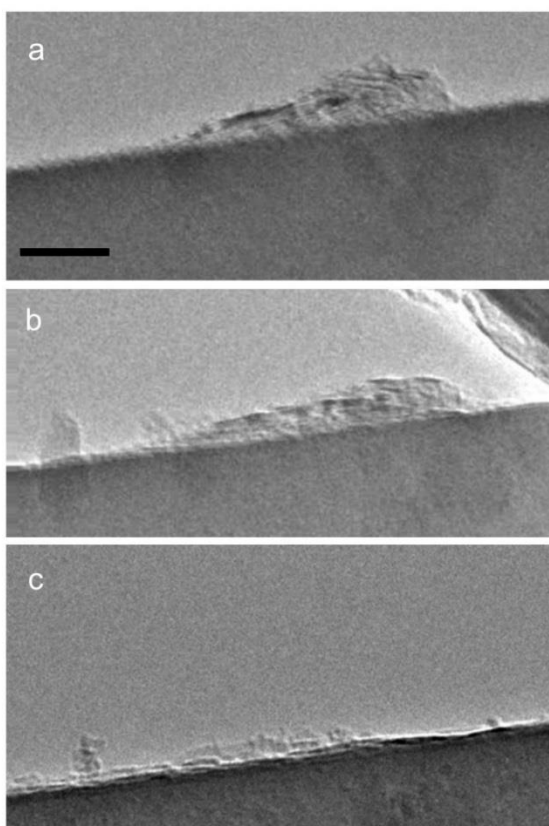


Figure 5.6 (a) Original MoS₂ flakes, (b) after 10 passes, and (c) after 1 coarse pass. Scale bar 50 nm.

During sliding, particles and transfer layers formed as part of the wear process. The stacks of flakes broke apart and then individual flakes broke apart. When the sheets were not parallel to the substrate surface, the wear sheets often became ball shaped. The balls then rolled as ball bearings without slipping. Figure 5.7 shows the extracted frames of a rolling ball and an image of the ball afterwards, extracted from Video 8, “Rolling.” The balls seemed to form in two main formations: a crumpled ball, Figure 5.7 d or a round flake, Figure 5.7 e. The round flake image in Figure 5.7 e is from Video 4 “Spot2_SIFT,” presented in Chapter 4 during the SIFT discussion. The two forms of balls showed different contrast in the bright field TEM. The crumpled ball had patchy contrast and rough edges. The minimal contrast of the round flake suggests it was very thin

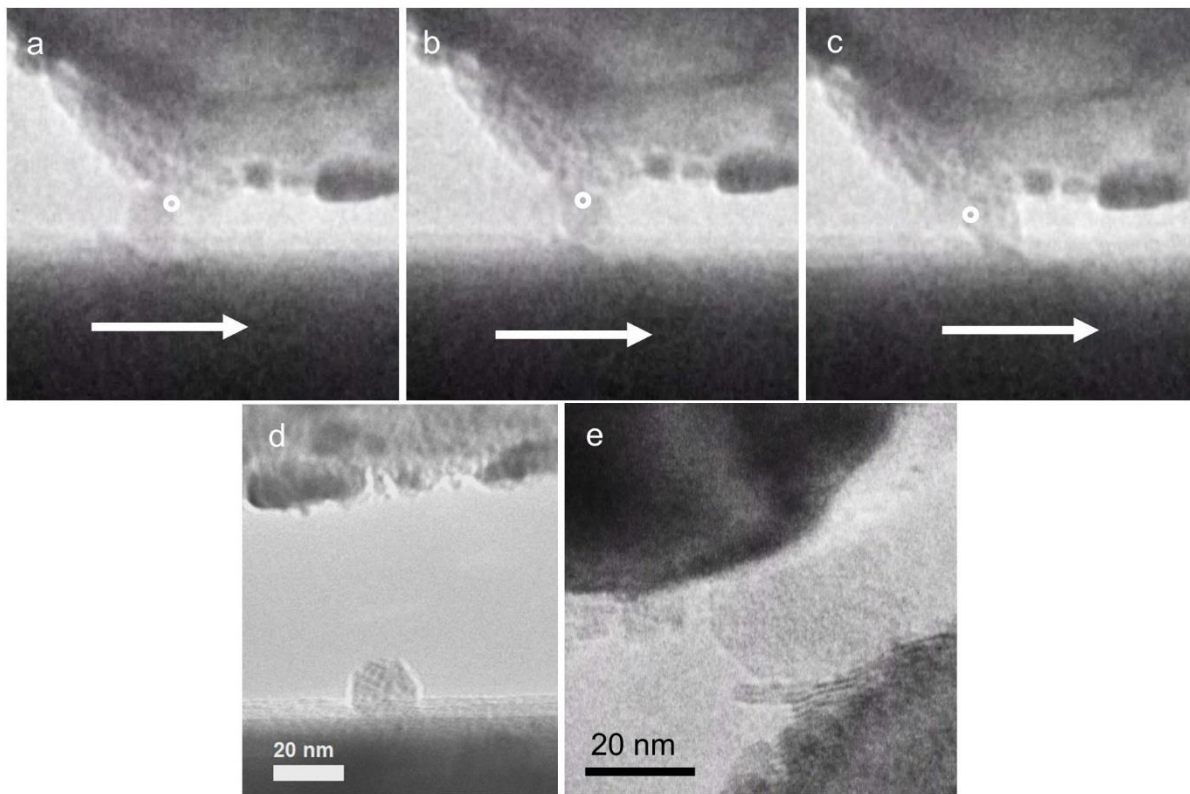


Figure 5.7 (a)-(c) Extracted frames of rolling of MoS₂ as the Si substrate moves to the right (Video 8). White circle showing the rolling contact. (d) The same crumpled ball after rolling with scale bar. (e) An alternative formation of a ball, a round flake (Video 4).

and uniform, which would be expected if a flake of 5-20 sheets thick was reoriented perpendicular to the beam. The round flake appeared to be like a disk rolling on its edge. Rolling was observed for ~5 cases for ball formation and ~2 cases for round flake formation. Rolling as ball bearings adds an additional sliding mechanism that can occur in lamellar lubricants.

In one case, a ball's wear evolution to a flake was captured. This MoS₂ was initially a flake, then rolled into a partially-crumpled ball, and then was reoriented into a transfer layer. The process is shown in Figure 5.8 and in Video 9, "BallPullApart." The flake was rolling on the surface, and then tore apart after contacting the asperity. The top adhered piece was reoriented during contact and became a tribolayer. This showed another mechanism of tribolayer formation and MoS₂ wear.

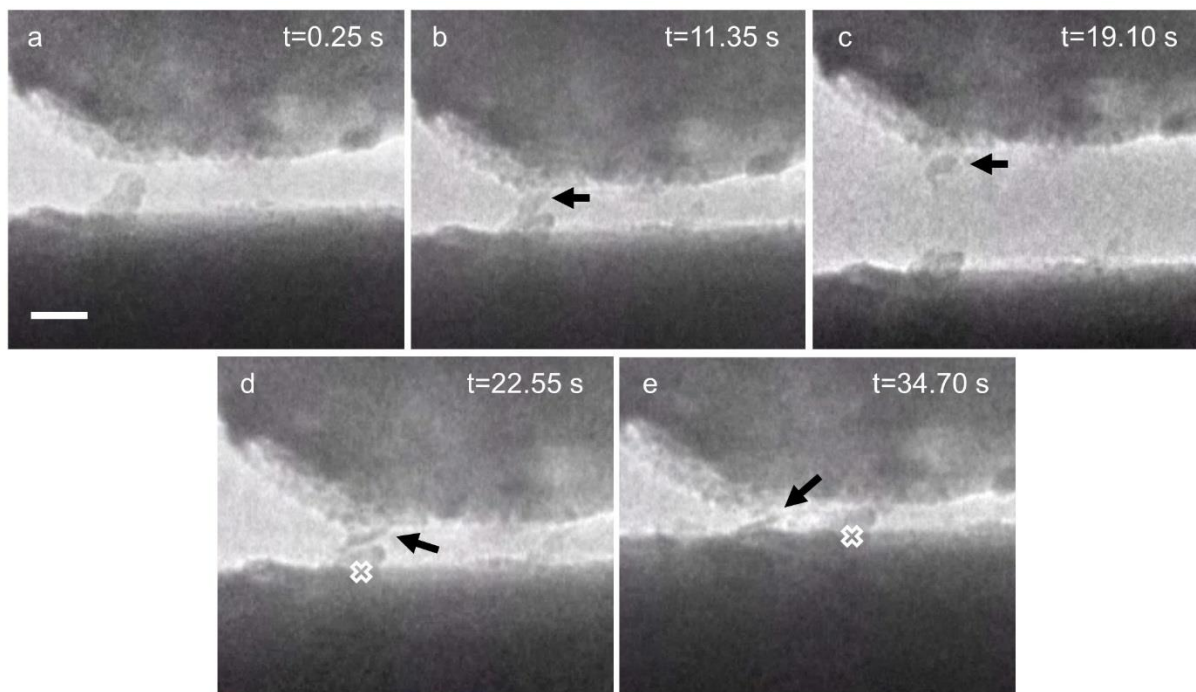


Figure 5.8 Extracted videos (Video 9) of (a) a ball of MoS₂. (b) When it comes in contact with the AFM tip, (c) the ball pulled apart, indicated with the black arrow. (d) When brought back in contact with the Si, the pulled apart flake reoriented parallel to the Si surface and then (e) as the Si substrate moved to the left, motion indicated by the white arrow, the flake became a transfer layer and slid with the AFM tip. Scale bar is 20 nm.

The flake breakdown and reorientation continued to evolve with additional contact and sliding. Many of the processes depended on orientation, adhesion, and sliding.

MoS₂ flake adhesion was measured more directly with contact and release experiments. Both the AFM tip and the Si substrate had an adhered flake of MoS₂ next to an exposed area. These surfaces allowed for the combination of MoS₂–MoS₂ contact and MoS₂–Si contact, as shown in Figure 5.9 a and b respectively. After bringing the substrate surface in contact with the AFM tip, the substrate was moved directly back until adhesion was broken. A video of this is Video 10, “ReleaseAndStickyRelease.” Figure 5.10 shows the difference in adhesion between the MoS₂–MoS₂ contact and the MoS₂–Si contact by showing the maximum deflection of the AFM tip during adhesion before breaking contact. The rest position of the AFM tip is Figure 5.10 a, the detached position for MoS₂–MoS₂ is Figure 5.10 b, and the detached position for MoS₂–Si is Figure 5.10 c.

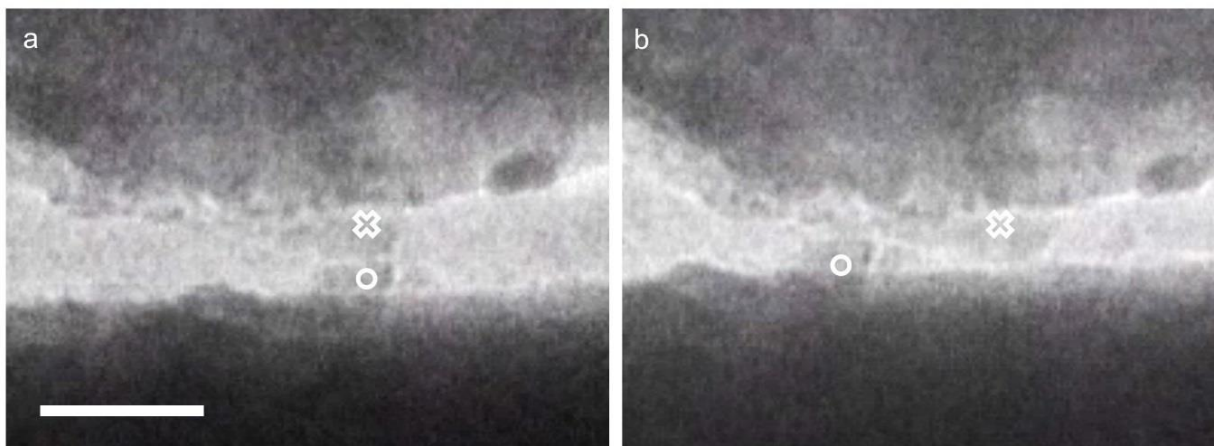


Figure 5.9 (a) MoS₂–MoS₂ flake that showed minimal adhesion and (b) MoS₂ flakes were offset and then in MoS₂–Si contact, which showed significant adhesion (Video 10).

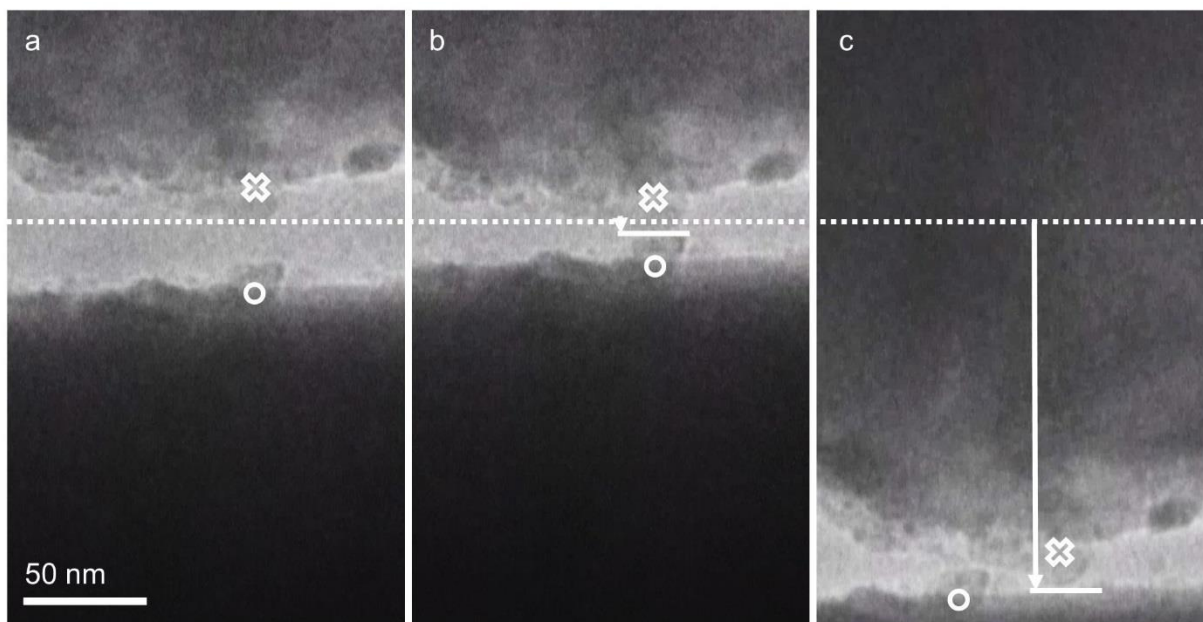


Figure 5.10 (a) Neutral position of the AFM tip, indicated by the dotted line. (b) MoS₂-MoS₂ contact displacement from adhesion the frame before the adhesion breaks, with the adhesion force per unit area ~ 22 MPa. (c) MoS₂ on Si contact displacement from adhesion the frame before the adhesion breaks, with the adhesion force per unit area ~ 270 MPa.

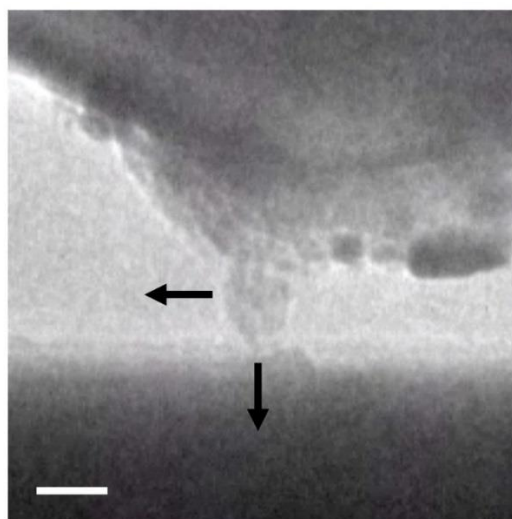


Figure 5.11 When the Si substrate was pulled down there was high adhesion. When the substrate was pulled left, then the MoS₂ ball rolled and there was minimal adhesion as it broke contact (Video 11). Scale bar is 20 nm.

For the MoS₂–MoS₂ contact, the tip was displaced by 5±1 nm from its rest position. Taking the value of the spring constant (5.6 N/m), the adhesion force was calculated to be 28±6 nN. Since the contact area was ~25 nm long and ~50 nm thick, the adhesion force per unit area was 22±4 MPa. For the MoS₂–Si adhesion, the displacement was 133 nm±13 nm, and the adhesion force was calculated to be 743±73 nN. The contact area was 55 nm long and 50 nm thick, thus the adhesion force per unit area was 270±27 MPa. The video was not at high enough magnification to observe the flake alignment or structure, yet we observed that MoS₂ significantly mitigated adhesion during contact. When the flakes were in contact with each other, there was almost no measurable adhesion, yet the MoS₂–Si contact had adhesion. This was seen even when going back and forth between the two contact modes. The flakes were stably adhered to the Si surfaces, and remained as whole nanoflakes during the pull adhesion testing. The weak interface of the MoS₂–MoS₂ contact was the surface for ideal sliding and low adhesion.

Besides mitigating friction as a ball bearing, the MoS₂ balls reduced adhesion during rolling as well. Figure 5.11 shows an extracted frame from Video 11, “StickyAndRollingRelease,” where the contact and release experiments were performed with this ball. When the substrate was pulled straight down, there was high adhesion, similar to the MoS₂–Si contact, which makes sense because this was also a MoS₂–Si contact. If the substrate was moved to the left, the ball began to roll until the surfaces separated. Then when the AFM tip and MoS₂ ball released, there was almost no adhesion. Even though it was a MoS₂–Si contact, the rolling motion minimized the adhesion.

Adhesion between the MoS₂ nanoflakes and the AFM tip was further demonstrated by the edges of the MoS₂ sheets. After sliding, edges of the MoS₂ sheets were exposed, seen in Figure 5.12 a, and could bend to contact the AFM tip, seen in Figure 5.12 b. These images were extracted

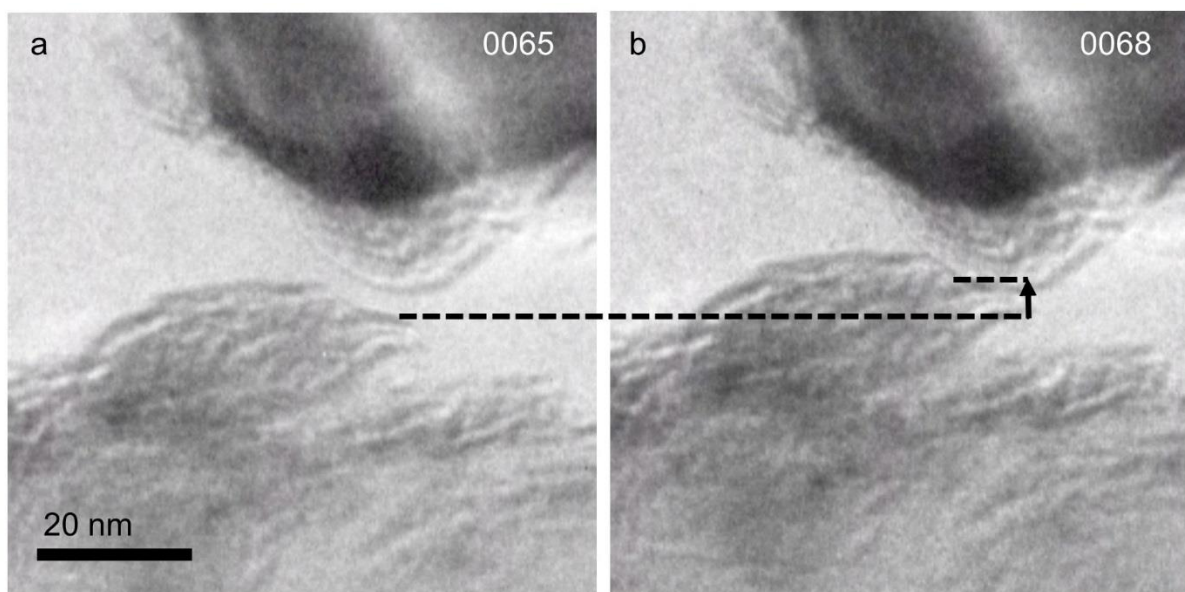


Figure 5.12 (a) MoS₂ flake before adhesion and (b) after the edges jumped to adhesion with the AFM tip, with the arrow being ~3.4 nm. The number indicates the frame number, with each frame being 0.05 s (Video 12).

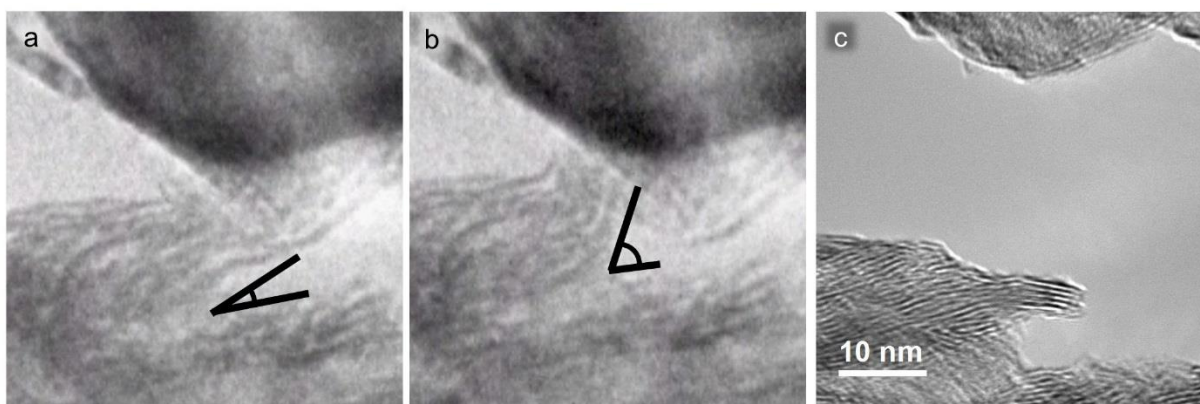


Figure 5.13 (a) The edges of the MoS₂ sheets in contact with the Si AFM tip. The sheets bent about 25° in contact, and (b) as the tip moved up the edges stayed in contact due to adhesion, bending up to 65° (Video 13). (c) Image after the sliding, showing five layers at the end of the flake.

from Video 12, “SnapContact.” This was an example of known snap-to-contact adhesion, yet this case differed because the sheets, not the AFM cantilever, bent to contact. The approximately five sheets jumped about 3.4 nm in 0.15 s, calculated from the video frame rate. Furthermore, Figure 5.13 b shows the extremes of the sheets bending along with a post-sliding high resolution image of the five sheets in Figure 5.13 c. The flakes bent easily, up to 40° before breaking contact with the AFM tip, shown in Video 13, “BrushEdges.”. This strong adhesion could be due to the sheets’ dangling bonds having higher adhesion than the flat top sheet, although this could not be calculated with this video information. The contact between the MoS₂ sheets, the substrate, and single asperities had many possible connections and progressions during triboactivity.

5.4 Discussion

Here we observed the buried interface of MoS₂ nanoflakes between a Si surface and a Si AFM tip using in situ electron microscopy. Through contact with the AFM tip asperity, stacks of MoS₂ flakes wore in a variety of modes. The various mechanisms were functions of sheet orientation, adhesion, sliding speed, and number of passes. The behaviors observed included MoS₂ sheets tearing apart, rolling into balls, rolling as ball bearings, reorienting during sliding, and mitigating adhesion. The flake morphology continuously changed throughout sliding.

Previously in the SIFT layer work, we were able to isolate one factor of lamellar lubrication behavior. Further observations of lubricant mechanisms, however, become increasingly complex. This work has shown that there are many processes that occur and that they are interdependent. Many of these mechanisms can be considered through the stable-energy-state framework. During sliding, the sheets continue to change until a stable morphology state is reached. From Newton’s

third law, the force that drives changes is the sum of the external load and the friction. If we are just sliding, this leads to the hypothesis that the sheets will continue to change until they achieve a low-friction configuration.

We have observed the evolution that can lead to the approximate morphology of this proposed low-friction state. The small, parallel nanoflakes that we observed fit the model as they stayed stable during sliding, such as the examples in Figure 5.5 and Figure 5.6. The misaligned, non-parallel particles seen in Figure 5.5 became wear particles, left the sliding surface, or started to reorient. The change occurred for the particles that were not in a stable state. In Figure 5.6 c, the sliding condition changed and more of the flake was removed during the coarse slide because the sliding conditions changed what was an optimum, or stable, flake. In Figure 5.8, we continue to see this framework supported with the torn-apart flake that reoriented during sliding until it became parallel. The flake in this example was not optimized so it fractured to create smaller particles and created a MoS_2 - MoS_2 sliding interface. When the transfer layer was created, no more fractures occurred. The stability analysis for the rolling balls that we observed is more complex than flakes because it was hard to determine changes to the ball during basic in situ sliding. The wear balls <20 nm seemed stable during our experiments as they did not noticeably change after 10-20 passes. The density of how tightly the ball is crumpled could play a role as during high shear sliding, while a less dense ball may begin to break-up. We would predict that the balls would break apart and start to have the sheets reorient and crystallize in the sliding direction.

With flakes undergoing rolling, transfer to asperity adhesion, and fracture, we argue that the flakes would continue to wear and evolve until as close as possible to the low-friction ideal lubrication coverage. Further experiments would be needed to show the endgame of the various

flake morphology to complete characterize the stability framework. Fleishauer et al. put forth these ideas of stability and size of nanoflakes and intercrystalline sliding in the 1980s, but could only do bulk measurements, primarily with X-rays [178]. Here we were able to probe specific flakes to observe behavior, which complements nicely with the previous studies and their findings.

Throughout these processes, adhesion played a major role. The fracture of the flake between the substrate and the tip in Figure 5.8 could not have happened unless the adhesion to the tip was greater than between the sheets within the flake. For this example, the resolution was not high enough to observe single sheet behavior. It does show that once a MoS₂ flake crumples into a ball, the lubricating properties are not gone. Sliding can continue to reorient sheets, especially if fresh surfaces of the substrate are exposed, which creates new adhesive surfaces for interaction. Furthermore, adhesion is important to consider because MoS₂ sheets must remain adhered to the surface in order to be lubricating. The interplay between adhesion and sliding shows how dynamic the nanoscale triboactive interface can be.

Through our observations, we began to show the pathways for proposed mechanisms through direct imaging during sliding. In this work, however, a major issue in analysis was that the video magnification was not high enough to see sheet orientation. This lack of detail limited the conclusions that could be made. In other high resolution videos, the sheet orientation, adhesion to other sheets, and adhesion to the substrate was clearly visible. Observing these details would be needed to fully characterize the ball crumpling, rolling, and reorienting into a tribolayer. Further variables such ball formation, force and angle of asperity contact, and orientation of the MoS₂ sheets also need to be investigated to fully understand mechanisms of stable MoS₂ film.

5.5 Conclusions

- ❖ The variations of MoS₂ behavior have been studied on the macroscale, we investigated further at the nanoscale.
- ❖ Using in situ TEM, fracture, rolling, reorientation, and adhesion mitigation were observed at the triboactive interface. The lamellar lubricant morphology continuously changed between different shapes and lubrication modes until stable films were created. Dynamic sliding conditions that eventually create a stable, low-friction sliding interface is not specific to MoS₂; we argue it is a general mechanism.

5.6 Video Captions

Video 4: 3-10_spot2_sift

Video of Figure 4.4 and Figure 4.5 of a rolling flake. Also shown in Figure 5.7.

Video 8: 11-2_9-2Rolling

Video of Figure 5.7 showing a ball of MoS₂ rolling.

Video 9: 11-2_10-1BallPullApart

Video of Figure 5.8. A ball was broken apart and then reoriented during sliding.

Video 10: 11-2_10-2Releaseandstickyrelease

Video of Figure 5.9. The two surfaces were brought into contact and the MoS₂–MoS₂ contact showed minimal adhesion, while the MoS₂–Si contact showed significant adhesion.

Video 11: 11-2_9-4_StickyAndRollingRelease

Video of Figure 5.11. A rolling ball of MoS₂ was pulled straight down with high adhesion. When the same ball was rolled sideways out of contact, there was minimal adhesion as it broke contact.

Video 12: 2-23_Spot2_SnapContact

Video of Figure 5.12. The edges of a stack of MoS₂ jumped to contact with the AFM tip.

Video 13: 2-23_Spot2_BrushEdges

Video of Figure 5.13. The edges of stack of MoS₂ contacted the AFM tip and bent up to 65° before the contact broke.

6 Graphitic Carbon Films Across Systems

This chapter is a review that developed from many conversations within the tribology community over the last few years. Many of the conversations were sparked by a previous publication from our group, Liao et al.'s "Graphitic tribological layers in metal-on-metal hip replacements," in *Science* in 2011 [16]. In that work, the carbonaceous film that forms on metal-on-metal hip replacements in the body was characterized at the nanoscale. The film was determined to be almost completely carbon (~95% carbon, ~5% oxygen) and the carbon was measured to be primarily graphitic carbon. The graphitic material was proposed to act as a solid lubricant in the hip joint. This finding was surprising to metal-on-metal hip researchers, and also to the tribology community. Inspired by this result, we began to look at other systems that incorporated carbonaceous lubricants in combination with tribologically active metal surfaces. Spurred by colleague discussions, we found that the development of graphitic carbon films spanned across disciplines, where a synthesizing review would be beneficial. We also found that others moved from initially being skeptical to accepting that this type of carbonaceous material was present in many other systems.

When metal surfaces come into contact, lubricants are used to overcome friction. Various forms of hydrocarbons play a central role in lubrication, through both liquid lubricants and surface coatings. Solid lubricants like graphite and complex surface coatings such as diamond like carbon have led to great advancements in friction mitigation. In addition to these designed carbon films, unintentional carbon films can also spontaneously form during metal-metal sliding. Here, we analyze various systems that produce carbon films, focusing on systems with cyclical metal sliding, hydrocarbon lubricants, and catalytic activity. The systems we analyze include friction

polymers, diamond like carbon coatings, varnish from industrial machines, metal-on-metal hip implants, microelectromechanical systems, and catalysis coke. These films, analyzed at the nanoscale, are primarily graphitic carbon with local regions of sp^2 bonding. The graphitic carbon can act as a lubricant in some systems and not in others. Through comparing these various fields, we seek to better understand the formation, evolution, and friction properties of carbon films. Through design and control of carbon films formation, we can control triboactivity to improve system performance.

Material in this chapter is reproduced from the article “Graphitic Carbon Films” by Emily E. Hoffman and Laurence D. Marks; *Tribology Letters*, 2016 [188]. Several of the figures are reproduced from the work of others, with permission, and sources are cited throughout.

6.1 Introduction

In research, forming deep connections to make significant progress is difficult. As science becomes more complex, fields specialize and concentrations deepen. Often large advancements require connections across fields: collaboration is necessary for innovative discoveries. Here we present a chapter that attempts to connect various fields that study graphitic films. We show commonalities between thin carbon films in seemingly diverse areas to demonstrate how the similarities between these fields of research can be utilized for practical advancements in lubrication.

When two surfaces come into sliding contact, the tribology is key to performance. The primary goal of tribology research is mitigating friction and finding beneficial lubrication methods. Understanding friction drives design of systems across size scales, from industrial motors to

precise micron-scale gears, seen in Figure 6.1 [189,190]. Surface coatings, liquid lubricants, and solid lubricants are all relevant to tribology.

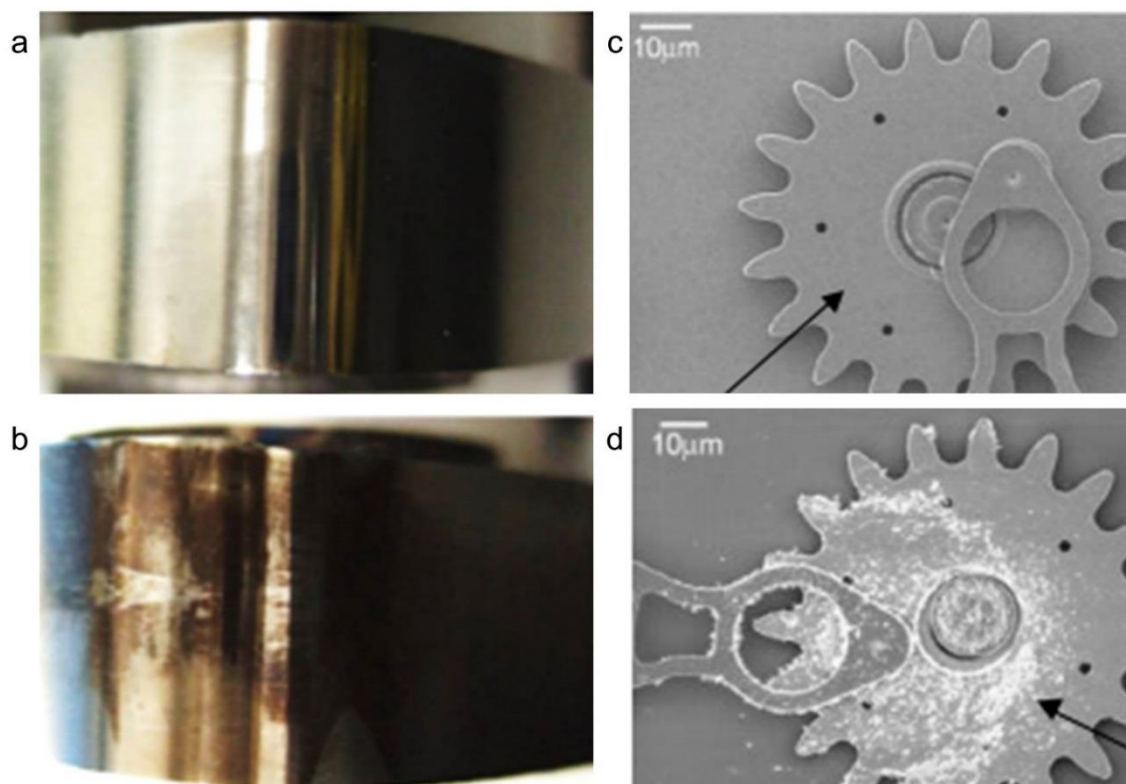


Figure 6.1 Wear tests using PAG oil formulations, forming (a) minimal wear and (b) varnish film formation [189]. At a different size scale, MEMS gears (c) before testing and (d) after failure caused by adhesion [190].

In lubrication methods, hydrocarbons play a central role. Hydrocarbons are used in standard industrial lubricating oils, are deposited as lubricious carbon films, and can be unintentionally incorporated into systems from the air. Carbon that unintentionally enters the system can spontaneously form deposits that become a film, similar to designed deposited films. Carbon in the system or from the environment reacts from heat, catalysis, friction, and cycling to continuously evolve to a final carbon film. This film is usually thin, slick, and described as a high molecular weight polymer. It is often graphitic, i.e. it contains some fraction of sp^2 carbon-carbon

double bonds and not just single sp^3 bonds. In general, these are local sp^2 bonds, or perhaps small nanoscale regions of continuous aromatic bonding, not a full continuous network of graphite sheets. This film is present in different systems by different names, yet on the nanoscale, it is the same thin layer of partially graphitic carbon. This concept is illustrated in Figure 6.2.

To explain the connections between these fields, this chapter will introduce systems of interest, explain mechanisms of film formation, and conclude with a discussion of opportunities. The systems included for analysis are major fields of tribology and carbon film research, where there is both recent and decades of older data to consider. The fields included are friction polymers, diamond like carbon (DLC) coatings, varnish from industrial lubricants, the tribolayer from metal-on-metal (MoM) hip replacements, microelectromechanical systems (MEMS), and catalysis coke. In these systems, all the films, except for coke, are considered tribolayers, layers that form during frictional contact. Tribolayers or tribofilms form due to triboactivity or tribochemical reactions. In catalysis there is no friction, so this system serves as a comparison as there are chemical reactions without triboactivity. Because coke is an included system, we refer to the graphitic carbon products as carbon *films* as opposed to carbon *tribolayers* when addressing all systems collectively.

The motivation for a combined study comes from the opportunity for mutually beneficial research. Hsu and Gates [191] discussed that our understanding of the nature of tribochemistry is limited, partly because it is largely empirical. The need for future understanding is crucial because as new materials emerge, use is often blocked by lack of knowledge of how the materials can be effectively lubricated. Ineffective lubrication can result in premature failure or product recall. In the presented systems, the carbon films affect performance differently, some are protective and some damaging. Even though they are all partially graphitic carbon films, the questions at hand

are: what causes the differences and can the beneficial systems be exploited for better design across systems?

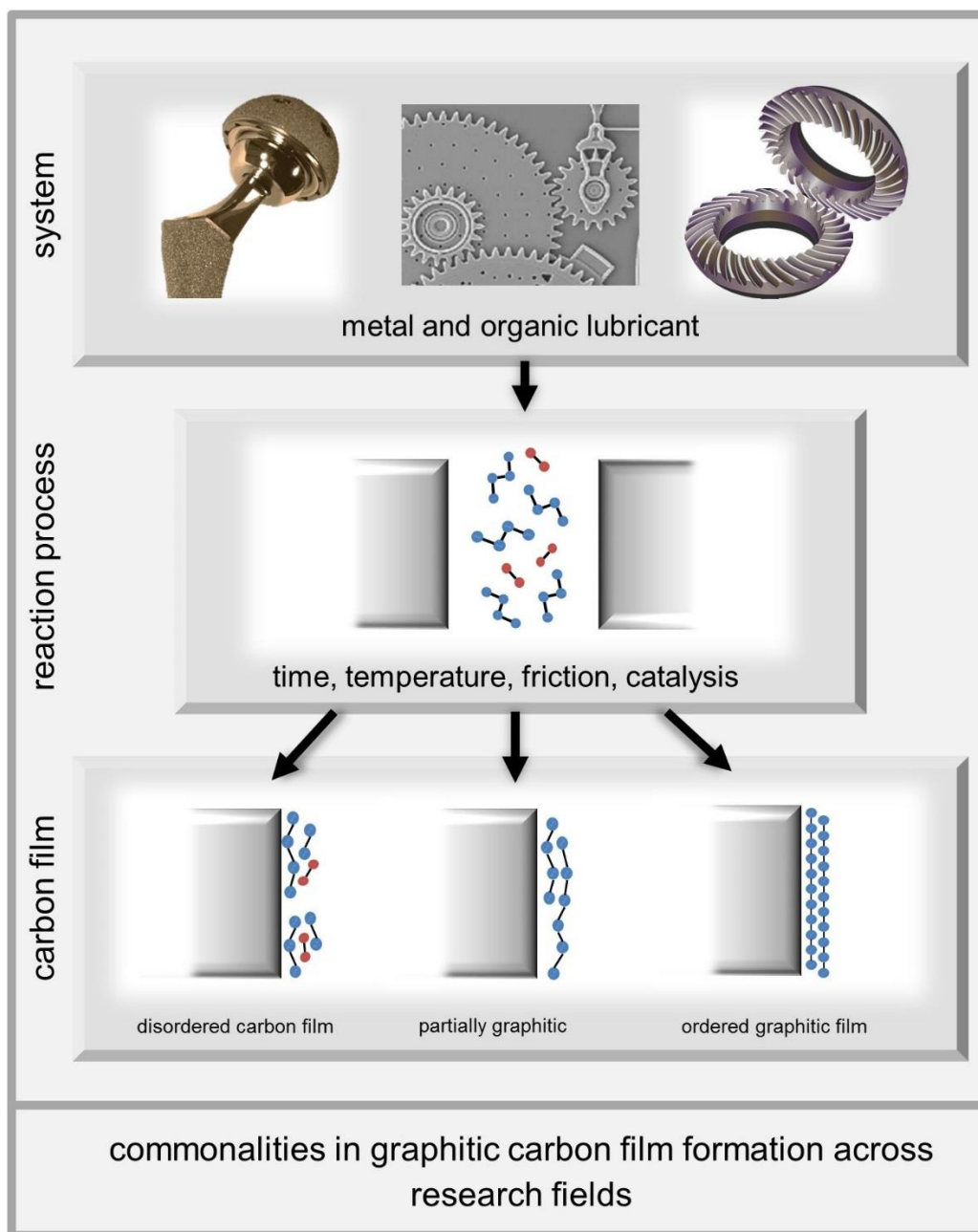


Figure 6.2 Metal-on-metal hip implants, MEMs gears, and industrial machines are all lubricated with hydrocarbons. Through friction and wear at the metal interface, the organic material reacts to form similar carbon films.

This chapter is organized into three sections: systems, mechanisms of formation, and discussion. The first section provides a general overview of the six primary systems: friction polymers, DLC coatings, varnish, hip implant tribolayers, MEMS, and coke. These represent general fields of research, each with a wide breadth of tribolayer research; we provide a brief summary and context for each. Finally, we give three specific examples of carbon tribolayers that are relevant for discussion. These systems and examples are not an exhaustive collection; we predict that more parallel systems could be compared from even broader fields.

The second section is on the mechanisms of formation of carbon films. This section describes processes and reactions that occur to convert organic precursors into graphitic carbon films. The mechanisms covered include pressure, temperature, and friction; deposition and absorption; polymerization and organometallics; catalytic activity; graphitization; and particle interaction. The mechanisms are often common across systems, and so they are grouped as mechanisms and not as systems.

The third and final section is the discussion section. We summarize the key similarities between the systems and mechanisms, highlighting the main trends. To link the different systems, we present a general thermodynamic argument for carbon developing into graphitic bonding. Lastly, the future opportunities between these fields are emphasized. The possible connections in research methods and analysis techniques show promise to significantly advance each field.

6.2 Systems

This section presents an introduction to the six primary systems: friction polymers, DLC coatings, varnish, hip implant tribolayers, MEMS, and coke. All of these films are primarily carbon

and have a significant portion of graphitic bonding. The systems are all triboactive, except for coke, which is catalytically and thermally active.

6.2.1 Friction Polymers

The name “friction polymer” is the most widely used term to describe carbonaceous deposits on triboactive surfaces. Narrower fields focus on specific tribofilms and give them more particular names, which we will explore in later sections. Friction polymer is also one of the oldest terms, with common use in research as far back as the 1950s [192]. Friction polymer systems tend to be metal-on-metal, such as electrical relay switches, gears, engines, and other machines with rolling, sliding, or rubbing contacts. Friction polymers include tribofilms that are classified as both helpful and harmful to performance, depending on the study. What makes a beneficial friction polymer is not always well understood.

In friction polymers, there are common descriptors that appear across studies. The appearance of a friction polymer is brown and slick, usually with a reddish hue. The friction polymer film has a buildup that can be wiped away and a thin, stubbornly adhered layer beneath, seen in Figure 6.3 a [193]. The polymer sometimes improves friction, yet the beneficial properties can change through small alterations of temperature, pressure, number of cycles, or carbon concentration [192,194]. The substrates that create friction polymers are usually oxide-forming metals, such as palladium, chromium, molybdenum, or iron, although usually just one surface needs to be metal [192,195-197]. The film’s carbon source can be standard lubricating oils or carbonaceous vapors, which replicate situations where the carbon source is from the atmosphere [198,199]. Often friction polymer work calls the carbon deposits amorphous, yet they also include descriptions that point to

signs of graphitic carbon. Many studies note evidence of reduced wear and Raman spectra showing graphitic bonding, such as in Figure 6.4 a [200,201]. To understand the tribochemical reactions that can lead to partially graphitic carbon, studies have characterized the organometallic species, insoluble products, and the molecular weight [202-204]. The mechanisms of these reactions will be discussed in the next section to show the common mechanisms across the carbon film systems. The direction of friction polymer research was well summarized in the 2006 review article by Hsu et al. [191]. They described the need to further understand the formation of these lubricating films because much of the information is empirical and limited to the steel-hydrocarbon system. The metals-hydrocarbons research suggests that thermochemistry and organometallics dominate the chemical reactions, whereas in semiconductors, electrostatic charge and electron emission is important for tribochemistry [204,205]. Through understanding reactivity and mechanisms, the various factors that create friction polymers can be understood, such as how organometallic chemistry is central to forming high molecular weight reaction products that lead to effective lubrication [204]. By understanding how the bond breakage and bond formation occurs in various systems, friction polymers can be predicted and controlled for effective lubrication. To emphasize the pending questions of the field, Hsu et al. asks “What constitutes an effective film? Under what conditions (i.e., reactions and starting materials) will an effective film be formed? Under what conditions will the film not form? What are the effects of nascent surfaces? Can we determine the kinetic rates of film formation?” [191]. Further nanoscale characterization of friction polymers could indicate how graphitic bonding and solid lubrication affects performance. In the following section, we continue to discuss films similar to friction polymers, and by connecting these fields, provide answers to some of these questions.

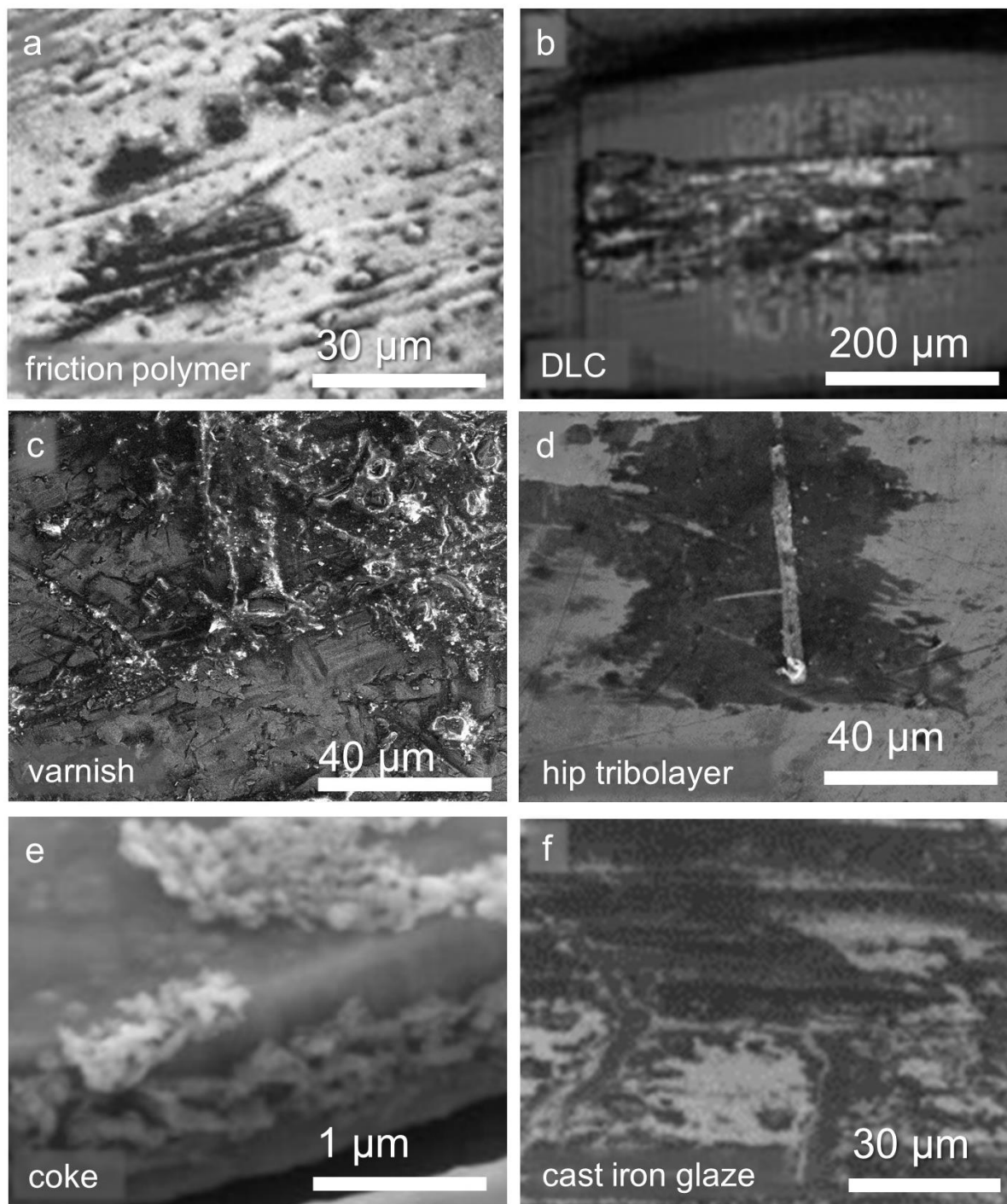


Figure 6.3 Similar micron-scale appearance of the carbon films after sliding contact. (a) Friction polymer [193], (b) DLC [206], (c) varnish tribolayer, (d) hip explant tribolayer [16], (e) MEMS wear film [190], and (f) cast iron glaze [207].

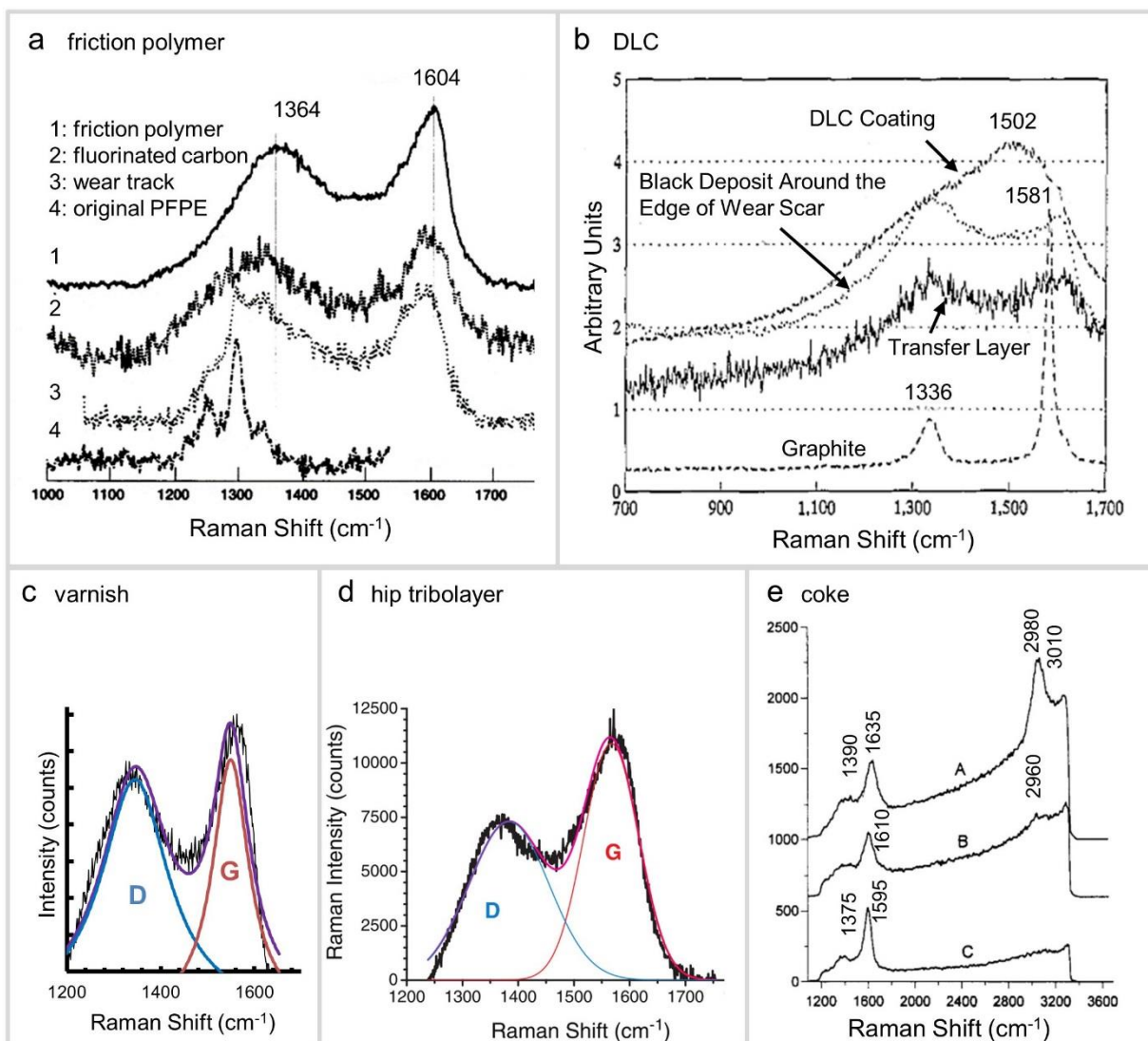


Figure 6.4 Raman spectra of (a) friction polymer [200], (b) DLC [208], (c) varnish, (d) hip explant tribolayer [16], and (e) catalyst [209]. All examples show a broad G band at $\sim 1550 \text{ cm}^{-1}$ and a D band at 1350 cm^{-1} indicating the presence of nanographitic carbon.

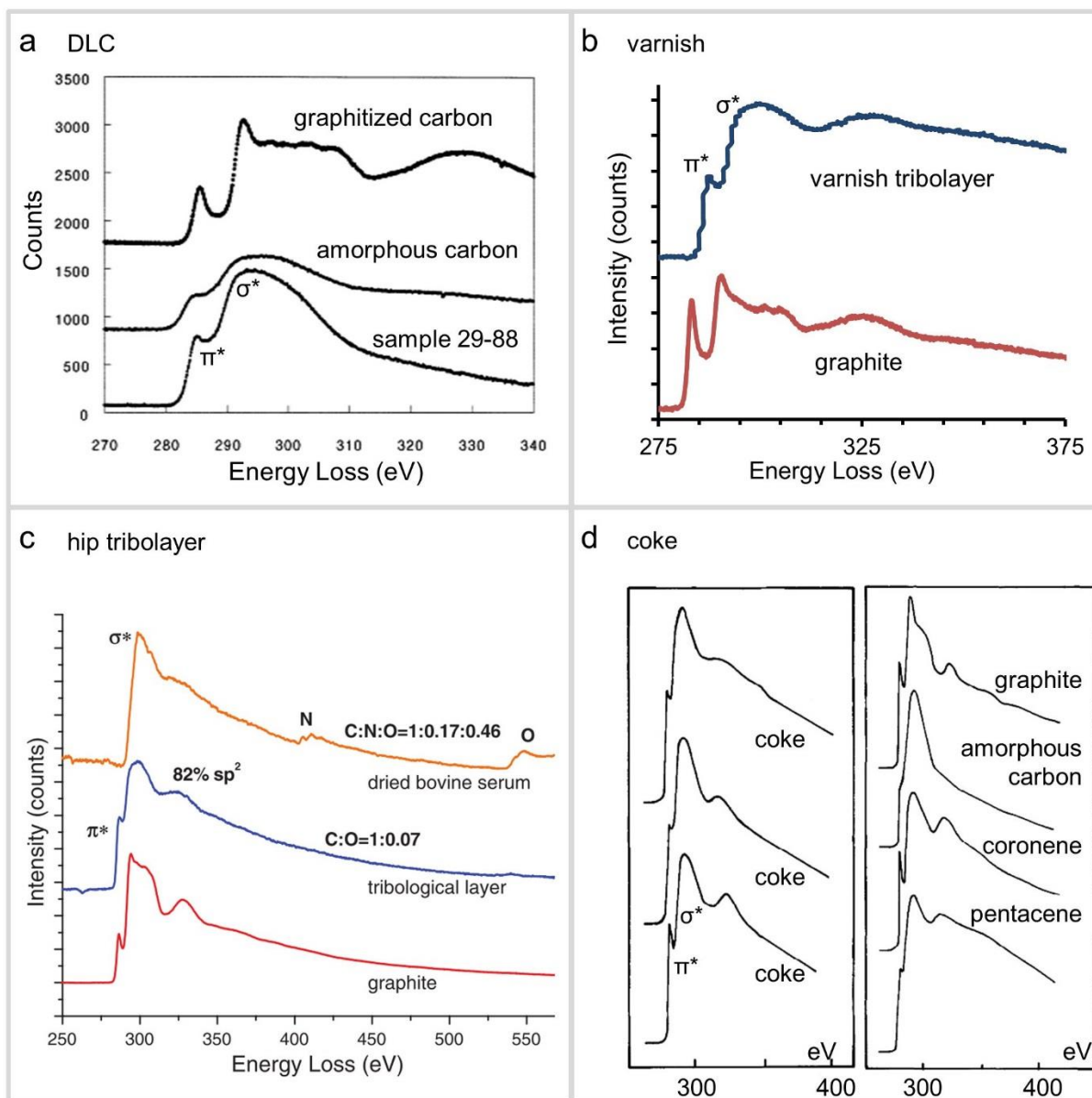


Figure 6.5 Electron energy loss spectroscopy of (a) DLC (sample 29-88 in figure) [210], (b) varnish, (c) hip explant tribolayer [16], and (d) catalyst substrate [211]. The ratio of the π^* peak to the σ^* peak indicate percent graphitic bonding [212,213]. All spectra include graphite for reference.

6.2.2 DLC Coatings

A commonly studied and well-known system of a carbon lubricant film is diamond like carbon (DLC). Carbon films have been studied as early as the 1950s [214], with comprehensive studies on DLC by Eisenberg and Chabot in the 1970s [215]. They showed that the carbon film had nearest neighbor distances similar to diamond, was highly insulating, and was transparent, among other electrical and structural similarities to diamond. As DLC films have been a popular research area, many functional varieties of the film and a breadth of applications have been explored. The breadth and depth of the DLC work can be used to help to explain the properties of other carbon films, across disciplines, designs, and phenomena.

DLC films are primarily made of carbon atoms that are extracted or derived from carbon-containing sources, such as solid carbon targets and liquid and gaseous forms of hydrocarbon and fullerenes. A DLC film after a sliding test is shown in Figure 6.3 b [206]. The modern multifunctional nanocomposite DLC films are now routinely produced by both chemical vapor depositions (CVD) and physical vapor deposition (PVD) [216]. The films can be designed to be extremely hard (~90 GPa) and resilient, while proving some of the lowest known friction coefficients [217]. A recent study showed an uncoated bearing failed after 32 million cycles, while a bearing with a one-sided DLC coating lasted 100 million cycles [218]. Applications including razor blades, microelectromechanical systems, engine parts, articulated hip joints, and machine tools have shown beneficial performance [219-222].

In a 2006 DLC review [217], Erdemir et al. discusses how the benefits of DLC come from the unique tribological properties, especially the transformation into a graphitic solid lubricant. It has been observed that sp^3 -bonded carbon atoms in DLC film experience transition into sp^2 -bonding

[217], as shown in the Raman spectra in Figure 6.4 b [208] and EELS spectra in Figure 6.5 a [210]. Pastewka et al. [223] performed MD simulation and suggested that sp^3 carbon bonds in diamond undergo a sp^3 -to- sp^2 order-disorder transition upon polishing. The frictional behavior can be controlled through the chemical, physical, and mechanical interaction, and physical roughness of the surface. The good adhesion of DLC films allows for high shear forces during sliding contact, while the friction values can range from 0.001-0.7 [218,224].

In the context of this chapter, DLC films are critical to include as DLC research demonstrates key aspects of the graphitization process [225,226]. We can use known phenomena of how DLC films are deposited, characterized, wear tested, and modified to extrapolate to other more uncontrolled or unknown systems. As discussed by Erdemir et al. [217], other forms of carbon including graphite, graphite fluoride, carbon-carbon composites, and glassy carbon are also valuable as low-friction, solid lubricant engineering materials [218,227-230].

6.2.3 Varnish in industrial machines

Varnish is found in industrial machinery. It is a carbon film that forms on metal surfaces when lubrication oil degrades. It is generally considered to be bad for applications, and much of varnish study is on how to remove it and prevent its formation. Information about varnish primarily comes from trade publications. These industrial articles are mostly written by companies that specialize in varnish filtration systems or varnish removal. Few industrial research studies focus on the composition of varnish once it has formed. We address varnish in two parts; the first part presents varnish as it is currently known in the field and the second part presents new nanoscale

characterization studies on varnish. This original varnish research allows for more fruitful discussion later in the mechanisms and opportunities sections.

6.2.3.1 Varnish Literature

Modern hydraulic machinery uses oil to reduce friction for improved operation, and when the lubrication fails, a carbon film called varnish forms in the machinery that drastically reduces performance. Varnish is different from the other films discussed because it is always considered damaging. Once lubricating oil begins to break down, the oil's contaminants form insoluble particles that deposit as a varnish film on moving parts [231-235]. The varnish film is an inhomogeneous, sticky brown residue that crusts to the surface of metal parts. It can have a cured, shiny appearance. Similar to other tribological films, two types of varnish are described. There are soft sludgy particles that stay in solution and can be removed with a filter; or on triboactive surfaces, there are thin, hard deposits that are difficult to remove, Figure 6.6 a and b respectively [236]. Varnish films play a role in friction and wear, but varnish can be extremely varied, so it has been typically characterized by appearance and not by chemistry [233].

Varnish, considered a "stubborn film," is a constant battle in machinery lubrication, with varnish causing 85% of hydraulic system failures [237]. Varnish causes sticking of moving mechanical parts, increase in component wear, and loss of heat transfer effectiveness [236,238,239]. Varnish is the product of the thermal/oxidative breakdown of hydrocarbons within oil which leads to a new chemistry of macromolecules [234-241]. This failure mode has become especially relevant as new developments in anti-oxidizing oils lead to oils that fail suddenly,

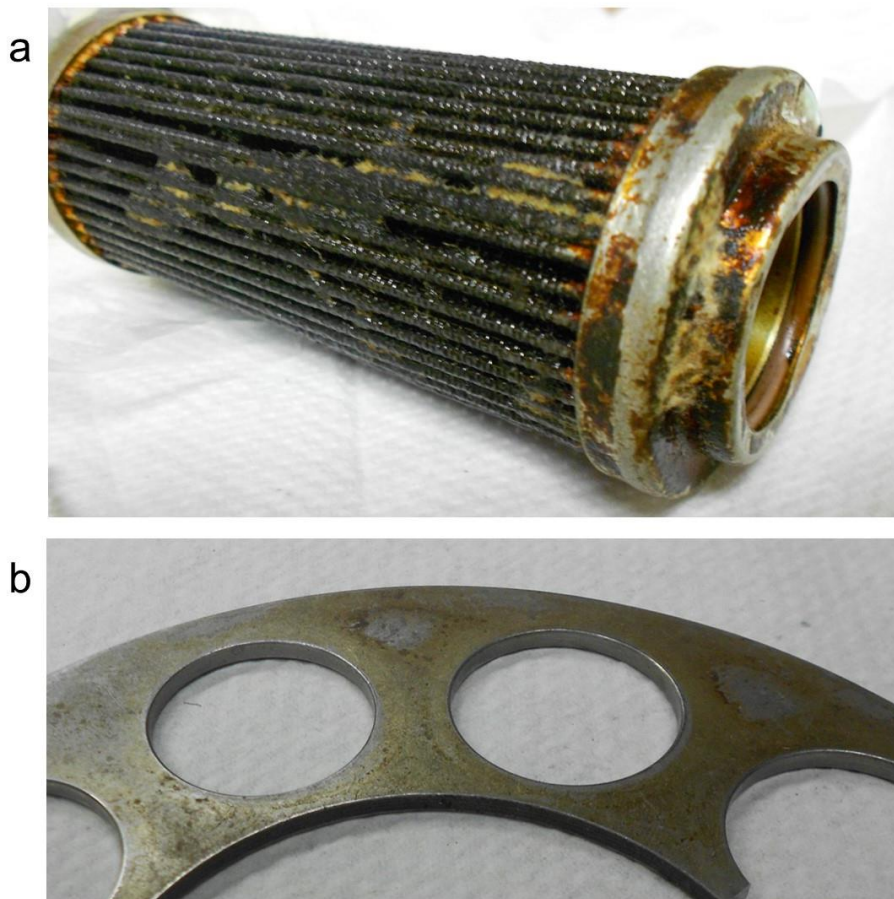


Figure 6.6 Two forms of varnish deposition: (a) show moving sludge varnish removed by a filter (part courtesy CC Jenson) and (b) deposited and cured shiny varnish film (part courtesy Dyna Power Parts).

without the slow and predictable degradation of previous oil formulas [233,236,242]. A majority of varnish literature comes from trade publications [234,237,238], where industrial leaders discuss the prevention and cleaning of varnish. Companies like Exxon-Mobil produce patents on varnish prevention systems [243,244]. There is also a large amount of information on how to measure the chemical composition of oil and how to strain sludge particle from oil [238]. Additionally, the size of the degraded particles has become an area of interest. Previously, the method was to simply look at the oil to see if it changed from a yellow to a reddish color; if it was reddish, it likely had varnish precursor particles. New techniques and ASTM standards [245] are recognizing sub-

micron macromolecules formation and the presence of nanoparticles [236]. The composition of varnish is rarely mentioned, as the early development for prevention and the cleaning methods are considered more apt.

6.2.3.2 *Original Varnish Research*

We performed original research to investigate the presence of graphitic carbon in varnish. This level of nanoscale characterization of the varnish film is not available in the literature.

A steel component with varnish buildup was acquired from Dynapower Parts. A SEM image of the thin area of varnish is shown in Figure 6.3 c. The part was a component of the Dynapower axial piston pump that run lubricants varying from 32-68 weight hydraulic oils to Dextron III. Samples examined came from one component from over 10 areas across the component; the results shown are representative. The exact pressures and temperatures of the varnished metal were not recorded during the machine's use, but varnish is known to be ubiquitous in a wide variety of machines under various operating conditions [238]. For the electron microscopy analysis described here, the varnish films were transferred by an Omniprobe in the FIB to a transmission electron microscopy (TEM) grid, with the method shown in Figure 6.7.

A thin and uniform area of varnish was measured with Raman spectroscopy using an Acton TriVista CRS Confocal Raman system with excitation radiation from an Ar-Kr 514.4 nm gas laser at ~10 mW. As shown in Figure 6.4 c, a broad G band was present at 1550 cm^{-1} , which showed the stretch vibration of sp^2 bonding, and a D band was present at 1350 cm^{-1} , which showed the breathing vibration in disordered sp^2 carbon [246]. In the Raman spectra, the G-line position and

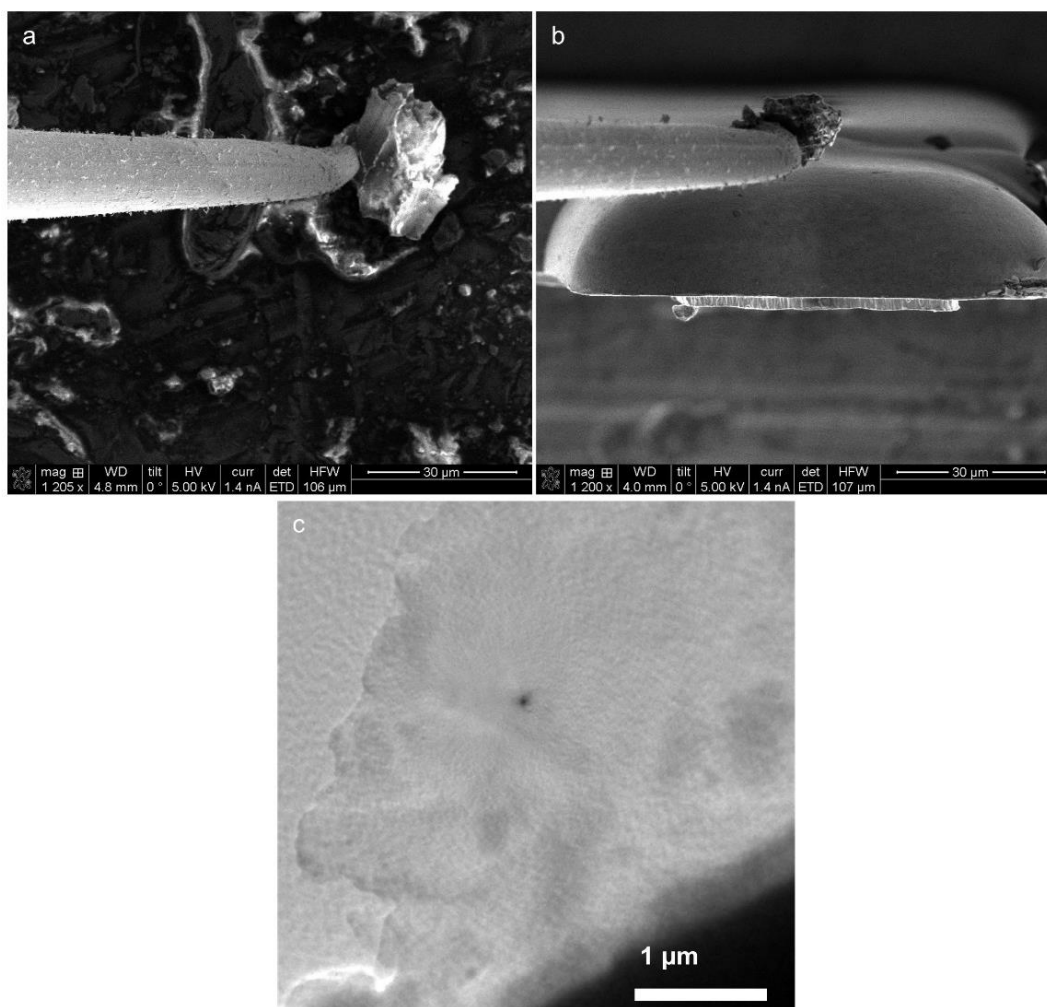


Figure 6.7 Inside the dual-beam SEM-FIB, the Omniprobe (a) came into contact with a varnish flake and (b) transferred the flake to a TEM grid. (c) In the TEM, a thin edge of the flake was found for EELS analysis.

broad D-line indicated that the film was composed of regions of nanographitic carbon [246]. The fraction of graphitic regions was determined from the intensity of the D peak relative to the intensity of G peak to be >80% based on the standard analytical methods for carbons, e.g. [247,248]. For the electron microscopy analysis, two different thin films were transferred to an Omniprobe transmission electron microscopy (TEM) grid. This method was developed from Liao et al., who also completed dosing studies to show the graphitization under the TEM beam is

negligible [16]. Approximately four different areas on the two varnish tribolayer TEM samples were analyzed using a Gatan Imaging Filtering in a JEOL 2100F at 200 kV. Electron Energy Loss Spectra (EELS) were calibrated using highly ordered pyrolytic graphite (HOPG). The varnish sample prepared was sufficiently thin, approximately 50 nm, to measure a carbon peak in EELS, as shown in Figure 6.5 b. The varnish π^* peak at 289 eV is characteristic of sp^2 bonding, while the σ^* at 299 eV is characteristic of amorphous sp^3 bonding, and the varnish peaks can be compared to the π^* peak found in the HOPG. The ratios of the varnish peaks show that the amount of graphitic carbon is approximately 80% [212,213]. To confirm the varnish analysis, Fourier transform infrared (FTIR) spectrum was also performed, shown in Figure 6.8. The measurement complements the Raman peaks, and confirms the presence of a mix of carbon-carbon and carbon-hydrogen bonding.

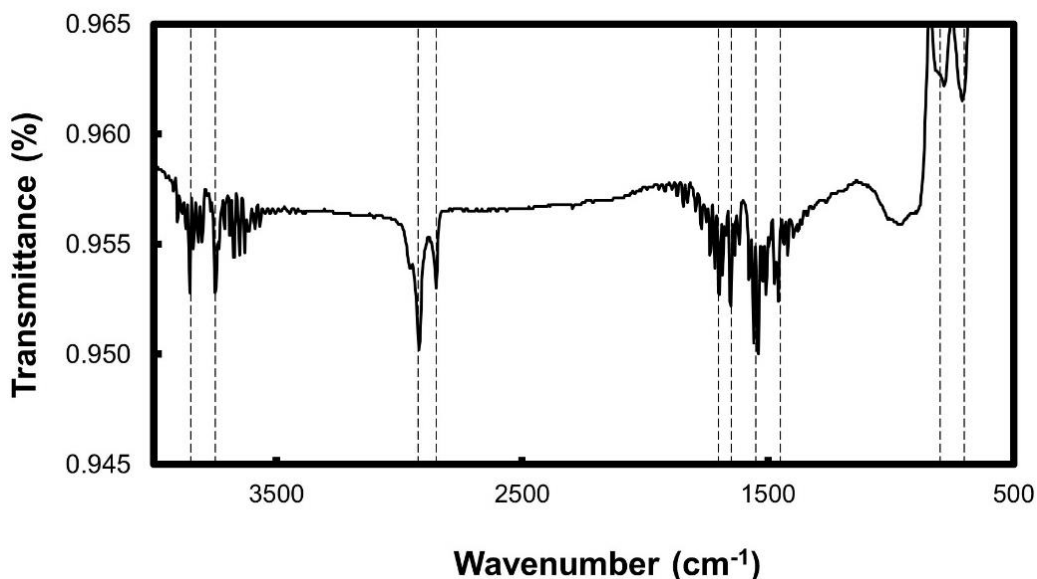


Figure 6.8 FTIR spectrum of the varnish coated metal surface after background subtraction and removal of CO₂ peak. Peaks indicate the presence of water (3850, 3750 cm⁻¹), sp^3 bonding (2925 cm⁻¹), and sp^2 bonding (2850, 1700, 1650, 1550, 1450, 800, 700 cm⁻¹).

Even though varnish has signatures of graphitic carbon, the varnish tribolayer formation is not within the design tolerances of the performance of hydraulic machine lubricating oils. The varnish causes damage to the machines and requires removal. Studying varnish, however, may allow for a controlled and beneficial film to form out of lubricating solutions. By understanding similar yet beneficial carbon films, such as DLC and MEMS coatings, improvements could be designed to reduce the negative impacts of varnish.

6.2.4 MoM Hips

Metal-on-metal (MoM) total hip replacements develop tribolayers after implantation in the human body, making this another informative system to study. Total hip replacements are made of two articulating components, the ball and cup, which can be made out of CoCrMo alloys, ultra-high molecular weight polyethylene (UHMWPE), or alumina. The MoM tribofilm has been primarily studied on the metal-on-metal interface after in vivo studies and has been shown to be graphitic [16].

Early studies of the hip tribolayers considered the deposits to be of peripheral importance as the layer was not intended to form during implantation in the first place [18,249-252]. The initial assumption was that that biological solution in a hip joint would adsorb protein molecules [253,254]. Through the adsorption and triboactivity, the protein molecules denature, which means the proteins lose their shape and begin to degrade. Through hip simulators, the parameters that control the formation of tribofilms were investigated, usually with bovine calf serum as the lubricant. The tribofilm was shown to form on the CoCrMo alloys and UHMWPE, but not on Al_2O_3 [18,254,255]. The investigation of the hip tribolayer formation has shown that both surface

protein adsorption and change in proteins molecular weight occur. As the tribolayer forms, it is thought to simultaneously wear away, expelling particles [254,256]. In explanted hips, the tribolayer was found to be between 30-40 nm by Buscher et al. [249]. To replicate this in vitro, the pressure (usually 30-200 MPa) and speed can be controlled to create films between 5 and 100 nm, with lower pressure and lower speed causing thicker films [253]. Another study demonstrated a range in thicknesses as a function of sliding speed (0-60 mm/s, 5 N), and categorized two film types. At low speed, a boundary layer of adsorbed protein molecules formed from aggregated protein molecules to form a gel. At high speed, the gel formed and then sheared to a thin film with a lower lubricant film thickness [257]. Contact of this protein phase is complex and dependent on a number of contact conditions and lubricant properties.

Further characterization in this field includes explant studies from patient hips, including light microscopy, SEM, TEM, EELS, EDS, XPS, and Raman spectroscopy [16,258]. By investigating at the nanoscale, Liao et al. characterized the articulating surfaces of explanted MoM replacement tribofilms, SEM shown in Figure 6.3 d [16]. With Raman and EELS, it was determined the tribolayer was primarily carbon (95%) and that the carbon was nanographitic (82%), Raman shown in Figure 6.4 d and EELS shown in Figure 6.5 c [16,18,249]. Reproducing these results was attempted in simulators, but the carbon graphitic bonding was only 65%, as opposed to 82% in Liao et al. [256]. Even with explant analysis and simulator studies, there is no clear consensus on the tribolayer's impact on performance. The tribolayer can be considered beneficial because graphitic film would act as a solid lubricant, but there are also concerns of tribolayer degradation into tissue. Wimmer et al. have shown reduced wear and electrochemical corrosion with the

presence of the tribolayer [258], yet Liao et al. acknowledge that graphitic fragments could travel into cells to cause damage [16].

6.2.5 MEMS

Microelectromechanical systems are another nano-featured, carbon rich environment incorporating tribology, electrical activity, graphitic carbon films, and wear products. Nanoelectromechanical or microelectromechanical systems (NEMS or MEMS) are devices that integrate mechanical and electrical functionality, and the mechanical function requires specific lubrication. MEMS have become common in consumer electronics accelerometers and in “lab on a chip” medical testing. MEMS are made using techniques of microfabrication, often pushing for smaller dimensions with new fabrication methods; with these length scales, typical lubricants cannot suffice [259]. A successful solution for MEMS longevity in applied devices has been using carbon film lubrication, especially vapor incorporation [260-262].

MEMS devices are successfully lubricated through use of carbon deposition that creates amorphous carbon films or through alcohol vapor that creates an adsorbed monolayer on the surface. The carbon deposition can create a wear film, seen in Figure 6.3 e [190], and the carbon covered surface can become partially graphitic [263,264]. Strawhecker et al. [260] found that linear alcohols between 1 and 10 carbon atoms long oxidized silicon at room temperature. At 10% saturation of alcohol vapor, a monolayer was adsorbed, and by 90% saturation, about 2-3 monolayers were adsorbed [260,265]. It was shown that surface treatments of chemisorbed monolayers via functional groups, although initially reduced adhesion, did not survive mechanical contact [266,267]. Carbon vapor, on the other hand, is seen to more permanently adsorb as a film,

condense to a polymer, and act as a graphitic solid lubricant [264,268-270]. A major advancement in vapor phase lubrication is that a hot surface is no longer needed to adsorb and decompose the carbon source to a carbon film [265,271]. Now the driving force for bond passivation is the reactivity of the surface and the kinetics of the adsorption [259]. This method, compared to hydrophobic coating which seize after 3000 cycles, can run longer than 10^8 cycles with no evidence of wear, particle formation or changing operation characterized. An example of wear prevention is seen in Figure 6.9, a MEMS switch lubricated with pentanol [272]. The enhanced performance

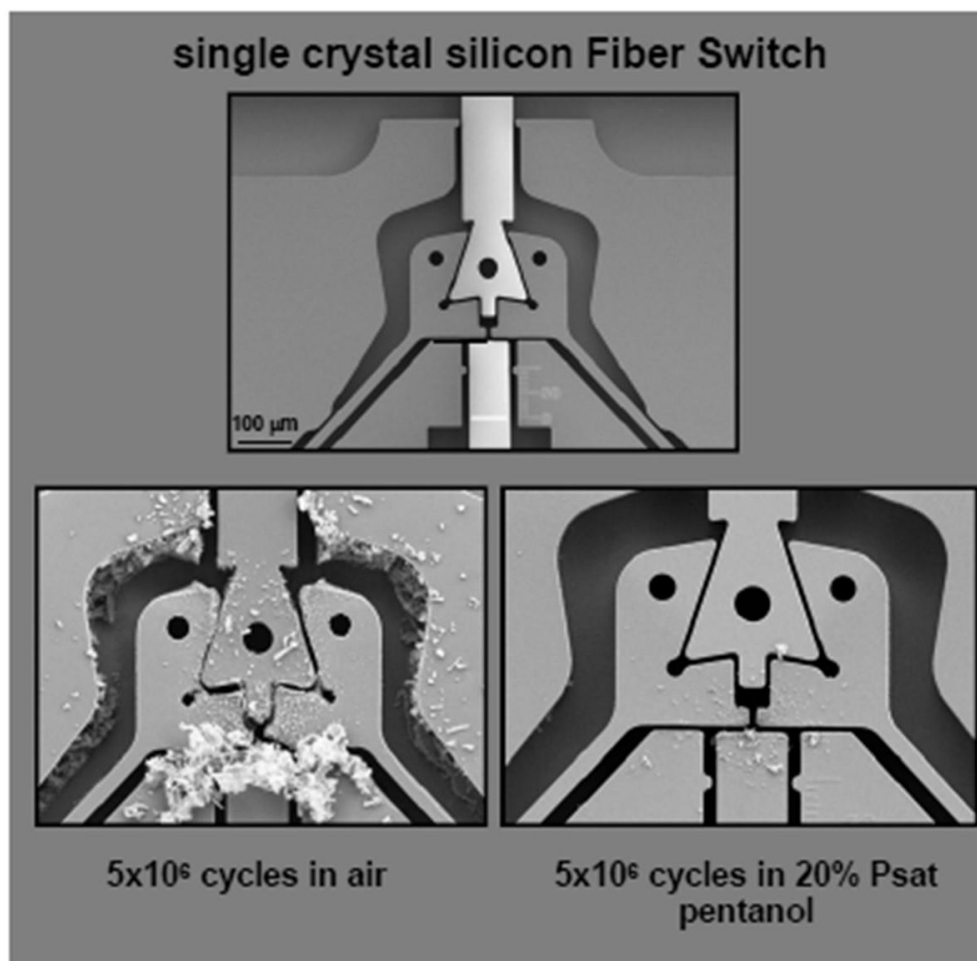


Figure 6.9 A MEMS switch lubricated in air and pentanol, showing the buildup of wear when unlubricated [272].

comes from the graphitization of the adsorbed carbon through sliding. Furthermore, if the layer is worn, vapor in the device can re-passivate the exposed surface for continuous lubrication [273].

MEMS lubrication has potential advancements as more complex defense and security applications require longer and tighter tolerances for performance, which means more cycles of reliable lubrication with minimal wear [259]. Single-component vapor species, however, have a vapor pressure that ranges by orders of magnitude over a narrow temperature range, where the necessary vapor for lubrication may instead become a condensed liquid. Additionally, filling a sealed volume with a known quantity of alcohol vapor presents some processing challenges for MEMS devices, as more control on vapor delivery and the possibility of polymer delivery design could be beneficial. By studying MEMS as a carbon lubricant system, the methods used for creating and characterizing these devices could be transferred to other triboactive systems, while other lubrication systems could help inspire the needed advancements for future MEMS designs.

6.2.6 Non-tribology: Catalysis Coke

By looking outside of tribology research, we can find similar nanographitic carbon films to inform carbon tribofilm systems. In catalysis, a parallel to graphitic tribolayers is seen in the formation of carbon coke. Coking is the accumulation of carbon on metal catalysts and supports through polymerization [274-276]. The process involves both chemical and physical bonding of carbon to form a film that eventually deactivates the catalyst. The process of coking has been studied thoroughly for reaction information, but can also be studied through the lens of carbon film composition and evolution [274,275,277]. Through studying a system with carbon, catalysis, and heat, but not tribology, mechanisms can be isolated for better understanding.

Similar to the reactions in tribochemistry, coke formation is considered a polymerization reaction, which forms surface coating carbon macromolecules. The reactions that lead to the film depend on the composition of the reaction mixture in addition to various reaction mechanism pathways. Through Raman spectroscopy, Li et al. showed that polyaromatic and pre-graphitic species are predominant in zeolites, shown in Figure 6.4 e [209]. Most coke research characterizes film as either polymerized [274,278-280], pre-graphitic [209,211], or graphitic [275,281]. In addition to Raman spectroscopy, NMR [282], EELS [211] or X-rays [281,283] are used to characterize the carbon bonding, with the EELS shown in Figure 6.5 d measuring 83% graphitic bonding [211]. Similar to tribofilms, there are often two types of coke described, an easy-to-remove initial formation, and a difficult-to-remove carbon film. The difficult to remove coke has less hydrogen content and has developed into insoluble carbonaceous deposits [274,282,283].

In a catalyst, the structure of energetically favorable available sites can affect the allowable reactions and rate of the coke formation. This surface dependence is similar to the structural surface parameters affecting tribofilms during contact [279]. In the catalyst system, we see that reaction time, temperature, pressure, nature of the reactant, and operating conditions all affect coke formation [275]. Coke is also known to occur with gas reactions, where monolayers of carbon containing molecules adsorb and react [276,284]. Trimm et al. notes that “carbon on catalysts behaves somewhat differently than graphite” [277,285,286], yet it may behave similarly to the nano-graphitic tribofilms. The important similarity is how the graphitic bonding evolves. There are similarities between coking in catalysts and triboactive systems, as triboactivity is only one factor in forming graphitic carbon films.

6.2.7 Other Examples: Cast Iron, Video Tape, Nanocomposite Coating

Carbon film generation is found in surprising places in the literature. We find that by looking beyond the initial search of “friction polymer” literature, more carbon films with striking triboactive and lubrication similarities are found. Here we present three examples of carbon tribofilms that complement the discussion.

One example is research done on video tape recorders by Mizoh et al. in the 1990s [287]. This research examines the beneficial mild wear in video tape recorders (VTR) as high speed rubbing on the magnetic tape produces a self-cleaning effect [287-290]. Without the wear, a polymer and brown stain form, which affects the reliability of the equipment. In the tribological system, the head factors, tape factors, and atmospheric factors are all found to determine formation of the tribolayer and whether wear occurs [287]. The real contact area and the friction coefficient are considered as key design choices [287,291]. The VTR system has a balance between the need for some wear for self-cleaning, but also the need to limit wear for longer head life. When humidity is high, the tribolayer causes film deterioration and is described as an easily removable, high molecular weight organic polymer with metal fragments; when humidity is low, the friction polymer formed sticks to the surface and reacts with the surface metal to cause seizure. It consists of iron, silicon and carbon of about 500-700 Å thickness [288,292]. These results echo the other fields discussed.

A second example is the glaze that forms during the run-in of cast iron. Cast iron is considered to have an important run-in period where smoothing of the surface and formation of a surface coating occurs [293]. The surface coating is considered to be derived primarily from the graphite present in the metal structure and the iron oxide, Fe_2O_4 . The glaze is measured to be as thick as 1

mm and ranges in carbon content from 30%-100%, shown in Figure 6.3 f [207,293]. The layer imparts a resistance to scuffing during the contact of mating surfaces, but just as importantly, it covers surface irregularities to produce a smoother surface [207]. This smoother surface allows higher loads to be carried by a fully hydrodynamic lubrication film without interaction of single asperities. An example of this used in industry is in internal combustion engine cylinder bores [293]. Montgomery et al. considers that the carbon was “doubtless in the form of graphite” and also assumes that there would be little to no thermal decomposition of the lubricating oil during the experiment [293]. It was assumed that the carbon comes from the graphite in the cast iron and could not come from the lubrication oil [293-295]. These experiments from the 1960s help to show the evolution of the carbon film research and help to identify where assumptions were made.

It is now known that lubrication oil decomposition is indeed possible, and can even start to be controlled [296]. This is demonstrated by a nanocomposite coatings patent [297]. The patent claims the production of a carbon lubricating film forming from deposits of a lubricating oil. The deposits form through reacting with the precisely designed nanocomposite active surface coating. The process of the lubricating film formation is remarkably similar to varnish formation, but in a more controlled way through the nanodesigned triboactive surface. The patented coating from Erdemir et al. [297] shows the design of a nanocomposite consisting essentially of a microstructural matrix of a catalytically active alloy of Cu, Ni, Pd, Pt and Re. The lubricant is catalytically broken down and is disposed on the nanocomposite coating during sliding, as seen in Figure 6.10 a and Figure 6.10 b [297]. This carbon film was characterized through Raman spectroscopy, as seen in Figure 6.10 c [297], and appears very similar to DLC films which are known to continue to develop graphitic bonding as they slide. With the current knowledge across

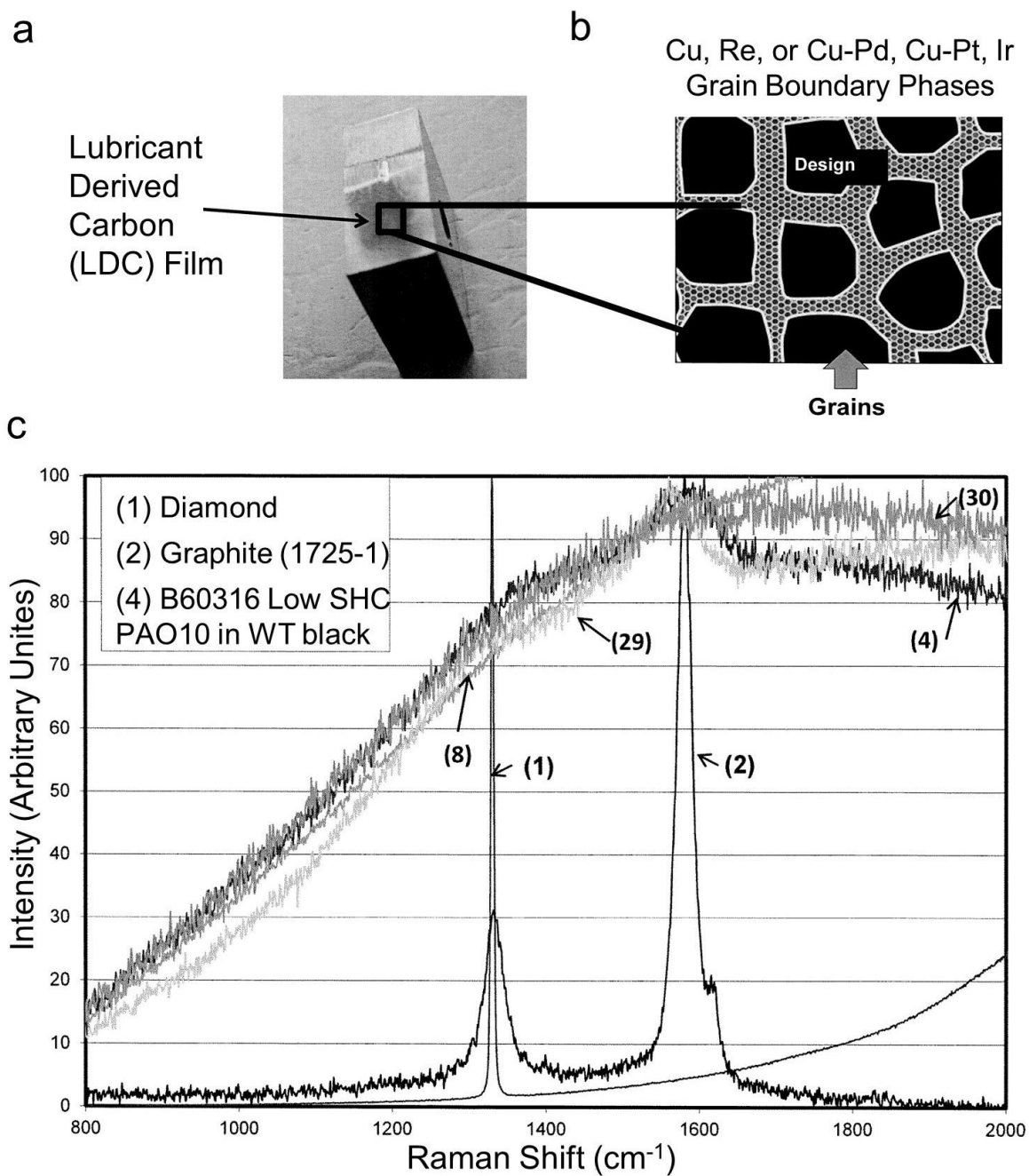


Figure 6.10 (a) The lubricant derived carbon film that forms during sliding on the nanocomposite surface, (b) design of the nanocomposite surface composition, and (c) Raman spectra of the film (indicated as 4 in the figure) presented with Raman spectra references of diamond (indicated with 1) and graphite (indicated with 2). United States Patent and Trademark Office [297].

fields, these example from literature and patents can be further explored through experiments to develop the next generation of designed advantageous tribofilms.

6.3 Mechanisms of Formation

Now that the carbon film systems have been profiled, we describe mechanisms of the film formation. In the carbon film generating systems presented, the composition and structure of the films are shown to be similar, and the mechanism share similarities as well. Here we present key mechanisms that have been proposed in the literature.

Some mechanisms, such as elevated localized heat, are frequently studied, whereas other contributors, like catalytic activity, have been researched thoroughly in some areas and seemingly forgotten in others. It is beneficial to study mechanisms, as some films are beneficial and some are harmful, and by finding differences in the mechanisms of formation, there is possibility to control film formation for advantageous properties. We lay out mechanisms by category, highlighting where seemingly disparate fields present parallel mechanisms, to show opportunity for future synergistic research.

6.3.1 Pressure, Temperature, and Friction

All mechanisms of film formation have interplay and codependence. The most prominent contributors are localized increases in pressure, temperature, and friction. Cyclic sliding magnifies the effects. In these systems, local temperature spikes are due to single asperity friction or bubble collapse. Often in experimental setup, however, the entire system is elevated to simulate local heat.

We address pressure, temperature, and friction together because they often cause one another. This triboactivity provides energy to induce graphitization.

As two surfaces come into contact with organic lubricant in-between, a system becomes tribochemically active. Friction occurs through the contact of nanoscale asperity features, and particularly the point of contact has high frictional forces. In 1958, Hermance et al. determined that “side to side motion was critical” for the organic deposit to form on metal surfaces in a benzene atmosphere [192]. It is known for friction polymers that contact causes flash temperatures and high pressures [191]. In metal-on-metal hip implants, cyclic loading is thought to aid and accelerate the deposition process of protein films through increased protein-protein interaction, protein transport, and rearrangement of adsorbed proteins [257,298]. Contact and shear forces contribute energy that allows lubricant molecules, whether proteins or hydrocarbons, to adsorb, react, and rearrange into a film. Friction at the surface, especially at the real contact area at single asperities, causes rupture of covalent bonds by frictional shearing [254]. Additionally, frictional forces are dependent on material and surface properties, as these factors also influence formation of tribolayers.

During asperity contact, high pressure and high temperature occur. The culprit is not overall system heat, but extreme pressures for small area and duration [192]. Especially in varnish, heat is considered the major issue [234]. Both friction between metal surfaces and bubbles imploding within lubricant create enough heat to cause oil molecules to oxidize; oxidized molecules then lead to polymerization [233,238]. The combination of oil-on-metal and metal-on-metal interactions can generate high temperatures and static charges that lead to spark discharge [234,238]. In hydraulic systems, microdieseling is the implosion of entrained air bubbles when oil passes through a high-

pressure pump in a hydraulic circuit [238]. Air compression bubbles can reach at least 1000 °C and can produce low molecular weight hydrocarbons from oil, as degradation can easily occur in the 300-900 °C range [238,239]. Similar to dieseling, adiabatic compressing can generate temperatures between 600-900 °C, while dark electrostatic discharge can cause temperature between 5,000-10,000 °C, whereas full spark discharge will generate a regular flash and nano-second temperatures from 10,000-20,000 °C [234]. This data is primarily reported in trade publications by authors from the company Kleentek USA, yet research on hip implants and catalysis also report temperature as a key factor. Research on CoCrMo alloy hip implants has shown that the mean temperature increased to 40-50 °C at the CoCrMo alloy head and to 55 °C at the ZrO₂ head surface. For in vivo, the peak temperature from frictional heating in a total hip implant has been measured at 43.1 °C at the center of the joint's head [254]. The human albumin proteins are partly changed through the thermal denaturation at the sliding contact [254]. While in catalysis, coke forms between 650 °C for the pyrolysis of hydrocarbons [286,299]. Another study reports that polyolefinic and aromatic species form around 25-425 °C [209]. These thermal increases across systems from friction and pressure provide the energy needed to react the carbon into film with graphitic bonding.

6.3.2 Depositions and Adsorption

For systems with liquid lubricant, film formation begins with particles accumulating on the triboactive surfaces. Particles precipitate out of solution to form deposits on the surface; this is the precursor for the tribolayer [253,254,256]. Carbon based lubricants go through chemical changes, due to pressure, heat, and friction, which cause chemical reactions. As the chemical products build

up in solution, they agglomerate, polymerize, and drop out of solution. Polymerization will be further addressed the next section. The majority of research for deposition and adsorption come from varnish and hip tribolayer research.

In varnish, chemical reactions generate products that lead to new chemistry, different than the oil and its additives [300]. Oil degrades into micron size particles of higher molecular weight products that precipitate out of solution [236,300]. Following precipitation, products deposit onto colder system surfaces such as cooler tanks and actuators. The low flow areas of the varnish circulation cause “soft” contaminants to form, whereas triboactive surfaces cause thin layers that harden over time [236]. Friction polymer research also describes the initial stages of polymer formation as “light colored and highly insoluble” deposits of saturated hydrocarbons [192]. Similarly in hip tribolayers, the proteins degrade by denaturing during triboactivity, and then deposit on sliding surfaces [254,256,257,298]. This adsorption of albumin to one or both of the sliding surfaces is found to be a crucial factor for hip tribofilm formation. Furthermore, it is found for the hip tribolayer that metal and polymer surfaces will adsorb deposits, but Al_2O_3 will not denature or adsorb albumin due to the hydrophilic surface [256,301]. The local metallurgy of femoral heads could also cause preferential adsorption [19].

For vapor carbon sources, the first steps of the reactions are adsorption on the surface and then reactions yielding an observable deposit. An early study showed friction polymer formation from benzene lubrication [192]. During the “highly efficient process,” a monolayer of benzene was converted to a solid product after each pass over the surface. The adsorption step is crucial here; it was shown that an initial introduction of hydrogen would block deposit formation [192]. MEMS devices are also lubricated with alcohol vapor that adsorbs to the surface. The reactions can be

measured through secondary ion mass spectroscopy (SIMS). For a MEMS device, wear did not occur if the carbon vapor pressure was at least 8% of the saturation pressure, or $P/P_{\text{sat}} \geq 8\%$ [273,302]. This saturation corresponds to a monolayer in coverage which created a lubricious environment that mitigated the friction and wear. Similarly with coke, the carbon source also comes from the air, and the carbon gas reactions happen when monolayers of carbon adsorb onto the catalyst and react into coke [284,303]. The adsorbed carbon creates the carbon building blocks for tribofilms.

6.3.3 Polymerization and Organometallics

With the energy from heat and friction, carbon lubricants react, drop out of solution, deposit, and continue to polymerize. Discussion of high molecular weight species, oligomers, and polymerization is prevalent throughout research in friction polymers, varnish, hip tribolayers, MEMS, and catalysis. The friction polymer found on video recording tape is even found to have a high molecular weight [287,291]. The commonalities show that polymerization is key to forming graphitic films.

Early research on polymerization in friction polymers showed that high molecular weight species developed between lubricant and metal surface. Hermance et al. [192], studying metallic contacts in 1958, assumed the organic deposit was “a very thin layer of high molecular weight material” and that it was likely crosslinked with little oxygen in the molecule [192]. Later in the 1970s, Hsu and Klaus, used gel permeation chromatography to identify the presence of high molecular weight species, including organo-iron species [203,204]. The species were identified as

high molecular weight organometallic polymers of variable molecular weights (10,000-100,000 MW) [195,233].

Across systems, high molecular weight polymers are present. In varnish the formation begins with the condensation and polymerization to form high molecular weight oligomers and the agglomeration of insoluble particles on metal surfaces [233,236]. In the hip tribolayer, the transformation of protein to graphitic carbon film is explained by first showing that lower molecular bands were formed during mechanical denaturation through rupture of covalent bonds in human serum albumin by frictional shearing motion [254]. The denatured proteins adsorb on the metal surface, forming a gel-like layer of higher molecular weight. This gel reacts into a graphitic tribolayer, which acts as a solid lubricant [257]. Similarly in MEMS, a high molecular weight product forms on the contacts, and it has been shown that “higher” alcohols ($4 < n < 11$) reduce friction and cause low wear rate as compared to the lower alcohols ($n < 4$) [304]. This would support the idea that they could polymerize to high molecular weight species, which could form a lubricating tribolayer [259]. It is postulated for MEMS that metal alkoxides condense to a polymer and act as lubricant, showing another example of the intertwined roles of oxidation, organometallics, and polymerization [270]. Coke on catalyst formation can also be considered a kind of condensation-polymerization reaction resulting in macromolecules [277]. Often the initial hydrogenated carbon molecules are characterized to be CH_x with x varying in studies to be $0.5 < x < 1$ [305], or $1 < x < 3$ [283], or $x = 2$ [280]. XAES spectra indicate that with longer reaction time, the hydrogenated carbon dehydrogenate slowly to amorphous or graphitic carbon [305]. The pathway to coke from olefins or aromatics can involve polymerization, cyclization to form benzenes, and formation of polynuclear aromatics [276,278,279,306]. This transformation in

polyaromatic carbon makes the film less reactive and difficult to remove [283,286,299]. Polymerization seems to present as the key step between carbon building blocks and graphitic film.

Organometallic formation is a step in the process of tribolayer formation. In friction polymers, the role of organometallics have been shown on a variety of metal surfaces to accelerate the rate of hydrocarbon oxidation [204]. It has been found that dynamic wear tests at room temperature form oil-soluble, metal-containing compounds [191], which are primarily high molecular weight organometallics [3]. Organometallic compounds have a relative molecular mass ranging from 100-100,000 MW. The carboxylic acids formed from hydrocarbon oxidation are proposed to react with the metal surface and two hydrogen atoms to form conjugated double bonds [202]. This shows a possible pathway for multi-elemental lubricant to become a primarily carbon film. In iron alloys, organometallic compounds are formed between the iron surface and base oil, and are considered essential to lubrication as this surface activity is part of the dominant tribochemical reaction. Similarly, CoCr alloys form organometallic layers during wear, showing that this is a possible mechanism inside the hip MoM contact as well [256,307,308].

6.3.4 Catalytic Activity and Fresh Surfaces

Catalytic activity is another step of the reaction process that helps explain how these tribochemical reactions are possible. In the case of coking on an intentional catalyst, the catalytic elements are obvious, and in the case of a triboactive system, exposure of a fresh surfaces can provide the catalytic activity. By looking at similarities between triboactive systems and coke, we can begin to isolate mechanisms and see how many steps are influential to form the carbon films seen across these systems.

Metal surfaces have been noted for their role in tribofilm formation from the early studies in the 1950s-1970s. Hermance et al. noted that the surface was an “active metal” and the reaction would come to a standstill when it was completely covered with tribofilms or if hydrogen was incorporated in the chamber [192]. Klaus et al. found that a variety of metal surfaces accelerated the rate the hydrocarbon oxidation, concluding that metal reacts directly the organic lubricant to form metal salts [191,204]. Nascent iron surfaces were shown to react with hydrocarbon molecules to form smaller molecular fragments, with the carbon source being liquid or gas [197,199,203]. Iron and steel are often studied [197,203]; early studies noted that palladium, molybdenum, tantalum, and chromium can form the carbon tribofilms as well [192].

In addition to metals, semiconductors and insulators can cause tribochemical reactions as well. When a new surface is created, residual electric charges can become active because of disrupted surface bonds [309-311]. For crystalline solids, dangling bonds have been observed as the major surface active site for reactions [205,312,313]. The surface chemical reactivity for these classes of solids can be dominated by defect sites and dangling bonds, especially when heated to bond dissociation temperatures or mechanically disrupted.

By looking at pure catalysts, we can discover that adsorption, polymerization, and graphitization can all occur with the encouragement of catalytic activity instead of with friction. Carbon gas reactions occur where monolayers of carbon adsorb and react on the catalyst surface [209,284]. Metal catalysts yield olefins, which polymerize on the acidic sites of the support and then stabilize through dehydrogenation [274,279]. The presence of catalytic elements in all the reviewed systems, even in small quantities as alloys, explains how catalytic activity provides energy pathways for graphitic film formation.

6.3.5 Graphitization

The process of graphitization, amorphous carbon turning to graphitic ordered carbon, is a well-studied phenomenon that is a key process in the formation of carbon tribolayers. Amorphous carbon deposits are often thermodynamically unstable, and when external thermal energy is provided, the atoms begin to rearrange and assume more thermodynamically stable bonding configurations, i.e. partially graphitic structures which contain more sp^2 bonding. While the end point may be an ordered graphite structure, more common is a disordered matrix with nanoscale regions of graphitic bonding. In DLC or diamond systems, this process is a rehybridization of the carbon-carbon bonds, but when the starting materials are oils, waxes or proteins, it is an oxidation since carbon-hydrogen or similar bonds are being converted to sp^2 carbon-carbon bonds. The graphitization process often turns a carbon containing film into a solid lubricant.

The tribochemical reactions between amorphous carbon sliding surfaces cause low-friction tribofilms to form [314,315]. For DLC films, graphitization, sometimes explained as rehybridization, is often investigated in as DLC become more lubricating during sliding because the amorphous film turns partially graphitic [225,226]. Heat and catalytic activity can also turn amorphous carbon to graphitic, but in most of these systems tribochemical contributions are most significant. Tribochemical transitions are mechanochemically active; amorphous atoms change position as they react [223]. Recent concepts of tribocharging, tribomicroplasma generation, and triboemission phenomena have been proposed to contribute to graphitization as well [316].

By looking at these systems together, we can find connections between the prominent DLC research and details found in other fields. For most DLC films, Raman spectroscopy and electron diffraction can show disordered graphite structure in transfer layers [208,317-320]. For MEMS,

graphitization is seen in parts fabricated of amorphous diamond, which produce a low-wear, DLC-like film. High-cycle varnish areas are found to be graphitic, as shown in the varnish Raman and EELS data, which point to tribochemical contributions (probably oxidative) causing graphitization in this system as well [233]. In coke, the process of carbon oligomers dehydrogenating to amorphous carbon and then to graphitic carbon is described by XANES measurements over time [283]. The graphitic content of carbon films is an important aspect, as this quality influences lubrication properties.

6.3.6 Nanoparticles and Metal Particles

The influence of wear and wear particles is often mentioned in carbon films research, but the ties to a mechanism of formation is not directly clear. Carbon nanoparticles form in varnish, starting at 10 nm to 2000 nm, but they are difficult to measure with standard industry practice [236]. In industry, the aim is to prevent and control these very small carbon-based particles through improved cleanliness monitoring, as the particles are thought to increase wear. These particles are most likely the initial form of the condensing polymers before aggregation, but research suggests that they influence lubrication in a different way when they are still soluble as opposed to once they deposit.

Metal nanoparticles are included in some system analysis, mostly in MoM hip or iron-based systems. In hip simulator experiments, the film created was organometallic in nature, containing a number of embedded particles. The particles in the film were smaller and smoother in morphology than those typically ejected from the bearing [254,256]. The hip simulator experiments show that metallic particles may cause the initial protein denaturation. This would indicate that metallic

particles are a precursor to tribolayer formation, yet this conclusion is not definitive [256]. Furthermore, in cast iron glaze, iron oxide nanoparticles are found in the run-in layer and considered to be a key component generated during wear and then tribolayer formation [293]. The presence of nanoparticles creates additional triboactive surfaces as they act as third body particles. It is not conclusive whether there is a specific mechanistic role of nanoparticles in tribofilm formation.

6.4 Discussion

After introducing key carbon film systems and breaking down the mechanism that cause film formation, we discuss particular similarities, reaction thermodynamics, and future opportunities.

6.4.1 Similarities

The systems summaries and mechanisms explanation present substantial evidence of similarities between these carbon films. There are similarities in appearance, chemical composition, chemical reactions, and influence on performance. The presence of carbon films has been heavily tied to performance – both good, detrimental, and mixed – yet film characterization provides insight that applies across systems.

The notable parallels begin with descriptions and word choice across fields. Friction polymers and varnish are noted to appear initially pale yellow and darken in time, often described as dark reddish-brown and sometimes shiny [192,198,236,238]. Even the early friction polymer from Hermance et al., once heated, was said to resemble a “coke-like residue” [192]. Beyond appearance, the dual formation of the carbon films was noted across systems - in friction polymer,

graphitized films. With these similar mechanisms, there are even parallel reaction diagrams showing organic precursors turning into pre-graphitic condensation products in friction polymers and in catalysis, as shown in Figure 6.11 a [321] and Figure 6.11 b [322] respectively. These parallel formation theories from vastly different fields are striking.

6.4.2 Thermodynamics

It is clear that the carbonaceous material from friction polymers, DLC, varnish, hip implants, MEMS, and catalytic coking share striking similarities. Something general is taking place – what? A phase map of carbon structures from the literature, shown in Figure 6.12 [247], provides important clues if we superimpose the approximate positions of amorphous carbon, proteins, oil products, and graphite [217]. Through heat, friction, catalytic activity, or some combination, the

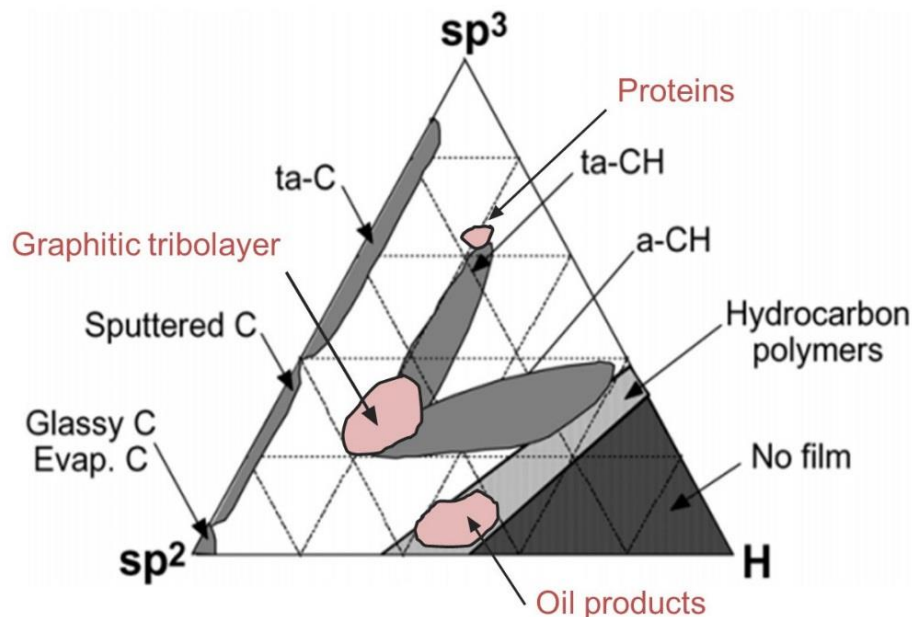


Figure 6.12 Ternary phase map based upon for various carbon films [247], including proposed approximate placement for proteins and oil lubricants, which shows their respective sp^2 , sp^3 , and hydrogen contents. This provides a map of the dynamic change of these materials into graphitic films.

carbon sp^3 bonding shifts to sp^2 graphitic bonding, coupled with loss of hydrogen and other elements as volatile gases or liquids such as water and carbon dioxide.

Experimental demonstrations can show how heat and sliding can both individually contribute to graphitization, which mirrors the thermodynamic evolution in different systems. A DLC study by Wu et al. annealed DLC films at different temperatures, then used Raman spectroscopy to characterize the graphitization at various temperatures. In Figure 6.13 a [225], it was shown that as the anneal temperature increases, the hydrogen was driven away and the formation of sp^2 bonding or graphitic microcrystallites began [225]. For comparison, in an experiment on nearly frictionless carbon by Merkle et al., carbon film underwent sliding with EELS measurements

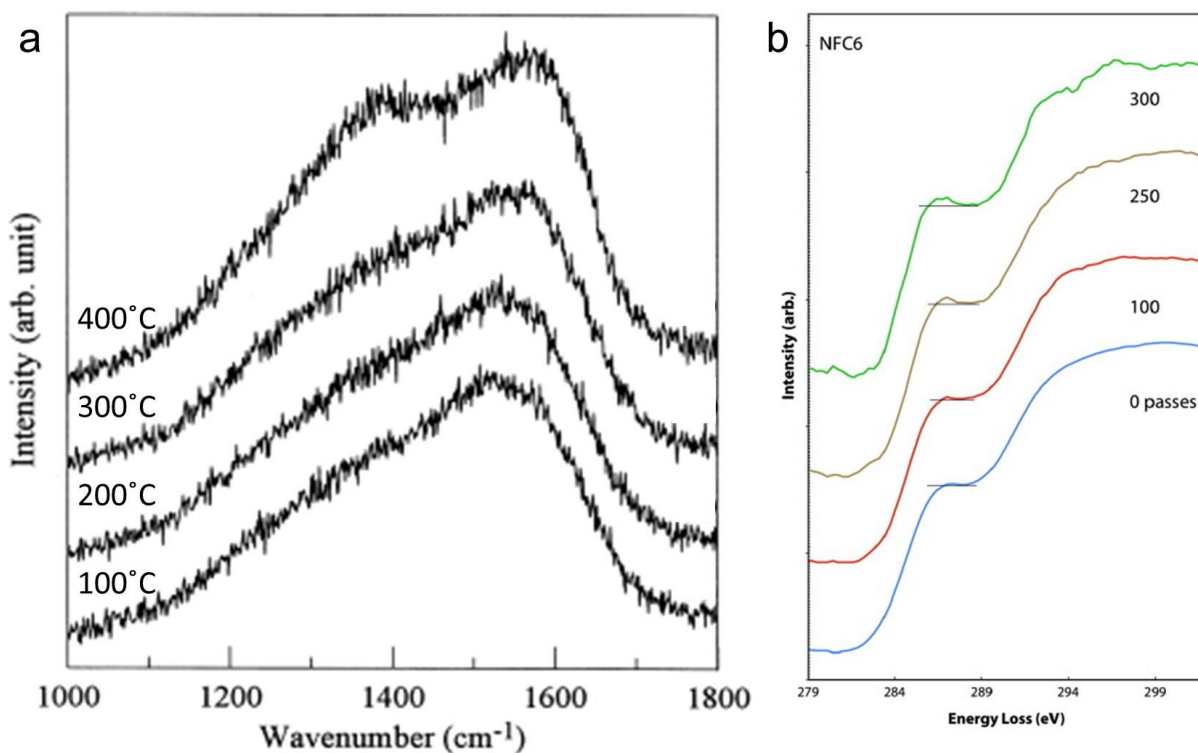


Figure 6.13 Examples of input energy causing graphitization in DLC and NFC carbon films. (a) At increasing heat treatment temperatures, DLC film became increasingly graphitic, measured by Raman spectroscopy [225]. (b) During in situ sliding, NFC film became more graphitic measured by EELS [59].

documenting increasing graphitic bonding, shown in in Figure 6.13 b [59]. The energetic input does not matter, the carbon composition reacts towards the lowest carbon form, graphitic bonding.

To further explain the possible reaction pathways, the carbon systems can be analyzed from the point of open system thermodynamics. Lubricant oils, proteins, and other carbon sources react to become primarily carbon in composition; the other elements become volatile products such as water and carbon monoxide. The driving force – heat, friction, or a combination – plus coming into contact with a catalytic metal surface increases the reaction constant by decreasing the activation barrier for sp^2 bonding. The probability that the bonding will shift from amorphous to graphitic can be calculated by

$$P(s) = \exp\left(\frac{-(E - \sigma * C)}{kT}\right)$$

Equation 6.1

where E is the energy barrier, σ is the stress applied, C is a constant, k is the Boltzmann constant, and T is temperature. We can compare a system at room temperature with an applied stress and a system at high temperatures with no applied stress to explain the stress-assisted graphitization of carbon. We can assume an energy barrier on the order of 1 eV for the amorphous carbon to graphitic transition [323,324] and 40 MPa for the applied stress similar to a hip implant or machine applied to a volume of $2\text{\AA} \times 2\text{\AA} \times 2\text{\AA}$ [325]. Graphitization can occur at 1500 K with no stress, and can occur around room temperature with assisted stress, although at a rate of about 5000 times slower. This model agrees with our observations across systems.

6.4.3 Future Opportunities

Connecting these fields of research could begin to answer why some films are advantageous and others are not. Friction polymers can be designed to be beneficial, yet small changes can degrade system performance. Changes such as film thickness or particle generation take a friction polymer outside the design tolerances. Machine tolerances may be why the varnish tribolayer is considered detrimental, as varnish is often uneven and inhomogeneous. It is deposited without intention, outside of the parameters of the machine. The hip tribolayer is also unintentional, yet it is experimentally theorized to be protective. By studying the formation of the two tribolayers together, beneficial tribolayers can be designed to form, similar to the patented nanocomposite system. Further opportunities come from understanding commonalities in the formation mechanisms. Both MEMS and friction polymer fields study the film formation differences between metal and organic substrates, connecting how the substrate leads to an effective film. Both metal hips and varnish deal with static charge that leads to spark discharge, and by studying the metal-on-metal contacts, it could be mitigated or controlled in both systems [234,238]. For film formation, MEMS, cast iron, and nanocomposite coatings all need a reservoir or carbon to begin and continue their formation, yet this evolution is not well understood [259,293,297]. Cast iron graphitic layers do not only act as a solid lubricant, but also as a cover to single asperities; these layers can inspire other film designs [293]. Additionally, there are carbon film systems not addressed here, possibility very specific to a field; those carbon films could be analyzed or applied across discipline for novel outcomes. Other forms of partially graphitic carbon, such as glassy carbon, could also be beneficial for comparison. These possible research connections can lead to improved design for better performance.

Mutually beneficial information can be exchanged through collaborative monitoring, characterization, and design techniques. For example, the multivariable analysis of SIMS used in MEMS analysis allows for rapid identification of subtle changes in chemistry. SIMS could be used for chemical evolution measurements of friction polymers to expand beyond the current steel-hydrocarbon system knowledge [302]. In varnish work, nanoparticle tracking analysis requires particle detection between 10 nm and 2000 nm, yet this work is complex and expensive, outside of the usual scope of varnish monitoring [233,236]. In academic laboratories, however, nanoscale characterization and monitoring is becoming standard. Through collaboration, research on varnish could also inform the work on nanoparticle condensation polymers that occur in friction polymers, hips tribolayers, and other systems. Through cross field research, designing controlled catalytic surfaces could lead to engineered varnish films as beneficial lubricants.

6.5 Conclusions

- ❖ Notable carbon films are present in many fields. The systems of friction polymers, diamond like carbon (DLC) coatings, varnish from industrial lubricants, the tribolayer from metal-on-metal (MoM) hip replacements, microelectromechanical systems (MEMS), and catalysis coke produce similar graphitic carbon films. Graphitic carbon films can be a helpful solid lubricant or can form a damaging deposit.
- ❖ Key mechanisms of formation of graphitic carbon films include pressure, temperature, and friction; deposition and absorption; polymerization and organometallics; catalytic activity; graphitization; and particle interaction. The energy inputs to a system, through heat,

friction, or catalysis, causes graphitization. The result is often regions of nanographitic bonding, creating a partially graphitic film.

- ❖ Through integrating research approaches, cross-field collaboration can allow for innovative developments. Creativity comes from bridging disciplines: a good idea from one discipline can be an innovate idea when applied to another.

7 Future Work

In this section, I propose continuation experiments on CoCrMo alloy corrosion, varnish characterization, and in situ sliding. Both immediate follow-up experiments and long-term directions for these projects will be explained. The MoS₂ and lamellar lubricant experiments are proposed in greater detail because this project is most recent and is still in development.

7.1 CoCrMo Alloy

7.1.1 Experiments with the Current CoCrMo Alloy Samples

The CoCrMo alloy samples used in Chapter 2 and 3 were originally made and annealed for the work by Panigrahi et al. [65]. There are still additional experiments that could be completed with these samples. In Panigrahi's initial experiments on the grain boundaries, anneals were performed at 1230 °C for 2 hours and 24 hours, with 24 hours being noted for best corrosion resistance [65]. The work in Chapter 2 and 3 used the wrought CoCrMo alloy samples with a 24-hour anneal at 1230 °C. I proposed that the 2-hour anneal time could be used to evaluate the evolution of the microstructure and to compare to the current 24-hour anneal results. Panigrahi's work showed that the 24-hour anneal was sufficient to change the primary corrosion type from ubiquitous pitting corrosion, as seen in the no-anneal and 2-hour anneal, to primarily localized and less intense intergranular corrosion in the 24-hour anneal. It was initially thought from SEM analysis that most intermetallic phases dissolved into the bulk alloy. However, my work using TEM on FIB grain boundary samples showed that there were nanoscale chromium carbides present that caused local chromium depletion. Examining the intermediate 2-hour time point could provide a useful sample for further carbide analysis.

Panigrahi's work and my work showed a tipping point where anneal time changes the corrosion from all-over pitting to localized grain boundary corrosion. Studying the 2-hour anneal would add another data point to the metallurgical development during the heat treatment. Similar FIB samples could be evaluated in TEM to look at chromium depletion. Also, the CSL of the earlier anneal could be examined in EBSD to see the evolution of the CSL growth. This 2-hour anneal would allow for better understanding of the carbide dissolution. Furthermore, the CoCrMo alloy is known to have a variety of carbide compositions, but currently, only chromium carbides have been investigated in these samples. The 2-hour anneal may show an interesting progression of the various carbides and their relative dissolution rates. These experiments could lead to noteworthy analysis, yet a thorough study may require new samples with more heat treatments to fully characterize carbide evolution.

7.1.2 Future Directions of CoCrMo Alloy Research

Beyond the anneal time studied here, other studies of heat treatments are needed to design future alloys with tightly controlled microstructure. Some CoCrMo alloy studies have looked at various anneals [84,107], yet microstructure as a consequence of thermal treatment is not completely understood. Panigrahi [65], Lin (in preparation, Chapter 3), and my work [66] (Chapter 2) begin to show these mechanisms, but more complex heat treatments should be explored. In steels, there are multistep heat treatments that can target specific second phase precipitates [326-328]. Similar treatments could allow for CoCrMo alloys with more ideal mechanical and corrosion properties specifically designed for biomedical use.

By investigating heat treatments, further analysis could be done specifically on carbide dissolution to determine when they are truly dissolved or no longer causing sensitization. Specific questions include: For the carbides and corrosion, is there a tipping point between 2 hours and 24 hours, where the process transitions from pitting to grain boundary corrosion? Is the transition gradual or sharp? At what size do the nano-carbides lose their carbide structure and fully anneal to a grain? Because we see that nanoscale carbides are linked with corrosion susceptibility, investigating the dissolution process of these carbides could show how the structure progresses during annealing. Understanding and then controlling the metallurgy could lead to better designed alloys with enhanced corrosion resistance.

Outside of heat treatments, there are also other areas of characterization needed for CoCrMo alloys. For the model on corrosion initiation at grain boundaries in Chapter 2, we drew many of our assumptions about CoCrMo alloys from stainless steel literature. The level of “sensitization” is not defined for CoCrMo alloys in the literature. For stainless steel, the amount of chromium depletion is determined from experiments and theory, but these experiments have not been done for CoCrMo alloys. The electrochemical corrosion potential of various concentrations of Cr in CoCrMo alloys has not been measured. This is relevant because, as the amount of Cr in a Cr₂O₃-forming alloy is reduced, it becomes easier to corrode, as measured by the electrochemical corrosion potential. For both of the Cr depletion and the corrosion potential values, we adapted ratios from stainless steel publications, but that is simply an estimate. Experiments on sensitization composition [88,106,120-122] and electrochemical values [132,133] of CoCrMo alloys would be a good start. For more advanced heat treatment and corrosion control, more parameters for CoCrMo alloys would need to be investigated. These values would allow for more accurate models

to be made, which could inform better alloy design. From our work, it seems that CSL and grain boundary engineering has potential to influence corrosion behavior, but controlling grain boundaries is a complex task. To begin working with metallurgists, more data is needed to actually do further alloy design. Factors such as composition, carbide sizes, and sensitization levels would need to be both understood theoretically and validated experimentally.

I believe the next steps of the research should have a greater metallurgical focus in order to define the CoCrMo alloy beyond the ASTM F 1537-08 [125]. The FDA uses this ASTM standard to certify CoCrMo alloy devices, yet Panigrahi [65] and I [66] have noted the lack of microstructure specification in the standard. Our studies showed that microstructure and nanostructure have a direct effect on corrosion performance. Even as tissue engineering and custom 3D printing become more common, metal implants still have a large potential patient population in the upcoming decades. There are still improvements possible for these biomedical alloys.

For long term research directions, joint corrosion and tribology is crucial. It is beneficial to examine independent parameters for in-depth analysis, but combination experiments are needed for complete understanding. Multi-parameter studies show the synergy of the tribocorrosion and allow for a more complete system to be evaluated. For my work on the CSL and non-CSL in CoCrMo alloys, it would be interesting to expand that work into the tribochemical testing realm. For example, an initial experiment could be to focus a sliding setup over a single, selected grain boundary. A sample with large grains could allow for a single CSL grain boundary to be found in an SEM /EBSD, and then aligned in an electrochemical cell with a micron-scale probe, possibly an AFM tip. By sliding in a physiologically relevant solution over a $\Sigma 5$ or a $\Sigma 25$ grain boundary,

the tribocorrosion effects for individual boundaries could be evaluated in a more realistic environment than static electrochemical tests. The sliding could take place on a micron/millimeter setup, but then the boundary corrosion could be characterized on the micron or nanometer scale through FIB cutting a TEM sample. Building a test apparatus as described may be complex, yet a successful setup could allow for tribocorrosion insights on a scale not yet available. Combining physically relevant solutions with tribological testing is necessary to simulate the numerous relevant parameters of the in vivo environment.

7.2 Varnish

Few studies have evaluated varnish from an academic standpoint. Future varnish research could include more controlled laboratory testing and nanoscale characterization. The samples evaluated as part of the review study came from varnish removal companies' spare parts. Additional studies on varnish would need to complement industrial samples with films that are lab-generated from a simulator or tribometer. Further partnerships with industry could yield more samples from machines to compare to the lab-produced samples. Varnish that was created with different run times, oils, or temperatures would be necessary for a complete study.

Doing various nanoscale chemical analysis is needed to fill the knowledge gaps across varnish, friction polymers, and solid lubricants. For example, the beginning of varnish formation is thought to be nanoparticles of agglomerated, oxidized lubricant molecules. The critical sizes or chemical characterizations, however, have not been studied. A study noted that these nanoparticles have not been investigated because it is outside of typical industry capabilities [233,236]. This type of nanoscale characterization could be a good industry-academia partnership.

Other chemical analysis techniques could be useful for varnish films or similar triboactive films. For my work on characterizing the varnish from Dyna Power Parts, we were able to show that standard nanofilm characterization techniques could be useful for varnish. I used Raman spectroscopy, FTIR, and EELS in TEM. These tools are useful for characterizing the elements and bonding in the deposited films. High resolution TEM and EELS are ideal for measuring graphitic bonding development. Varnish could also be tested with other common tribofilm methods. For example, in a dimethyl disulfide lubricant system, Raman and X-ray photoelectron spectroscopies measured sliding reactions in situ. The sliding reactions caused the lubricant to adsorb, react, and then form a tribolayer, which was characterized at each step of the reaction [329]. Similarly, SIMS has been used to characterize sliding surfaces, so that could be applied to varnish as well [206,302]. This type of work could bring more detailed information to understand the tribochemical activity. Various conditions of temperature, sliding, and chemistry could be tested and compared for more systematic analysis.

The most significant development for varnish research would be to develop collaborations between academia and industry. Partnerships would allow for transfer of samples from relevant industrial environments to academic labs and for appropriate simulation conditions to be built in labs. Then academic research could help to prevent varnish, which is the industrial goal, but also understand the chemistry of its development, which may offer powerful solutions to other lubricant systems.

7.3 In situ

For in situ work, there is a variety of further studies that could be accomplished. Specifically, with our situ setup, there are basic improvements to the experimental methods, further clarification experiments for the work already done on MoS₂, and directions for new MoS₂ experiments. To continue expanding the in situ tribology work, similar lamellar solid experiments should be investigated. Additionally, there are collaborations in development with researchers who work on lubricating solid materials. Finally, we reflect on how this work could be relevant to lubrication applications.

7.3.1 Improving our Experimental Setup

Chapters 4 and 5 present work investigating the lubrication mechanisms of MoS₂ with in situ TEM. During these experiments, the equipment was functional, but there are improvements that could be made by future users. The first would be to use the force measurement capabilities of the Nanofactory holder and software. This would allow capturing of force-displacement plots for the Y-direction in the microscope, see Figure 7.1 for geometry of AFM tip and sample inside the microscope.

Another improvement is that a sharper AFM tip should be used for future experiments. A smaller tip radius would give more precise contact point on the MoS₂ flake. This could lead to better post facto video analysis, such as estimating the contact area more accurately. A ~10-20 nm tip radius would be an improvement for sliding experiments, but even sharper would be better. The tips from the Nanofactory manufacturer are no longer commercially available; we currently have

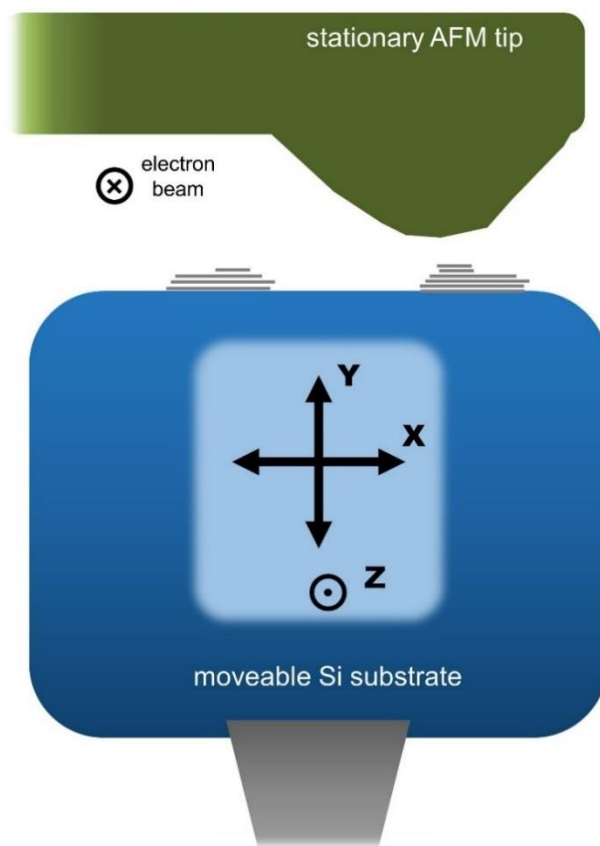


Figure 7.1 The geometry of the AFM tip, Si substrate sample that is movable in three directions, and the MoS₂ flakes that sit at the edge.

three in our stock, see Figure 7.2 a. There are two methods to make sharp AFM tips that are compatible with the Nanofactory holder. The first method has been done before by group member Yifeng Liao. He broke off the Nanofactory AFM tip, glued on a new AFM tip, and calibrated the spring constant, see Figure 7.2 b. For Liao's tip, the spring constant was calibrated in the NUANCE Facility KECK-II Center at Northwestern University. This "homemade" technique invalidates the electronic wires that connect the AFM tip to the computer. With the homemade AFM tip, the tradeoff is that you get a sharp tip, but you lose the ability to measure the force from the electronics run by the computer. The second technique would be to sharpen the tip in the FIB, mounting it at different angles in the FIB to get the various faces of the tip. This technique has not been attempted

before and it does also risk damaging the electronic connections. If the ion imaging and milling was isolated to just the tip, then damaging other parts of the AFM mount, including the wires that connect the tip to the computer, might be avoided. Avoiding touching tweezers to the gold wires would be particularly important. The process of sharpening a current tip would be difficult, but with correct geometric placement in the FIB, the method could be accomplished and highly useful.

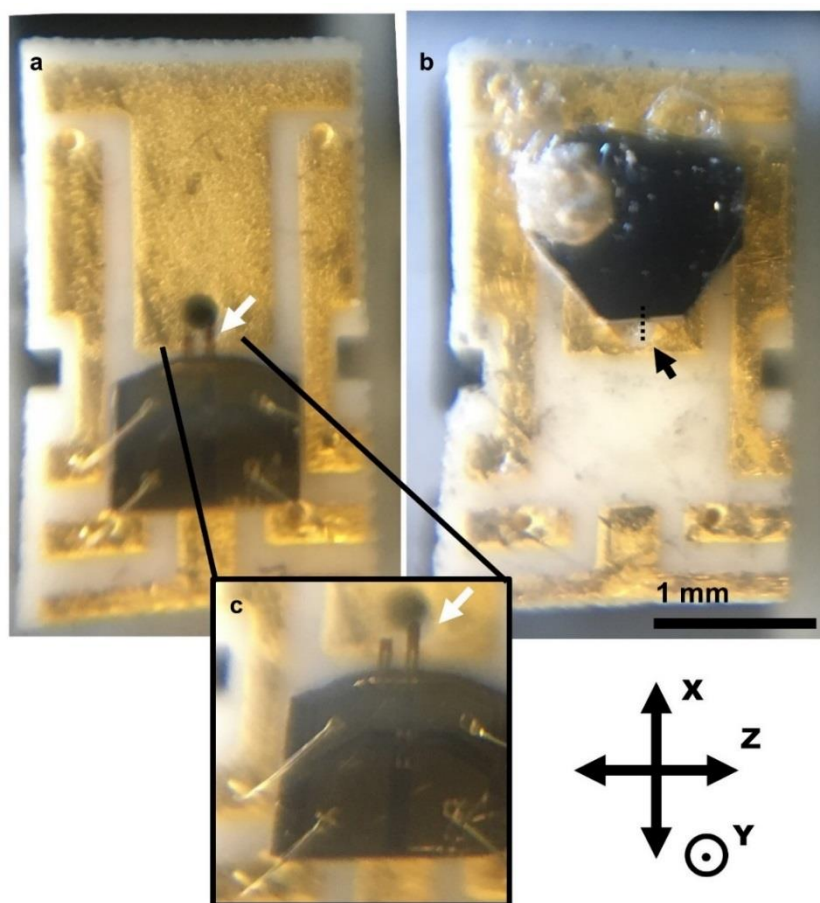


Figure 7.2 (a) The standard AFM tip from Nanofactory, (b) the homemade tip by Yifeng Liao, and (c) a close up of the AFM cantilever in the Nanofactory tip. The white arrows indicate the AFM cantilever, the cantilever next to it is for comparison in the electronic circuit. The black arrow points to where the cantilever was on the homemade AFM tip, and the dotted line indicates where it was before it broke off. The gold wires and patterning on the chip allow for connection to the computer software. The in situ coordinates system is indicated.

It is possible that another force in the in situ setup could be measured that we have not attempted: the lateral or friction force, in the X-direction. This would be back-calculated from the observed AFM tip deflection. This has been theorized to be possible, but not yet implemented in our group or others, as far I am aware. First, the spring constant of the AFM tip would need to be calibrated in the X-direction, see Figure 7.3 for the coordinates system. In the same way that we back-calculate the force of adhesion in the Y-direction from the tip deflection during contact, we could back-calculate the sliding friction from the AFM cantilever deflection in the X-direction, see Figure 7.4. This should be possible because we can measure the cantilever tip deflection on the order of nanometers. This calibration and experiment could only be done with the home-made glued tip because the AFM tip would need to be calibrated in both X and Y directions. A sharp tip would also help show the X-direction deflection in the post facto video analysis. The risk is that this experiment method requires difficult tip fabrication and leads to complicated post analysis calculations. The data obtained from measuring sliding friction force for various arrangements of MoS₂ flakes, however, may make this difficult experiment very worthwhile.

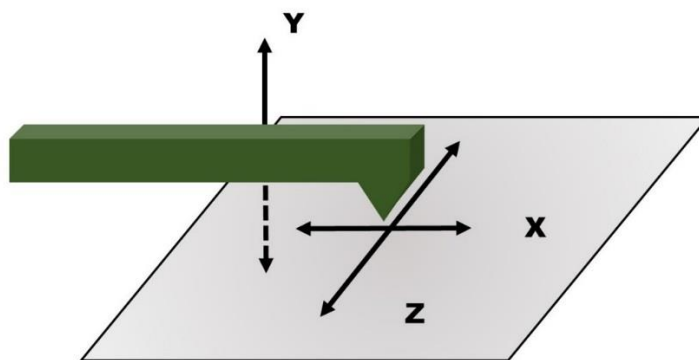


Figure 7.3 A homemade AFM tip would need to be calibrated. The in situ coordinates system is crucial to note because the Y-direction is important for adhesion force and the X-direction is important to the friction force.

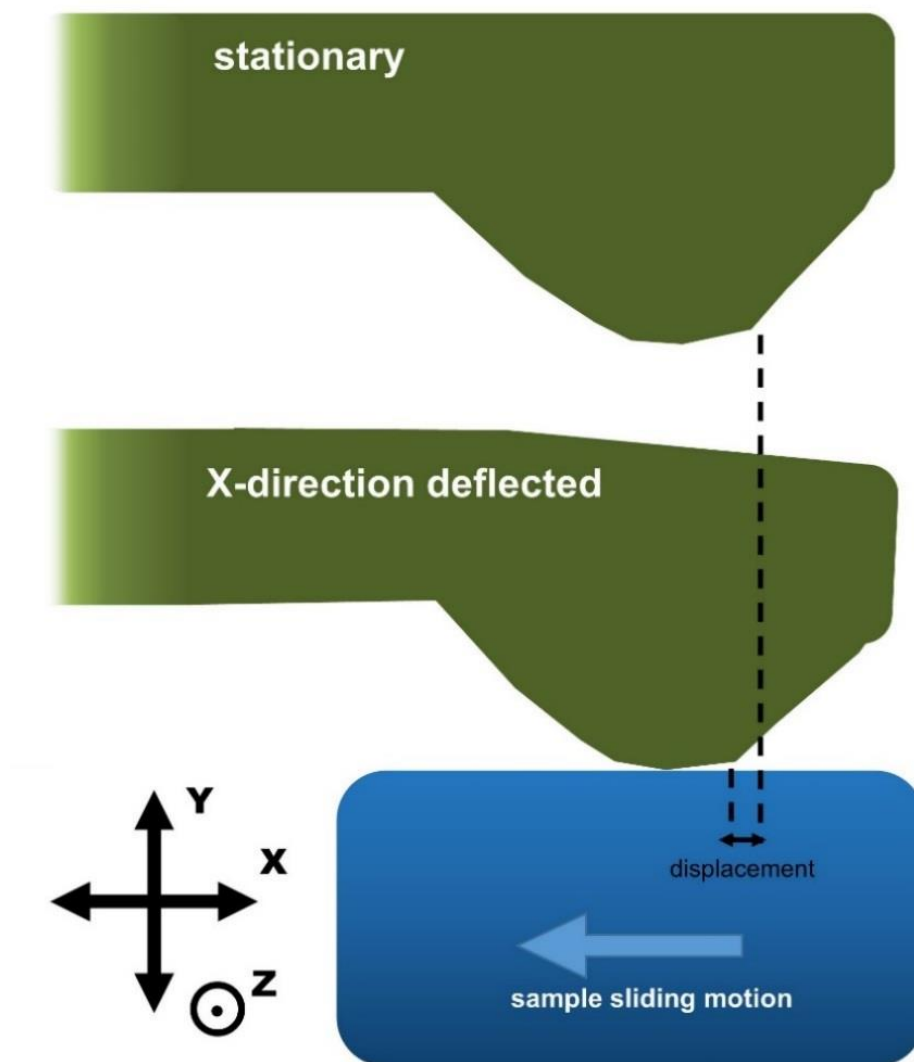


Figure 7.4 The theoretical method to measure the friction force during sliding. As the sample moves to the left, indicated by the blue arrow, the displacement of the AFM tip can be measured in the X-direction, indicated by the black arrows. This measurement would be done in post facto video frame-by-frame analysis.

7.3.2 Further Analysis of Current Experiments

There are more characterization studies that could be done with MoS₂ nanoflakes on Si substrates. MoS₂ is a solid lubricant with many applications in industry and space lubrication. It proves a good lubricating film to study, as the mechanisms can also help us understand other

lamellar lubricants, such as other dichalcogenides or graphite. Continuing work to control the angle of attack, the adhesion forces, and the force in the piezo controller would all be useful to have more quantitative measurements.

With our current in situ sliding methods, one simple aspect to explore is to increase the Y-direction force through moving the sample into further deflection of the AFM cantilever. The force can be approximated through the deflection. The experiments in Chapters 4 and 5 were primarily done at neutral normal force. The sliding, rolling, adhesion measurements of MoS₂ could be redone at two or more levels of increased force. Similarly, as another potential control, the adhesion pull-off force could be measured for snap-to-contact natural adhesion versus adhesion after being held at an elevated force. The time held at the higher force contact could be varied to determine if force impacts the adhesion bonding.

The sheet spacing of MoS₂ nanoflakes could also be investigated at higher forces. Questions include: Does the sheet spacing change by a measurable amount with increased force? What about the ball wear particle, do those squish under a certain applied force? If the diameter of the ball reduces from compression, it may indicate how crumpled the balls are when they roll up (tightly packed or loosely bent up into a sphere?). With any of the tests at higher forces, a concern would be breaking the AFM cantilever. The experimenter would need to keep the amount of deflection in mind. Another relevant concern would be if the forces applied are applicable to real-world forces exhibited in MoS₂ coatings, which could be estimated with force per unit area calculations. Overall, simple changes in forces and time of contact could present valuable comparison situations that would reveal nanoscale interactions in the MoS₂ sheets.

Previous experiments, particularly the SIFT experiments in Chapter 4, showed that a stack of flakes would continue to fracture until a single flake was left adhered to the surface. Figure 5.8 showed this flake progression; after about six flake fractures, the bottom flake was stable. The control still needs to be done of how stable this last flake actually is. Relevant questions include: What force would it take to remove the last flake after multiple SIFT layers have been created? For how many slides back and forth could it remain stable: 10, 100, or 1,000? If that single flake can be exfoliated, how does it break up? How is it different than SIFT? We know that there are many mechanisms that occur in these lamellar lubricants, so we would expect a new mechanism to govern after SIFT layers form.

For simple chemical analysis of the MoS₂ nanoflakes, EELS spectra could be collected for Mo or S during sliding to see if there are chemical changes during sliding. This does not seem like it would be apparent, but it would be a good control. One chemical process important to MoS₂ is oxidizing in a humid environment. Currently, the MoS₂ samples are stored in air and then analyzed in vacuum. The amount of time sitting in air could be control and measured to see if that changes the sliding properties. The effects of storing in air have not been apparent, but it would be a good control to check for damaging oxidation. The best method to study the atmospheric effects on MoS₂ would be to do these in situ experiments in an environmental TEM (ETEM). The humidity could be controlled during sliding through introducing water. Our holders have been used in an ETEM before by M'ndange-Pfupfu et al. [330], and his study was able to capture tribocorrosion reactions in situ. Similarly, graphite has poor performance in vacuum, and in situ sliding could be analyzed in humid and dry environments. ETEM could provide interesting tribochemical environments for MoS₂ and graphite.

7.3.3 Similar Materials

Future experiments with other lamellar solids could easily be adapted from the current sample preparation techniques. Similar sliding testing could be done in situ, including testing for SIFT behavior, wear, and adhesion. MoS₂ is a dichalcogenide, others include WS₂ and NbSe₂ [20,27]. The MoS₂ nanoflakes were available commercially at a minor cost, so it would be worthwhile to see what varieties of MoS₂ and other lamellar solids are easily available. Even similar studies involving graphite nanoflakes could be interesting for comparison. For example, do graphite nanoflakes have similar SIFT layer forming behavior? The size or morphology of the flake may also change the mechanisms during sliding. It could be interesting to purchase various types of flakes and test their differences.

Another research direction could be to investigate the amorphous-to-crystalline transition that is known to occur for lamellar solid lubricants during sliding. This basal plane reorientation has been shown for MoS₂ at the macroscale in films [36,175], yet has not been demonstrated at the nanoscale. An in situ progression of the transition could be insightful. Purchasing or synthesizing amorphous MoS₂ may be difficult, however, and the geometry of the experiment may be better suited for the Nanofactory STM holder. In that setup, the crystallinity would be measured through diffraction through a film of MoS₂. More preparation would need to be done to determine if this amorphous transition experiment is possible and worthwhile.

7.3.4 New Collaborations for In Situ Sliding

Another possibility for in situ sliding experiments is to test materials from collaborators. Obtaining collaborator materials is especially enticing if their materials are difficult to synthesize,

interesting tribologically, and are nanoscale particles in solution. Solutions can be drop cast on a fractured Si substrate, which we are already doing now for the MoS₂ samples. Collaborations can be particularly beneficial if the material is being investigated on the macroscale and has been statically characterized on the nanoscale, yet the nanoscale sliding mechanisms are unknown. One possible material for in situ sliding in the AFM setup is from Dr. Diana Berman, who works with Dr. Ali Erdimer at Argonne National Laboratory. Berman investigates nanosheets of graphene and nanodiamonds as surface lubricants, with results recently published in Science [331]. She has found that the graphene sheets roll around the nanodiamonds to form nanoscrolls, which are particularly beneficial lubricants. She has observed the nanoscrolls in TEM post facto. Molecular dynamic simulations have predicted how the graphene wraps around the nanodiamonds during sliding, but the actual mechanism of formation has not been shown in situ. In situ sliding tests could clarify the MD simulations.

Another in situ experiment could be to roll the nanodiamonds between two rough surfaces. This is inspired by a proposed mechanism by Olga Shenderova from Adámas Nanotechnologies, Inc. / International Technology Center, USA during the Gordon Research Conference on Tribology. She suggested that nanodiamonds polish a rough surface during in situ lubrication. The polishing was just theorized though, and drawn as a cartoon. Many questions were brought up if this was possible. Sliding against nanodiamonds could be a possible in situ experiment to demonstrate what happens with nanodiamonds during use.

One collaboration with Dr. Gordon Krauss and Dr. Albert Dato from Harvey Mudd College is already underway. This project will be continued with Alex Lin and Xiao-xiang Yu. Dato synthesizes crumpled graphene, which are wrinkly graphene nanoscale sheets a few sheets thick.

They can control the amount of crumple through sonication. They have found that during tribometer tests in oil, the friction is lower with the crumpled graphene as opposed to regular graphene. They are curious why the crumpled graphene performs better and what the sliding mechanism might look like. For the initial investigations, we plan to use the sample fractured Si substrate and drop casting of the crumpled graphene. Using the same AFM holder, we can look at the edge profile of the material to see how the sliding, deformation, and degradation take place.

For MoS₂ investigations, there are two directions for these experiments. The first is more theoretical and mechanistic: to look at the nanoscale shape, size, morphology, and behavior of MoS₂ during various sliding conditions. Sheet interactions and degradation processes could be modeled. The ability to observe the buried interface is the strength of the in situ holder, and these very fundamental studies are good directions for future experiments. The other direction to consider, however, is the more applied direction. Some MoS₂ particles are commercially available as sprays and some have been tested as base oil additives. Focusing in situ research on the more industrially-inclined particles may develop some knowledge that can be more quickly applied to industry. Along with in situ work, applied studies would be needed in conjunction, such as using the particles in oil in a tribometer. Other research specialties, including industrial collaborations, would be necessary to make the research fruitful.

8 References

1. Dowson, D.: History of tribology. Addison-Wesley Longman Limited, London, England (1979)
2. Jost, H.P.: Tribology—origin and future. *Wear* **136**(1), 1-17 (1990).
3. Schmitt, G.: Global needs for knowledge dissemination, research, and development in materials deterioration and corrosion control. New York, NY: The World Corrosion Organization (2009).
4. Luan, B., Robbins, M.O.: The breakdown of continuum models for mechanical contacts. *Nature* **435**(7044), 929-932 (2005).
5. Bowden, F., Tabor, D.: Friction and Lubrication of Solids, vol. I. Clarendon. In. Oxford, (1950)
6. Bowden, F., Tabor, D.: Mechanism of metallic friction. *Nature* **150**(3798), 197-199 (1942).
7. Hallab, N., Merritt, K., Jacobs, J.J.: Metal sensitivity in patients with orthopaedic implants. *J Bone Joint Surg Am* **83-A**(3), 428-436 (2001).
8. Kurtz, S., Ong, K., Lau, E., Mowat, F., Halpern, M.: Projections of primary and revision hip and knee arthroplasty in the United States from 2005 to 2030. *J Bone Joint Surg* **89**(4), 780-785 (2007).
9. Pramanik, S., Agarwal, A.K., Rai, K.N.: Chronology of total hip joint replacement and materials development. *Trends Biomat Artif Organs* **19**(1), 15-26 (2005).
10. Complete Total Hip Replacement System. In. Drexel University Implant Research Center, biomed.drexel.edu/implantcenter/, (2013)
11. Clemow, A.J., Daniell, B.L.: Solution treatment behavior of Co-Cr-Mo alloy. *J Biomed Mater Res* **13**(2), 265-279 (1979). doi:10.1002/jbm.820130208
12. Gomez, M., Mancha, H., Salinas, A., Rodrigues, J., Escobedo, J., Castro, M.R., Mendez, M.: Relationship between microstructure and ductility of investment cast ASTM F-75 implant alloys. *J Biomed Mater Res* **34**(2), 157-163 (1997).
13. Nevelos, J., Shelton, J., Fisher, J.: Metallurgical considerations in the wear of metal-on-metal hip bearings. *Hip Int* **14**, 1-10 (2004).

14. Ratner, B.D., Hoffman, A.S., Schoen, F.J., Lemons, J.E. (eds.): *Biomaterials Science: An Introduction to Materials in Medicine*, 2 ed. Elsevier Academic Press, London (2004)
15. Saldivar-Garcia, A.J., Lopez, H.F.: Microstructural effects on the wear resistance of wrought and as-cast Co-Cr-Mo-C implant alloys. *J Biomed Mater Res A* **74**(2), 269-274 (2005). doi:10.1002/jbm.a.30392
16. Liao, Y., Pourzal, R., Wimmer, M.A., Jacobs, J.J., Fischer, A., Marks, L.D.: Graphitic Tribological Layers in Metal-on-Metal Hip Replacements. *Science* **334**(6063), 1687-1690 (2011). doi:10.1126/science.1213902
17. Wimmer, M.A., Fischer, A., Büscher, R., Pourzal, R., Sprecher, C., Hauert, R., Jacobs, J.J.: Wear mechanisms in metal-on-metal bearings: The importance of tribochemical reaction layers. *Journal of Orthopaedic Research* **28**(4), 436-443 (2010). doi:10.1002/jor.21020
18. Wimmer, M.A., Sprecher, C., Hauert, R., Tager, G., Fischer, A.: Tribochemical reaction on metal-on-metal hip joint bearings - A comparison between in-vitro and in-vivo results. *Wear* **255**(7-12), 1007-1014 (2003). doi:10.1016/S0043-1648(03)00127-3
19. Milošev, I., Remškar, M.: In vivo production of nanosized metal wear debris formed by tribochemical reaction as confirmed by high-resolution TEM and XPS analyses. *Journal of Biomedical Materials Research Part A* **91A**(4), 1100-1110 (2009). doi:10.1002/jbm.a.32301
20. Scharf, T.W., Prasad, S.V.: Solid lubricants: a review. *J Mater Sci* **48**(2), 511-531 (2013). doi:10.1007/s10853-012-7038-2
21. Singer, I.L., Dvorak, S.D., Wahl, K.J., Scharf, T.W.: Role of third bodies in friction and wear of protective coatings. *Journal of Vacuum Science & Technology A* **21**(5), S232-S240 (2003). doi:10.1116/1.1599869
22. Singer, I.L., Pollock, H.: *Fundamentals of friction: macroscopic and microscopic processes*, vol. 220. Springer Science & Business Media, Braunlage, Germany (2012)
23. Conley, P.L.: *Space vehicle mechanisms: elements of successful design*. John Wiley & Sons, New York, NY (1998)
24. Zhao, X., Perry, S.S.: The Role of Water in Modifying Friction within MoS₂ Sliding Interfaces. *ACS Applied Materials & Interfaces* **2**(5), 1444-1448 (2010). doi:10.1021/am100090t

25. Voevodin, A., Zabinski, J.: Nanocomposite and nanostructured tribological materials for space applications. *Composites Science and Technology* **65**(5), 741-748 (2005). doi:10.1016/j.compscitech.2004.10.008
26. Holmberg, K., Matthews, A.: *Coatings Tribology: Properties, Mechanisms, Techniques and Applications in Surface Engineering*. Elsevier Science, Amsterdam (2009)
27. Sliney, H.E.: Solid lubricant materials for high temperatures—a review. *Tribol Int* **15**(5), 303-315 (1982). doi:10.1016/0301-679x(82)90089-5
28. Martin, J.-M., Erdemir, A., Martin, J.: *Superlubricity of Molybdenum Disulfide*. Elsevier BV: Oxford, UK, (2005)
29. Mosleh, M., Atnafu, N.D., Belk, J.H., Nobles, O.M.: Modification of sheet metal forming fluids with dispersed nanoparticles for improved lubrication. *Wear* **267**(5-8), 1220-1225 (2009). doi:10.1016/j.wear.2008.12.074
30. Yanxia, W., Hongxuan, L., Li, J., Yinping, Y., Jianmin, C., Huidi, Z.: Preparation and properties of MoS₂/a-C films for space tribology. *Journal of Physics D: Applied Physics* **46**(42), 425301 (2013).
31. Khare, H.S., Burris, D.L.: The Effects of Environmental Water and Oxygen on the Temperature-Dependent Friction of Sputtered Molybdenum Disulfide. *Tribol Lett* **52**(3), 485-493 (2013). doi:10.1007/s11249-013-0233-8
32. Hisakado, T., Tsukizoe, T., Yoshikawa, H.: Lubrication Mechanism of Solid Lubricants in Oils. *Journal of Lubrication Technology* **105**(2), 245-252 (1983). doi:10.1115/1.3254585
33. Li, J.L., Xiong, D.S.: Tribological properties of nickel-based self-lubricating composite at elevated temperature and counterface material selection. *Wear* **265**(3-4), 533-539 (2008). doi:10.1016/j.wear.2007.09.005
34. Godet, M.: The third-body approach: A mechanical view of wear. *Wear* **100**(1-3), 437-452 (1984). doi:10.1016/0043-1648(84)90025-5
35. Singer, I.L., Fayeulle, S., Ehni, P.D.: Friction and Wear Behavior of Tin in Air - the Chemistry of Transfer Films and Debris Formation. *Wear* **149**(1-2), 375-394 (1991). doi:10.1016/0043-1648(91)90386-9
36. Hu, J.J., Wheeler, R., Zabinski, J.S., Shade, P.A., Shiveley, A., Voevodin, A.A.: Transmission Electron Microscopy Analysis of Mo–W–S–Se Film Sliding Contact Obtained by Using

- Focused Ion Beam Microscope and In Situ Microtribometer. *Tribol Lett* **32**(1), 49-57 (2008). doi:10.1007/s11249-008-9360-z
37. Wahl, K.J., Dunn, D.N., Singer, I.L.: Wear behavior of Pb–Mo–S solid lubricating coatings. *Wear* **230**(2), 175-183 (1999). doi:10.1016/s0043-1648(99)00100-3
38. Lahouij, I., Dassenoy, F., de Knoop, L., Martin, J.M., Vacher, B.: In Situ TEM Observation of the Behavior of an Individual Fullerene-Like MoS₂ Nanoparticle in a Dynamic Contact. *Tribol Lett* **42**(2), 133-140 (2011). doi:10.1007/s11249-011-9755-0
39. Tannous, J., Dassenoy, F., Lahouij, I., Le Mogne, T., Vacher, B., Bruhacs, A., Tremel, W.: Understanding the Tribochemical Mechanisms of IF-MoS₂ Nanoparticles Under Boundary Lubrication. *Tribol Lett* **41**(1), 55-64 (2011). doi:10.1007/s11249-010-9678-1
40. Lahouij, I., Dassenoy, F., Vacher, B., Martin, J.M.: Real Time TEM Imaging of Compression and Shear of Single Fullerene-Like MoS₂ Nanoparticle. *Tribol Lett* **45**(1), 131-141 (2012). doi:10.1007/s11249-011-9873-8
41. Lahouij, I., Dassenoy, F., Vacher, B., Sinha, K., Brass, D.A., Devine, M.: Understanding the Deformation of Soot Particles/Agglomerates in a Dynamic Contact: TEM In Situ Compression and Shear Experiments. *Tribol Lett* **53**(1), 91-99 (2014). doi:10.1007/s11249-013-0246-3
42. Lahouij, I., Vacher, B., Dassenoy, F.: Direct observation by in situ transmission electron microscopy of the behaviour of IF-MoS₂ nanoparticles during sliding tests: influence of the crystal structure. *Lubrication Science* **26**(3), 163-173 (2014).
43. Binnig, G., Quate, C.F., Gerber, C.: Atomic Force Microscope. *Physical Review Letters* **56**(9), 930-933 (1986).
44. Mate, C.M., McClelland, G.M., Erlandsson, R., Chiang, S.: Atomic-Scale Friction of a Tungsten Tip on a Graphite Surface. *Physical Review Letters* **59**(17), 1942-1945 (1987).
45. Lin, L.Y., Kim, D.E., Kim, W.K., Jun, S.C.: Friction and wear characteristics of multi-layer graphene films investigated by atomic force microscopy. *Surf Coat Tech* **205**(20), 4864-4869 (2011). doi:10.1016/j.surfcoat.2011.04.092
46. Krim, J., Solina, D.H., Chiarello, R.: Nanotribology of a Kr Monolayer - a Quartz-Crystal Microbalance Study of Atomic-Scale Friction. *Physical Review Letters* **66**(2), 181-184 (1991).

47. Watts, E.T., Krim, J., Widom, A.: Experimental-Observation of Interfacial Slippage at the Boundary of Molecularly Thin-Films with Gold Substrates. *Phys. Rev. B* **41**(6), 3466-3472 (1990).
48. Dawson, B.D.: Tribo-induced temperature rise and melting at a single asperity sliding contact. Ph.D., North Carolina State University (2010)
49. Tabor, D., Winterto.Rh: Direct Measurement of Normal and Retarded Van Der Waals Forces. *Proceedings of the Royal Society of London Series a-Mathematical and Physical Sciences* **312**(1511), 435-450 (1969).
50. Scharf, T.W., Singer, I.L.: Monitoring Transfer Films and Friction Instabilities with In Situ Raman Tribometry. *Tribol Lett* **V14**(1), 3-8 (2003).
51. McDevitt, N.T., Donley, M.S., Zabinski, J.S.: Utilization of Raman-Spectroscopy in Tribochemistry Studies. *Wear* **166**(1), 65-72 (1993).
52. Cann, P.M., Spikes, H.A.: In Lubro Studies of Lubricants in Ehd Contacts Using Ftir Absorption-Spectroscopy. *Tribology Transactions* **34**(2), 248-256 (1991).
53. Scharf, T.W., Singer, I.L.: Quantification of the thickness of carbon transfer films using Raman tribometry. *Tribol Lett* **14**(2), 137-145 (2003).
54. Jean-Michel, M., Hong, L., Thierry Le, M., Maryline, M.: Low-Temperature Friction in the XPS Analytical Ultrahigh Vacuum Tribotester. *Tribol Lett* **V14**(1), 25-31 (2003).
55. Gnecco, E., Bennewitz, R., Meyer, E.: Abrasive wear on the atomic scale. *Phys Rev Lett* **88**(21), 215501 (2002). doi:10.1103/PhysRevLett.88.215501
56. Gotsmann, B., Lantz, M.A.: Atomistic wear in a single asperity sliding contact. *Phys Rev Lett* **101**(12), 125501 (2008). doi:10.1103/PhysRevLett.101.125501
57. Bhaskaran, H., Gotsmann, B., Sebastian, A., Drechsler, U., Lantz, M.A., Despont, M., Jaroenapibal, P., Carpick, R.W., Chen, Y., Sridharan, K.: Ultralow nanoscale wear through atom-by-atom attrition in silicon-containing diamond-like carbon. *Nat Nanotechnol* **5**(3), 181-185 (2010).
58. Figuera, J.d.l., Pohl, K., Fuente, O.R.d.l., Schmid, A.K., Bartelt, N.C., Carter, C.B., Hwang, R.Q.: Direct observation of misfit dislocation glide on surfaces. *Physical Review Letters* **86**(17), 3819-3822 (2001).

59. Merkle, A., Erdemir, A., Eryilmaz, O., Johnson, J., Marks, L.: *In situ* TEM studies of tribo-induced bonding modifications in near-frictionless carbon films. *Carbon* **48**(3), 587-591 (2010).
60. M'Ndange-Pfupfu, A., Eryilmaz, O., Erdemir, A., Marks, L.: Quantification of sliding-induced phase transformation in N3FC diamond-like carbon films. *Diam Relat Mater* **20**(8), 1143-1148 (2011).
61. M'ndange-Pfupfu, A., Ciston, J., Eryilmaz, O., Erdemir, A., Marks, L.: Direct observation of tribochemically assisted wear on diamond-like carbon thin films. *Tribol Lett* **49**(2), 351-356 (2013).
62. Liao, Y., EswaraMoorthy, S., Marks, L.: Direct observation of tribological recrystallization. *Philosophical Magazine Letters* **90**(3), 219-223 (2010).
63. Liao, Y., Marks, L.D.: Direct observation of layer-by-layer wear. *Tribol Lett* **59**(3), 1-11 (2015).
64. Liao, Y., Hoffman, E., Marks, L.D.: Nanoscale abrasive wear of CoCrMo in *In Situ* TEM sliding. *Tribol Lett* **57**(3), 1-6 (2015).
65. Panigrahi, P., Liao, Y., Mathew, M.T., Fischer, A., Wimmer, M.A., Jacobs, J.J., Marks, L.D.: Intergranular pitting corrosion of CoCrMo biomedical implant alloy. *J Biomed Mater Res B Appl Biomater* **102**(4), 850-859 (2014). doi:10.1002/jbm.b.33067
66. Hoffman, E.E., Lin, A., Liao, Y., Marks, L.D.: Grain Boundary Assisted Crevice Corrosion in CoCrMo Alloys. *Corrosion* **72**(11), 1445-1461 (2016). doi:10.5006/2108
67. Bashinskaya, B., Zimmerman, R.M., Walcott, B.P., Antoci, V.: Arthroplasty Utilization in the United States is Predicted by Age-Specific Population Groups. *ISRN Orthop* **2012**, 185938 (2012). doi:10.5402/2012/185938
68. Mihalko, W.M., Wimmer, M.A., Pacione, C.A., Laurent, M.P., Murphy, R.F., Rider, C.: How have alternative bearings and modularity affected revision rates in total hip arthroplasty? *Clinical Orthopaedics and Related Research* **472**(12), 3747-3758 (2014).
69. Gilbert, J.L., Buckley, C.A., Jacobs, J.J.: In-Vivo Corrosion of Modular Hip-Prosthesis Components in Mixed and Similar Metal Combinations - the Effect of Crevice, Stress, Motion, and Alloy Coupling. *Journal of Biomedical Materials Research* **27**(12), 1533-1544 (1993). doi:10.1002/jbm.820271210

70. Yan, Y., Neville, A., Dowson, D., Williams, S.: Tribocorrosion in implants - assessing high carbon and low carbon Co-Cr-Mo alloys by in situ electrochemical measurements. *Tribol Int* **39**(12), 1509-1517 (2006). doi:10.1016/j.triboint.2006.01.016
71. Gilbert, J., Mali, S., Urban, R.M., Silverton, C., Jacobs, J.J.: In vivo oxide-induced stress corrosion cracking of Ti-6Al-4V in a neck-stem modular taper: Emergent behavior in a new mechanism of in vivo corrosion. *J Biomed Mater Res B* **100B**(2), 584-594 (2012).
72. Merritt, K., Brown, S.A.: Distribution of cobalt chromium wear and corrosion products and biologic reactions. *Clin Orthop Relat R* **329**, S233-S243 (1996).
73. Witzleb, W.C., Zeigler, J., Krummenauer, F., Neumeister, V., Guenther, K.P.: Exposure to chromium, cobalt and molybdenum from metal-on-metal total hip replacement and hip resurfacing arthroplasty. *Acta Orthop* **77**(5), 697-705 (2006).
74. Vendittoli, P.A., Mottard, S., Roy, A.G., Dupont, C., Lavigne, M.: Chromium and cobalt ion release following the Durom high carbon content, forged metal-on-metal surface replacement of the hip. *J Bone Joint Surg Br* **89**(4), 441-448 (2007).
75. Amstutz, H.C., Campbell, P.A., Dorey, F.J., Johnson, A.J., Skipor, A.K., Jacobs, J.J.: Do ion concentrations after metal-on-metal hip resurfacing increase over time? A prospective study. *J Arthroplasty* **28**(4), 695-700 (2013).
76. Bain, E., Aborn, R., Rutherford, J.: The nature and prevention of intergranular corrosion in austenitic stainless steels. *Transactions of the American Society for Steel Treating* **21**(1), 481-509 (1933).
77. Smethurst, E., Waterhouse, R.B.: Causes of Failure in Total Hip Prostheses. *J Mater Sci* **12**(9), 1781-1792 (1977). doi:10.1007/Bf00566238
78. Placko, H.E., Brown, S.A., Payer, J.H.: Effects of microstructure on the corrosion behavior of CoCr porous coatings on orthopedic implants. *J Biomed Mater Res* **39**(2), 292-299 (1998). doi:10.1002/(sici)1097-4636(199802)39:2
79. Palumbo, G., Aust, K.T.: Structure-Dependence of Intergranular Corrosion in High-Purity Nickel. *Acta Metall Mater* **38**(11), 2343-2352 (1990). doi:10.1016/0956-7151(90)90101
80. Bruemmer, S.M., Charlot, L.A.: Development of Grain-Boundary Chromium Depletion in Type-304 and Type-316 Stainless-Steels. *Scripta Metall Mater* **20**(7), 1019-1024 (1986). doi:10.1016/0036-9748(86)90428-X

81. Jacobs, J.J., Urban, R.M., Gilbert, J.L., Skipor, A.K., Black, J., Jasty, M., Galante, J.O.: Local and Distant Products From Modularity. *Clinical Orthopaedics and Related Research* **319**, 94-105 (1995).
82. Jacobs, J.J., Gilbert, J.L., Urban, R.M.: Current Concepts Review - Corrosion of Metal Orthopaedic Implants*. *The Journal of Bone & Joint Surgery* **80**(2), 268-282 (1998).
83. Julian, L.C., Munoz, A.I.: Influence of microstructure of HC CoCrMo biomedical alloys on the corrosion and wear behaviour in simulated body fluids. *Tribol Int* **44**(3), 318-329 (2011).
84. Vidal, C.V., Munoz, A.I.: Effect of thermal treatment and applied potential on the electrochemical behaviour of CoCrMo biomedical alloy. *Electrochim Acta* **54**(6), 1798-1809 (2009). doi:10.1016/j.electacta.2008.10.018
85. Hernandez-Rodriguez, M., Mercado-Solis, R., Perez-Unzueta, A., Martinez-Delgado, D., Cantú-Sifuentes, M.: Wear of cast metal-metal pairs for total replacement hip prostheses. *Wear* **259**(7), 958-963 (2005).
86. Hall, E.L., Briant, C.L.: Chromium Depletion in the Vicinity of Carbides in Sensitized Austenitic Stainless-Steels. *Metall Trans A* **15**(5), 793-811 (1984). doi:10.1007/Bf02644554
87. Briant, C.L., Andresen, P.L.: Grain-Boundary Segregation in Austenitic Stainless-Steels and Its Effect on Intergranular Corrosion and Stress-Corrosion Cracking. *Metall Trans A* **19**(3), 495-504 (1988). doi:10.1007/Bf02649264
88. Stawstrom, C., Hillert, M.: An Improved Depleted-Zone Theory of Intergranular Corrosion of 18-8 Stainless Steel. *J Iron Steel I* **207**, 77-85 (1969).
89. Gertsman, V.Y., Bruemmer, S.M.: Study of grain boundary character along intergranular stress corrosion crack paths in austenitic alloys. *Acta Materialia* **49**(9), 1589-1598 (2001). doi:10.1016/S1359-6454(01)00064-7
90. Briant, C.L.: Grain-Boundary Segregation of Phosphorus and Sulfur in Type-304l and Type-316l Stainless-Steel and Its Effect on Intergranular Corrosion in the Huey Test. *Metall Trans A* **18**(4), 691-699 (1987). doi:10.1007/Bf02649485
91. Song, G., Atrens, A.: Recent insights into the mechanism of magnesium corrosion and research suggestions. *Adv Eng Mater* **9**(3), 177-183 (2007). doi:10.1002/adem.200600221

92. Song, G.L., Atrens, A.: Understanding magnesium corrosion - A framework for improved alloy performance. *Adv Eng Mater* **5**(12), 837-858 (2003). doi:10.1002/adem.200310405
93. Winzer, N., Atrens, A., Song, G.L., Ghali, E., Dietzel, W., Kainer, K.U., Hort, N., Blawert, C.: A critical review of the stress corrosion cracking (SCC) of magnesium alloys. *Adv Eng Mater* **7**(8), 659-693 (2005). doi:10.1002/adem.200500071
94. Zhao, M.C., Liu, M., Song, G.L., Atrens, A.: Influence of the beta-phase morphology on the corrosion of the Mg alloy AZ91. *Corros Sci* **50**(7), 1939-1953 (2008). doi:10.1016/j.corsci.2008.04.01
95. Houdremont, R., Bennek, H.: Federstahle. *Stahl u. Eisen* **52**, 660 (1932).
96. Kain, V., Prasad, R.C., De, P.K.: Testing sensitization and predicting susceptibility to intergranular corrosion and intergranular stress corrosion cracking in austenitic stainless steels. *Corrosion* **58**(1), 15-37 (2002).
97. Clarke, W., Cowan, R., Walker, W.: Comparative methods for measuring degree of sensitization in stainless steel. *Intergranular Corrosion of Stainless Alloys*, ASTM STP **656**, 99 (1978).
98. Singh, R., Chowdhury, S.G., Kumar, B.R., Das, S.K., De, P.K., Chattoraj, I.: The importance of grain size relative to grain boundary character on the sensitization of metastable austenitic stainless steel. *Scripta Mater* **57**(3), 185-188 (2007). doi:10.1016/j.scriptamat.2007.04.017
99. Singh, R., Ravikumar, B., Kumar, A., Dey, P.K., Chattoraj, I.: The effects of cold working on sensitization and intergranular corrosion behavior of AISI 304 stainless steel. *Metall Mater Trans A* **34a**(11), 2441-2447 (2003). doi:10.1007/s11661-003-0004-5
100. Zhou, Y., Aust, K.T., Erb, U., Palumbo, G.: Effects of grain boundary structure on carbide precipitation in 304L stainless steel. *Scripta Mater* **45**(1), 49-54 (2001). doi:10.1016/S1359-6462(01)00990-3
101. Trillo, E.A., Murr, L.E.: A TEM investigation of M₂₃C₆ carbide precipitation behaviour on varying grain boundary misorientations in 304 stainless steels. *J Mater Sci* **33**(5), 1263-1271 (1998). doi:10.1023/A:1004390029071
102. Almanza, E., Murr, L.E.: A comparison of sensitization kinetics in 304 and 316 stainless steels. *J Mater Sci* **35**(13), 3181-3188 (2000). doi:10.1023/A:1004886213848

103. Pardo, A., Merino, M., Coy, A., Viejo, F., Carboneras, M., Arrabal, R.: Influence of Ti, C and N concentration on the intergranular corrosion behaviour of AISI 316Ti and 321 stainless steels. *Acta Materialia* **55**(7), 2239-2251 (2007).
104. Leiva-Garcia, R., Munoz-Portero, M.J., Garcia-Anton, J.: Evaluation of Alloy 146, 279, 900, and 926 sensitization to intergranular corrosion by means of electrochemical methods and image analysis. *Corros Sci* **51**(9), 2080-2091 (2009). doi:10.1016/j.corsci.2009.05.036
105. Bruemmer, S.M.: Composition-Based Correlations to Predict Sensitization Resistance of Austenitic Stainless-Steels. *Corrosion* **42**(1), 27-35 (1986).
106. Bruemmer, S.M., Chariot, L.A., Arey, B.W.: Sensitization Development in Austenitic Stainless Steel: Correlation between STEM-EDS and EPR Measurements. *Corrosion* **44**(6), 328-333 (1988). doi:10.5006/1.3583945
107. Valero-Vidal, C., Casabán-Julián, L., Herraiz-Cardona, I., Igual-Muñoz, A.: Influence of carbides and microstructure of CoCrMo alloys on their metallic dissolution resistance. *Materials Science and Engineering: C* **33**(8), 4667-4676 (2013).
108. Rodrigues, W.C., Broilo, L.R., Schaeffer, L., Knornschild, G., Espinoza, F.R.M.: Powder metallurgical processing of Co-28%Cr-6%Mo for dental implants: Physical, mechanical and electrochemical properties. *Powder Technol* **206**(3), 233-238 (2011). doi:10.1016/j.powtec.2010.09.024
109. Lewis, A., Kilburn, M., Papageorgiou, I., Allen, G., Case, C.: Effect of synovial fluid, phosphate-buffered saline solution, and water on the dissolution and corrosion properties of CoCrMo alloys as used in orthopedic implants. *Journal of Biomedical Materials Research Part A* **73**(4), 456-467 (2005).
110. Bettini, E., Eriksson, T., Boström, M., Leygraf, C., Pan, J.: Influence of metal carbides on dissolution behavior of biomedical CoCrMo alloy: SEM, TEM and AFM studies. *Electrochim Acta* **56**(25), 9413-9419 (2011). doi:10.1016/j.electacta.2011.08.028
111. Bruemmer, S.M., Arey, B.W., Charlot, L.A.: Influence of Chromium Depletion on Intergranular Stress-Corrosion Cracking of 304 Stainless-Steel. *Corrosion* **48**(1), 42-49 (1992).
112. Montero-Ocampo, C., Salinas Rodriguez, A.: Effect of carbon content on the resistance to localized corrosion of as-cast cobalt-based alloys in an aqueous chloride solution. *Journal of biomedical materials research* **29**(4), 441-453 (1995).

113. Schlegel, S.M., Hopkins, S., Frary, M.: Effect of grain boundary engineering on microstructural stability during annealing. *Scripta Mater* **61**(1), 88-91 (2009). doi:10.1016/j.scriptamat.2009.03.013
114. Lin, P., Palumbo, G., Erb, U., Aust, K.T.: Influence of Grain-Boundary-Character-Distribution on Sensitization and Intergranular Corrosion of Alloy-600. *Scripta Metallurgica Et Materialia* **33**(9), 1387-1392 (1995). doi:10.1016/0956-716x(95)00420-Z
115. Randle, V.: Twinning-related grain boundary engineering. *Acta Materialia* **52**(14), 4067-4081 (2004). doi:10.1016/j.actamat.2004.05.031
116. Randle, V.: The coincidence site lattice and the 'sigma enigma'. *Mater Charact* **47**(5), 411-416 (2001). doi:10.1016/S1044-5803(02)00193-6
117. Lehockey, E.M., Brennenstuhl, A.M., Thompson, I.: On the relationship between grain boundary connectivity, coincident site lattice boundaries, and intergranular stress corrosion cracking. *Corros Sci* **46**(10), 2383-2404 (2004). doi:10.1016/j.corosci.2004.01.019
118. Shimada, M., Kokawa, H., Wang, Z.J., Sato, Y.S., Karibe, I.: Optimization of grain boundary character distribution for intergranular corrosion resistant 304 stainless steel by twin-induced grain boundary engineering. *Acta Materialia* **50**(9), 2331-2341 (2002). doi:10.1016/S1359-6454(02)00064-2
119. Tedmon, C.S., Vermilye, D.A., Rosolowski, J.H.: Intergranular Corrosion of Austenitic Stainless Steel. *J Electrochem Soc* **118**(2), 192-202 (1971). doi:10.1149/1.2407966
120. Bennett, B.W., Pickering, H.W.: Effect of grain boundary structure on sensitization and corrosion of stainless steel. *Metallurgical Transactions A* **18**(6), 1117-1124 (1991).
121. Povich, M.: Low temperature sensitization of type 304 stainless steel. *Corrosion* **34**(2), 60-65 (1978).
122. Sahlaoui, H., Makhoul, K., Sidhom, H., Philibert, J.: Effects of ageing conditions on the precipitates evolution, chromium depletion and intergranular corrosion susceptibility of AISI 316L: experimental and modeling results. *Mat Sci Eng a-Struct* **372**(1-2), 98-108 (2004). doi:10.1016/j.msea.2003.12.017
123. Stemmer, P., Pourzal, R., Liao, Y.F., Marks, L., Morlock, M., Jacobs, J.J., Wimmer, M.A., Fischer, A.: Microstructure of Retrievals Made from Standard Cast HC-CoCrMo Alloys. *Am Soc Test Mater* **1560**, 251-267 (2013). doi:10.1520/Stp156020120033

124. Palumbo, G., Aust, K.T., Lehockey, E.M., Erb, U., Lin, P.: On a more restrictive geometric criterion for "special" CSL grain boundaries. *Scripta Mater* **38**(11), 1685-1690 (1998). doi:10.1016/S1359-6462(98)00077-3
125. F1537-11, A.: Standard Specification for Wrought Cobalt-28Chromium-6Molybdenum Alloys for Surgical Implants (UNS R31537, UNS R31538, and UNS R31539). ASTM International (2011). doi:10.1520/f1537-11
126. Brandon, D.: The structure of high-angle grain boundaries. *Acta metallurgica* **14**(11), 1479-1484 (1966).
127. Blunt, R.T.: White Light Interferometry—a production worthy technique for measuring surface roughness on semiconductor wafers. In: Proceedings of CS MANTECH Conference, Vancouver, British Columbia, Canada 2006, pp. 59-62
128. Miller, M.K., Russell, K.F., Thompson, K., Alvis, R., Larson, D.J.: Review of Atom Probe FIB-Based Specimen Preparation Methods. *Microscopy and Microanalysis* **13**(06), 428-436 (2007). doi:10.1017/S1431927607070845
129. Fournelle, R., Clark, J.: The genesis of the cellular precipitation reaction. *Metallurgical Transactions* **3**(11), 2757-2767 (1972).
130. Mehmood, M., Zhang, B.-P., Akiyama, E., Habazaki, H., Kawashima, A., Asami, K., Hashimoto, K.: Experimental evidence for the critical size of heterogeneity areas for pitting corrosion of Cr-Zr alloys in 6 M HCl. *Corros Sci* **40**(1), 1-17 (1998).
131. Lucente, A.M., Scully, J.R.: Pitting and alkaline dissolution of an amorphous–nanocrystalline alloy with solute-lean nanocrystals. *Corros Sci* **49**(5), 2351-2361 (2007).
132. Kelly, W.K., Iyer, R.N., Pickering, H.W.: Another Grain Boundary Corrosion Process in Sensitized Stainless Steel. *J Electrochem Soc* **140**(11), 3134-3140 (1993). doi:10.1149/1.2220998
133. Frankenthal, R., Pickering, H.: Intergranular corrosion of a ferritic stainless steel. *J Electrochem Soc* **120**(1), 23-26 (1973).
134. Alonso, J.A., March, N.H.: *Electrons In Metals And Alloys*. Elsevier Science, San Diego (2012)

135. Shibuta, Y., Takamoto, S., Suzuki, T.: Dependence of the grain boundary energy on the alloy composition in the bcc iron-chromium alloy: A molecular dynamics study. *Comp Mater Sci* **44**(4), 1025-1029 (2009). doi:10.1016/j.commatsci.2008.07.013
136. Sangwal, K.: *Etching of Crystals: Theory, Experiment and Application*. Elsevier Science, North-Holland (2012)
137. Chatterjee, U.K., Bose, S.K., Roy, S.K.: *Environmental Degradation of Metals: Corrosion Technology Series*. Taylor & Francis, New York (2001)
138. Wood, G.C., Wright, I.G., Hodgkiess, T., Whittle, D.P.: A Comparison of the Oxidation of Fe&&bond;Cr, Ni□Cr and Co□Cr alloys in oxygen and water vapour. *Materials and Corrosion* **21**(11), 900-910 (1970). doi:10.1002/maco.19700211105
139. Martin, E.J., Pourzal, R., Mathew, M.T., Shull, K.R.: Dominant role of molybdenum in the electrochemical deposition of biological macromolecules on metallic surfaces. *Langmuir* **29**(15), 4813-4822 (2013).
140. Mathew, M.T., Jacobs, J.J., Wimmer, M.A.: Wear-Corrosion Synergism in a CoCrMo Hip Bearing Alloy Is Influenced by Proteins. *Clinical Orthopaedics and Related Research*® **470**(11), 3109-3117 (2012). doi:10.1007/s11999-012-2563-5
141. Lin, A., Hoffman, E., Marks, L.: Effects of Grain Boundary Misorientation and Chromium Segregation on Corrosion of CoCrMo Alloys. *Corrosion* (2016).
142. Wolford, M.L., Palso, K., Bercovitz, A.: Hospitalization for total hip replacement among inpatients aged 45 and over: United States, 2000-2010. *NCHS Data Brief*(186), 1-8 (2015).
143. Jacobsson, S.A., Djerf, K., Wahlstrom, O.: 20-year results of McKee-Farrar versus Charnley prosthesis. *Clinical Orthopaedics and Related Research*(329), S60-S68 (1996).
144. Hart, A.J., Quinn, P.D., Sampson, B., Sandison, A., Atkinson, K.D., Skinner, J.A., Powell, J.J., Mosselmans, J.F.: The chemical form of metallic debris in tissues surrounding metal-on-metal hips with unexplained failure. *Acta Biomater* **6**(11), 4439-4446 (2010). doi:10.1016/j.actbio.2010.06.006
145. Dorr, L.D., Wang, Z.I., Longjohn, D.B., Dubois, B., Murken, R.: Total hip arthroplasty with use of the metasul metal-on-metal articulation - Four to seven-year results. *Journal of Bone and Joint Surgery-American Volume* **82A**(6), 789-798 (2000).

146. Delaunay, C.P., Bonnomet, F., Clavert, P., Laffargue, P., Migaud, H.: THA using metal-on-metal articulation in active patients younger than 50 years. *Clin Orthop Relat Res* **466**(2), 340-346 (2008). doi:10.1007/s11999-007-0045-y
147. Pande, C.S., Suenaga, M., Vyas, B., Isaacs, H.S., Harling, D.F.: Direct evidence of chromium depletion near the grain boundaries in sensitized stainless steels. *Scripta Metall Mater* **11**(8), 681-684 (1977). doi:10.1016/0036-9748(77)90138-7
148. Montero-Ocampo, C., Martínez, E.L.: Effect of carbon content on the electrochemical impedance of as-cast CoCrMo Alloys. *ECS Transactions* **19**(33), 37-48 (2009).
149. Liao, Y., Pourzal, R., Stemmer, P., Wimmer, M.A., Jacobs, J.J., Fischer, A., Marks, L.D.: New insights into hard phases of CoCrMo metal-on-metal hip replacements. *J Mech Behav Biomed Mater* **12**, 39-49 (2012). doi:10.1016/j.jmbbm.2012.03.013
150. Watanabe, T., Tsurekawa, S.: The control of brittleness and development of desirable mechanical properties in polycrystalline systems by grain boundary engineering. *Acta Materialia* **47**(15-16), 4171-4185 (1999). doi:10.1016/S1359-6454(99)00275-X
151. Pan, Y., Adams, B.L., Olson, T., Panayotou, N.: Grain-boundary structure effects on intergranular stress corrosion cracking of Alloy X-750. *Acta Materialia* **44**(12), 4685-4695 (1996).
152. Watanabe, T.: Structural Effects on Grain Boundary Segregation, Hardening and Fracture. *Journal de Physique Colloques* **46**(C4), 555-566 (1985).
153. Liu, H.W., Gao, M., Harlow, D.G., Wei, R.P.: Grain-Boundary Character, and Carbide Size and Spatial-Distribution in a Ternary Nickel-Alloy. *Scripta Metallurgica Et Materialia* **32**(11), 1807-1812 (1995). doi:Doi 10.1016/0956-716x(95)00015-N
154. van Beers, P.R.M., Kouznetsova, V.G., Geers, M.G.D., Tschopp, M.A., McDowell, D.L.: A multiscale model of grain boundary structure and energy: From atomistics to a continuum description. *Acta Materialia* **82**, 513-529 (2015). doi:10.1016/j.actamat.2014.08.045
155. Nakayama, Y., Narita, T., Mori, A., Uesaka, S., Miyazaki, K., Ito, H.: The effects of age and sex on chondroitin sulfates in normal synovial fluid. *Arthritis Rheum* **46**(8), 2105-2108 (2002). doi:10.1002/art.10424
156. Jordan, J.M., Luta, G., Stabler, T., Renner, J.B., Dragomir, A.D., Vilim, V., Hochberg, M.C., Helmick, C.G., Kraus, V.B.: Ethnic and sex differences in serum levels of cartilage

- oligomeric matrix protein: the Johnston County Osteoarthritis Project. *Arthritis Rheum* **48**(3), 675-681 (2003). doi:10.1002/art.10822
157. Maleki-Fischbach, M., Jordan, J.M.: New developments in osteoarthritis. Sex differences in magnetic resonance imaging-based biomarkers and in those of joint metabolism. *Arthritis Res Ther* **12**(4), 1 (2010).
158. Warrington, D.H., Bufalini, P.: Coincidence Site Lattice and Grain Boundaries. *Scripta Metall Mater* **5**(9), 771-& (1971). doi:Doi 10.1016/0036-9748(71)90161-X
159. Cahoon, J.R., Li, Q.Y., Richards, N.L.: Microstructural and processing factors influencing the formation of annealing twins. *Mat Sci Eng a-Struct* **526**(1-2), 56-61 (2009). doi:10.1016/j.msea.2009.07.021
160. Rabaso, P., Ville, F., Dassenoy, F., Diaby, M., Afanasiev, P., Cavoret, J., Vacher, B., Le Mogne, T.: Boundary lubrication: Influence of the size and structure of inorganic fullerene-like MoS₂ nanoparticles on friction and wear reduction. *Wear* **320**, 161-178 (2014). doi:10.1016/j.wear.2014.09.001
161. Singer, I.L.: Mechanics and chemistry of solids in sliding contact. *Langmuir* **12**(19), 4486-4491 (1996). doi:10.1021/la951056n
162. Onodera, T., Morita, Y., Nagumo, R., Miura, R., Suzuki, A., Tsuboi, H., Hatakeyama, N., Endou, A., Takaba, H., Dassenoy, F., Minfray, C., Joly-Pottuz, L., Kubo, M., Martin, J.M., Miyamoto, A.: A computational chemistry study on friction of h-MoS(2). Part II. Friction anisotropy. *J Phys Chem B* **114**(48), 15832-15838 (2010). doi:10.1021/jp1064775
163. Ribarsky, M.W., Landman, U.: Microscopic Mechanisms of Tribological and Wear Processes: Molecular Dynamics Simulations. In: *Approaches to Modeling of Friction and Wear: Proceedings of the Workshop on the Use of Surface Deformation Models to Predict Tribology Behavior*, Columbia University in the City of New York, December 17–19, 1986. pp. 159-166. Springer New York, New York, NY (1988)
164. Fleischauer, P.D., Bauer, R.: The influence of surface chemistry on MoS₂ transfer film formation. *ASLE transactions* **30**(2), 160-166 (1987).
165. Miyoshi, K., Chung, Y.: *Surface Diagnostics in Tribology: Fundamental Principles and Applications*. World Scientific, Singapore (1993)
166. Sawyer, W.G., Wahl, K.J.: Accessing inaccessible interfaces: in situ approaches to materials tribology. *MRS Bull* **33**(12), 1145-1150 (2008).

167. Marks, L.D., Warren, O.L., Minor, A.M., Merkle, A.P.: Tribology in Full View. *MRS Bull* **33**(12), 1168-1173 (2008). doi:10.1557/mrs2008.247
168. Liao, Y., Marks, L.: In situ single asperity wear at the nanometre scale. *International Materials Reviews*(In production) (2016).
169. Casillas, G., Liao, Y., Jose-Yacamán, M., Marks, L.D.: Monolayer Transfer Layers During Sliding at the Atomic Scale. *Tribol Lett* **59**(3), 1-5 (2015). doi:10.1007/s11249-015-0563-9
170. Oviedo, J.P., Kc, S., Lu, N., Wang, J., Cho, K., Wallace, R.M., Kim, M.J.: In situ TEM characterization of shear-stress-induced interlayer sliding in the cross section view of molybdenum disulfide. *ACS Nano* **9**(2), 1543-1551 (2015). doi:10.1021/nn506052d
171. Castellanos-Gomez, A., Poot, M., Steele, G.A., van der Zant, H.S., Agrait, N., Rubio-Bollinger, G.: Elastic properties of freely suspended MoS₂ nanosheets. *Adv Mater* **24**(6), 772-775 (2012). doi:10.1002/adma.201103965
172. Casillas, G., Santiago, U., Barrón, H.c., Alducin, D., Ponce, A., José-Yacamán, M.: Elasticity of MoS₂ Sheets by Mechanical Deformation Observed by in Situ Electron Microscopy. *The Journal of Physical Chemistry C* **119**(1), 710-715 (2014).
173. Tang, D.M., Kvashnin, D.G., Najmaei, S., Bando, Y., Kimoto, K., Koskinen, P., Ajayan, P.M., Yakobson, B.I., Sorokin, P.B., Lou, J., Golberg, D.: Nanomechanical cleavage of molybdenum disulphide atomic layers. *Nat Commun* **5**, 3631 (2014). doi:10.1038/ncomms4631
174. Singer, I.L.: How third-body processes affect friction and wear. *MRS Bull* **23**(6), 37-40 (1998). doi:10.1557/S088376940003061X
175. Wahl, K.J., Sawyer, W.G.: Observing Interfacial Sliding Processes in Solid–Solid Contacts. *MRS Bull* **33**(12), 1159-1167 (2011). doi:10.1557/mrs2008.246
176. Hilton, M.R., Fleischauer, P.D.: Structural studies of sputter-deposited MoS₂ solid lubricant films. In: *MRS Proceedings 1988*, p. 227. Cambridge Univ Press
177. Hilton, M.R., Fleischauer, P.D.: TEM lattice imaging of the nanostructure of early-growth sputter-deposited MoS₂ solid lubricant films. *Journal of Materials Research* **5**(02), 406-421 (1990).

178. Fleischauer, P.D., Bauer, R.: Chemical and structural effects on the lubrication properties of sputtered MoS₂ films. *Tribology Transactions* **31**(2), 239-250 (1988).
179. Nafari, A., Karlen, D., Rusu, C., Svensson, K., Olin, H., Enoksson, P.: MEMS Sensor for *In Situ* TEM Atomic Force Microscopy. *Journal of Microelectromechanical Systems* **17**(2), 328-333 (2008). doi:10.1109/jmems.2007.912714
180. Bhushan, B.: *Modern Tribology Handbook, Two Volume Set*. CRC Press, New York (2000)
181. Scharf, T., Kotula, P., Prasad, S.: Friction and wear mechanisms in MoS₂/Sb₂O₃/Au nanocomposite coatings. *Acta Materialia* **58**(12), 4100-4109 (2010).
182. Lahouij, I., Vacher, B., Martin, J.-M., Dassenoy, F.: IF-MoS₂ based lubricants: influence of size, shape and crystal structure. *Wear* **296**(1), 558-567 (2012).
183. Tevet, O., Von-Huth, P., Popovitz-Biro, R., Rosentsveig, R., Wagner, H.D., Tenne, R.: Friction mechanism of individual multilayered nanoparticles. *Proc Natl Acad Sci U S A* **108**(50), 19901-19906 (2011). doi:10.1073/pnas.1106553108
184. Kalin, M., Kogovsek, J., Remskar, M.: Mechanisms and improvements in the friction and wear behavior using MoS₂ nanotubes as potential oil additives. *Wear* **280**, 36-45 (2012). doi:10.1016/j.wear.2012.01.011
185. An, V., Irtegov, Y., Izarra, C.d.: Study of tribological properties of nanolamellar WS₂ and MoS₂ as additives to lubricants. *Journal of Nanomaterials* **2014**, 188 (2014).
186. Xu, Z.Y., Hu, K.H., Han, C.L., Hu, X.G., Xu, Y.F.: Morphological influence of molybdenum disulfide on the tribological properties of rapeseed oil. *Tribol Lett* **49**(3), 513-524 (2013).
187. Rapoport, L., Moshkovich, A., Perfilyev, V., Laikhtman, A., Lapsker, I., Yadgarov, L., Rosentsveig, R., Tenne, R.: High Lubricity of Re-Doped Fullerene-Like MoS₂ Nanoparticles. *Tribol Lett* **45**(2), 257-264 (2011). doi:10.1007/s11249-011-9881-8
188. Hoffman, E.E., Marks, L.D.: Graphitic Carbon Films Across Systems. *Tribol Lett* **63**(3), 1-21 (2016). doi:10.1007/s11249-016-0720-9
189. Gangopadhyay, A., McWatt, D., Zrodowski, R., Liu, Z., Elie, L., Simko, S., Erdemir, A., Ramirez, G., Cuthbert, J., Hock, E.: Development of Modified PAG (polyalkylene glycol) High VI High Fuel Efficient Lubricant for LDV Applications. In: Ford Motor Company Presentation 2014

190. Tanner, D.M., Smith, N.F., Irwin, L.W., Eaton, W.P., Helgesen, K.S., Clement, J.J., Miller, W.M., Miller, S.L., Dugger, M.T., Walraven, J.A.: MEMS reliability: infrastructure, test structures, experiments, and failure modes. In. Sandia National Labs., Albuquerque, NM (US); Sandia National Labs., Livermore, CA (US), (2000)
191. Hsu, S.M., Gates, R.S.: Effect of materials on tribochemical reactions between hydrocarbons and surfaces. *J Phys D Appl Phys* **39**(15), 3128-3137 (2006). doi:10.1088/0022-3727/39/15/S02
192. Hermance, H.W., Egan, T.F.: Organic Deposits on Precious Metal Contacts. *At&T Tech J* **37**(3), 739-776 (1958). doi:10.1002/j.1538-7305.1958.tb03885.x
193. Antler, M.: Tribology of Metal Coatings for Electrical Contacts. *Thin Solid Films* **84**(3), 245-256 (1981). doi:10.1016/0040-6090(81)90022-5
194. Furey, M.J.: The formation of polymeric films directly on rubbing surfaces to reduce wear. *Wear* **26**(3), 369-392 (1973). doi:10.1016/0043-1648(73)90188-9
195. Gates, R.S., Jewett, K.L., Hsu, S.M.: A Study on the Nature of Boundary Lubricating Film: Analytical Method Development. *Tribology Transactions* **32**(4), 423-430 (1989). doi:10.1080/10402008908981909
196. Hsu, S.M.: Fundamental Mechanisms of friction and lubrication of materials. *Langmuir* **12**(19), 4482-4485 (1996). doi:10.1021/la9508856
197. Morecroft, D.W.: Reactions of octadecane and decoic acid with clean iron surfaces. *Wear* **18**(4), 333-339 (1971). doi:10.1016/0043-1648(71)90076-7
198. Chaikin, S.W.: On Frictional Polymer. *Wear* **10**(1), 49-60 (1967). doi:10.1016/0043-1648(67)90106-8
199. Mori, S., Imaizumi, Y.: Adsorption of Model Compounds of Lubricant on Nascent Surfaces of Mild and Stainless Steels under Dynamic Conditions. *Tribology Transactions* **31**(4), 449-453 (1988). doi:10.1080/10402008808981847
200. Herrera-Fierro, P., Shogrin, B.A., Jones, W.R.: Spectroscopic analysis of perfluoropolyether lubricant degradation during boundary lubrication. *Lubrication Engineering* **56**(2), 23-29 (2000).
201. Zhang, J., Demas, N.G., Polycarpou, A.A., Economy, J.: A new family of low wear, low coefficient of friction polymer blend based on polytetrafluoroethylene and an aromatic

- thermosetting polyester. *Polym Advan Technol* **19**(8), 1105-1112 (2008). doi:10.1002/pat.1086
202. Hsu, S.M., Klaus, E.E., Cheng, H.S.: A Mechano-Chemical Descriptive Model for Wear under Mixed Lubrication Conditions. *Wear* **128**(3), 307-323 (1988). doi:10.1016/0043-1648(88)90066-X
203. Hsu, S.M., Klaus, E.E.: Estimation of the Molecular Junction Temperatures in Four-Ball Contacts by Chemical Reaction Rate Studies. *A S L E Transactions* **21**(3), 201-210 (1978). doi:10.1080/05698197808982875
204. Hsu, S.M., Klaus, E.E.: Some Chemical Effects in Boundary Lubrication Part I: Base Oil-Metal Interaction. *A S L E Transactions* **22**(2), 135-145 (1979). doi:10.1080/05698197908982909
205. Lenahan, P.M., Curry, S.E.: First observation of the ^{29}Si hyperfine spectra of silicon dangling bond centers in silicon nitride. *Applied Physics Letters* **56**(2), 157 (1990). doi:10.1063/1.103278
206. Eryilmaz, O.L., Erdemir, A.: TOF-SIMS and XPS characterization of diamond-like carbon films after tests in inert and oxidizing environments. *Wear* **265**(1-2), 244-254 (2008). doi:10.1016/j.wear.2007.10.012
207. Sugishita, J., Fujiyoshi, S.: The effect of cast iron graphites on friction and wear performance I: Graphite film formation on grey cast iron surfaces. *Wear* **66**(2), 209-221 (1981).
208. Erdemir, A., Bindal, C., Pagan, J., Wilbur, P.: Characterization of transfer layers on steel surfaces sliding against diamond-like hydrocarbon films in dry nitrogen. *Surf Coat Tech* **76-77**(1-3), 559-563 (1995). doi:10.1016/0257-8972(95)02518-9
209. Li, C., Stair, P.C.: Ultraviolet Raman spectroscopy characterization of coke formation in zeolites. *Catal Today* **33**(1-3), 353-360 (1997). doi:10.1016/S0920-5861(96)00120-4
210. Ponsonnet, L., Donnet, C., Varlot, K., Martin, J.M., Grill, A., Patel, V.: EELS analysis of hydrogenated diamond-like carbon films. *Thin Solid Films* **319**(1-2), 97-100 (1998). doi:10.1016/S0040-6090(97)01094-8
211. Gallezot, P., Leclercq, C., Guisnet, M., Magnoux, P.: Coking, aging, and regeneration of zeolites: VII. Electron microscopy and EELS studies of external coke deposits on USHY, H-OFF, and H-ZSM-5 zeolites. *Journal of Catalysis* **114**(1), 100-111 (1988).

212. Pappas, D.L., Saenger, K.L., Cuomo, J.J., Dreyfus, R.W.: Characterization of Laser Vaporization Plasmas Generated for the Deposition of Diamond-Like Carbon. *Journal of Applied Physics* **72**(9), 3966-3970 (1992). doi:10.1063/1.352249
213. Cuomo, J.J., Pappas, D.L., Bruley, J., Doyle, J.P., Saenger, K.L.: Vapor deposition processes for amorphous carbon films with sp^3 fractions approaching diamond. *Journal of Applied Physics* **70**(3), 1706-1711 (1991).
214. Schmellenmeier, H.: Die Beeinflussung von festen Oberflächen durch eine ionisierte. *Experimentelle Technik der Physik* **1**, 49-68 (1953).
215. Aisenberg, S.: Ion-Beam Deposition of Thin Films of Diamondlike Carbon. *Journal of Applied Physics* **42**(7), 2953 (1971). doi:10.1063/1.1660654
216. Ali, E., Christophe, D.: Tribology of diamond-like carbon films: recent progress and future prospects. *Journal of Physics D: Applied Physics* **39**(18), R311 (2006).
217. Erdemir, A., Donnet, C.: Tribology of diamond-like carbon films: recent progress and future prospects. *J Phys D Appl Phys* **39**(18), R311-R327 (2006). doi:10.1088/0022-3727/39/18/R01
218. Singh, H., Ramirez, G., Eryilmaz, O., Greco, A., Doll, G., Erdemir, A.: Fatigue resistant carbon coatings for rolling/sliding contacts. *Tribol Int* **98**, 172-178 (2016). doi:10.1016/j.triboint.2016.02.008
219. Lawes, S.D.A., Fitzpatrick, M.E., Hainsworth, S.V.: Evaluation of the tribological properties of DLC for engine applications. *J Phys D Appl Phys* **40**(18), 5427-5437 (2007). doi:10.1088/0022-3727/40/18/S03
220. Grill, A.: Tribology of diamondlike carbon and related materials: an updated review. *Surf Coat Tech* **94-5**(1-3), 507-513 (1997). doi:10.1016/S0257-8972(97)00458-1
221. Lettington, A.H.: Applications of diamond-like carbon thin films. *Carbon* **36**(5-6), 555-560 (1998). doi:10.1016/s0008-6223(98)00062-1
222. Hauert, R.: A review of modified DLC coatings for biological applications. *Diam Relat Mater* **12**(3-7), 583-589 (2003). doi:10.1016/S0925-9635(03)00081-5
223. Pastewka, L., Moser, S., Gumbsch, P., Moseler, M.: Anisotropic mechanical amorphization drives wear in diamond. *Nat Mater* **10**(1), 34-38 (2011). doi:10.1038/Nmat2902

224. Moon, M.W., Jensen, H.M., Hutchinson, J.W., Oh, K.H., Evans, A.G.: The characterization of telephone cord buckling of compressed thin films on substrates. *J Mech Phys Solids* **50**(11), 2355-2377 (2002). doi:10.1016/S0022-5096(02)00034-0
225. Wu, W.J., Hon, M.H.: Thermal stability of diamond-like carbon films with added silicon. *Surf Coat Tech* **111**(2-3), 134-140 (1999). doi:10.1016/S0257-8972(98)00719-1
226. Scharf, T.W., Singer, I.L.: Role of Third Bodies in Friction Behavior of Diamond-like Nanocomposite Coatings Studied by In Situ Tribometry. *Tribology Transactions* **45**(3), 363-371 (2002). doi:10.1080/10402000208982561
227. Savage, R.H.: Graphite Lubrication. *Journal of Applied Physics* **19**(1), 1-10 (1948). doi:10.1063/1.1697867
228. Rabinowicz, E., Imai, M.: Frictional properties of pyrolytic boron nitride and graphite. *Wear* **7**(3), 298-300 (1964). doi:10.1016/0043-1648(64)90092-4
229. Fusaro, R.L., Sliney, H.E.: Graphite Fluoride (CF_x)_n—A New Solid Lubricant. *A S L E Transactions* **13**(1), 56-65 (1970). doi:10.1080/05698197008972282
230. Kato, K., Umehara, N., Adachi, K.: Friction, wear and N₂-lubrication of carbon nitride coatings: a review. *Wear* **254**(11), 1062-1069 (2003). doi:10.1016/s0043-1648(03)00334-x
231. Shen, Y., Xu, J.J., Jin, M., Wang, J.J., Wang, L., Han, X.G., Zhang, H.P., Zhang, Y.D.: Tribological Behavior among Piston Ring-Hydrorefined Mineral Oil-Cylinder Liner for Diesel Engine. *Applied Mechanics and Materials* **148**, 1307-1311 (2012).
232. Johnson, M., Spurlock, M.: Strategic oil analysis: Estimating remaining lubricant life. *Tribology & Lubrication Technology* (2010).
233. Livingstone, G., Oakton, D.: The Emerging Problem of Lubricant Varnish. *Maintenance & Asset Management* (2010).
234. Lucas, L.: Problems and sources of varnish in hydraulic fluid. *Hydraulics&Pneumatics* (2007).
235. Sasaki, A., Uchiyama, S., Kawasaki, M.: Varnish formation in the gas turbine oil systems. *Journal of ASTM International* **5**(2), 1-12 (2008).

236. Phillips, W.D., Staniewski, J.W.G.: The origin, measurement and control of fine particles in non-aqueous hydraulic fluids and their effect on fluid and system performance. *Lubrication Science* **28**(1), 43-64 (2016). doi:10.1002/lis.1300
237. Atherton, B.: How to stop varnish before it costs you. *Plastics Today* (2008).
238. Atherton, B.: Discovering the Root Cause of Varnish Formation. *Practicing Oil Analysis* (2007).
239. Phillips, W.D.: The high-temperature degradation of hydraulic oils and fluids©. *Journal of Synthetic Lubrication* **23**(1), 39-70 (2006). doi:10.1002/jsl.11
240. Sasaki, A., Uchiyama, S., Yamamoto, T.: Generation of static electricity during oil filtration. *Lubrication Engineering* **55**(9), 14-21 (1999).
241. Barber, A., Filippini, B., Profflet, R., Tam, N.: A Fluid Solution to Preventing Varnish Formation in Hydraulic Systems. In: *Lubricants SYMPOSIUM 2008* 2008, pp. 175-175
242. Ribeiro, N.M., Pinto, A.C., Quintella, C.M., da Rocha, G.O., Teixeira, L.S.G., Guarieiro, L.L.N., Rangel, M.D., Veloso, M.C.C., Rezende, M.J.C., da Cruz, R.S., de Oliveira, A.M., Torres, E.A., de Andrade, J.B.: The role of additives for diesel and diesel blended (Ethanol or biodiesel) fuels: A review. *Energy & Fuels* **21**(4), 2433-2445 (2007). doi:10.1021/ef070060r
243. Heo, G., Lee, S., Kim, H., Park, U., Lee, G., Han, D., Chu, M., Choi, U., Hur, K., Lee, S.G., Kim, H.S., Park, W.K., Lee, K.C., Han, D.H., Chu, M.K., Choi, W.J.: Varnishing processing unit for processing surface of workpiece, has circulating pump provided with nozzle in which hydro static ball pressurizes exterior of workpiece, where circulating pump supplies hydraulic fluid to varnishing tool. KR2010095230-A; KR1077093-B1,
244. Hum, W., Holt, D.G.L., Blumenfeld, M.L., Galiano-Roth, A.S.: Improving varnish control in a mechanical device requiring hydraulic fluids, turbine oils, industrial fluids, circulating oils, or combinations by supplying the mechanical device with a lubricating composition. US2015099675-A1; WO2015050690-A1,
245. ASTM: Standard Test Method for Measurement of Lubricant Generated Insoluble Color Bodies in In-Service Turbine Oils using Membrane Patch Colorimetry, ASTM International, West Conshohocken. In, vol. ASTM D7843-12. ASTM International, (2012)
246. Robertson, J.: Diamond-like amorphous carbon. *Mat Sci Eng R* **37**(4-6), 129-281 (2002). doi:10.1016/S0927-796x(02)00005-0

247. Ferrari, A.C., Robertson, J.: Interpretation of Raman spectra of disordered and amorphous carbon. *Phys. Rev. B* **61**(20), 14095-14107 (2000). doi:10.1103/PhysRevB.61.14095
248. Chu, P.K., Li, L.H.: Characterization of amorphous and nanocrystalline carbon films. *Mater Chem Phys* **96**(2-3), 253-277 (2006). doi:10.1016/j.matchemphys.2005.07.048
249. Buscher, R., Tager, G., Dudzinski, W., Gleising, B., Wimmer, M.A., Fischer, A.: Subsurface microstructure of metal-on-metal hip joints and its relationship to wear particle generation. *J Biomed Mater Res B Appl Biomater* **72**(1), 206-214 (2005). doi:10.1002/jbm.b.30132
250. Zahiri, C.A., Schmalzried, T.P., Ebramzadeh, E., Szuszczewicz, E.S., Salib, D., Kim, C., Amstutz, H.C.: Lessons learned from loosening of the McKee-Farrar metal-on-metal total hip replacement. *J Arthroplasty* **14**(3), 326-332 (1999). doi:10.1016/s0883-5403(99)90059-1
251. Tager, K.H.: Studies on Surface and New Joint Capsule of Mckee-Farrar Prosthesis Implanted for Several Years. *Arch Orthop Traum Su* **86**(1), 101-113 (1976). doi:10.1007/Bf00415308
252. Walker, P.S., Salvati, E., Hotzler, R.K.: The wear on removed McKee-Farrar total hip prostheses. *J Bone Joint Surg Am* **56**(1), 92-100 (1974).
253. Mavraki, A., Cann, P.M.: Lubricating film thickness measurements with bovine serum. *Tribol Int* **44**(5), 550-556 (2011). doi:10.1016/j.triboint.2010.07.008
254. Mishina, H., Kojima, M.: Changes in human serum albumin on arthroplasty frictional surfaces. *Wear* **265**(5-6), 655-663 (2008). doi:10.1016/j.wear.2007.12.006
255. Wang, A., Yue, S., Boby, J.D., Chan, F.W., Medley, J.B.: Surface characterization of metal-on-metal hip implants tested in a hip simulator. *Wear* **225**, 708-715 (1999). doi:10.1016/S0043-1648(98)00384-6
256. Hesketh, J., Ward, M., Dowson, D., Neville, A.: The composition of tribofilms produced on metal-on-metal hip bearings. *Biomaterials* **35**(7), 2113-2119 (2014). doi:10.1016/j.biomaterials.2013.11.065
257. Myant, C., Cann, P.: In contact observation of model synovial fluid lubricating mechanisms. *Tribol Int* **63**, 97-104 (2013). doi:10.1016/j.triboint.2012.64.029
258. Wimmer, M., Mathew, M., Laurent, M., Nagelli, C., Liao, Y., Marks, L., Pourzal, R., Fischer, A., Jacobs, J.: Tribochemical reactions in metal-on-metal hip joints influence wear and

- corrosion. Paper presented at the ASTM Symposium on Metal-on-Metal Total Hip Phoenix, AZ,
259. Dugger, M.T.: Tribological Challenges in MEMS and Their Mitigation Via Vapor Phase Lubrication. In: George, T., Islam, M.S., Dutta, A.K. (eds.) *Micro- and Nanotechnology Sensors, Systems, and Applications Iii*, Orlando, Florida 2011. Proceedings of SPIE
 260. Strawhecker, K., Asay, D., McKinney, J., Kim, S.: Reduction of adhesion and friction of silicon oxide surface in the presence of n-propanol vapor in the gas phase. *Tribol Lett* **19**(1), 17-21 (2005).
 261. Asay, D.B., Dugger, M.T., Kim, S.H.: In-situ Vapor-Phase Lubrication of MEMS. *Tribol Lett* **29**(1), 67-74 (2007). doi:10.1007/s11249-007-9283-0
 262. Asay, D.B., Kim, S.H.: Molar volume and adsorption isotherm dependence of capillary forces in nanoasperity contacts. *Langmuir* **23**(24), 12174-12178 (2007). doi:10.1021/la701954k
 263. Carroll, B., Gogotsi, Y., Kovalchenko, A., Erdemir, A., McNallan, M.J.: Effect of humidity on the tribological properties of carbide-derived carbon (CDC) films on silicon carbide. *Tribol Lett* **15**(1), 51-55 (2003). doi:10.1023/A:1023508006745
 264. Ersoy, D.A., McNallan, M.J., Gogotsi, Y., Erdemir, A.: Tribological Properties of Carbon Coatings Produced by High Temperature Chlorination of Silicon Carbide. *Tribology Transactions* **43**(4), 809-815 (2000). doi:10.1080/10402000008982412
 265. Graham, E., Klaus, E.: Lubrication from the vapor phase at high temperatures. *ASLE transactions* **29**(2), 229-234 (1986).
 266. Hook, D.A., Timpe, S.J., Dugger, M.T., Krim, J.: Tribological degradation of fluorocarbon coated silicon microdevice surfaces in normal and sliding contact. *Journal of Applied Physics* **104**(3), 034303 (2008).
 267. Tanner, D.M., Miller, W.M., Eaton, W.P., Irwin, L.W., Peterson, K.A., Dugger, M.T., Senft, D.C., Smith, N.F., Tangyonyong, P., Miller, S.L.: The effect of frequency on the lifetime of a surface micromachined microengine driving a load. In: *Reliability Physics Symposium Proceedings, 1998. 36th Annual. 1998 IEEE International*, Reno, NV, USA 1998, pp. 26-35. IEEE
 268. Sung, D., Gellman, A.: The surface chemistry of alkyl and arylphosphate vapor phase lubricants on Fe foil. *Tribol Int* **35**(9), 579-590 (2002).

269. Singer, I., Mogne, T.L., Donnet, C., Martin, J.: Friction behavior and wear analysis of SiC sliding against Mo in SO₂, O₂ and H₂S at gas pressures between 4 and 40 Pa. *Tribology transactions* **39**(4), 950-956 (1996).
270. Hibi, Y., Enomoto, Y., Tanaka, A.: Lubricity of metal ethoxide formed on sliding surfaces of Si₃N₄-TiN-Ti composites in ethanol. *J Mater Sci Lett* **19**(20), 1809-1812 (2000). doi:10.1023/A:1006742323483
271. Barnick, N.J., Blanchet, T.A., Sawyer, W.G., Gardner, J.E.: High temperature lubrication of various ceramics and metal alloys via directed hydrocarbon feed gases. *Wear* **214**(1), 131-138 (1998).
272. Dugger, M.: Nano/Micro-Tribology of MEMS. In., vol. SAND2014-4771C. U.S. Department of Energy, Albuquerque, NM, (2014)
273. Asay, D.B., Dugger, M.T., Ohlhausen, J.A., Kim, S.H.: Macro- to nanoscale wear prevention via molecular adsorption. *Langmuir* **24**(1), 155-159 (2008). doi:10.1021/la702598g
274. Barbier, J.: Deactivation of Reforming Catalysts by Coking - a Review. *Appl Catal* **23**(2), 225-243 (1986). doi:10.1016/S0166-9834(00)81294-4
275. Forzatti, P., Lietti, L.: Catalyst deactivation. *Catal Today* **52**(2-3), 165-181 (1999). doi:10.1016/S0920-5861(99)00074-7
276. Trimm, D.L.: Control of coking. *Chemical Engineering and Processing: Process Intensification* **18**(3), 137-148 (1984). doi:10.1016/0255-2701(84)80003-3
277. Trimm, D.L.: Coke formation and minimisation during steam reforming reactions. *Catal Today* **37**(3), 233-238 (1997). doi:10.1016/s0920-5861(97)00014-x
278. Rostrup-Nielsen, J., Tottrup, P.: Symp. "Science of Catalysis Applications in Industry". In: FPDIL Sindri, India 1979, vol. 39 p. 379
279. Guisnet, M., Magnoux, P.: Coking and Deactivation of Zeolites - Influence of the Pore Structure. *Appl Catal* **54**(1), 1-27 (1989). doi:10.1016/S0166-9834(00)82350-7
280. Rostrup-Nielsen, J.R.: Industrial relevance of coking. *Catal Today* **37**(3), 225-232 (1997). doi:10.1016/s0920-5861(97)00016-3
281. Corthals, S., Van Nederkassel, J., Geboers, J., De Winne, H., Van Noyen, J., Moens, B., Sels, B., Jacobs, P.: Influence of composition of MgAl₂O₄ supported NiCeO₂ZrO₂ catalysts on

- coke formation and catalyst stability for dry reforming of methane. *Catal Today* **138**(1-2), 28-32 (2008). doi:10.1016/j.cattod.2008.04.038
282. Behera, B., Ray, S.S., Singh, I.D.: NMR Studies of FCC Feeds, Catalysts and Coke. In: Ocelli, M.L. (ed.) *Fluid Catalytic Cracking Vii Materials: Methods and Process Innovations*, vol. 166. *Studies in Surface Science and Catalysis*, pp. 163-200. Amsterdam (2007)
283. Liu, B.S., Jiang, L., Sun, H., Au, C.T.: XPS, XAES, and TG/DTA characterization of deposited carbon in methane dehydroaromatization over Ga-Mo/ZSM-5 catalyst. *Applied Surface Science* **253**(11), 5092-5100 (2007). doi:10.1016/j.apsusc.2006.11.031
284. Hardiman, K.M., Cooper, C.G., Adesina, A.A., Lange, R.: Post-mortem characterization of coke-induced deactivated alumina-supported Co-Ni catalysts. *Chemical Engineering Science* **61**(8), 2565-2573 (2006). doi:10.1016/j.ces.2005.11.021
285. Tiratsoo, E.N.: *Natural gas: a study*, vol. 1979. Gulf Pub Co, London (1979)
286. Rostrup-Nielsen, J.R.: Aspects of CO₂-reforming of Methane. In: Curry-Hyde, H.E., Howe, R.F. (eds.) *Studies in Surface Science and Catalysis*, vol. Volume 81. pp. 25-41. Elsevier, Amsterdam (1994)
287. Mizoh, Y.: Wear of tribo-elements of video tape recorders. *Wear* **200**(1-2), 252-264 (1996). doi:10.1016/S0043-1648(96)07278-X
288. Bharat, B., Hahn, F.W.: Stains on magnetic tape heads. *Wear* **184**(2), 193-202 (1995).
289. Rabinowicz, E.: The Tribology of Magnetic Recording Systems—An Overview. *Tribology and Mechanics of Magnetic Storage Systems* **3**, 1-7 (1986).
290. Mizoh, Y.: Wear of magnetic video head. *J Jpn Soc Tribologis* **40**(12), 981-986 (1995).
291. Osaki, H.: Flexible media - recent developments from the tribology point of view. *Tribol Int* **33**(5-6), 373-382 (2000). doi:10.1016/S0301-679x(00)00057-8
292. Kuroe, A., Shinoda, F., Mikoda, M.: An experimental analysis of the recorded signal decrease phenomena in the repeated tape running. *Electrical Information Society* **74**, 194-200 (1991).
293. Montgomery, R.S.: Run-in and Glaze Formation on Gray Cast Iron Surfaces. *Wear* **14**(2), 99- & (1969). doi:10.1016/0043-1648(69)90340-8

294. Takeuchi, E.: The mechanisms of wear of cast iron in dry sliding. *Wear* **11**(3), 201-212 (1968). doi:10.1016/0043-1648(68)90558-9
295. Leach, P.W., Borland, D.W.: The Unlubricated Wear of Flake Graphite Cast-Iron. *Wear* **85**(2), 257-266 (1983). doi:10.1016/0043-1648(83)90068-6
296. Erdemir, A.: Review of engineered tribological interfaces for improved boundary lubrication. *Tribol Int* **38**(3), 249-256 (2005). doi:10.1016/j.triboint.2004.08.008
297. Erdemir, A., Eryilmaz, O.L., Urgan, M., Kazmanli, K.: Method to Produce Catalytically Active Nanocomposite Coatings. In. Google Patents, (2013)
298. Dowson, D., Jin, Z.M.: Metal-on-metal hip joint tribology. *Proc Inst Mech Eng H* **220**(2), 107-118 (2006). doi:10.1243/095441105x69114
299. Rostrup-Nielsen, J.R.: Sulfur-passivated nickel catalysts for carbon-free steam reforming of methane. *Journal of Catalysis* **85**(1), 31-43 (1984). doi:10.1016/0021-9517(84)90107-6
300. Fang, S., Lin, G.X.: Managing Varnish of Turbine oil. In: Kim, Y.H., Yarlagadda, P. (eds.) *Materials, Mechanical and Manufacturing Engineering*, vol. 842. *Advanced Materials Research*, pp. 341-344. Guilin, China (2014)
301. Bell, J., Tipper, J.L., Ingham, E., Stone, M.H., Fisher, J.: The influence of phospholipid concentration in protein-containing lubricants on the wear of ultra-high molecular weight polyethylene in artificial hip joints. *Proceedings of the Institution of Mechanical Engineers Part H-Journal of Engineering in Medicine* **215**(H2), 259-263 (2001). doi:10.1243/0954411011533661
302. Keenan, M.R., Kotula, P.G.: Accounting for Poisson noise in the multivariate analysis of ToF-SIMS spectrum images. *Surface and Interface Analysis* **36**(3), 203-212 (2004).
303. Tang, S., Gao, S., Hu, S., Wang, J., Zhu, Q., Chen, Y., Li, X.: Inhibition Effect of APCVD Titanium Nitride Coating on Coke Growth during n-Hexane Thermal Cracking under Supercritical Conditions. *Industrial & Engineering Chemistry Research* **53**(13), 5432-5442 (2014). doi:10.1021/ie401889p
304. Hibi, Y., Enomoto, Y.: Mechanochemical reaction and relationship to tribological response of silicon nitride in n-alcohol. *Wear* **231**(2), 185-194 (1999). doi:10.1016/S0043-1648(99)00094-0

305. Mccarty, J.G., Wise, H.: Hydrogenation of Surface Carbon on Alumina-Supported Nickel. *Journal of Catalysis* **57**(3), 406-416 (1979). doi:10.1016/0021-9517(79)90007-1
306. Dowden, D.A.: Crystal and Ligand Field Models of Solid Catalysts. *Catalysis Reviews* **5**(1), 1-32 (1972). doi:10.1080/01614947208076863
307. Yan, Y., Neville, A., Dowson, D., Hollway, F.: Biotribocorrosion of CoCrMo orthopaedic implant materials - Assessing the formation and effect of the biofilm. *Tribol Int* **40**(10-12), 1728-1728 (2007). doi:10.1016/j.triboint.2007.02.019
308. Yan, Y., Neville, A., Dowson, D., Williams, S., Fisher, J.: Tribofilm formation in biotribocorrosion – does it regulate ion release in metal-on-metal artificial hip joints? *Proceedings of the Institution of Mechanical Engineers, Part J: Journal of Engineering Tribology* **224**(9), 997-1006 (2010). doi:10.1243/13506501jet762
309. Nakayama, K.: Triboemission of Charged-Particles from Various Solids under Boundary Lubrication Conditions. *Wear* **178**(1-2), 61-67 (1994). doi:10.1016/0043-1648(94)90129-5
310. Nevshupa, R.A., Nakayama, K.: Triboemission behavior of photons at dielectric/dielectric sliding: Time dependence nature at 10^{-4} – 10^4 s. *Journal of Applied Physics* **93**(11), 9321 (2003). doi:10.1063/1.1570934
311. Nevshupa, R.A., Nakayama, K.: Effect of nanometer thin metal film on triboemission of negatively charged particles from dielectric solids. *Vacuum* **67**(3-4), 485-490 (2002). doi:10.1016/S0042-207x(02)00234-8
312. Ferrante, J.: Exoelectron Emission from a Clean, Annealed Magnesium Single Crystal During Oxygen Adsorption. *A S L E Transactions* **20**(4), 328-332 (1977). doi:10.1080/05698197708982851
313. Warren, W.L., Lenahan, P.M.: Electron-nuclear double-resonance and electron-spin-resonance study of silicon dangling-bond centers in silicon nitride. *Phys. Rev. B* **42**(3), 1773-1780 (1990).
314. Podgornik, B., Hren, D., Vižintin, J.: Low-friction behaviour of boundary-lubricated diamond-like carbon coatings containing tungsten. *Thin Solid Films* **476**(1), 92-100 (2005). doi:10.1016/j.tsf.2004.09.028

315. de Barros'Bouchet, M.I., Martin, J.M., Le-Mogne, T., Vacher, B.: Boundary lubrication mechanisms of carbon coatings by MoDTC and ZDDP additives. *Tribol Int* **38**(3), 257-264 (2005). doi:10.1016/j.triboint.2004.08.009
316. Nakayama, K.: Triboemission of electrons, ions, and photons from diamondlike carbon films and generation of tribomicroplasma. *Surf Coat Tech* **188**, 599-604 (2004). doi:10.1016/j.surfcoat.2004.07.103
317. Sanchez-Lopez, J.C., Erdemir, A., Donnet, C., Rojas, T.C.: Friction-induced structural transformations of diamondlike carbon coatings under various atmospheres. *Surf Coat Tech* **163**, 444-450 (2003). doi:10.1016/S0257-8972(02)00641-2
318. Liu, Y., Erdemir, A., Meletis, E.I.: Influence of environmental parameters on the frictional behavior of DLC coatings. *Surf Coat Tech* **94-5**(1-3), 463-468 (1997). doi:10.1016/S0257-8972(97)00450-7
319. Erdemir, A., Bindal, C., Fenske, G.R., Zuiker, C., Wilbur, P.: Characterization of transfer layers forming on surfaces sliding against diamond-like carbon. *Surf Coat Tech* **86-7**(1-3), 692-697 (1996). doi:10.1016/S0257-8972(96)03073-3
320. Kim, D.S., Fischer, T.E., Gallois, B.: The Effects of Oxygen and Humidity on Friction and Wear of Diamond-Like Carbon-Films. *Surf Coat Tech* **49**(1-3), 537-542 (1991). doi:10.1016/0257-8972(91)90113-B
321. Lhomme, V., Bruneau, C., Soyer, N., Brault, A.: Thermal behavior of some organic phosphates. *Industrial & Engineering Chemistry Product Research and Development* **23**(1), 98-102 (1984). doi:10.1021/i300013a021
322. Appleby, W.G., Gibson, J.W., Good, G.M.: Coke Formation in Catalytic Cracking. *Industrial & Engineering Chemistry Process Design and Development* **1**(2), 102-110 (1962). doi:10.1021/i260002a006
323. Mangolini, F., Rose, F., Hilbert, J., Carpick, R.W.: Thermally induced evolution of hydrogenated amorphous carbon. *Applied Physics Letters* **103**(16), 1-5 (2013). doi:10.1063/1.4826100
324. Nalwa, H.S.: *Handbook of Surfaces and Interfaces of Materials*, Five-Volume Set. Elsevier Science, Los Angeles, CA, U.S.A. (2001)
325. Liao, Y., Marks, L.D.: Modeling of Thermal-Assisted Dislocation Friction. *Tribol Lett* **37**(2), 283-288 (2010). doi:10.1007/s11249-009-9520-9

326. Lopez, N., Cid, M., Puiggali, M.: Influence of σ -phase on mechanical properties and corrosion resistance of duplex stainless steels. *Corros Sci* **41**(8), 1615-1631 (1999). doi:10.1016/s0010-938x(99)00009-8
327. Gladman, T.: Precipitation hardening in metals. *Materials science and technology* **15**(1), 30-36 (1999).
328. Weiss, B., Stickler, R.: Phase instabilities during high temperature exposure of 316 austenitic stainless steel. *Metallurgical Transactions* **3**(4), 851-866 (1972).
329. Lara, J., Blunt, T., Kotvis, P., Riga, A., Tysoe, W.T.: Surface chemistry and extreme-pressure lubricant properties of dimethyl disulfide. *Journal of Physical Chemistry B* **102**(10), 1703-1709 (1998). doi:10.1021/jp980238y
330. M'ndange-Pfupfu, A., Ciston, J., Eryilmaz, O., Erdemir, A., Marks, L.D.: Direct Observation of Tribochemically Assisted Wear on Diamond-Like Carbon Thin Films. *Tribol Lett* **49**(2), 351-356 (2013). doi:10.1007/s11249-012-0074-x
331. Berman, D., Deshmukh, S.A., Sankaranarayanan, S.K., Erdemir, A., Sumant, A.V.: Macroscale superlubricity enabled by graphene nanoscroll formation. *Science* **348**(6239), 1118-1122 (2015).

9 Curriculum Vitae

Emily Hoffman
 330-903-1050
 Emilyhoffman2016@u.northwestern.edu

RESEARCH INTERESTS

Scientific

Transmission electron microscopy
 Tribology
 Metal-on-metal hip implants

Professional

Effective science communication
 Science and technology policy
 Long-term government research funding

EDUCATION

Northwestern University, Evanston, Illinois *Fall 2016*
 PhD
 Materials Science and Engineering
 GPA: 3.920/4.0

Case Western Reserve University, Cleveland, Ohio *May 2011*
 Bachelor of Science
 Major: Biomedical Engineering, Orthopedic Biomaterials
 Minor: Materials Science and Engineering
 GPA: 3.822/4.0 (magna cum laude)
 GRE: Verbal 600, Math: 800 (taken 2010)

RESEARCH EXPERIENCE

Graduate Research *2011-present*
 Northwestern University, Evanston, Illinois
 Adviser: Dr. Laurence Marks

- Exploring nanotribology properties of hip implants using transmission electron microscopy as part of a multidisciplinary teams with microscopists, surgeons, and tribologists
- Evaluating corrosion and grain boundary segregation in CoCrMo alloys

International Research Experience for Undergraduates (iREU) *Summer 2011*
 IMEC, Leuven, Belgium, Adviser: Dr. Hercules Neves

- Deposition and characterization of ruthenium films for neural probe electrode applications
- Developed deposition protocols to maximize charge storage capacity

Research Experience for Undergraduates (REU) *Summer 2010*
 Cornell University, Ithaca, New York, Adviser: Dr. Harold Craighead

- Designed and tested a microfluidic system for the purification and detection of biomolecules
- Trained in the Cornell NanoScale Science and Technology Facility Class 1000 clean room

AWARDS

| | |
|--|--|
| National Defense Science and Engineering Graduate Fellowship • Earned three years, full funding based on competitive application • Insures that I own my research path and can steer my project | <i>2013-2016</i> |
| National Science Foundation Graduate Fellowship - Honorable Mention • Honorable mention for the most competitive graduate fellowship | <i>2013</i> |
| Delta Gamma Foundation Graduate Fellowship • Earned funding based on academics on sorority alumni involvement | <i>2013-2014</i> |
| Northwestern Biotechnology Training Program Fellowship • Earned funding for two quarters through competitive applications process • Training program including giving lectures and organizing speakers | <i>2012-2013</i> |
| Case Western Reserve Presidential Scholarship Tau Beta Pi, Engineering Honor Society | <i>2007-2011</i> <i>inducted 2009</i> |

PROGRAMS

| | |
|---|--|
| McKinsey & Co. Insight Program for Scientists and Engineers Boston Consulting Group Bridge to BCG • Highly selective training programs for PhD students interested in consulting | <i>Summer 2015</i> <i>Summer 2015</i> |
| National Academy of Engineering, Communications and Media Relations • Promoted engineering to the general public through the Mirzayan Science Policy Fellowship • Launched campaign of “The Next MacGyver” competition and interviewed scientist for radio | <i>Winter 2015</i> |
| Management for Scientist and Engineers Program, Northwestern University • Eight week course though Kellogg School of Management • Introduction to economics, finance, entrepreneurship, and business practice | <i>Summer 2014</i> |
| Ready, Set, Go Lecture Series, Northwestern University • Program focused on effective communication including presentation visuals, nonverbal communication, and public perception of scientists | <i>2012-2013</i> |
| Arizona State University Winter School, Tempe, AZ • Transmission electron microscopy, week-long intensive course • Received selected scholarship for workshop fees | <i>January 2013</i> |
| PLEN Women in Science and Technology Policy Seminar, Washington, DC • Scholarship to attend a week-long policy seminar for science majors | <i>January 2009</i> |
| College Scholars Program, Case Western Reserve University University Honors Program • Prepared our own interdisciplinary curriculum each semester with my student cohort • Fundraised, organized, and hosted campus lectures by prominent scientists, authors, and researchers | <i>2008-2010</i> |

SCHOLARSHIP

Publications

1. Lin, A., **Hoffman, E.**, Marks, L.D. "Effects of Grain Boundary Misorientation and Chromium Segregation on Corrosion of CoCrMo Alloys." *Corrosion*, (2016). doi: <http://dx.doi.org/10.5006/2233>.
2. **Hoffman, E.E.**, Marks, L.D., Soft Interface Fracture Transfer in Nanoscale MoS₂. *Tribology Letters*, 64(1) 16 (2016). doi:10.1007/s11249-016-0743-2.
3. **Hoffman, E.E.**, Marks, L.D.: Graphitic Carbon Films Across Systems. *Tribology Letters*, 63(3), 1-21 (2016). doi:10.1007/s11249-016-0720-9.
4. **Hoffman, E.E.**, Lin, A., Liao, Y., Marks, L., Grain Boundary Assisted Crevice Corrosion in CoCrMo Alloys. *Corrosion*, 72(11), 1445-1461 (2016). <http://dx.doi.org/10.5006/2108>.
5. McMorrow, J.J., Walker, A.R., Sangwan, V.K., Jariwala, D., **Hoffman, E.**, Everaerts, K., Facchetti, A., Hersam, M.C., Marks, T.J., Solution-Processed Self-Assembled Nanodielectrics on Template-Stripped Metal Substrates. *ACS Applied Materials & Interfaces*, 7(48), 26360-26366 (2015).
6. Lin, A., **Hoffman, E.**, Marks, L.D., Classifying the Severity of Grain Boundary Corrosion in CoCrMo Biomedical Implants. *Microscopy and Microanalysis*, 21(S3), 773-774 (2015).
7. Liao, Y., **Hoffman, E.**, Marks, L.D., "Nanoscale Abrasive Wear of CoCrMo in In Situ TEM Sliding." *Tribology Letters*, 57(3) 1-6 (2015).
8. **Hoffman, E.**, Liao, Y., Marks, L., Towards Understanding Tribocorrosion in Hip Replacements. *Microscopy and Microanalysis*, 19(S2), 176-177 (2013).
9. Liao, Y., **Hoffman, E.**, Wimmer, M., Fischer, A., Jacobs, J., Marks, L., CoCrMo metal-on-metal hip replacements. *Physical Chemistry Chemical Physics* 15(3), 746-756 (2013).
10. **Hoffman, E.**, Wu, D., Deposition and Characterization of Ruthenium Films for Neural Electrodes. *2011 NNIN REU Research Accomplishments*, 112-115 (2011).
11. **Hoffman, E.**, Portable Diagnostic System for the Purification and Detection of Biomolecules. *2010 NNIN REU Research Accomplishments*, 16-17 (2010).

Presentations

1. Grain Boundary Assisted Crevice Corrosion in CoCrMo Alloys. ASM Chicago Chapter Meeting. Chicago, Illinois, February 2016.
2. Alex Lin, **Emily E. Hoffman**, Laurence D. Marks, Classifying the Severity of Grain Boundary Corrosion, Microscopy and Microanalysis, Portland, Oregon, August 2015.
3. Man and Machine: The Generation of Graphitic Tribolayers. Hilliard Symposium, Materials Science and Engineering Department Seminar, Evanston, Illinois, May 2015.
4. Man and Machine: The Generation of Graphitic Tribolayers. Gordon Research Seminar, Student Presentation. Bentley University, Waltham, Massachusetts, July 2014.
5. Towards Understanding Tribocorrosion in Metal-on-Metal Hip Implants. NACE National Corrosion Society Conference, RIP: Biomaterials. San Antonio, Texas, March 2014.
6. Towards Understanding Tribocorrosion in Metal-on-Metal Hip Implants. Microscopy and Microanalysis Conference, Platform Presentation. Indianapolis, Indiana, August 2013.
7. Purification and Detection of Biomolecules. 2010 NNIN REU Convocation, University of Minnesota, Minneapolis, Minnesota. August 2010.

Posters

1. *Soft Interface Fracture Transfer in Nanoscale MoS₂. Argonne National Laboratory User Meeting, Lemont, Illinois, May 2016.
2. *Soft Interface Fracture Transfer in Nanoscale MoS₂. Gordon Research Conference, Student Poster Session. Bates College, Lewiston, Maine, June 2016.
3. *Alex Lin, **Emily E. Hoffman**, Laurence D. Marks, Classifying the Severity of Grain Boundary Corrosion, Poster Presentation, NACE Corrosion Conference, Vancouver, Canada, March 2016.
4. Alex Lin, **Emily E. Hoffman**, and Laurence Marks. Classifying the Severity of Grain Boundary Corrosion in Cobalt-Chromium-Molybdenum Biomedical Implants, Microscopy and Microanalysis Poster Session, Portland, Oregon, August 2015.
5. Man and Machine: The Generation of Graphitic Tribolayers. Northwestern University Postdoctoral Forum Conference, Invited Graduate Student, Chicago, Illinois, September 2014.
6. Man and Machine: The Generation of Graphitic Tribolayers. Gordon Research Conference, Student Poster Session. Bentley University, Waltham, Massachusetts, July 2014.
7. Towards Understanding Tribocorrosion in Metal-on-Metal Hip Implants. Rush University Medical Center, Invited Speaker for Biomechanics Research Seminar, Chicago, Illinois, June 2014.
8. Towards Understanding Tribocorrosion in Metal-on-Metal Hip Implants. NACE National Corrosion Society Conference, Student Poster Section. San Antonio, Texas, March 2014.
9. Man and Machine: Formation of a Varnish Tribolayer. Conference on Friction and Energy Dissipation in Man-made and Biological Systems, International Centre for Theoretical Physics, Trieste, Italy. November 2013.
10. Towards Understanding Tribocorrosion in Metal-on-Metal Hip Implants. Seeing at the Nanoscale Conference, Northwestern University, Evanston, Illinois. April 2013.
11. Thermal Reversibility of a Diels-Alder Thermosetting Polymer. Program for Women in Science and Engineering Summer Program, Iowa State University, Ames, Iowa. August 2009.

*indicates best poster award

Google Scholar profile: <https://scholar.google.com/citations?user=IJqtWxYAAAAJ&hl=en>
Papers available online: <http://www.numis.northwestern.edu/Research/Articles/articles.shtml>

LEADERSHIP AND OUTREACH

- Gordon Research Seminar Co-Chair *2016*
 • Selected talks, planned program, and organized meeting of ~50 young tribology researchers
 • Ensured successful transition to next leadership team by creating a planning packet
- Communication for Scientists Convention (ComSciCon-Chi) Planning Board *2014 – 2016*
 • Organized a communication conference for 100 current PhD researchers in Chicagoland
 • Focusing on science communication careers and presenting to a non-science audience
- Materials Science Student Association *2011 – 2016*
 • Elected President 2012-2013 school year
 • Increased student participation and increased professor attendance to department events
 • Coordinated new student recruiting weekend by successfully delegating tasks to the board
- Society of Women Engineers *2009 – present*
 • Planning and leading the national convention graduate programming as the Graduate Programming Coordinator-Elect for the 2016 national convention
 • Developed and presented an academic session at the SWE International Convention (one presentation in October 2014, two presentations in October 2015, two presentations in October 2016)
 • Taught engineering lessons to a group of 30 middle school girls for summer STEM program (2014, 2015)
 • Graduate mentor to undergraduate female engineer (2012-2013)
- Letters to a Pre-scientist, Pen Pal Program to Middle School Students *2012 – 2016*
 • Write four letters a year to a middle school student in a disadvantaged school
 • Explain my work as a researcher and motivate the student to pursue STEM
- Delta Gamma Fraternity *2008 – present*
 • Chicago Northshore Alumni Chapter *2011 – 2015*
 • Undergraduate: Scholarship Director, Honor Board Member *2010*
- Undergraduate Student Government, Case Western Reserve University *2009 – 2011*
 • Engineering Representative
 • Finance Committee
- Professional Memberships *2009 – present*
 • Society of Women Engineers (SWE) *2014 – present*
 • Materials Research Society (MRS) *2016 – present*
 • American Association for the Advancement of Science (AAAS)

TEACHING EXPERIENCE

Teaching Assistant, Northwestern University *2013-2014*

Course: Introduction to Transmission Electron Microscopy

- Taught weekly TEM lab sections covering fundamental skills
- Planned weekly office hours to review key concepts and to help with homeworks

Design a Demo Coach, Northwestern University *Spring 2013*

Course: Materials Science 101, materials science for non-engineers

- Explained basic materials science concepts and related topics to tangible experiences
- Guided non-engineering students to design a classroom demonstration to show a concept from the introduction to materials science class

Teaching Assistant, Case Western Reserve University *Spring 2011*

Course: Chemistry of Materials, Engineering Core Curriculum

- Planned and lead a weekly review recitation with a section of the class
- Wrote, administered, and graded weekly quizzes, along with evaluating tests and projects

SKILLS

Nanoscale characterization

- Microscopy: TEM, STEM, SEM, EDS, EELS, FIB, EBSD
- Nanofactory in-situ microscopy, AFM and STM holders
- Raman Spectroscopy

Logistics: program planning, group leadership, task division, online document management

Data visualization: Matlab, SolidWorks, Excel

Media editing: Adobe Audition, Audacity, iMovie

ACTIVITIES

IM Football (2015 Champions), Northwestern University *2011 – 2015*

Varsity Tennis (Scholar Athlete), Case Western Reserve University *2007 – 2009*